Light Coupling in Dimension Mismatch Waveguides for Silicon Photonic Integrated Circuits

by

Md Asaduzzaman

Thesis submitted in total fulfilment of the degree of

Doctor of Philosophy

Department of Electrical and Electronic Engineering

The University of Melbourne

Australia

February 2018

Abstract

In recent years silicon photonics has become a considerable mainstream technology, especially in telecommunications fields to overcome the limitations imposed by copper-based technology. Nanoscale photonic technologies have attracted a lot of attention to co-develop photonic and electronic devices on silicon (Si) to provide a highly integrated electronic–photonic platform. Silicon-on-insulator (SOI) technology that relies heavily on the contrasted indices of Si and SiO_2, enables the design and integration of these photonic devices in submicronic scales, similar to the devices produced by a standard CMOS fabrication platform in the electronics industry. One of the key challenges with these submicronic waveguide devices is to enable efficient coupling with fibre, which is mainly due to the mode-field differences between fibre and the waveguide, and their relative misalignments. To overcome this challenge, various techniques including prism, butt and grating coupling have been proposed. Among them, although butt coupling is an elegant solution for low loss and wideband operation, it often requires post-processing for accurate polishing and dicing to taper the waveguide edges. Therefore, it is not suitable for wafer-scale testing. Grating couplers, which mostly perform out of the plane coupling between a fibre and a waveguide, are also an attractive solution as light can be coupled in and out everywhere on the chip, opening the way for wafer-scale testing.

However, despite such advantages, grating couplers often exhibit low coupling efficiency (CE) due to downward radiation of light that propagates towards substrate through buried oxide (BOX) which comprises 35%-45% of total incident light. Grating couplers are also very sensitive to the wavelength of the light as different wavelengths exhibit specific diffraction properties at the grating, which cause a narrow coupling bandwidth.

In this thesis we have studied various techniques to improve the coupling efficiency and coupling bandwidth of the grating couplers. We have used the finite difference time domain (FDTD) and Eigenmode Expansion (EME) methods to study the interaction of light with grating. The directionality of the coupler which determines the

coupling efficiency has been improved by means of silicon mirrors in the BOX layer that essentially redirect the light propagates toward substrate. For improvement of directionality, an ultra-subwavelength grating coupler has also been developed with an engineered grating structure which exhibits high coupling efficiency and bandwidth without the need for bottom mirrors.

The grating coupler only converts vertical dimension into nano scale, leaving the lateral width in micrometre range typically >15 μm. In order to connect the grating coupler with a nanophotonic waveguide, the grating structure needs to be matched in dimensions both vertically and laterally. Conventionally, to meet the requirement the width of grating structure is gradually tapered to nano scale. The coupling efficiency relies highly on the taper length, which is typically hundreds of micrometres. Such a long taper waveguide causes an unnecessarily large footprint of the photonic integrated circuits. In order to minimise the length of the taper while retaining high coupling efficiency, we have designed two different types of tapered waveguides. One of them is a partially overlaid tapered waveguide and the other is a hollow tapered waveguide.

Preface

The dissertation ultimately discussed the designing of various Grating couplers for light coupling between optical fibre and nano photonic waveguides. None of the text of the dissertation is taken directly from previously published or collaborative articles.

Chapters 4, 5, 6 and 7 are the contributory chapters and presented my original works. I was the lead investigator for the works described in chapters 4, 5, 6 and 7 where I was responsible for all major areas of concept formation, data collection and analysis, as well as the majority of manuscript compositions.

The versions of chapter 4, 6 and 7 are already published in journals while a version of chapter 5 is submitted for publication and is under review. All papers produced from this thesis are co-authored by Dr. Masududzzaman Bakaul, Prof. Efstratios Skafidas and Md Rezwanul Haque Khandokar. I conceive the idea of the works presented in this dissertation and major calculations and analysis performed by me. Dr. Masuduzzaman and Prof. Efstratios have supervised the works. My colleague Md Rezwanul time to time has assisted me to perform the simulations. All authors have contributed in discussion of the results presented in this thesis.

The writing of the thesis is edited by Greg Rowe, New Zealand. He is a professional proofreader and has completed a correspondence course in editing and proofreading provided by an Australian university. Mr. Greg has assisted to improve the quality of writing by editing the English language used to write the thesis.

Declaration

This is to certify that

1. This thesis comprises only my original work towards my PhD candidature.
2. Due acknowledgement has been made in the text to all other materials used.
3. The thesis is less than 100,000 words in length, exclusive of tables, maps, bibliographies and appendices.

……..

Md Asaduzzaman

Acknowledgements

I would like to take this opportunity to thank those who have helped me throughout my PhD. First of all, my utmost gratitude to my supervisors Dr. Masduzzaman Bakaul and Prof. Stan Skafidas. Without their continuous support both intellectually and mentally this thesis wouldn't be realised. I would like to thank Prof. Thas Nirmalathas, chair of my advisory committee, for his valuable comments and ideas throughout my PhD. My sincere thanks to my colleague Md Rezwanul Haque Khandokar for valuable discussions about any hurdles in this work. I am also grateful to all the staff of the department of Electrical and Electronic Engineering and the School of Graduate Research for providing the necessary administrative supports and obviously to The University of Melbourne. Thanks to National ICT Australia (NICTA) for the scholarship, publications and travel funding throughout the candidature.

I am thankful to Dr. Faruq Hossain, Dr. Akter Hossain, Dr. Hemayet Uddin, Dr. Razibul Islam, Dr. Apel Mahmud, Dr. Sajib Saha, Md. Rezwanul Haque Khandokar, Dr. Md. Tauhidul Islam and Ishita Akhter all of whom have helped to make my university life comfortable and friendly.

My sincere thanks to my parents and my brothers and sisters, especially to my elder brother, Abdur Razzaque, for his efforts to make me reach this far.

Finally, I would like to express my heartiest thanks to my lovely wife, Dr. Saifunnahar, and my beautiful daughter, Urshia Zaman, for their sacrifices and encouragement toward the completion of this thesis.

Table of Contents

List of Figures

List of Tables

Chapter 1

Introduction

1.1 Background

The modern electronic IC industries evolved from the concept of Jack Kilby in 1958 where he proposed that it was possible to fabricate resistors, capacitors and transistors using single-crystal silicon [1]. This idea led the technology towards the invention of the first truly integrated circuit: the importance of this invention was recognized by the award of a Nobel Prize to Kilby in 2000. Since then, the microelectronics industry has forged towards the reduction of the individual device size and increases in chip functionality. An example is shown in Fig.1. 1. In parallel with Gordon Moore's prediction in 1962, the trend in the microelectronics industry is towards doubling the device density approximately every two years. The International Technology Roadmap for Semiconductors (ITRS) was formed in 1993 based on Moore's prediction and later evolved as International Roadmap for Devices and Systems (IRDS), which remains relevant today. The roadmap, a document of needs-driven, assumes that the Integrated Circuit (IC) industry will be dominated by Complementary Metal Oxide Semiconductor (CMOS) silicon technology. In fact, the MOSFET have become the basic elements of most standard devices such as high-speed

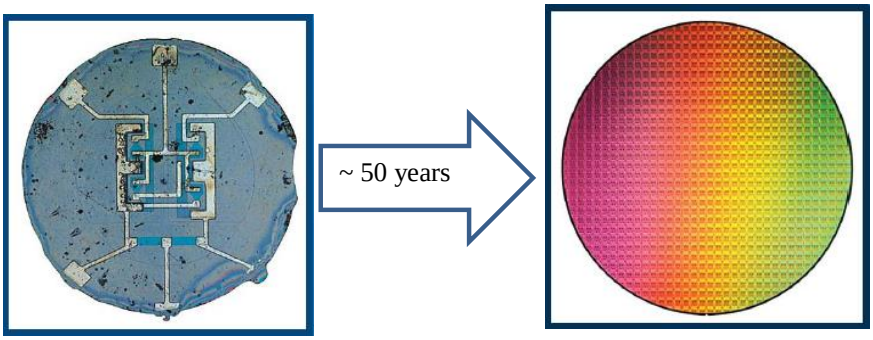

1959, First Silicon IC (Noyce and Kilby)

Today, Billions of Transistors

Fig.1. 1: Density of integration over the past half-century [Courtesy of Intel]

MPU, DRAM and SRAM. The optimum properties of this individual device do not possesses a single material in an integrated circuit. However, silicon has become the base material for integrated circuits in which all the required devices can be fabricated to an acceptable level of performance specification.

By taking the design and fabrication concept from the established microelectronic industry, several research projects were initiated in the 1980s where silicon was the base material for the fabrication of photonic circuits; for example, those circuits that use light as the information carrier rather than electrical charges. Among the projects of that time, the works of Richard Soref at the Rome Air Development Centre in Maine, USA, [2] and of Graham Reed at the University of Surrey, UK [3] were significantly notable. The work of Reed's group was particularly important for the future commercialization of silicon photonic technology as they showed that in silicon-on-insulator (SOI) rib waveguides, a structure in which light could be confined and manipulated and very low loss propagation was possible.

Silicon possesses many optical properties that make it the ideal material for planar lightwave circuit (PLC) fabrication. Silicon is transparent to wavelengths > 100nm while its oxide shares its chemical composition with glass fibre, providing a degree of compatibility with long-haul, fibreoptic technology. The high index contrast between silicon (~3.5) and its oxides (~1.5) allows the fabrication of waveguides on the nanometre scale. However, other than the advantageous properties of silicon stated above, there is an unsettled limitation of silicon in the photonic arena. Silicon is an indirect bandgap material which prevents the efficient emission of light and hence the inability to form optical sources from silicon (the greatest challenge for silicon photonic researchers), detectors compatible with subbandgap wavelengths.

In the early days of integrated silicon photonics, prior to 2000, applications were found mainly in the area of telecommunications. At that stage (first-generation, earlier than 2004) the waveguide cross-section was relatively large (~ 10-100 μm^2) and so was suitable for use in optical networking, e.g. wavelength division multiplexing and optical switching. The explosive growth of telecommunications in the late 1990s further increased the motivation for integrated photonic circuit fabrication in this field. At that time, Bookham Technology of the UK (founded by Andrew Rickman, a graduate of

Graham Reed's Surrey group) showed that photonic circuits can be fabricated in large volumes of devices in a cost-effective way with procedures used by the microelectronic industry. In the 1990s there was a dramatic increase in the number of engineers and scientists who were dedicated to development of photonic devices. This consequently led to the production of a wide array of photonic devices and at the same time the role of photonic devices beyond the telecommunication arena has been realized.

In early 2004, Intel Corporation demonstrated an optical device developed by the group led by Mario Paniccia. This device was fabricated wholly in silicon with the same techniques and protocols that are used for fabrication of transistors and the modulation of an embedded optical signal was achieved at speeds greater than 1 GHz by this device [4]. With this demonstration, the potential for excessive power dissipation reduction in microelectronics circuits by integrating photonic and electronic functionality has been realized. In the same year, text books were published specifically based on the topic of silicon photonic technology [5] [6]: this is a further indication that the silicon photonic is the future of mainstream technology. The field of silicon photonic then expanded rapidly due to its prominent technological applications, the need for miniaturization and high performance. Nowadays, the dimensions of waveguides are in the scale of nanometres rather than microns and modulation speeds greater than 20 GHz have been demonstrated [7]. The possibility of subbandgap detection has been reported in [8] at speeds compatible with fast modulation speeds of > 40 GHz. Perhaps the most significant development in silicon photonic technology is the integration of laser technology with silicon circuits [9].

The evolution of microelectronic technology has now reached the stage where device features that are significantly smaller than the optical wavelength can easily be fabricated with very high precision. To take advantage of this trend, it is necessary to make correspondingly small optical devices. A very high degree of miniaturization demands a high index contrast, in order to achieve small bend radii and greater confinement. On the other hand, such high index contrast structures are more susceptible to process inaccuracies and scattering due to surface roughness. These problems are being addressed by continued progress in microelectronics fabrication.

Semiconductor systems such as InP/air and Si/SiO_2 offer the high index contrast necessary to create such structures. Additionally, these semiconductors exhibit very low absorption at 1.55 μm, which is the wavelength of interest for optical communications. While the InP/air system is very attractive on account of the potential to integrate optically active and passive devices on a single chip, InP is still beset by processing issues, and is not the material of choice in the electronics industry. This issue assumes special importance since many optical devices require the presence of significant electronic control in order to work effectively. A silicon-based material system, on the other hand, offers the possibility of integrating both electronic and optical functions on a single substrate, with processing technology that is already well understood and is in wide industrial use. The rest of this chapter will briefly discuss silicon optoelectronics, with specific reference to the Si/SiO_2 material system that offers great potential for the integration of both electronic and optical functions on a single substrate. In particular, we will discuss the problem of coupling light into an SOI nanophotonic IC, which will motivate the work in the rest of this dissertation.

1.2 Silicon Waveguides

The fundamental building blocks for all silicon photonic circuits are silicon waveguides. Thus it is worth to describe the structure briefly.

The bandgap of silicon is 1.12 eV, making the absorption band edge of silicon at a wavelength of 1100 nm. For wavelengths shorter than 1100 nm, silicon is a highly absorbent material and is thus very important for photonic detectors. On the other hand, for wavelengths longer than 1100 nm, pure silicon becomes transparent and hence appropriate for optical waveguides to propagate light efficiently. The wavelengths for optical telecommunications bands center at 1300 nm and 1550 nm where silicon is transparent and thus highly integrated silicon photonic circuits are designed for use at these longer wavelengths, mostly for wavelengths around 1550 nm where a significant compatibility exists for long-haul fibreoptic communications.

The light confinement of an optical signal depends on the material systems that possess the right variations in the refractive index [10] [11]. This is also a requirement to support low-order optical mode propagation such as single-mode propagation [12].

There are several ways to fabricate such systems using silicon. For instance, a variation in the refractive index can be achieved by creating a silicon composite alloy or by doping in pure silicon. This highly doped low-index silicon acts as the cladding for silicon waveguide layers [13]. In some cases silicon-germanium alloys have been used as optical waveguides as such alloys have a higher refractive index than that of pure silicon while pure silicon used as substrate [14]. However, in the last few years, silicon-on-insulator (SOI) has become the most appropriate platform for fabrications of silicon photonic devices. The well-established microelectronics industry is based on the SOI material and hence the availability of the SOI for the fabrication of photonic devices is guaranteed. The variation of dimensions of Si and SiO_2 layers on SOI allows flexibility to fabricate an array of photonic devices required in an integrated chip. The strong vertical confinement of light propagating in the silicon overlayer of SOI is achieved by utilizing the properties of high contrast of refractive index between Si and SiO_2 while for the lateral confinement rib structures may be used by inducing a variation in the effective index of silicon overlayers [15] [16].

Despite the advantages of high confinement of optical mode in silicon-on-insulator (SOI), it suffers from high birefringence which causes differences in refractive indices for TE and TM polarisations [17]. Such birefringence of the materials is introduced because of the cross-sectional geometry of the device and various stress levels throughout the device regions. Due to fabrication limitations, the effects of birefringence may not be eliminated totally but can be reduced with improved fabrication techniques [18] [19].

Using a SOI platform, the dimensions of the waveguides reduce to a sub-micronic level but it introduces propagation constraints due to surface roughness [20] [21]. In order to minimise this surface roughness, several fabrication processes have been developed, such as the thermal oxidation process [22] [23] and suppressed scattering [24]. Althogh these process improve the quality of the waveguides, thay also have their own limitations e.g. residual stress in silicon and harsh prosessing conditions such as high temperatures. The reduced surface roughness is achived in [25] based on self-perfection by liquefaction (SPEL) with a very high processing speed. Waveguides with smooth side walls have been fabricated using an etchless process [26][29]. The

transmission loss due to material absorption in silicon slot waveguides have been investigated for different wavelengths including the telecommunications band [30] [31] and high silicon absorption band [32] [33]. Several studies have reported low loss waveguides for photonics applications with improvments in fabrication techniques [34] [39].

The silicon waveguides also suffer from temperature sensitvity which complicates the development of ultra-densed integration of the photonic integrated circuits [40]. Several methods have been proposed to to minimise the thermal effects of silicon waveguides. In [41] the positive thermo-optical (TO) coefficient is reduced using polymer cladding with negation TO coefficient. A temperature-independent subwavelength and bridged subwavelength grating-based waveguides are demonstrated in [42] [43] where the grating grooves are filled with polymer with a suitable filling factor. The dimensions of waveguides have been further controlled to achieve fundamental mode propagation only, such as single-mode, with low-loss (< 1 dB/cm) [44].

1.3 Fibre coupling into nano photonic waveguides

While the use of a high-contrast refractive index such as SOI allows fabricating ultra-low scale photonic waveguides, it severely complicates the interfacing between optical fibres and these low-scale waveguides. In the integrated silicon-based photonic devices and systems, the most dominant source of loss in SOI waveguides is the coupling to the optical fibre. It is mainly due to the large difference in both mode size and index contrast between the single mode fibre and the waveguide as shown in Fig. 1.2. So the direct coupling between them causes highly excessive loss of light. This may be one of the most critical problems that high-contrast devices face in practical applications.

Another major source for propagation loss in a SOI waveguide operating at $\lambda=1.55\ \mu m$ is the waveguide surface roughness, which is caused by imperfections in the waveguide during fabrication processes [45]. For achieving low propagation loss below 1 *dB/cm*, very precise fabrication processes and very accurate lithography technology are required [46]. Over the years, novel strategies have been demonstrated to achieve

ultra-low loss silicon waveguides fabricated without any silicon etching, making it possible to reduce propagation loss down to 0.3 *dB/cm* [47].

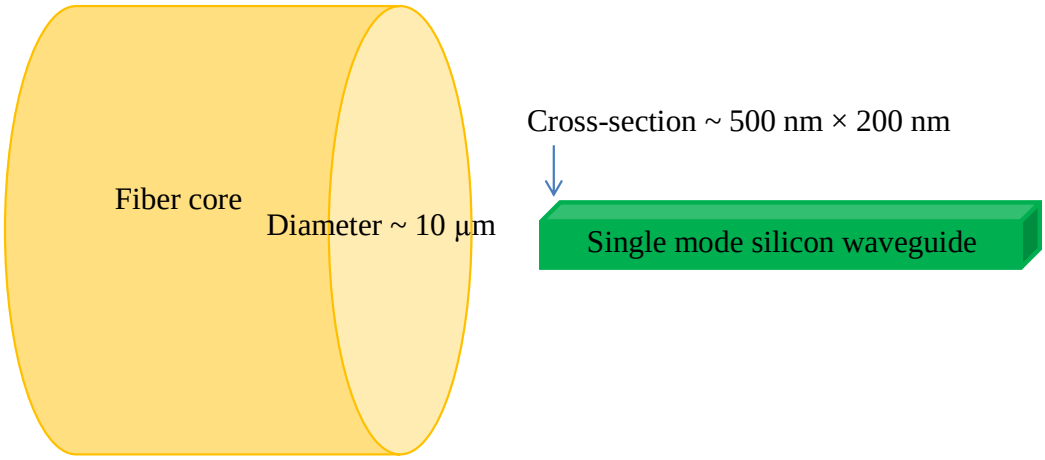

Fig.1. 2: Typical dimension of optical fibre core and nano photonic waveguide.

From the calculation of the power overlap integral between the electric field profile of the fundamental mode in the fibre (E_f) and in the waveguide (E_{wg}) at the fibre-waveguide interface, we can evaluate the coupling loss factor due to differences in mode size between the optical fibre and the SOI waveguide at any point of direction of propagation. The overlap loss factor (i.e. at z = 0) is given in [5] as

$$\Gamma = \left(\frac{\int_{-\infty}^{\infty}\int_{-\infty}^{\infty} \left|E_{wg}\left(x,y,z=0\right)\right|\left|E_{f}\left(x,y,z=0\right)\right| dxdy}{\sqrt{\int_{-\infty}^{\infty}\int_{-\infty}^{\infty} \left|E_{wg}\left(x,y,z=0\right)\right|^{2} dxdy \int_{-\infty}^{\infty}\int_{-\infty}^{\infty} \left|E_{f}\left(x,y,z=0\right)\right|^{2} dxdy}} \right)^{2} \qquad \text{(Eq.1.3.1)}$$

where the denominator of Equ. (1.3.1) is basically a normalising factor. The loss factor Γ gives the value between 0 and 1, and therefore characterizes the range between no coupling (for Γ=0) and total coupling (for Γ=1) due to field overlap. The loss factor value 1 indicates that the field overlaps completely and 0 indicates no overlap at all between field profiles.

Impedance mismatching between two surface boundaries due to the difference in the index contrast causes coupling loss. We can evaluate this coupling loss factor by

using the expression for the normal reflection in a discontinuity between two materials [48].

$$R = \left| \frac{n_{eff,f} - n_{eff,wg}}{n_{eff,f} + n_{eff,wg}} \right| \qquad \text{(Eq.1.3.2)}$$

where R is the reflection of the surface interface, $n_{eff,f}$ and $n_{eff,wg}$ are the fibre and waveguide fundamental mode effective indices, respectively.

Finally, power input coupling loss (L_c) taking into account both factors or terms, and so expressed in *dB*, is:

$$L_c = -10\log_{10}\Gamma - 10\log_{10}\left[(1-R)^2\right] \qquad \text{(Eq.1.3.3)}$$

For solving Equ. 1.3.1, the electric field profile of the optical mode in the fibre (E_f) can be approximated by a Gaussian-like profile, according to the following expression [49]:

$$\left|E_f(x,y,z=0)\right| = E_{\max}.e^{-\left(\frac{x^2+y^2}{\omega_0^2}\right)} \qquad \text{(Eq.1.3.4)}$$

where ω_0 is defined as the diameter of the beam for which the electric field amplitude has decayed to ($1/e$) of its maximum value, E_{max}. The mode field diameter of an optical fibre (MFD) is related to ω_0 by means of [50]:

$$MFD = 2\omega_0 \qquad \text{(Eq.1.3.5)}$$

Beside the fact that high coupling losses are obtained when butt-coupling an optical fibre to a SOI waveguide, there is another important fact to be considered in the coupling. Due to reflections in the fibre-waveguide coupling plane, the waveguide behaves as a Fabry-Perot cavity. So, when the light is injected into the waveguide, output optical intensity (I_o) is related to input intensity (I_i) according to the following well-known Fabry Perot formula [5]:

$$\frac{I_0}{I_i} = \frac{(1-R)^2 e^{-\alpha L}}{\left(1-R\cdot e^{-\alpha L}\right)^2 + 4\cdot R\cdot e^{-\alpha L}\sin^2\left(\phi/2\right)} \qquad \text{(Eq.1.3.6)}$$

where R is the reflection in the waveguide edges (assuming it is the same in the input as in the output), α is the waveguide propagation loss, L is the waveguide length, and ϕ is the phase difference between each succeeding reflection in the cavity, and is related to the wavelength (λ) by (for normal incidence) [5]:

$$\phi = \left(\frac{2\pi}{\lambda}\right) 2nL \qquad \text{(Eq.1.3.7)}$$

where n is the refractive index in the cavity.

Therefore, an efficient fibre-to-chip coupling structure will basically aim to accomplish two main objectives. On one hand, it will try to decrease the coupling losses between the optical fibre and the SOI access waveguide of the chip as much as possible. On the other hand, it will try to overcome the Fabry-Perot resonance effect, thus trying to get a flat spectral response.

1.4 Research focus

Coupling light between optical fibres and a nano photonic waveguide is a non-trivial task. The prospect of downsizing the footprint of photonic integrated circuits (PICs) with utilising the SOI facility often raises issues when coupling them with outside uses, for instance, with optical fibre. From long and short haul optical communications to chip-to-chip or even intra-chip communications, they all require connection with optical fibre. However, connecting the optical fibre is not straightforward as the physical dimensions of fibre and photonic waveguides differ by the order of 10^3. Therefore, direct connection between them causes excessive loss of light. Among the various coupling methods, the grating coupler is the preferred solution, mainly due to CMOS compatibility. However, low coupling efficiency and bandwidth limits their implementations in many applications.

In this thesis we have investigated various techniques to improve the coupling efficiency and coupling bandwidth. In a grating coupler, the leakage power that propagates through BOX and coupled into substrate can reach up to 45% of incident power. Such a large power loss causes poor coupling efficiency of the grating coupler. By improving the directionality of a coupler, this leakage can be minimised. In this

work we have designed a grating coupler with multiple pairs of Si-SiO_2 in a BOX layer to enhance directionality. Another way to improve directionality is to utilise the subwavelength structure. In such a design, the number of diffraction orders is reduced and power can be concentrated into a single order: by modifying the diffraction angle, the directionality of the coupler is improved.

The grating coupler only converts the vertical dimension into nano scale leaving the lateral width in micrometre range, typically >15 μm. In order to connect the grating coupler with the photonic waveguide, the grating structure needs to be matched both vertically and laterally. Conventionally, to meet this requirement the width of grating structure is gradually tapered to a nano scale. The coupling efficiency relies strongly on the taper length, which typically is hundreds of micrometres. Such a long taper waveguide causes an unnecessarily large footprint of the photonic integrated circuits. In order to minimise the length of the taper while conserving high coupling efficiency, we have designed two different types of tapered waveguides. One of them is a partially overlaid tapered waveguide and other is a hollow tapered waveguide.

1.5 Thesis outline

This thesis has eight chapters including this introduction and a conclusion, and is organised as follows.

Chapter 2: Literature review

In this chapter we discuss the evolution of the grating coupler and prior works on coupling mechanisms. The main categories of coupling schemes that appear most in the literature are the butt coupling and grating coupling. The working principle of butt coupling is the modal conversion in a tapered waveguide whereas a grating coupler works based on the diffraction principle of light.

Chapter 3: Theory of grating coupler

This chapter explores the theoretical background of the grating coupler. The incident wave of light on grating surface is diffracted in infinite numbers of discrete orders, called diffraction order, due to the effect of the grating. Although the diffraction

orders are theoretically infinite, only a few orders physically exist in a specific design. Total incident power is then divided into those diffraction orders which are redirected into a transmission medium with a certain angle, called the diffraction angle. To find the coupling efficiency of the grating coupler, one has to find the power in an individual diffraction order, called diffraction efficiency, and the corresponding diffraction angle. Using a grating equation, the diffraction angle can be calculated. However, finding diffraction efficiency requires solving Maxwell's equations which often require computer-aided design and simulation. Such solutions of Maxwell's equations can be found based on a finite difference time domain (FDTD) method with the help of Yee's algorithm and Eigenmode Expansion (EME) method.

Chapter 4: Silicon Reflector Based Grating Couplers

This chapter describes the design of a highly efficient, wideband silicon coupler for interconnection between fibre and nano-scale waveguides by simultaneously applying techniques of light redirection, mirror-reflection, and surface gratings. We took advantage of using a silicon-mirror in the grating coupler that effectively overcomes the efficiency- limiting factors associated with coupling through the buried oxide (BOX) layer and low bandwidth response of coupled light.

As indicated earlier, coupling efficiency largely relies on how successfully the part of light passing through the BOX and the Si-substrate of a typical single layered structure can be reflected towards the waveguide. To enable such reflection, instead of a thicker SiO_2 BOX layer, a wafer structure with multiple thinner layers of Si-SiO_2 paired onto the Si-substrate can be developed. Each Si-SiO_2 interface acts as a mirror to reflect a certain amount of light, and after several reflections, most of the light passed through the BOX and the Si-substrate combines with the light towards the waveguide. The insertion of Si and SiO_2 layers, however, is not straightforward, as the structure will complement coupling efficiency only if the reflected light waves from the Si-SiO_2 interfaces interfere constructively with the originally guided light wave towards the waveguide. To obtain optimum thickness of the layers, numerical method is developed.

Chapter 5: Engineered Subwavelength Grating Coupler for High Directionality

The enhancement of the directionality of coupler based on subwavelength grating is discussed in this chapter. Exploiting such a structure, the diffraction orders can be reduced to fewer orders and even can be left with only single diffraction order along with specular 0^{th} order diffraction. The incident power then can be concentrated in that order by an appropriate modification of the grating structure and, by manipulating the effective refractive index, more power can be redirected toward the waveguide. Therefore the efficiency of the coupler improves significantly.

Chapter 6: Compact Grating Coupler with Partially Overlay Tapered Waveguide

To connect the grating coupler to a nano photonic waveguide, the structure needs to be tapered into a nano scale. In this chapter we describe the design of a partially overlay tapered waveguide structure that converts the lateral width of a grating structure within a very short length without much compromise with coupling efficiency and bandwidth. That ensures the small footprint of the coupler in photonic integrated circuits.

Chapter 7: Compact Grating Coupler based on Hollow Tapered Waveguide

In this chapter, designing of compact grating coupler based on hollow tapered waveguide (HTW) is proposed and investigated for lateral matching of the coupler with a nano photonic waveguide. In HTW, light is guided through a tapered hollow core where the optical modes are converted from loosely confined mode to highly confined mode. HTW is designed by inserting two Si strips one ends of which are connected with grating waveguide and other ends merge together to form a hollow core. For effective recapturing of the mode to couple to the nano-scale waveguide device, the widths of the Si strips are adiabatically increased until it supports a mode to confine within the merged Si strips which eventually connected with nano waveguide.

Chapter 8: Conclusion and future works

This chapter summarises the works and outlines the directions towards future motivations.

1.6 Contributions and major outcomes

Keeping the research focus in mind as described in the previous section, a summary of the main findings and contributions are here presented.

Chapter 4:

- Investigate the enhancement of coupling efficiency and bandwidth of a silicon reflector- based grating coupler.
- Mathematical formulas have been developed to calculate optimum thickness of the layers for constructive interference.
- A wafer structure with multiple pairs of Si-SiO_2 is proposed to redirect the light that passes through BOX towards waveguide.
- The effects of various grating parameters have been studied and optimised for maximum coupling efficiency and bandwidth.
- With this optimised design, the grating coupler shows coupling efficiency of 78% and 1-dB coupling bandwidth of 77 nm.

Chapter 5:

- Subwavelength grating structure has been employed to design the coupler with high directionality.
- With the basic design and normal incident of light, coupling efficiency of 43% is achieved with 1-dB coupling bandwidth of 26 nm.
- Higher directionality is achieved by breaking the symmetry of the structure using asymmetric grating trenches.
- Additional ultra-subwavelength structure is designed for further enhancement of the directionality and coupling efficiency of 85% is calculated with optimised parameters where the 1-dB coupling bandwidth is 53 nm.

Chapter 6:

- In order to connect the grating coupler with nano photonic waveguides, partially overlay tapered waveguide is designed.
- Both the conventional and inverse taper have also been studied for the purposes of comparison with the partially tapered waveguide.
- This study shows that with an inverse taper, the coupling efficiency can be improved but at the expense of a longer taper compared with a conventional taper.
- Using conventional taper length of ~ 800 µm, the coupling efficiency of 58% is achieved. Whereas an inverse taper provides ~ 80% coupling efficiency, but the length was ~ 1600 µm.
- In contrast with conventional and inverse tapers, the partially overlay tapered waveguide shows coupling efficiency of ~ 78 % for taper lengths as short as ~ 60 µm.

Chapter 7:

- A new compact silicon grating coupler enabling fibre-to-chip light coupling at a minimized taper length is proposed.
- The proposed coupler, which incorporates a hollow tapered waveguide, converts the spot-size of optical modes from micro- to nano-scales by reducing the lateral dimension from 15 µm to 300 nm at a length equals to 60 µm.
- The incorporation of such a coupler in photonic integrated circuit causes a physical footprint as small as 81 µm × 15 µm with coupling efficiency and 3-dB coupling bandwidth as high as 72% and 69 nm respectively.

1.7 List of publications

The results from this PhD work have been published in various journals and conferences. Some of them were recently submitted and are under peer review process. The list of the papers is presented below.

1. **Md Asaduzzaman**, Masuduzzaman Bakaul, Efstratios Skafidas, Md Rezwanul Haque Khandokar, "Compact grating coupler with hollow tapered waveguide", *Scientific Reports* 8:2540, 2018. DOI: 10.1038/s41598-018-20875-3.
2. **Md Asaduzzaman**, Masuduzzaman Bakaul, Stan Skafidas, Md Rezwanul Haque Khandokar, "Compact grating coupler with partially overlay tapered waveguide", *IEEE Photonics Journal*, Vol. 9, No. 2, 2017.
3. **Md Asaduzzaman**, Masuduzzaman Bakaul, Stan Skafidas, Md Rezwanul Haque Khandokar, "Multiple Layers of Silicon-Silica (Si-SiO_2) Pair onto Silicon Substrate towards Highly Efficient, Wideband Silicon Photonic Grating Coupler", *Optical and Quantum Electronics*, 48(10), 1-13, 2016. DOI: 10.1007/s11082-016-0746-0.
4. **Md Asaduzzaman**, Masuduzzaman Bakaul, Efstratios Skafidas, Md Rezwanul Haque Khandokar, "Perfectly Vertical Broadband Fiber-to-chip Grating Coupler Based on Asymmetric Grating Trenches", *Nanophotonics*, (under review).
5. Md Rezwanul H Khandokar, Masuduzzaman Bakaul, Stan Skafidas, Thas Nirmalathas, **Md Asaduzzaman**, "Characterization of Geometry and Depleting Carrier Dependence of Active Silicon Waveguide in Tailoring Optical Properties", *Photonics Research*, Vol.5, No. 4, pp.305-314, 2017.
6. Md Rezwanul H Khandokar, Masuduzzaman Bakaul, Stan Skafidas, Thas Nirmalathas, **Md Asaduzzaman**, "Performance of Planar, Rib, and Photonic Crystal Silicon Waveguides in Tailoring Group-Velocity Dispersion and Mode Loss", *IEEE Journal of Selected Topics in Quantum Electronics*, Vol.: 22, Issue: 2, 2016.
7. Md Rezwanul H Khandokar, Masuduzzaman Bakaul, **Md Asaduzzaman**, Stan Skafidas, Thas Nirmalathas, "Performance Enhanced Butt Coupling for Effective Interconnection between Fiber and Silicon Nanowire", *IEEE Journal of Quantum Electronics*, Vol. 52, No. 9, 2016.

Some papers have been presented at international conferences and published in the conference proceedings as listed below:

8. **Md Asaduzzaman**, Masuduzzaman Bakaul, Stan Skafidas, Md Rezwanul Haque Khandokar, "Ultra-compact Broadband High Efficient Grating Coupler *", 2015 IEEE International Broadband & Photonics Conference (IBP),* p. 31-34, 2015**.**
9. Md Rezwanul H Khandokar, Masuduzzaman Bakaul, Stan Skafidas, Thas Nirmalathas, **Md Asaduzzaman**, "Electrical and Optical Response of Depleting Carrier in Active PIN Silicon Waveguides", *2015 IEEE International Broadband & Photonics Conference (IBP),* p49-54, 2015**.**
10. Md Rezwanul H Khandokar, Masuduzzaman Bakaul, Stan Skafidas, Thas Nirmalathas, **Md Asaduzzaman**, "Controlling Group Delay in Single and Multi-stage Slotted Ring Resonator with Fabrication Tolerances", *2015 IEEE International Broadband & Photonics Conference (IBP),* p27-30, 2015**.**
11. **Md Asaduzzaman**, Masuduzzaman Bakaul, Stan Skafidas, Md Rezwanul Haque Khandokar, "High Signal-to-Noise Ratio and High Efficient Broadband Grating Coupler with Metal Reflector", *5th Internatinal Conference on Metamaterials, Photonic Crystals and Plasmonics, META'14 Conference,* Singapore, 20 – 23 May, 2014.
12. Md Rezwanul H Khandokar, Masuduzzaman Bakaul, Stan Skafidas, Thas Nirmalathas, **Md Asaduzzaman**, "Dispersion and Loss Analysis in Circular and Bragg Core Passive Silicon Waveguides", *Asia Communications and Photonics Conference (ACP),* China, 11-14 November, 2014.
13. Md Rezwanul H Khandokar, Masuduzzaman Bakaul, Stan Skafidas, Thas Nirmalathas, **Md Asaduzzaman**, "Performance Bounds of Geometry Dependent Silicon Waveguides", *5th Internatinal Conference on Metamaterials, Photonic Crystals and Plasmonics, META'14 Conference,* Singapore, 20 – 23 May, 2014.
14. **Md Asaduzzaman**, Masuduzzaman Bakaul, Stan Skafidas, Md Rezwanul Haque Khandokar, "High Efficient Multi-layered Silicon Mirror Based Grating Coupler with High SNR", *Australian and New Zealand Conference on Optics and Photonics (ANZCOP),* Australia, 8-11 December 2013.

15. **Md Asaduzzaman**, Masuduzzaman Bakaul, Stan Skafidas, Md Rezwanul Haque Khandokar, "Wide Band Silicon Mirror Based Grating Coupler for Silicon Integrated Photonics", *4th Internatinal Conference on Metamaterials, Photonic Crystals and Plasmonics, META'13 Conference,* 18–22 March 2013.
16. Md Rezwanul H Khandokar, Masuduzzaman Bakaul, Stan Skafidas, Thas Nirmalathas, **Md Asaduzzaman**, "Performance Bounds of Silicon Waveguides in Engineering Dispersion", *Australian and New Zealand Conference on Optics and Photonics (ANZCOP),* Australia, 8-11 December, 2013.
17. Md Rezwanul H Khandokar, Masuduzzaman Bakaul, Stan Skafidas, Thas Nirmalathas, **Md Asaduzzaman**, "Tailoring Dispersion by Exploiting Geometry of Silicon Waveguides", *Australian and New Zealand Conference on Optics and Photonics (ANZCOP),* Australia, 8-11 December, 2013.

Chapter 2

Literature Review

2.1 Overview

The copper-based communication system networks struggling to handle high data traffic due to their inherent limitations of resistivity and capacitance cause excessive loss of data with distance transmission and limited bandwidth of the systems. Another field that is also suffering from this limitation is the data transfer in intra-chip and between chips, especially for high-speed computing due to inefficient data transfer into and out of processors and memory [51]. To overcome such limitations, the data can be transferred by means of light pulses instead of electronics. Optical fibre is used to transmit the light pulses over long distances without those losses experienced in copper-based transmissions. Hence, more and more data can be transferred using high bandwidth which eases handling high data traffic demands. The use of light pulses requires photonic devices to be developed and integrated into existing electronic devices. The demand of integration of photonic and electronic devices raises an issue about the choice of materials for photonic devices. The materials in Groups III-V of the periodic table e.g. GaAs, InP, possess good optical properties. Unfortunately they are not the first choice of materials for the well-matured CMOS-based electronic industry: rather, it uses silicon to build the devices. Here we are fortunate that silicon also exhibits optical characteristics. The band gap of silicon is such that it becomes transparent at wavelengths over 1100 nm and the telecommunications band lies in the range of ~1300 nm - 1600 nm with a centre wavelength at ~ 1550 nm of our interest. So at this band of wavelength silicon is a good material for transmitting light through it and hence can be used as an optical waveguide. However, there are other challenges in using silicon at these wavelengths: as it becomes transparent it is very difficult to realize silicon as an optical source and detector. That is another topic of the research. In this dissertation we consider silicon as the material for building optical waveguides at telecommunications wavelengths. Here we use the term “silicon photonics” as the

photonic components are built onto silicon. Silicon photonics is currently a very important topic being discussed around the world, not only in universities but also in big industries like IBM, Intel, Luxtera [52]-[54].

2.2 Coupling schemes

As described in Chapter 1, the coupling of light into a nano photonic waveguide is not trivial. The dimension mismatch between optical fibre and a nano waveguide is in the order of 10^{-3}. Therefore, direct coupling between them is like pouring water from a bucket into a straw. Most of the light from the fibre passes out of the waveguide and causes excessive loss of light. So in order to couple light between fibre and a nano waveguide efficiently, some sort of technique is necessary. Among many approaches, prism coupling, butt coupling, end-fire coupling and grating coupling are those which have most commonly appeared in the literature [5]. Based on the fibre positions, these coupling techniques are categorised into two different types:

i) Vertical coupling, and

ii) Lateral coupling

2.2.1 Vertical coupling

In vertical coupling techniques, light is injected onto the surface of the waveguide at a specific angle. We call them vertical coupling techniques because the optical fibre is placed vertically over the waveguide. The most important vertical coupling techniques are found in the prism coupler and grating coupler [5]. The coupling principles of these techniques are depicted schematically in Fig.2. 1 and Fig.2. 2 respectively.

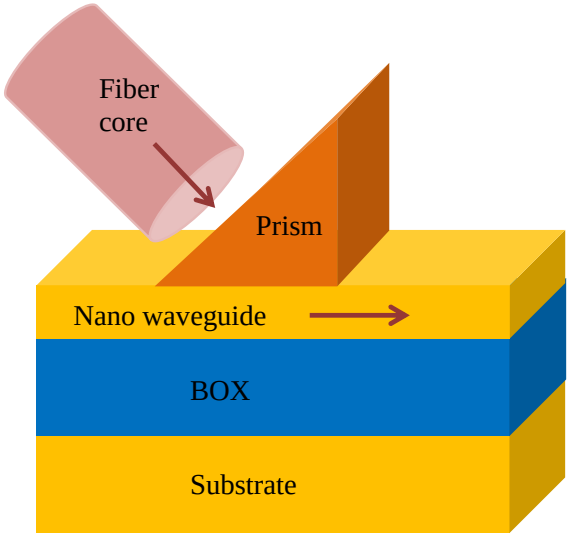

Fig.2. 1: Structure of the Prism coupler

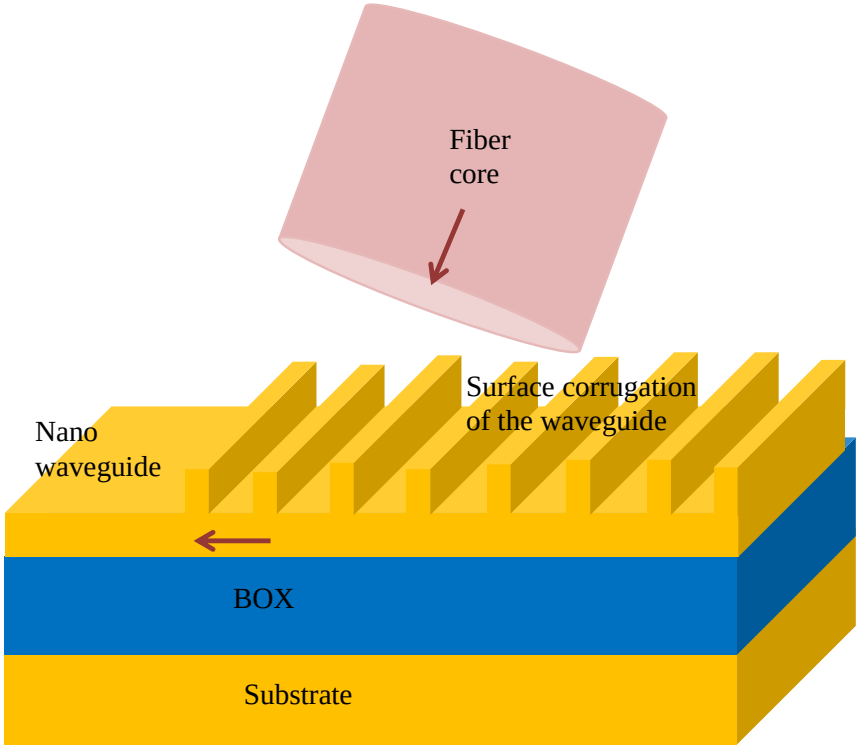

Fig.2. 2: Structure of the grating coupler

Among these techniques, prism coupling is not particularly useful for the purposes of a semiconductor waveguide evaluation. This is because the working principle of the prism coupler is such that prism material should have a higher refractive index than that of the waveguide. This condition seriously limits the possibilities, especially for silicon which already has a relatively high refractive index (n ~ 3.5). Not many other materials

having a refractive index higher than silicon also possess optical properties and are also compatible with complementary metal oxide semiconductor (CMOS) process technology. Although prisms could be made from other materials, such as germanium, other limitations apply to make that technique inferior to other techniques. These limitations include damaging the surface of the waveguide, which is inappropriate when a surface cladding is used, and prism coupling is certainly not suitable for material systems that utilise rib waveguides such as the silicon technology [5]. Such limitations of the prism coupler restrict its application in photonic circuitry. Nevertheless, using a prism coupler in principle means that light can be coupled efficiently from fibre into a nano waveguide as reported in [55] that ~ 75% coupling efficiency has been achieved utilizing the prism coupler.

Therefore, given those limitations, we will focus on grating couplers as a vertical coupling and butt-coupling as a lateral coupling technique.

A grating coupler is basically a one dimensional (1D) diffractive structure that can be designed to couple light onto the waveguide surface by means of one of its orders of diffraction. One of the pioneer grating couplers for efficiently coupling single mode fibres onto compact planar SOI waveguides was demonstrated in [50], and is illustrated in Fig.2.2. A grating coupler is based on the diffraction principle of light, the phenomenon that is widely observed in nature, e.g. the rainbow. The diffraction law states that the direction of light propagation can be modified using edges of objects. In a grating coupler, the change in direction of light is effected using the corrugated structure of the waveguide surface as shown in Fig.2.2. The grating coupler allows wafer level testing and avoids dicing and polishing of the edges and facets, offering mass production at low cost. Despite such advantages, the grating coupler has weaknesses regarding coupling efficiency and bandwidth. As it operates on the diffraction principle, it is highly dependent on wavelengths with a narrow coupling bandwidth when compared to butt coupling [56]-[62].

2.2.2 Lateral coupling

In both butt coupling and end-fire coupling, the light from one waveguide end shines onto another waveguide end. The only difference is that in case of end-fire coupling, a lens is employed between the two ends of the waveguides. Fig.2. 3 shows the schematic of a butt coupler while Fig.2. 4 shows the schematic of an end-fire coupler. In the latter, the light from the fibre is shone onto a common focal point of the waveguide using a lens. In butt coupling, a lens can be used at the fibre tip (called lensed fibre) which squeezes the mode field of the fibre and improves coupling efficiency.

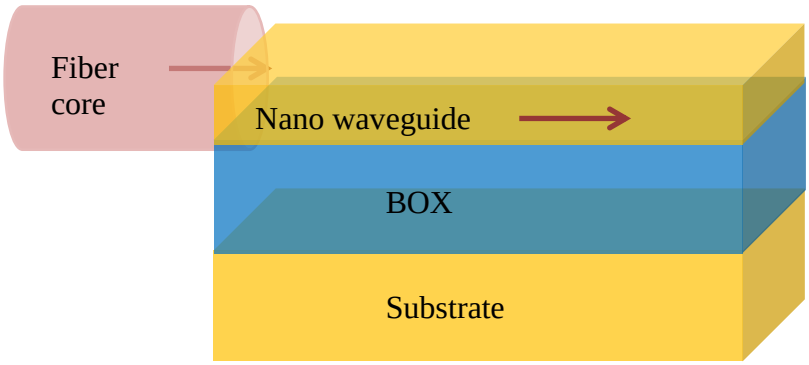

Fig.2. 3: Butt coupler

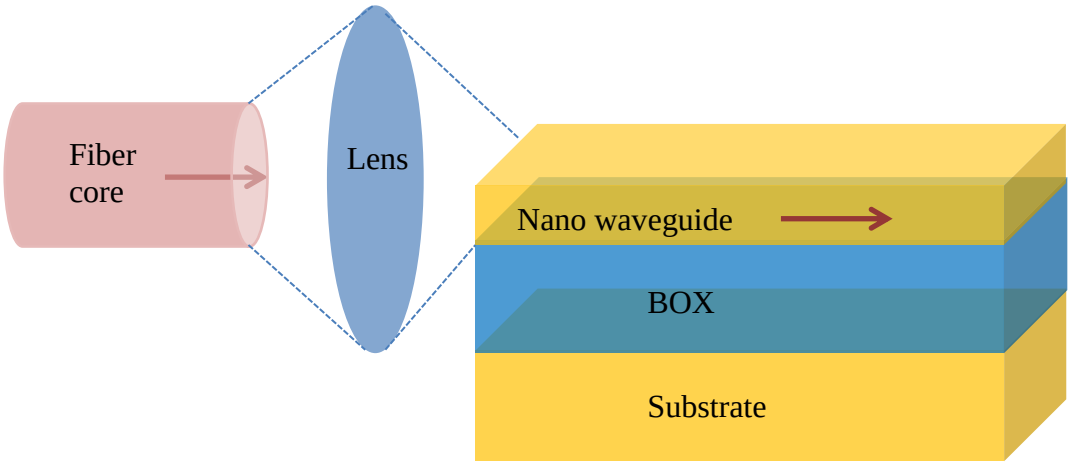

Fig.2. 4: End-fire coupler

As a direct butt-coupling between a standard SMF and a nanophotonic SOI waveguide means suffering ultra-high coupling loss, a solution for an efficient butt-coupling relies on the use of tapered spot-size converters (SSC) [63]. A tapered spot-size converter (or taper) is a waveguide whose dimensions change along the propagation direction from chip to fibre, creating a transition from a small to a large mode. It is thus able to convert the small size optical mode of the nanophotonic waveguide into a larger size optical mode, and vice-versa. If the taper transition is slow enough that the conversion is 100% efficient, the taper is then called an adiabatic taper. The most suitable theoretical solution to the waveguide-fibre mode conversion problem is 3-D tapered waveguide, which increases the size both laterally and vertically in the direction of chip-to-fibre (see Fig.2. 5) [64]. Due to the major difference in size between the optical modes of the fibre and the waveguide, such a taper should be in the order of several millimetres long. Moreover, the fabrication of such a 3-D structure is rather complicated, as it is not compatible with planar CMOS mass-production processes. Another solution is based on the fact that the optical mode in the waveguide is expanding out from the core as the waveguide core gets smaller. So, a 3-D taper with decreasing dimensions both laterally and vertically along the waveguide-to-fibre direction (also known as inverted taper or inverse taper) is proposed [65]. Although shorter tapers can be obtained, fabrication of this structure is still beyond planar fabrication limits, as it still remains a complicated 3-D structure. Actually, not many experimental results have been reported in literature on the 3-D taper. A more elegant solution which is in planar geometry is a planar single-stage inverted taper [66] (see Fig.2. 6). The nanophotonic waveguide is tapered down laterally until its tip width is of the order of tens of nanometres. Thus, the mode is forced to leave the silicon waveguide and start propagating into another low-medium index contrast fibre-adapted waveguide which is placed over the silicon material (see Fig.2. 6). Due to its planar geometry (constant height), this structure can be fabricated using conventional CMOS-compatible machinery. The main drawback of this structure is the high lithography resolution needed to achieve such a narrow inverted taper tip in many cases. When studying horizontal coupling techniques, we will so focus on single-stage planar inverted taper-based structures.

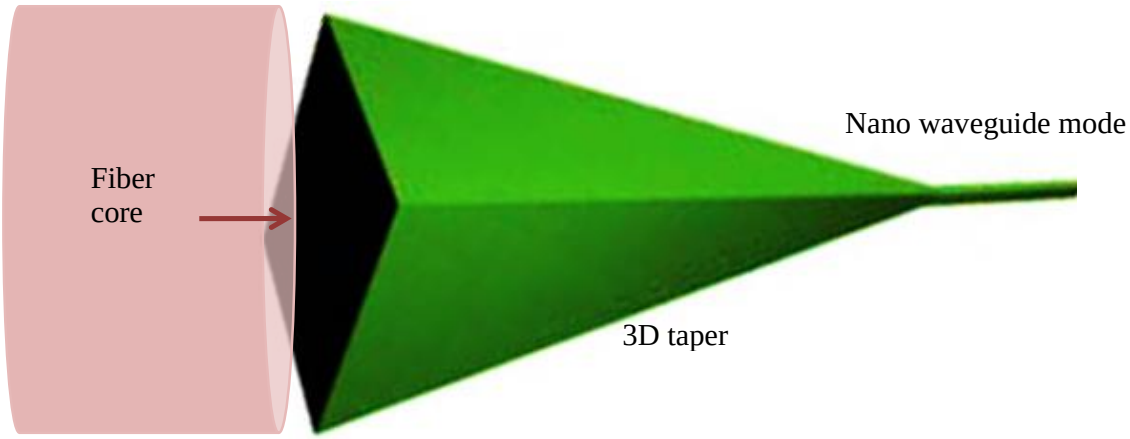

Fig.2. 5: Fibre-waveguide coupling using a 3D taper

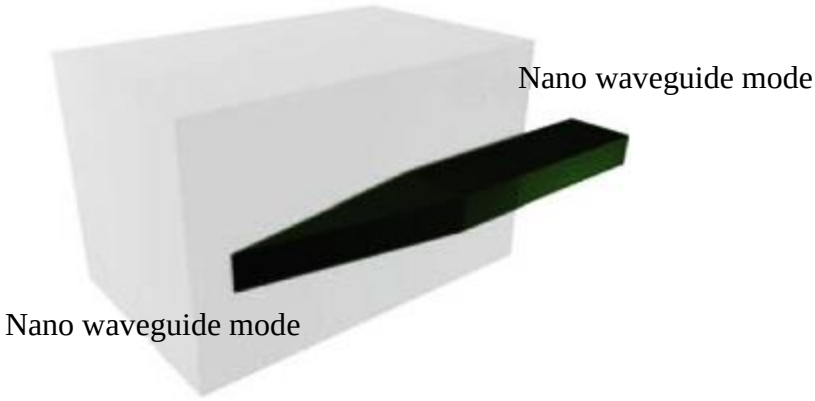

Fig.2. 6: 2-D single stage inverted silicon taper with polymer waveguide on top [66]

2.3 Prior works

2.3.1 Tapered waveguide

For efficient butt coupling, the waveguide between fibre and a nano waveguide needs to be tapered from larger dimension (fibre face) to lower dimension to match the nano waveguide. To improve coupling efficiency of the taper, in 1975 Winn and Harris proposed a horn shape structure [67] which is now known as a taper. In this design, it is suggested that to achieve coupling efficiency of > 90%, the taper length should be in the order of 2000 of wavelength. In [68] the waveguide was tapered adiabatically where a

mode conversion does not occur in the device. These tapers are very long in the range of millimetres which causes a larger footprint in the nano photonic chip. So to reduce the taper length, a bilevel mode converter is proposed in [69] where the structure is designed with top and bottom tapers. The simulation results of this design show high coupling efficiency with polarization independency. A double stage taper was proposed in [70] [71] as shown in Fig.2. 7. The length of such design was 20 µm and within this length the dimension of the waveguide is converted from 25 µm to 800 nm. The simulated coupling loss for this design is reported as 0.2 dB but experimental results show a coupling loss of 0.4 dB. In comparison with previous designs [67], using this double stage taper the light can be coupled with considerably lower coupling loss within a short taper length. The coupling of light was investigated between high numerical apertures (NA) fibre and nano waveguide in [72]. The results show that the coupling loss of 8 dB is achievable to transfer light from a fibre with mode field diameter (MFD) of 3.7 µm into a rib waveguide with cross-sectional dimension of 750 nm (width) × 1500 nm (height). The loss has been further reduced to < 5 dB using a 1 D taper with initial width of 4 µm. To minimize the loss associated with vertical mismatch, the taper was further modified with an initial height of 3 µm and the loss was further minimized to 2 dB.

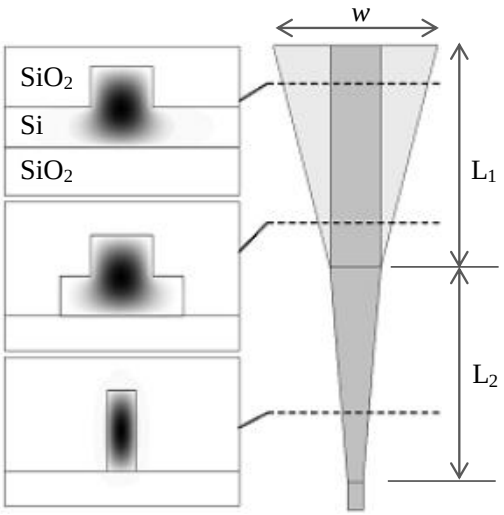

Fig.2. 7: Double stage tapered waveguides [70]

A summary of the most relevant properties of the major SOI fibre coupling techniques (grating coupler and inverted taper) was presented in [73], for a wavelength λ=1.55 μm, and considering standard single mode fibres (SMF).

Typical coupling loss are about 5-6 dB for a conventional 1D grating coupler structure, with a footprint area of 10 μm × 10 μm, when coupling to a butt-fibre with 10 μm MFD [57]. For coupling via an inverted taper by using the same fibre, a double stage coupling structure is usually used in literature, as a single stage is not enough to achieve an efficient mode conversion to 10 μm MFD standard butt-fibres. In double-stage inverted taper structures, the mode conversion is achieved in two different steps by using a bottom taper on top of a lower taper, thus creating a complicated 3D structure. Typical coupling losses of 1.5 dB are achieved for a 800-1000 μm long double stage inverted taper, and a 9 μm × 9 μm cross-section dimension fibre-adapted waveguide [74] [75]. However, the complexity of the fabrication process is more than double a single-stage inverted taper coupler. In this latter case, the mode conversion is achieved with one less complex inverted taper structure in just one step.

Most of the inverted taper structures referred to in literature are single stage, but are optimized for coupling to lensed fibres with a lower spot size diameter of 2.5-4 μm. In this case, a minimum coupling loss less than 1 dB can be obtained. One of the pioneer inverted tapers is found in [66]. They demonstrate less than 1dB coupling loss from 0.3 × 0.3 μm^2 silicon waveguides to single-mode fibres with Mode Field Diameter (MFD) of 4.3 μm for the TE mode, for an inverted taper length of 200 μm, and using a polymer fibre-adapted waveguide on top of the inverted taper with cross-section dimensions 3μm × 3μm. One of the special features of this type of coupler is polarization insensitive behaviour of the structure for small inverted taper tip width values, such as below 40 nm.

In order to decrease the taper length, [76] proposed a novel configuration consisting of using a SiO_2 slab layer on top of a parabolic shape taper, instead of using a polymer waveguide. The optimal length of the taper is reduced to 40μm due to the quadratic shape of the taper, but achieving a polarization dependency to the inverted taper tip width. 0.5dB coupling loss to 4.9μm MFD fibres are achieved for optimal

designs with 120*nm* and 50*nm* tip width for TE and TM polarization, respectively. The main problem with this configuration is that the device needs to be cleaved exactly by the inverted taper tip, and may require special cleaving and polishing techniques. In [77], such a coupler has been fabricated using standard CMOS process technology where an insertion loss of 1.9 dB to 2.5 μm MFD fibres was achieved for the TE mode, by using a $3\mu m \times 1.3\mu m$ (Benzocyclobutene) BCB type polymer waveguide on top. The optimal obtained length of the taper is $175\mu m$, and the inverted taper tip width is 175*nm*, thus being compatible with CMOS UV lithography. In [78], the insertion loss of such coupler is minimized to 0.5 dB by optimizing the coupler for the TE mode. Another similar coupler which utilizes silicon rib waveguide has been reported in [79], where a 0.7 dB coupling loss is achieved for the TE mode. Recently, the optimization for an inverted taper for TM mode was proposed in [80], for the case of ridge waveguides. They obtained coupling losses of 0.36 dB and 0.66 dB for the TM and TE modes, respectively. However, there was extra excess loss, mainly due to the fibre lensing process of the lensed fibres used, so that final average insertion loss of about 3 dB is obtained in many cases.

A compact 1×2 3-dB tapered multimode interference (MMI) coupler is demonstrated in [81] using a parabolically-tapered structure with high uniformity of 0.28 dB and fibre – chip – fibre excess loss of 9.9 dB which claimed to be much less than that of a InP-based MMI coupler. Mode expanders based on modal interference between the supermodes in the taper structure formed by an active rib waveguide and an underlying fibre-matched ARROW is proposed in [82] where low-loss mode transformation and good fibre-coupling efficiencies and far-field divergence angles were obtained for much shorter lengths compared with adiabatic tapers. Another SOI-based MMI coupler [83] comprises shallowly etched regions, bi-level tapered regions and deeply etched regions with high uniformity.

A monolithically–integrated, asymmetric graded index (GRIN) or step-index mode converters for microphotonic waveguides is reported in [84] which operates over a wide range of wavelengths with low polarization dependence. The rigorous and accurate numerical simulations to examine the implementation of lateral, vertical, and combined spot-size converters in a silica structure was presented in [85]. It was

demonstrated that coupling efficiency and device compactness can be significantly improved by optimizing the fabrication parameters. Instead of using SiO_2 as the cladding, a low-loss Sub-Micron polycrystalline silicon waveguide clad by SiON with an effective coupler is presented in [86], the design of which is shown in Fig.2. 8. The propagation losses of 6.45±0.3 dB/cm and 7.11±0.5 dB/cm were measured for TE and TM modes respectively over the whole C-band wavelength.

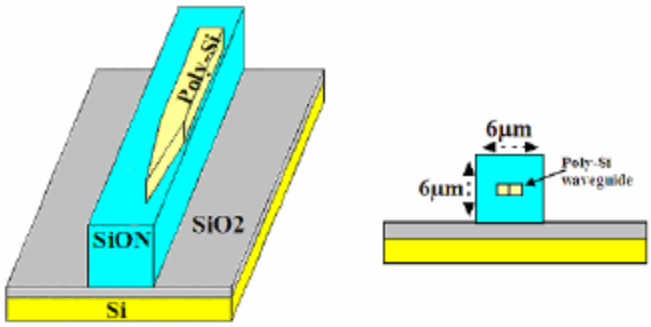

(a) Top view (b) Cross-section

Fig.2. 8: Schematic diagram of the SiON coupler [86]

A laterally tapered undercut active-waveguide for an optical spot-size converter (SSC) is proposed and fabricated simply by a wet etching-based technique [87] where an optical mode transfer loss of -1.6 dB is observed between the bottom passive waveguide and the active waveguide. A highly efficient and polarization-independent compact mode coupling between an active waveguide and a passive waveguide using fully bimodal interference is presented in [88]. The modal transformation losses as low as 0.1 dB is achieved using much shorter lengths than the adiabatic taper. High coupling efficiency using a non-zero tip width inverse taper is reported in [89]: the design is based on impedance matching conditions. An intra-chip cantilever coupler using stress-engineered SiO_2 cantilevers for fibre-to-chip coupling to Si photonic circuits is designed with coupling losses of 1.6 dB per connection for TE polarization and 2 dB per connection for TM polarization in [90]. A fibre-to-waveguide mode size converter on the SOI platform composed of a suspended SiO2 waveguide and overlapped Si nano-tapers located in the centre of a suspended SiO_2 waveguide is developed in [91]. The

measured coupling loss using a lensed fibre with 5 μm spot diameter is 1.7 ~2.0 dB/facet for TE mode and 2.0 ~2.4 dB/facet for TM mode in the wavelength range of 1520 ~1600 nm is reported. An efficient adiabatic in-plane fibre-to-chip coupler design is proposed [92]. In this design, the light from the fibre is coupled into a low-index waveguide with matching mode size. The mode is first adiabatically reduced in size with a rib taper, and then transferred into a high-index (e.g. silicon) waveguide with an inverse taper. The two-stage design allows the coupler length to be reduced multiple times in comparison with pure inverse taper-based couplers of similar efficiency. The magnitude of length reduction increases with the refractive index of the low-index waveguide and the fibre mode size. A schematic of the design is shown in Fig.2. 9. The

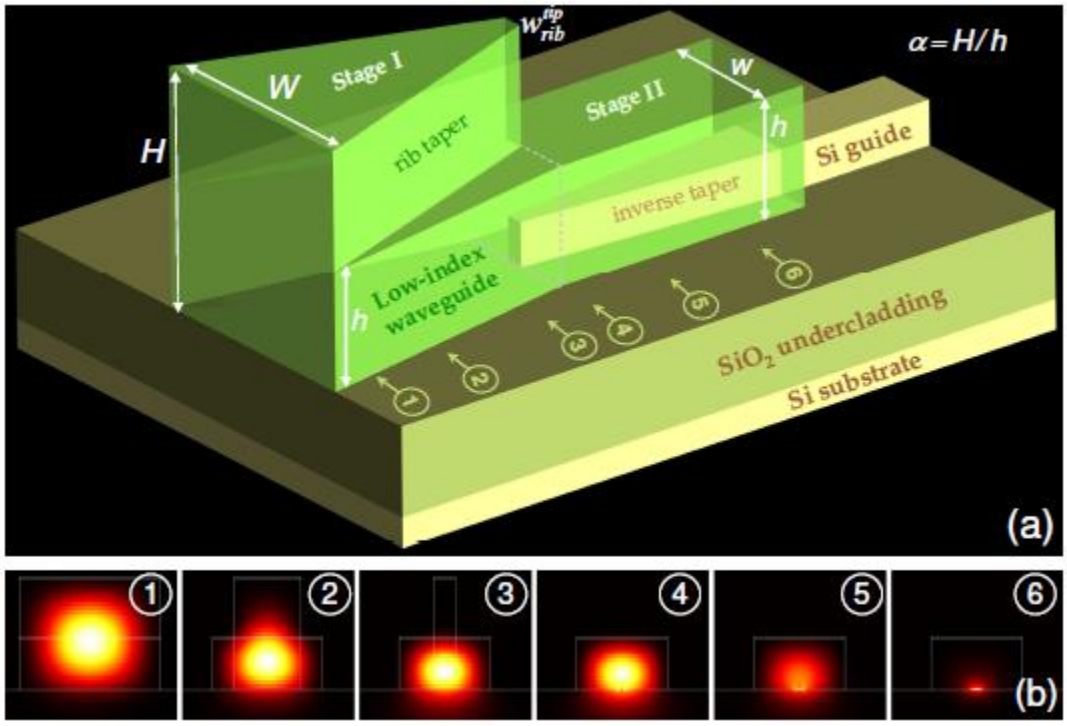

Fig.2. 9: (a) Layout of the two-stage adiabatic coupler (not drawn to scale). The light from the fibre is coupled into the fibre-matched low-index waveguide, transferred into a smaller waveguide in Stage I using a rib taper, and coupled into sub-micron Si waveguide in Stage I using a rib taper, and coupled into sub-micron Si waveguide in Stage II using an inverse Si taper. (b) Intensity distribution of the fundamental TE mode at positions labelled with numbers in Fig. 1(a) of Ref. [92]. Positions 1-3 correspond to the rib taper and 4-6 to the inverse taper [92].

optical mode size transformation is achieved between SSMF and 0.26 μm-thick Si-waveguide by a 12μm-thick Si/SiO_2 multilayer on-chip GRIN lens of lengths 16μm or 24μm butt-jointed to a 10μm-wide terminated Si waveguide in [93]. The overall coupling loss of the coupler was measured at 3.45dB.

A two-dimensional electromagnetic coupler is proposed in [94] that can compress the beam width with little change in its profile. The main benefits of such a design include compact volume and low reflections compared with traditional tapers. The cantilever technique based on a chip-to-chip vertical light coupling is demonstrated in [95] [96]. Using such a technique, the chip-to-chip coupling losses were measured [96] as low as 0.62 dB and 0.50 dB per connection for quasi-TE mode and for TM mode respectively for the C band. Almost 100% transmission efficiency is reported in [97] by employing a transmission optics approach in the design. A two-port polarization-insensitive SSC [98] utilizes a concatenated horizontal up-taper and vertical down-taper with reported coupling losses for E_{11}^{y} and E_{11}^{x} modes are 2.8 dB and 2.7 dB/port respectively.

Based on the principle of adiabatic mode transformation, an optical coupler between SOI and polymer waveguides is designed in [99] where coupling losses of 0.8-1.1 dB for TE polarization and 0.8-1.3 dB for TM polarization are reported. A fibre-to-chip coupler is demonstrated in [100]. This consists of a silicon-inverted taper and a silicon oxynitride (SiON) double stage taper, where the cascaded taper structure enables adiabatic mode transfer between a submicron silicon waveguide and a single mode fibre. Coupling losses of 3.6 and 4.2 dB for TM and TE polarizations respectively are reported. A heterogeneous III–V/Si integrated structure with a short vertical interconnect access for optical coupling is demonstrated in [101]. Coupling efficiency has been extracted from waveguide loss measurement and is estimated to be above 90% at a tapering length of around 50 μm. A transformation optics based coupler is designed in [102] with taper length as short as 3μm and coupling efficiency of 94.5%. An efficient mode-size converter based on intermediate material SiON for the coupling between a cleaved SMF and HIC waveguide is reported in [103]. Combining an inverse taper and suspended structure, the coupling losses are 1.2 and 1.4 dB/facet for TE and TM modes respectively. A SOI adiabatic taper was designed in [104] by reducing the

incidence of mode conversion to higher-order and radiation modes inside the waveguide. 98.3% coupling efficiency was achieved when connecting a 12-μm-wide input waveguide of a grating coupler to a 0.5-μm-wide output waveguide.

An ultra-compact coupler is proposed in [105] by using a tri-sectional tapered structure to transform the light between a silicon wire waveguide of 220 nm height and a Si/III–V hybrid waveguide for Si/III–V heterogeneous integration. Over 95% coupling efficiency in a bandwidth of over 100 nm is reported in that design. SSCs with a SiO_2 spacer inserted between the Si wire waveguide and SiON secondary waveguide are demonstrated in [106]. With such a SSC, low-loss and small-polarization-dependence fibre-to-chip coupling of 1.45 and 1.50 dB/facet for quasi-TE and TM modes, respectively, were achieved. A subwavelength refractive index engineered broadband fibre-chip edge coupler is presented in [107] to mitigate loss and wavelength resonances by suppressing diffraction effects, enabling a coupling efficiency over 92% (0.32 dB) and polarization independent operation for a broad spectral range exceeding 100 nm.

A new type of fibre-chip edge coupler proposed in [108] with a large mode when the total coupling efficiency exceeded 90% (0.42 dB). An important advantage of this coupler is that the mode size is substantially increased while minimizing the substrate leakage loss through the BOX. This was achieved by increasing the effective index of the upper SiO_2 cladding with subwavelength index engineered thin Si_3N_4 layers. Adiabatic tapers for heterogeneously integrated devices are proposed in [109] where the couplers employ a broad intermediate waveguide to facilitate highly alignment-tolerant coupling. Such couplers could be useful for transfer-printing-based heterogeneous integration of active III-V devices such as semiconductor optical amplifiers (SOAs), photodetectors, electro-absorption modulators (EAMs) and single wavelength lasers on silicon photonic integrated circuits. A broadband bilayer polarization insensitive inverse taper edge coupler is demonstrated [110] with coupling loss of 1.7 dB from a focused fibre with 5 μm mode diameter. The design and fabrication procedures are described in [111] for surface-trimmed silicon-on-insulator waveguide with adiabatic SSCs where the insertion loss of ~0.25 dB for TE-like polarization is recorded for a wide range of wavelengths of 1500 nm-1600 nm. Based on the principle of transformation optics, a compact optical waveguide coupler is investigated in [112]. To supress the reflection

loss, a scaling function is developed to make the material nonmagnetic for TM polarization. A new compact tapered SSC structure is designed in [113] with a taper length as short as 15 µm on a SOI platform. The schematic of the design is shown in Fig.2. 10. The proposed taper, along with linear grating couplers for spot-size conversion, exhibits no degradation in the coupling efficiency compared to a standard focusing grating in the 1550 nm band.

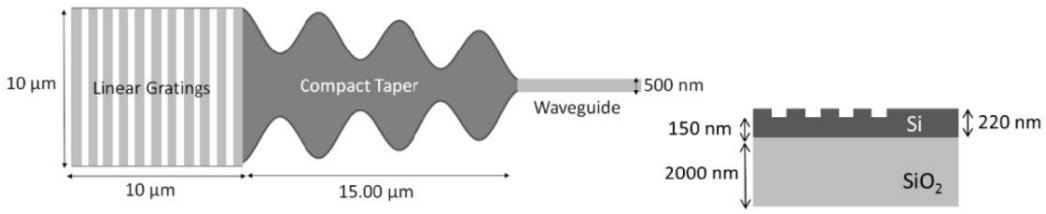

Fig.2. 10: Schematic illustration of the proposed compact taper structure [113].

2.3.2 Grating coupler

Utilizing the diffraction principle of light, the first grating coupler was developed back in 1970 by Dakss et al [114]. In this structure, a corning 8390 dense flint glass film was used as substrate and on top of that substrate corning 8390 was used as a waveguide with a refractive index of 1.73. With this design, a relatively high coupling efficiency of 40% was achieved and this encouraged many to consider a grating coupler as an alternative to a butt coupler. From the fabrication point of view, the grating coupler is much simpler than a butt coupler. Unlike a butt coupler, a grating coupler offers the flexibility to place it anywhere in the photonic chip. A grating coupler does not need the edges and facets to be diced and polished (a process required by the butt coupler) opening the way for wafer level testing and mass production at low cost. A theoretical study in [115] shows that the light from a waveguide can be coupled into the superstrate of a grating structure in a leaky mode as shown in Fig.2. 11. The leaky modes can be either in the direction of light propagation or in the opposite direction, depending on the grating period (ʌ). Such characteristics of the grating coupler offer more flexibility for use in photonic circuits. A comprehensive theoretical discussion on

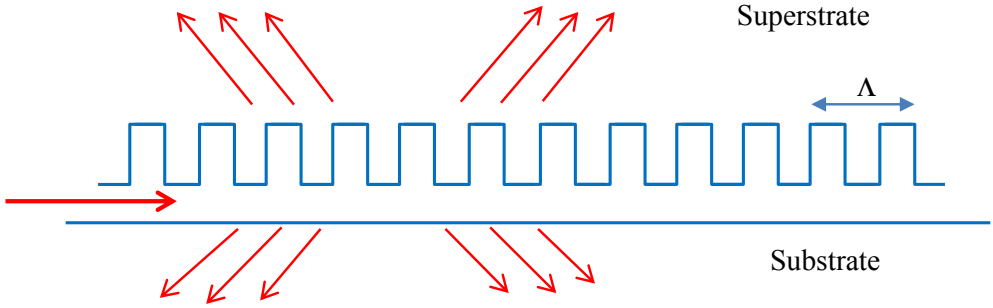

Fig.2. 11: Leaky modes in superstrate and substrate of grating coupler

coupling efficiency of a grating coupler is presented in [116] where it is shown that coupling efficiency of 80% is achievable. Power loss in the grating coupler was studied in [117] [118] and it was found that the wave attenuated more because of residual photo resistance remaining in the device during fabrication than was attributable to grating tooth shape imperfections. The remaining photo resistance reduces the difference of refractive index between grating tooth and groove and also significantly increases reflections on the surface, which ultimately causes power degradation in the grating coupler. Based on the perturbation theory and network analysis, a simplified and generalised design procedure of a dielectric grating coupler is described in [119].

In the early days, grating couplers were realized in material systems other than silicon, and especially in Groups III-V materials in the periodic table, such as GaAs, InP and LiNbO [120]-[125]. The first comparison between a silicon grating coupler and III-V materials coupler was studied by Emmons in 1991. The results of a glass waveguide and GaAs waveguide showed that the coupling efficiency is more sensitive in silicon waveguide height than in other waveguides with different materials, as shown in Fig.2. 12. That study found that such sensitivity is the result of reflections at the material interface for SOI where the refractive index contrast is higher than other materials. It is shown that this reflection phenomenon can be utilized to improve coupling efficiency with a proper design for constructive interference between the guided wave and reflected waves. Further studies by the same author describe that, utilizing a SOI platform, the low loss leaky mode can be supported and substrate loss minimized to below 1dB/cm [126]. It is shown that the performance of the grating coupler relies

strongly on the geometry of the structure, such as the grating period and thicknesses of the layers [127]. The study claims that over 90% coupling efficiency is obtainable, using an extra buffer layer of silicon nitride on the surface of the grating with a coupling length of ~ 100 µm. They also suggest using a bottom grating beneath the waveguide to minimize substrate leakage in order to improve coupling efficiency. The grating profile used by Emmons is sinusoidal, the fabrication accuracy of which is very difficult to achieve and especially for deep etched gratings.

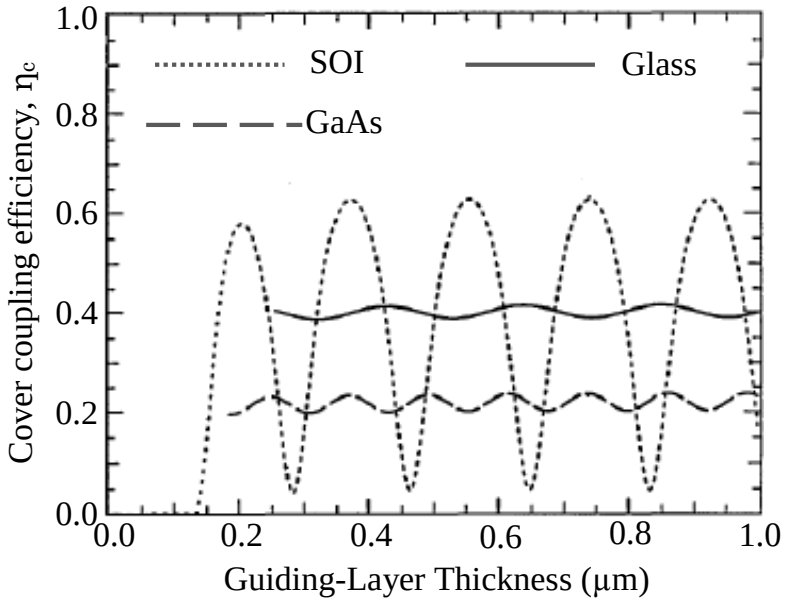

Fig.2. 12: Upward coupling efficiencies for various waveguide thicknesses of different materials.

Rectangular shape gratings are mostly appearing in current designs [128]. This type of garing is easier to fabricate as the side walls are vertical which can be fabricated using photolithography or electron beam lithography employed with inductively-coupled plasma or the reactive ion dry etching process. In [128] the detuning grating coupler was investigated and it was found that introducing second order diffraction reduces the overall coupling efficiency of the coupler. Such second order diffraction has been removed using even detuning by half the amount that occurs in InGaAs/AlGaAs. Eventually, only the first order diffraction remains, one in the substrate and another in the superstrate. It is found that a small angle is required to remove second order diffraction and ultimately improves the coupling efficiency of the grating coupler. The study also suggests that the coupling efficiency depends on the shape of the grating, and

that was confirmed in [129][131]. In [129] and [132], similar studies showed the difference in coupling efficiencies in simulation and experimental results. The peak wavelength shifted more in experimental data than in simulated data and the reflectivities also varied in experimental data.

Based on the pertubation theory, K. C. Chang predicted that 70% coupling efficiency is achievable in a grating coupler [133]. Using the SOI platform, a grating coupler was demonstrated in [134] where coupling efficiency of 70% was reported: this confirmed Chang's prediction. The coupling efficiency of the grating coupler also studied in other works [134][137] for the various grating types, e.g. rectangular and blaze gratings. The investigations demonstrate that using blazed grating, coupling efficiency can be improved significantly. [134] showed that with uniform rectangular grating, the coupling efficiency was 71%, but by using blazed grating efficiency improved to 84%. A compact size grating coupler was demonstrated in [138] with a cross-section of 100 µm (length) × 30 µm (width) and showed 55% coupling efficiency. Comprehensive simulation methods were described in [139] and 53% coupling efficiency was achieved using a rectangular grating structure. To increase coupling efficiency, the use of a super lattice reflector in the substrate was proposed in [140]. Substantial improvement in coupling efficiency also achieved with second order grating [141] although such grating was supposed to offer lower coupling efficiency compared with first order grating. With a grating length of 320 µm, coupling efficiency of 94% was achieved with second order grating: this indicates the significance of that study.

To maintain single mode operation of the waveguide a grating coupler on 1.5 µm-thick SOI rib waveguides has been demonstrated [142] and a coupling efficiency of −2.2 dB is achieved with a 3 dB bandwidth of 40 *nm*. By reducing back reflection, the coupling efficiency has been improved in [143] by eliminating the mode mismatch and index mismatch between the grating and waveguide regions, significantly using a rib tip which adiabatically connects the rib waveguide and slab waveguide modes. The total 3 dB coupling loss is measured in this design when interfacing a SMF for in- or out-coupling and 1.5 dB when interfacing a MMF for out-coupling. A wide spectral FWHM of 58nm and a low back reflection of −27 dB are achieved. Although these

demonstrations show some advantages, they also introduce more fabrication complexities as they use inverted tapers. A fibre-to-fibre coupler fabricated on a 200-mm wafer based on the standard CMOS technology has also recently been demonstrated in [144]. The special feature of this coupler is that it is polarization insensitive. Coupling losses < 1 dB were measured in the wavelength spectral range of 1520 *nm*-1600 *nm* from a 2.5-μm MFD lensed fibre into a 500-nm-wide SOI waveguide and < 3 dB for wavelength range of 1300 *nm*-1600 *nm*.

With respect to the basic grating couplers, coupling loss can be reduced to 1 dB (near 80% coupling efficiency) by implementing more complex grating coupler designs. To obtain lower loss grating couplers, different strategies have been proposed. By redirecting the downward light to the waveguide coupled to the grating using a bottom mirror, coupling losses can be minimized to 1 dB. The bottom mirror can be either a metallic mirror [145] or a distributed Bragg reflector-type (DBR) mirror [59]. Another way is to increase the grating directionality by depositing a poly-silicon overlay on a non-uniform grating structure and then optimizing the grating parameters separately [146]. With this solution, a modification in the effective index along the grating is obtained by chirping the grating, so that the radiated electric field profile of the grating can be Gaussian-like reshaped for better matching to the optical fibre beam. Using a silicon overlay, an enhanced grating directionality and hence the coupling efficiency of a SOI fibre-to-chip grating couplers has recently been presented in [147]. However, an advanced CMOS-compatible SOI platform is required for the fabrication of that kind of structure [147]. An alternate scheme for high directionality is proposed and designed in [148]: it implements optimum waveguide thickness configuration and designs the grating filling factor to vary the grating coupling strength.

Even though the coupling efficiency of the grating couplers has been significantly improved and elevates other performances compare to edge couplers with many approaches, reported grating couplers exhibit a relatively narrow bandwidth and the coupling bandwidth mechanism is not described clearly [149]. A relationship between the coupling bandwidth and the fibre numerical aperture is reported in [150], which can provide an approximation of the bandwidth in waveguide to fibre coupling, but for fibre to waveguide coupling, the intrinsic bandwidth property of grating couplers is not

clearly described except in a few theoretical discussions [60] [65] [146] [151]. These theories are based on a multi-parameter sweep process and do not mention any general procedure to follow. A generalized formula which can be applied to predict the possible bandwidth range for a specific grating structure has been proposed in [149] and to maximize the coupling efficiency for general layered waveguide structures a simplified optimization approach is proposed.

Another possibility for an efficient effective index modification of the grating coupler is the use of subwavelength waveguide gratings [152]. Recently, a Sub-Wavelength Grating (SWG) structure-based coupler has been developed. Based on this technology a through-etched grating coupler has been demonstrated [153] where the gratings are made of arrays of 80 nm × 343 nm rectangular air holes and patterned in a single lithography/etch, thus simplifying the fabrication process. The gratings are patterned on the SOI platform with a 1-μm-thick Buried-Oxide (BOX) layer and 59% peak coupling efficiency at 1551.6 nm and a 3 dB bandwidth of 60 nm are achieved for the TE mode. The efficiency achieved with this coupler is comparable to gratings requiring much more complicated fabrication processes. Another demonstration is reported based on the subwavelength structure [154] which has incorporated apodized-focusing grating to avoid adiabatic tapers, thus minimizing the size of the coupler. A modified phase matching formula is employed to design the apodized focusing SWG. The maximum coupling efficiency as high as -3.0 dB with 3 dB bandwidth of ~50 nm is measured experimentally. However, to pattern such gratings required several steps, which increases fabrication complexity.

All the previous design configurations require the optical fibre to be slightly tilted with respect to the grating's normal direction to avoid a large second-order Bragg reflection back into the SOI waveguide, which dramatically increases coupling loss. This fact is important for practical applications, which implies either angled polished fibres or mounting the fibre holder under an angle with respect to the grating's normal direction, which also implies an increase in the final costs of the photonic component's assembling and packaging [155]. To avoid this, slanted [156] and stratified [157] grating couplers were proposed to achieve low coupling loss for perfectly vertical coupling. Vertically-etched slits based on an asymmetric grating structure was also

proposed in [158]. But implementing all these more complex grating designs is costly, requiring more complex fabrication processes, thus increasing both the complexity of the designs and the fabrication process. In many cases, this is not suitable from an integration point of view [59] [159]. In some other cases, the restrictions on the design parameters are beyond optical lithography limits [146] [158]. So there is always a trade-off between cost and optimum performance. An important feature in grating couplers' development is achieved by Luxtera, Inc. in the holographic lens type grating in [159]. They demonstrate a high efficiency structure, with a focusing triangular footprint area, so there is no need to use a long SSC between the wide grating coupler and the narrow SOI waveguide.

Regarding the fibre-to-chip alignment tolerances, the grating coupler features higher alignment tolerances than the inverted taper. Coupling tolerances of about ±1 μm for 1 dB penalty are found for the grating [60], whereas for the inverted taper, just ±300 *nm* tolerances are found for the same penalty loss. When considering wavelength dependence of the structures, we find that the inverted taper is broadband (> 100 *nm* bandwidth), while the grating coupler presents strong wavelength dependency (3 dB bandwidth is about 50-60 nm). However, it is supposed to be enough for covering the C-band in optical communication systems. With respect to polarization dependency, weak polarization-dependent inverted taper designs can be obtained by choosing an optimum inverted taper tip width in many cases [160], whereas grating couplers are found to be strongly polarization dependent [161]. Finally, and due to the alignment tolerance issue, grating couplers are suitable for coupling multiple I/O fibres (i.e. fibre array (FA)) to multiport circuits, whilst (in general terms) inverted tapers are not so suitable, due to lower alignment tolerances [75]. A comprehensive review of different techniques for the purpose of light coupling from silicon waveguides to different types of structures was presented in [162]. They compared different vertical and horizontal coupling mechanisms applied to different applications, and found that the choice of the coupling method will depend on the required coupling efficiency, the desired bandwidth, the available footprint and technological considerations for any given application.

Using BenzoCycloButene wafer bonding grating couplers with gold bottom mirrors is presented in [163]: measured coupling efficiency to fibre is 69% for SOI grating couplers and 56% for bonded InP membrane grating couplers. Continuously variable grating strength achieved by using subwavelength microstructure is reported in [164] with minimized back reflection and 50% coupling efficiency for TM polarization. A reflectionless grating coupler on a SOI platform is proposed and it is shown that for a shallow-etched grating the reflection as low as -40 dB and for deeply-etched gratings -28 dB are achieved [165]. To overcome the challenge of a dual polarization operation of the grating coupler, polarization- independent grating couplers are also studied [166] [167]. More than 50% coupling efficiency for both TE and TM polarizations is reported in [166] for couplers having T-shaped grooves. Micrometric rib waveguide structure is proposed in [167] with coupling efficiency of -2.8 dB for both polarizations. A double-etched fibre-to-waveguide grating coupler (shown in Fig.2. 13) with engineered periods based on a SOI platform is demonstrated using deep UV photolithography [168] with measured coupling efficiency of -1.5 dB and 3-dB in a bandwidth of 54 nm. A fully etched apodized grating coupler based on photonic crystals has been demonstrated,

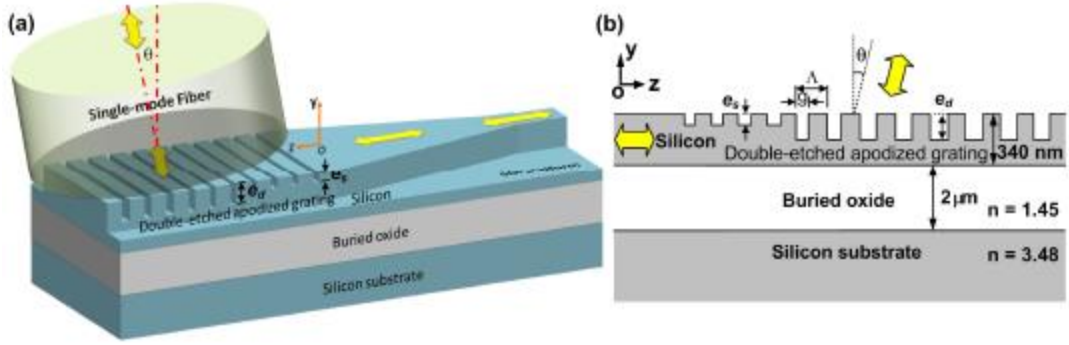

Fig.2. 13: (a) Schematic of the double-etched diffractive apodized waveguide grating coupler. (b) Cross-sectional view of the double-etched apodized grating coupler [168].

showing a low coupling loss of −1.74 dB with a 3 dB bandwidth of 60 nm [169]. Fibre-to-chip grating couplers with aligned silicon nitride (Si_3N_4) and silicon (Si) grating teeth for wide bandwidths and high coupling efficiencies is demonstrated in [170], a schematic of which is shown in Fig.2. 14. The 1-dB bandwidth of 80 nm and peak

coupling efficiency of -1.3 dB are measured in that design, which is competitive with the best Si-only grating couplers.

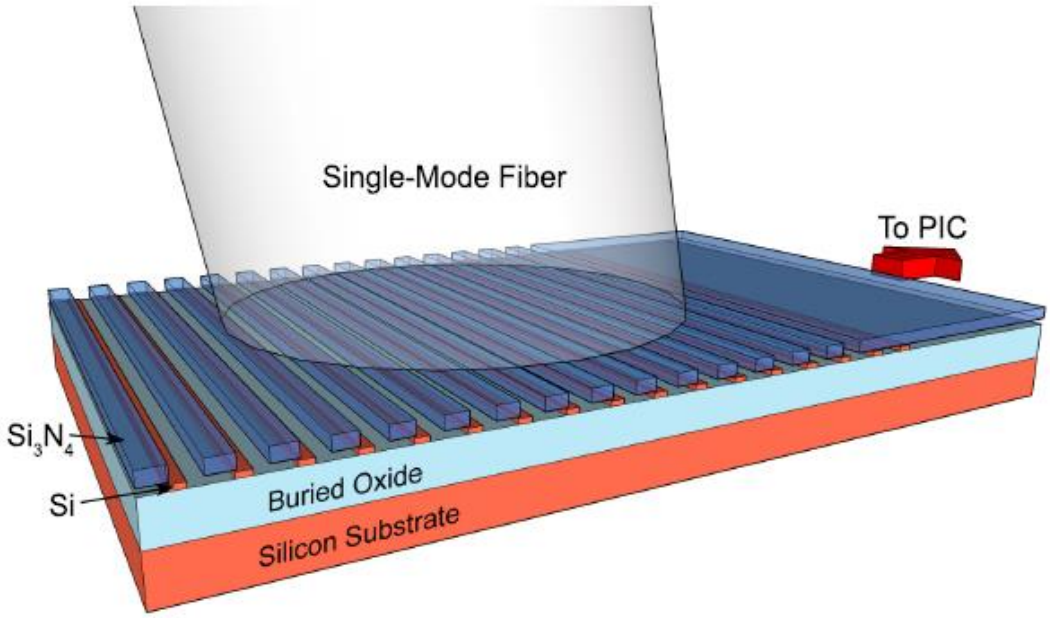

Fig.2. 14: Perspective schematic of the Si_3N_4-on-SOI dual-level grating coupler [170].

Fully-etched fibre-waveguide focused grating couplers with sub-wavelength gratings are reported in [171] with low back-reflections for both TE and TM modes. The insertion losses are measured at 4.1 dB for TE and 3.7 dB for TM modes with 1-dB bandwidth of 30.6 nm and 47.5 nm respectively. The polarization-insensitive focusing SWG coupler based on air cladding is demonstrated on SOI [172] as shown in Fig.2. 15. The coupling efficiencies of -3.2 dB and -4.3 dB are reported with 1-dB bandwidth of 28 nm and 58 nm for TM and TE polarizations respectively, measured for apodized gratings.

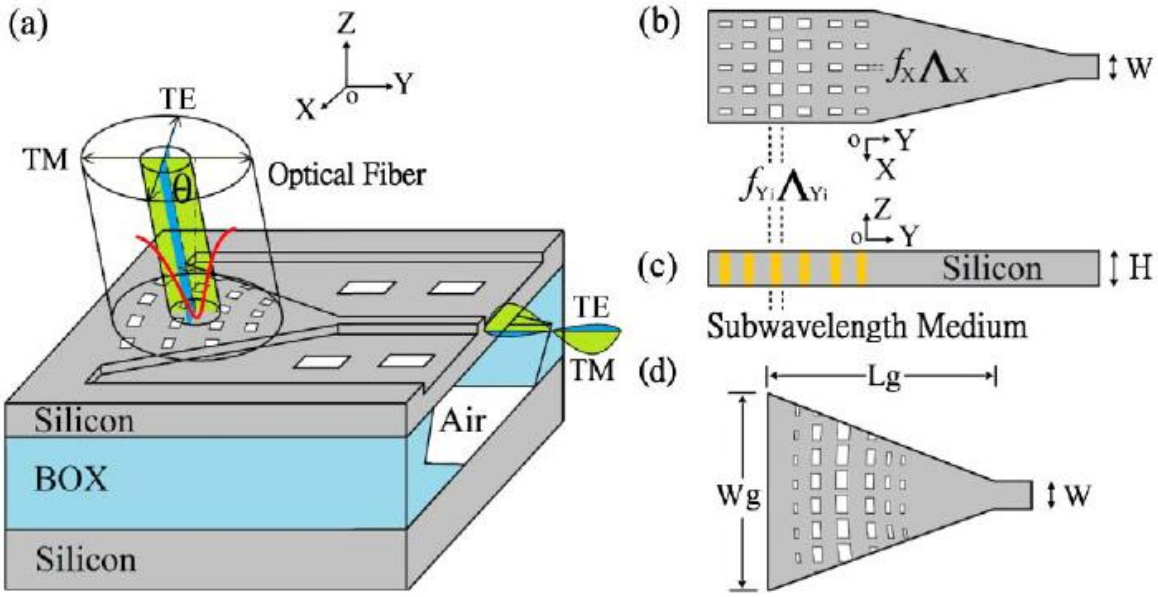

Fig.2. 15: (a) Schematic of an apodized focusing SWG for coupling two polarizations into a single mode waveguide. (b) Top view of an apodized SWG. (c) Cross-section of the apodized SWG. (d) Top view picture of the apodized focusing SWG [172].

A photonic crystal–based, fully-etched subwavelength grating coupler is demonstrated where the directionality is enhanced using a bonded aluminium mirror in the BOX layer [173]. The effects of coupling angle and fabrication errors are also investigated and coupling efficiency of -0.58 dB with 3-dB bandwidth of 71 nm are reported. Utilizing interleaved full (220 nm) and shallow (70 nm) etch trenches, upward directionality of 95% is reported in [174]. The schematic of this design is shown in Fig.2. 16. The coupling efficiency of −1.05 dB and 1-dB bandwidth of 30 nm are measured. A subwavelength refractive index engineered grating coupler on SOI is demonstrated in [175] to mitigate loss and wavelength resonances by suppressing diffraction effects, enabling a coupling efficiency over 92% (0.32 dB) and polarization-independent operation for a broad spectral range exceeding 100 nm. Another refractive index engineered with a metamaterial SWG coupler is demonstrated in [176] and coupling efficiency of -0.69 dB and 3-dB bandwidth of 60 nm are measured using a backside metal reflector.

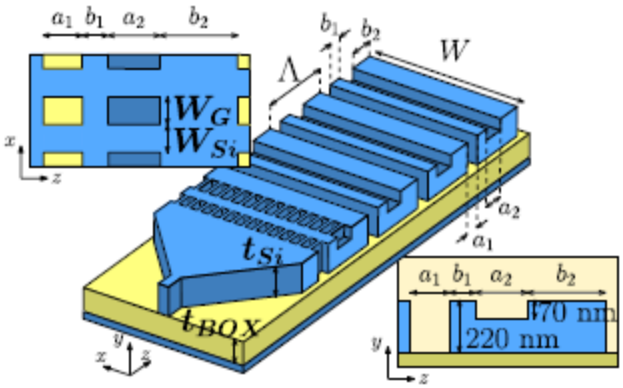

Fig.2. 16: Schematic representation of the grating coupler with interleaved 220 and 70 nm deep-etched trenches and subwavelength transition stage [173].

A new silicon nitride (Si_3N_4) grating coupler with a Si grating reflector in the BOX layer is proposed in [177] (shown in Fig.2. 17) with simplified fabrication processes compared to a distributed Bragg reflector (DBR) and a metal reflector. The reflectivity of over 90% is obtained with this Si-based grating reflector. Optimizing the distance between the Si_3N_4 grating coupler and the Si grating reflector, a low coupling loss of -1.47 dB for uniform structure is theoretically obtained. By apodizing the Si_3N_4 grating coupler, a record ultralow loss of -0.88 dB is further predicted.

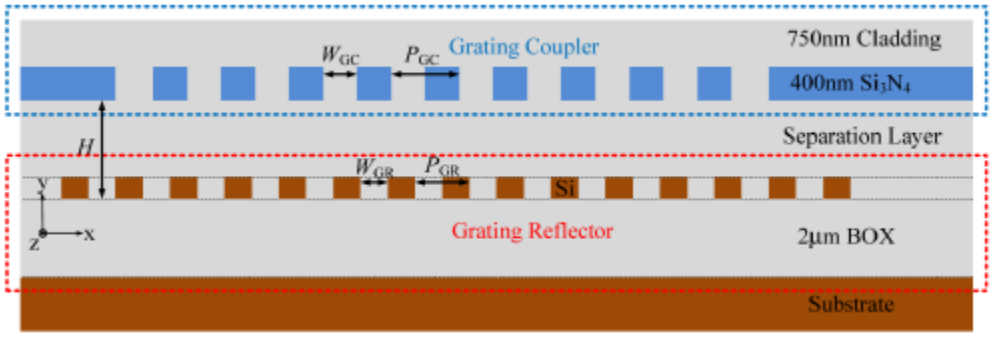

Fig.2. 17: Schematic of a Si3N4 grating coupler with bottom Si grating reflector [177].

Using interleaving trenches, a fibre-chip grating coupler is demonstrated in [178] that exploits the blazing effect, a schematic of which is shown in Fig.2. 18. Utilizing

such concepts, the directionality of the coupler can be enhanced without changing the BOX thickness. The measured coupling efficiency of -1.3 dB into a 220 nm SOI waveguide is reported.

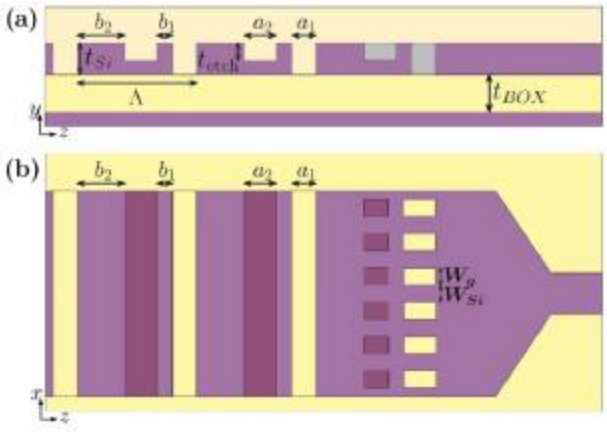

Fig.2. 18: Schematic of the dual-etch fibre-chip grating coupler with interleaved deep and shallow etched trenches: (a) side view and (b) top view [178].

For broadband operations, a grating coupler on 700-nm-thick silicon nitride-on-insulator (SNOI) is presented in [179]. This coupler can be used for nonlinear applications. The peak coupling efficiency is −3.7 dB and the 1-dB bandwidth is 54 nm is measured. A larger aperture, achieved by decreasing the effective index of the nanostructure and a larger lateral period, subwavelength nanostructure grating couplers are demonstrated for TE polarization with a coupling efficiency of 35% at 1560 nm wavelength [180].

By applying anti-phase reflection coatings (APRCs) on the core layer of GC, the anti-phase field can be returned into the core to cancel downward scattering from the gratings by destructive interference and to enhance directionality [181]. By exploiting the concept of SWG refractive index engineering, a grating coupler on SOI is demonstrated in [182]. Peak coupling efficiencies of -2.7 dB (54%) and -2.5 dB (56%) were measured for uniform and apodized structures, respectively. A grating coupler for interfacing between a SOI waveguide and a SMF at a perfectly vertical direction is demonstrated in [183] based on a tilted membrane structure. In this structure, the

gratings are formed on a tilted waveguide while fibre is placed vertically on the grating surface, in contrast with a conventional grating coupler as shown in Fig.2. 19. The coupling efficiency is experimentally measured at 28.5% with 1-dB bandwidth of 38 nm.

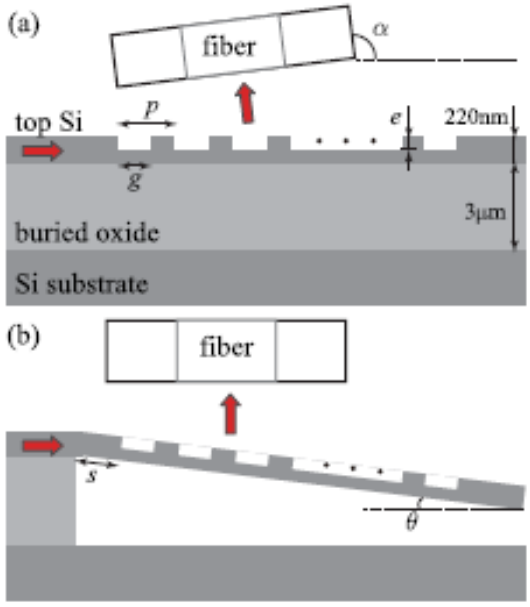

Fig.2. 19: Schematic structures of (a) a conventional grating coupler for an oblique fibre and (b) the proposed grating coupler for a perfectly vertical fibre based on a tilted membrane structure [183].

A dual-etched and apodised grating coupler is designed with predicted coupling efficiency of 85% (-0.7 dB) while experimentally -1.9 dB is measured [184]. Two subwavelength grating couplers (SWGC) are optimized separately for higher coupling efficiency and broadband operation in [185] for "O" band application. The high-efficiency SWGC has a measured peak coupling efficiency of -3.8 dB and a 3-dB bandwidth of 40 nm and the broadband SWGC has a measured peak coupling efficiency of -4.3 dB and a 3-dB bandwidth of 71 nm. A grating coupler on a SOI platform is demonstrated in [186] with higher directionality realized by using *L*-shaped grating structures, a schematic of which is shown in Fig.2. 20. By implementing a metamaterial transition stage between the injection waveguide and the grating, the back reflections are significantly reduced. This has been realized by exploiting the concept of the SWG

structure. In this structure, the measured coupling efficiency reaches a peak of −2.7 dB at wavelength of 1565 nm, with a 3-dB bandwidth of 62 nm.

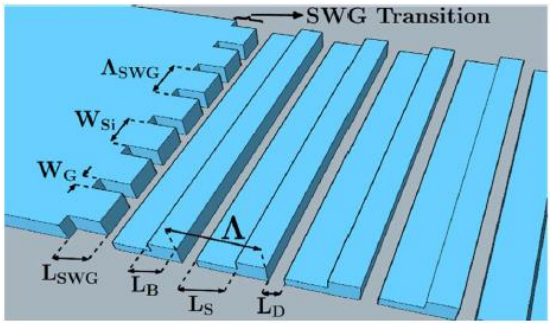

Fig.2. 20: Schematic view of a proposed L-shaped fibre-chip grating coupler with a subwavelength transition stage [186].

2.3.3 Grating couplers for transparency to polarization

It is well-established that the use of high refractive index contrast waveguide structures implies that the photonic integrated circuit behaves very differently for TE and TM polarized light [145]. This is also the case for the 1D grating couplers which was discussed in the previous section. In general, practical applications often require polarization-independent operation of the photonic integrated circuits due to an unknown polarization state of the light in the optical fibre and time variant nature of the state. The use of 2D grating structures allows this problem to be tackled by using a polarization diversity configuration. This is schematically depicted in Fig.2.21 [187]. The 2D grating structure can be seen as the superposition of two 1D grating structures, which are identical and are designed to efficiently couple a single polarization (i.e. TE) to the waveguide circuit. By placing these 1D grating structures orthogonal to each other, hence creating a square lattice grating structure, this 2D grating structure allows efficient interfacing with both polarizations of light in the optical fibre, by coupling the orthogonal polarizations in the optical fibre to identically (TE) polarized modes in the orthogonal waveguides. This approach realizes polarization-independent operations of (intrinsically very polarization-dependent) high index contrast waveguide structures by having identical photonic integrated circuits in each arm of the polarization diversity configuration as shown in Fig.2. 21. In this approach, a polarization rotator is not

required. This is a major advantage of this configuration because the integration of polarization rotators on a chip is very difficult. Although the two-dimensional grating structure is an elegant way of solving both the

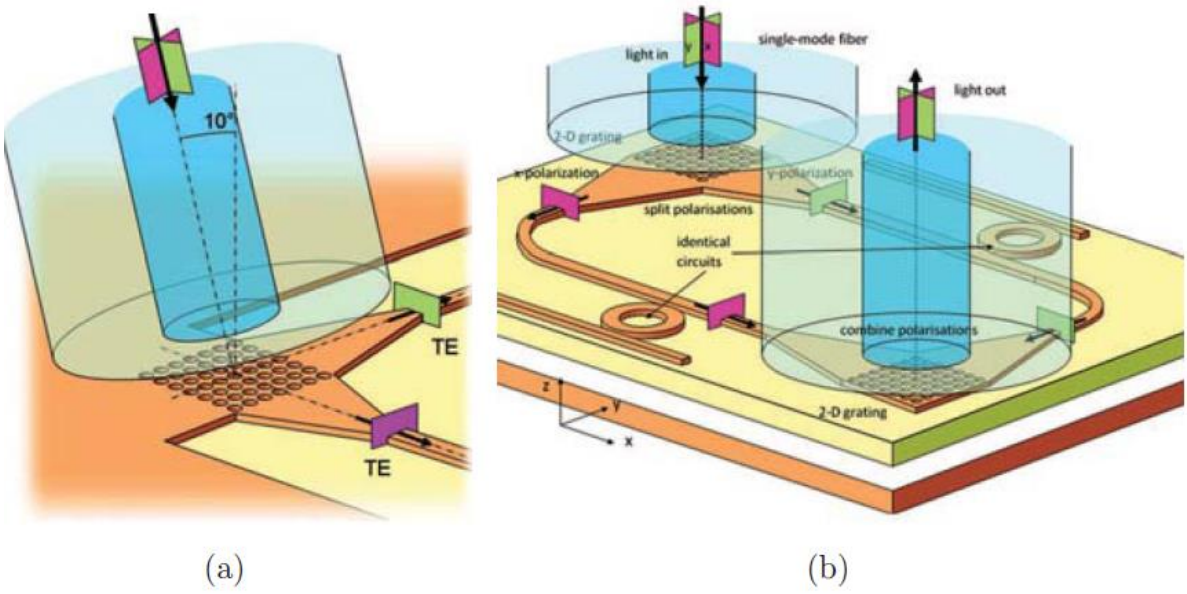

Fig.2. 21: Operation principle of a 2D grating structure: (a) two-dimensional grating structure in a polarization diversity configuration; (b) polarization-insensitive operation of high index contrast waveguide structures [187].

fibre-chip coupling problem and the polarization dependence of photonic integrated circuits, the limited bandwidth over which low polarization dependence is obtained can be an issue in practical applications [187]. Recently, a 2D grating coupler on SOI with a low polarization-dependent loss was demonstrated in [188] which covers the C-band. That design employed a grating cell consisting of five cylinders (shown in Fig.2. 22) and, by carefully optimizing the distances between the cylinders, polarization-dependent loss of 0.25 dB is realized.

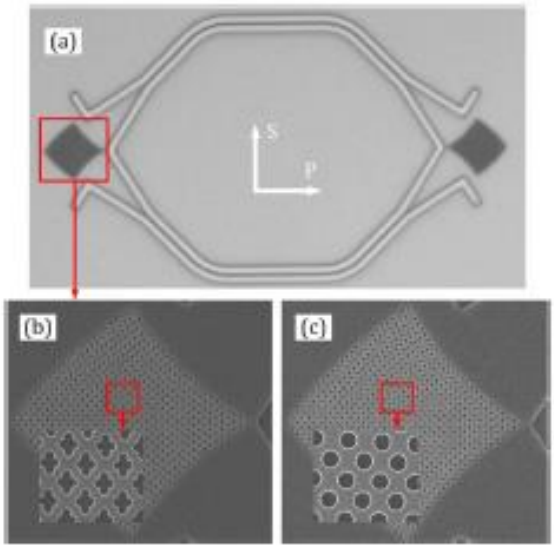

Fig.2. 22: (a) Optical micrograph of back-to-back cascaded 2D GCs. (b) SEM pictures of proposed 2D GC. (c) SEM pictures of conventional 2D GC [188].

Another way to implement a polarization independent fibre-chip grating coupler on a SOI platform is to utilize subwavelength gratings [189], a schematic of which is shown in Fig.2. 23. In this design, the effective indices are engineered for the

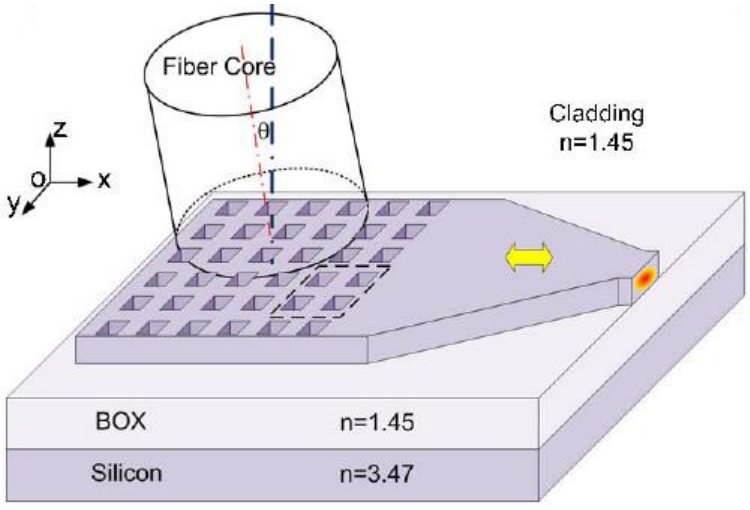

Fig.2. 23: Three-dimensional schematic illustration of the polarization-independent fibre-chip grating coupler with subwavelength structures [189].

TM and TE modes using second order Effective Medium Theory (EMT). The results show considerably high coupling efficiency for both TM and TE polarizations with improved coupling bandwidth.

2.4 Summary

After reviewing previous works on coupling mechanisms, we can conclude that each coupling technique, grating and butt, has its advantages and drawbacks. Butt coupling offers high coupling efficiency and bandwidth with polarization-insensitive features. However, incompatibility with standard CMOS-process technology, including issues with fibre/waveguide alignment, stimulates the search for other techniques. Moreover, the attainment of coupling efficiency in butt coupling is highly reliant on the transitional length of the tapered waveguide which causes a much larger footprint in a photonic integrated circuit (PIC). A grating coupler, on the other hand, offers high compatibility with CMOS technology and can be placed arbitrarily in a PIC, paving the way for low-cost mass production. However, poor coupling efficiency and bandwidth limit their application. Such limitations can be improved with engineering the grating structures which yet again increases complexity for fabrication with standard CMOS. Finally, it can be supposed that there is little to either acceptance or rejection of the coupling approach to be implemented, the choice being closely related to the device's application and also with the available technology know-how in particular.

Chapter 3

Grating Coupler Theory and Simulation Methods

3.1 Theory and operating principle of grating coupler

3.1.1 Diffraction of light

The word “diffraction” originates from the word “diffractio” devised by Italian physicist Francesco Grimaldi who, in 1665, conducted an experiment with a small pencil-like light source in a dark room. He placed a rod in front of the light and observed that the shadow shaped by the rod was wider than the shadow estimated based on geometric optics and that at the edge of the shadow there are various colours of light. Grimaldi named this behaviour of the light "diffraction", meaning “breaking up”. This was later called diffraction [190]. According to the law of diffraction, when a wave of light encounters an opaque object, some parts of the light travel beyond the object and create a diffraction pattern due to interference to the wave [191]. One of the most important applications of the diffraction phenomenon of the wave is that, for repetitive placement of the opaque objects, light can produce periodic alterations of the amplitude and phase of the light. In such a case the objects are said to be the diffraction grating.

3.1.2 Specifications of diffraction gratings

Diffraction gratings redirect the incident light with some discrete angles specific to individual diffractive orders. These angles are very sensitive to the wavelength of the incident light. For such wavelength selective features, diffraction gratings are widely used in the application of spectroscopy. In diffraction gratings, the total incident power is shared among the diffraction orders. There are two main features in diffraction gratings:

i) The angle of diffraction or the direction of the diffractive order for a given incident angle and wavelength, and

ii) The power efficiency of each diffraction order.

The angle of the diffraction order relies on the grating period and the refractive indices of the incident and transmitted media. The solution for a diffraction angle can be found based on the geometric relationship among incident and transmitted light. The power of the diffraction order depends on the physical parameters of the gratings, such as grating shape, depth and width. There is no straightforward solution for calculating the diffraction efficiency. However, a special analytical solution, for example a rigorous coupled mode analysis, can be used. These require computer aided simulations.

3.1.3 Grating equation

In this section we will look at how the gratings essentially interact with incident light which causes redirection of the light in the form of diffraction orders. The diffraction grating can be characterised with a grating vector K, the magnitude of which is defined as

$$|K| = \frac{2\pi}{\Lambda} \qquad \text{(Eq. 3.1.3.1)}$$

where Λ is the period of the grating and the direction is along the periodicity.
The starting point to derive the diffraction equation is that we assume incident of light on a waveguide surface without a grating as shown in Fig.3. 1.

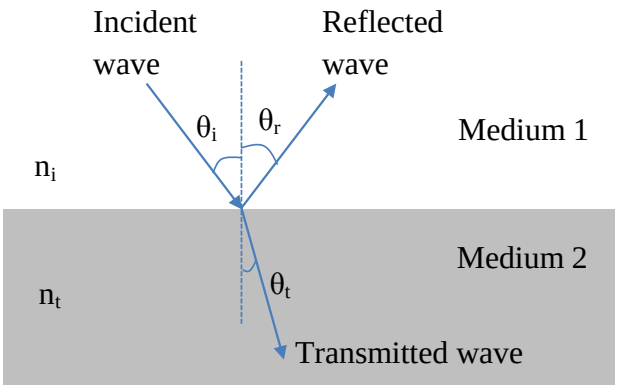

Fig.3. 1: Light propagations between two different materials

In that case, the problem can be simply solved by using Snell's law. Let us assume that the medium of incident is Medium 1 with refractive index n_i and the redirected beam is transmitted in Medium 2 with refractive index n_t. Considering the common case $n_t > n_i$, a portion of incident light reflected into the same medium as incident wave with $\theta_r = \theta_i$ and another portion is transmitted in Medium 2 (n_t) with $\theta_t < \theta_i$. Now, if we use gratings on the surface of Medium 2, the interaction of light with the grating can be defined by adding each diffracted grating vector with the undiffracted wave vector: this condition is called a "Floquet condition". The resulting infinite numbers of wave vectors are called "Floquet waves". Mathematically, the Floquet condition can be written as:

$$k_m = k_{un} - mK \qquad \text{(Eq. 3.1.3.2)}$$

where:

$m = 0, \pm 1, \pm 2....$ is the number of diffraction orders

k_{un} is the wave vector of the undiffracted wave

K is defined in Equation 3.1.5.1

k_m is the wave vector of m^{th} diffraction order

In Equation 3.1.3.2 the value of m is from negative infinity to positive infinity. This implies that there are infinite numbers of Floquet waves in the diffraction grating. However, only a certain number of diffraction orders can physically exist. Let us consider the two-dimensional geometry of the wave vectors' components of the diffracted waves as shown in Fig.3. 2.

The boundary condition to apply an electric field requires that the tangential components at the boundary be continuous. Therefore, the vector components of the diffraction orders in Equation 3.1.5.2 can be expressed as

$$\frac{2\pi n_t}{\lambda}\left(\sin\theta_m \hat{x} + \cos\theta_m \hat{z}\right) = \frac{2\pi n_t}{\lambda}\left(\sin\theta_{un} \hat{x} + \cos\theta_{un} \hat{z}\right) - m\frac{2\pi}{\Lambda}\hat{x} \qquad \text{(Eq. 3.1.3.3)}$$

where:

θ_m is the diffraction angle of m^{th} order

θ_{un} is the angle of the undiffracted wave

n_t is the refractive index of the medium of transmission

λ is the wavelength of the light

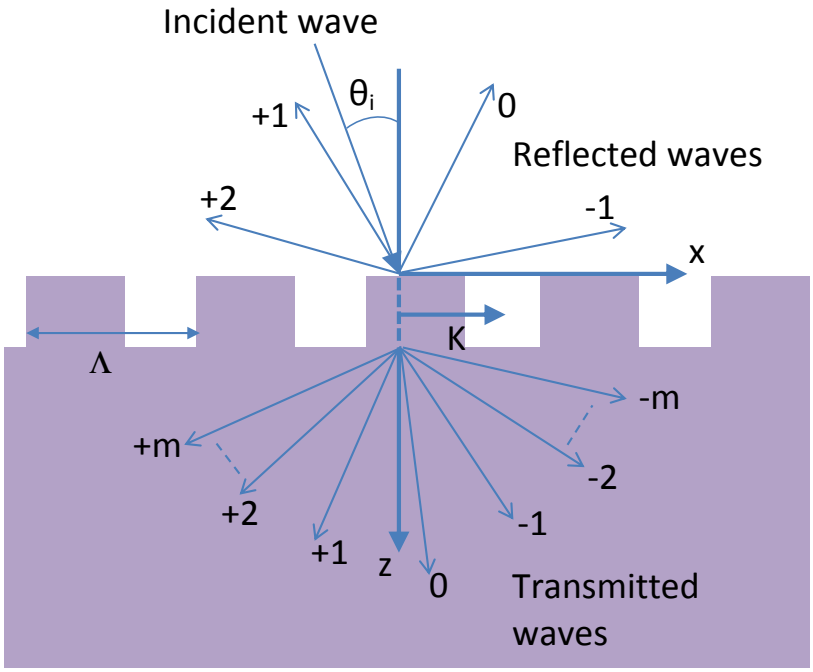

Fig.3. 2: Diffraction orders in a grating structure

In order to calculate the diffraction angle of an individual diffraction order, we can solve Equation 3.1.3.3 for $\sin\theta_m$ as

$$n_t \sin\theta_m = n_t \sin\theta_{un} - m\frac{\lambda}{\Lambda} \qquad \text{(Eq. 3.1.3.4)}$$

Using Snell's law it can be shown that

$$n_t \sin\theta_{un} = n_i \sin\theta_i \qquad \text{(Eq. 3.1.3.5)}$$

By substituting Equation 3.1.5.5 into Equation 3.1.5.4 we have

$$n_t \sin\theta_m = n_i \sin\theta_i - m\frac{\lambda}{\Lambda} \qquad \text{(Eq. 3.1.3.6)}$$

Equation 3.1.3.6 relates the diffraction of light in the medium of incident and transmission and is known as the diffraction equation. From this equation we can see that the diffraction waves are highly dependent on wavelength. For very short grating periods the diffraction angle changes significantly, which affects the dispersive nature of the grating and consequently is widely used in spectroscopy.

While solving Equation 3.1.3.6 for θ_m, it can be realized that if $\left(n_i \sin\theta_i - m\frac{\lambda}{\Lambda} \right) > n_t$, then θ_m becomes complex and thus non-physical. This condition gives a range of values for the number of diffraction order *m* as follows:

$$ceiling\left[\frac{\Lambda}{\lambda}\left(n_i \sin\theta_i + n_t\right)\right] \leq m \leq floor\left[\frac{\Lambda}{\lambda}\left(n_i \sin\theta_i - n_t\right)\right] \qquad \text{(Eq. 3.1.3.6)}$$

where the ceiling denoted rounds *up* to nearest integer value of *m*, whereas the floor denoted rounds *down* to nearest integer value of *m*. From Equation 3.1.3.6 it can be seen that number of diffraction order *m* is higher when $\frac{\Lambda}{\lambda}$ is higher. This is the ratio of grating period to the wavelength. The number of the diffraction order also depends on the refractive index of the incident and transmission media.

3.1.4 Wave vector diagram

A wave vector diagram represents the diffraction orders and angles graphically. It is a handy tool for analysing the diffraction grating. As indicated in the previous section. diffraction gratings are characterised by a k-vector. Therefore, the vector diagram also can be named a k-space diagram. The magnitude of the *k* wave vector is determined by the radii of concentric circles drawn based on the incident angle and refractive indices of the media and the wavelength. As described earlier, that is based on the Floquet condition; the individual diffraction order can be found by additing the integer multiples of the grating vector to the undiffracted wave vector.

In a k-space diagram, the Floquet condition also can be represented by adding the tail of the diffracted wave vectors to the head of the undiffracted wave vector. The calculation of the actual magnitude and angle of the diffracted waves requires applying a boundary condition for the electric field tangential that are continuous at the boundary. The purpose of applying this boundary condition is to achieve phase matching which can be represented by drawing lines from the head of Floquet wave and the lines are normal to the boundary of the circles that were drawn initially for measuring the magnitudes in incident and transmission media. Finally, the magnitude of the Floquet waves is measured from the centre of the circles to the lines of phase match that

intersect the circles. An example of a wave vector diagram is shown in Fig.3. 3. The wave vector diagram provides information only for the angle of diffraction order and not for the diffraction efficiency. Other numerical methods are required for finding the diffraction efficiencies of the orders.

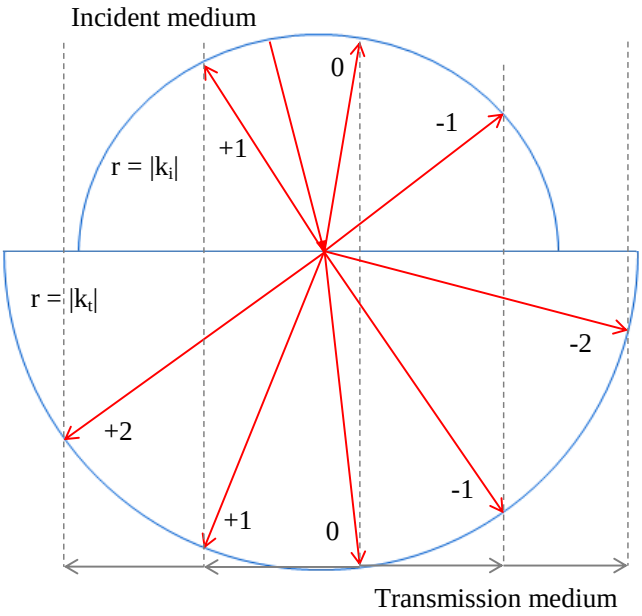

Fig.3. 3: Example of vector diagram for diffraction grating

Several methods have been developed to determine the coupling efficiency numerically [192] [193]. However, to model an appropriate grating structure, computer-aided design and simulation are necessary. The coupling efficiency can be calculated using the eigenmode expansion method [194] by determining the power which is coupled out of the grating and into the Gaussian shaped fibre mode [195].

The structural parameters such as thickness of the buried oxide layer, thickness of the waveguide, grating depth, filling factor and grating period each have a significant and indvidual effect on coupling efficiency [196]. These effects are discussed in detail in the following chapters.

3.1.5 Definitions of the parameters in a grating coupler

A general grating coupler with basic design parameters is shown in Fig.3. 4.

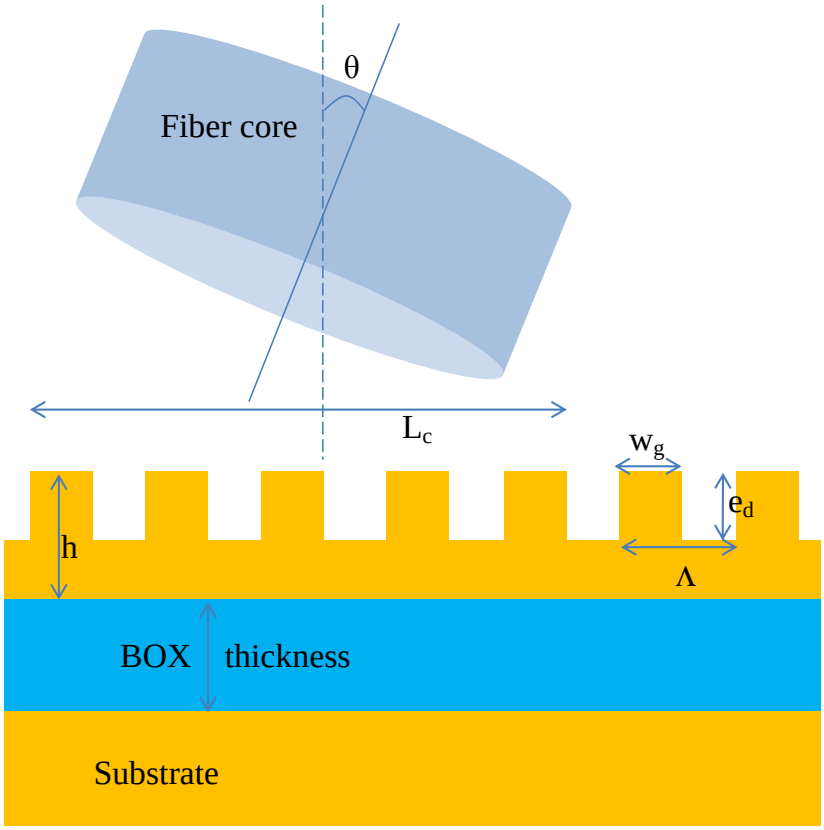

Fig.3. 4: Schematic of a general grating coupler with design parameters

- Grating period (Λ): This is one of the most important basic parameters for designing the grating coupler. The value of the grating period is defined based on the Bragg condition which has the following expression [195] [197] [198]:
-

$$\Lambda = \frac{\lambda}{n_{eff} - n_{top} \sin\theta} \qquad \text{(Eq. 3.1.5.1)}$$

where λ is the wavelength of the light, n_{eff} is the effective refractive index of the optical mode, n_{top} is the refractive index of the top cladding and θ is the titled angle of the fibre normal to the grating surface.

- Etching depth (e_d): This, also called the grating depth, is defined as the depth of the etched portion of the waveguide.

- Grating width (w_g): This is the width of the tooth.
- Waveguide height (h): This is the total thickness of the waveguide which is the sum of etch depth and non-etched thickness of the waveguide. For a fully etched grating, the etch depth and waveguide height are equal.
- BOX thickness (t_{BOX}): The thickness of the buried oxide (BOX) layer plays a vital role in the performance of the grating coupler. It acts as a buffer layer between waveguide and substrate. Moreover, the thickness should be chosen carefully because the reflections from BOX-substrate interface significantly affect coupling efficiency. Constructive interference between reflected and guided waves will improve coupling efficiency, but destructive interference results in lower coupling efficiency.
- Incident angle (θ): As indicated earlier, in order to break the symmetry the optical fibre is positioned at a slightly tilted angle. The perfectly vertical fibre also causes second order reflections which result in lower coupling efficiency.
- Filling factor (ff): This is the portion of the grating period which is filled. Mathematically it can be expressed as w_g / Λ.
- Number of period (N): The length of the grating region should be such that it will be totally illuminated by the optical fibre.
- Coupling length (L_c): This is the length between the fibre core and the beginning of the grating, where maximum coupling occurs in the direction of the grating. It can be calculated by [198]:

$$L_c = \frac{w_0}{1.37 \cos\theta} \qquad \text{(Eq. 3.1.5.2)}$$

where w_0 is the half of the width (MFD) of the Gaussian beam.

- Effective index (n_{eff}): Equation 3.1.5.1 requires that to determine the optimal grating period, it is necessary to find the effective refractive index. To find the total effective index, the grating structure can be divided into two sections; only one of which is etched. The effective index of each section is calculated separately and the final effective index is determined

by the average value of the two sections. Fig.3. 5 shows the process of calculation of an effective index.

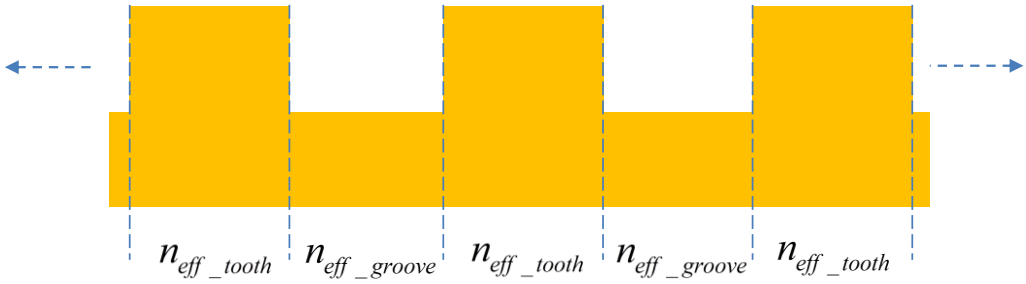

Fig.3. 5: Process to calculate effective index

n_{eff_tooth} and n_{eff_groove} are the effective refractive indices of the etched section (grating tooth) and without the etched (groove) section respectively. n_{eff_tooth} and n_{eff_groove} can be calculated using the effective index method [5]. As there is an equal number of tooths and grooves, the final effective index is found relating to the filling factor as:

$$n_{eff} = (1 - ff) \cdot n_{eff\_groove} + ff \cdot n_{eff\_tooth} \qquad \text{(Eq. 3.1.5.3)}$$

3.2 Simulation methods for designing a grating coupler

3.2.1 Overview

Simulations of photonic devices help us to have an intuitive idea of how the light interacts with matter in different structures. In designing a grating coupler, the first step is to extract the design parameters to achieve the desired performance of the coupler. Finding parameters only through experimentation is always time-consuming and expensive as the experiments may need to be performed several times before finding the optimum parameters. On the other hand, the design parameters can be found easily by numerical methods. After extracting the optimized parameters for the desired outcome of the coupler, they can be used for designing the coupler. The device is first designed using computer-aided software and simulated for best performance.

3.2.2 Geometry of the grating coupler in simulation

The grating coupler is a 3-D problem. For simplicity of the calculation, the structure can be assumed to be a 2-D structure with high accuracy as the width of the gratings is much larger than the height of waveguides and wavelength. The fundamental TE mode of a 12 μm-wide SOI waveguide is shown in Fig.3. 6 [195]. The field distribution along the waveguide axis and the direction of the propagation can be approximated [199] as $\varphi(x,y)=\varphi_1(x)\cdot\varphi_2(y)$, where $\varphi_1(x)$ represents the lateral mode profile and $\varphi_2(y)$ a field component of the slab mode. The coupling efficiency of a 2-D grating structure with a waveguide width much higher than the height is given [195] by

$$\eta=\left|\iint E(x)E(y=y_0,z)Ae^{-\frac{(x-x_0)^2+(z-z_0)^2}{w_0^2}}e^{\left(jn\frac{2\pi}{\lambda}z\sin\theta\right)}dxdz\right|^2 \quad \text{(Eq. 3.2.2.1)}$$

where the constant *A* describes the normalized Gaussian beam, w_0 is the beam width, *n* represents the refractive index of the material between fibre and gratings.

For a constant distance of fibre from the surface of the grating and the width of the grating sufficiently longer than the height, the gratings can be treated as a 1-D structure and Equation 3.3 can be reduced to calculate efficiency as

$$\eta=\left|\int E(x,y=y_0)Ae^{-\frac{(x-x_0)^2}{w_0^2}}e^{\left(jn\frac{2\pi}{\lambda}x\sin\theta\right)}dx\right|^2 \quad \text{(Eq. 3.2.2.2)}$$

Although equations 3.2.2.1 and 3.2.2.2 provide a method to calculate the coupling efficiency, they still do not contain any structural information.

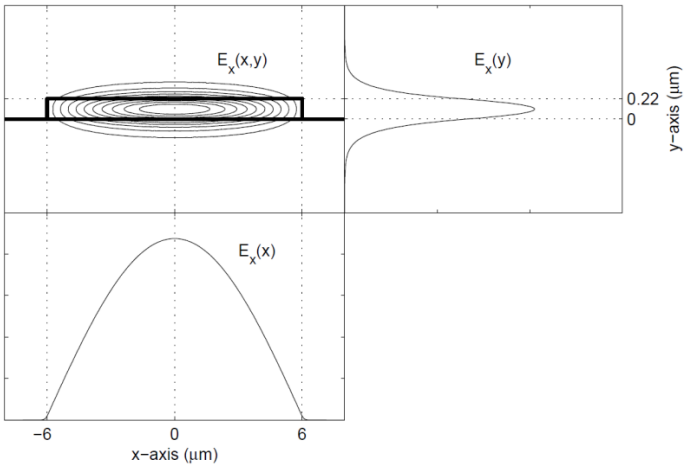

Fig.3. 6: Fundamental TE mode of a 12 µm-wide SOI waveguide.

3.2.3 Finite Difference Time Domain (FDTD) Method

Simulations of the grating coupler with a finite difference time domain method allow us to investigate the propagation of light through the structure. In the FDTD method, the time-dependent Maxwell's equations are solved based on central difference approximations to the space and time partial derivatives.

3.2.3.1 Maxwell's Equations

To understand the behaviour of electro-magnetic radiations, in 1864 James Maxwell presented four sets of equations which are generally transcribed in differential form as follows [200] [201]:

$$\nabla \times H = \frac{\partial}{\partial t} D + J \qquad \text{(Eq. 3.2.3.1.1)}$$

$$\nabla \times E = -\frac{\partial}{\partial t} B \qquad \text{(Eq. 3.2.3.1.2)}$$

$$\nabla \cdot D = \rho \qquad \text{(Eq. 3.2.3.1.3)}$$

$$\nabla \cdot B = 0 \qquad \text{(Eq. 3.2.3.1.4)}$$

where

E = Electric field strength

H = Magnetic field strength

D = Electric displacement

B = Magnetic flux density

J = Current density

ρ = Charge density.

In a source-free condition, $\rho = 0$ and $J = 0$ which is our situation as we are interested in working in the photonics environment. This also entails that the material system we are working with is isotropic. This material system implies that

$$D = \varepsilon E \qquad \text{(Eq. 3.2.3.1.5)}$$

$$B = \mu H \qquad \text{(Eq. 3.2.3.1.6)}$$

where ε and μ are the permittivity and permeability of the material respectively and are scalar quantity.

Finally considering the photonics working environment and isotropic materials, the differential form of Maxwell's equations can be written as

$$\nabla \times H = \frac{\partial}{\partial t}\mu H \qquad \text{(Eq. 3.2.3.1.7)}$$

$$\nabla \times E = -\frac{\partial}{\partial t}\varepsilon E \qquad \text{(Eq. 3.2.3.1.8)}$$

$$\nabla \cdot E = 0 \qquad \text{(Eq. 3.2.3.1.9)}$$

$$\nabla \cdot H = 0 \qquad \text{(Eq. 3.2.3.1.10)}$$

In the finite difference time domain (FDTD) method, these four equations are solved in conjunction with the Yee algorithm [202] to define the nature of H and E in a space of materials with μ and ε over time.

The accuracy of the simulation for electromagnetic properties in FDTD is highly reliant on the spacing between the grids. For accurate calculation of E and H, the distance from one grid to another should be the least possible so that it minimizes changes in the fields between adjacent grids.

For a given grid size of $\Delta x, \Delta y, \Delta z$ and temporal step Δt the equations (3.2.3.1.7) and (3.2.3.1.8) can be discretised as follows.

$$F^n(i,j,k) = F(i\Delta x, j\Delta y, k\Delta z, n\Delta t) = F(x,y,z,t) \quad \text{(Eq. 3.2.3.1.11)}$$

For computational stability the following condition must be satisfied:

$$\Delta t \le \frac{n}{c}\left(\frac{1}{(\Delta x)^2}+\frac{1}{(\Delta y)^2}+\frac{1}{(\Delta z)^2}\right)^{-\frac{1}{2}} \quad \text{(Eq. 3.2.3.1.12)}$$

where n is the refractive index of the medium, and c is the speed of light in vacuum.

3.2.3.2 FDTD specifications for a grating coupler

In this thesis, the grating structures are simulated based on the finite difference time domain method. High accuracy of the results can be achieved with this method as it calculates electric and magnetic fields at ample points in space over a period of time. However, three-dimensional (3D) simulations in FDTD require enormous memory, e.g. as found in a supercomputer. Fortunately, two dimensional (2D) simulations are also applicable in FDTD which we have used for the simulations of our grating coupler. In a 2D simulation, the light can be parted into transverse electric (TE) and transverse magnetic (TM) polarisations as shown in Fig.3. 7.

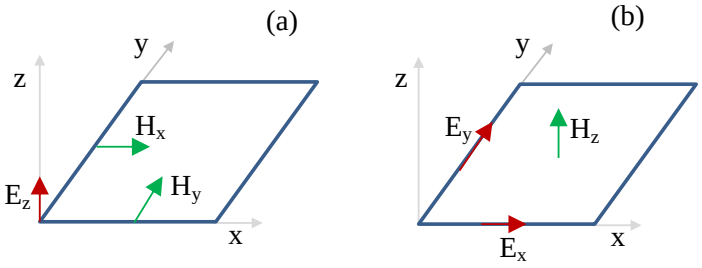

Fig.3. 7: 2D-FDTD unit cells for (a) TE polarization and (b) TM polarization

Considering TE polarisation where the electric field is perpendicular to the plane of incident, the fields can be represented as $E = \hat{y}E_y$ and $H = \hat{x}H_x + \hat{z}H_z$ with all other components are set to zero. Similarly for TE polarisation, the fields are $H = \hat{y}H_y$ and $E = \hat{x}E_x + \hat{z}E_z$ again with all other components set to zero.

For TE polarisation Equation 3.2.3.1.7 can be written as

$$\begin{aligned} \frac{\partial}{\partial z} E_y &= \mu \frac{\partial}{\partial t} H_x \\ \frac{\partial}{\partial x} E_y &= -\mu \frac{\partial}{\partial t} H_z \\ \frac{\partial}{\partial z} H_x - \frac{\partial}{\partial x} H_z &= \varepsilon \frac{\partial}{\partial t} E_y \end{aligned} \qquad \text{(Eq. 3.2.3.1.13)}$$

and for TM polarisation

$$\begin{aligned} -\frac{\partial}{\partial z} H_y &= \varepsilon \frac{\partial}{\partial t} E_x \\ \frac{\partial}{\partial x} H_y &= \varepsilon \frac{\partial}{\partial t} E_z \\ \frac{\partial}{\partial z} E_x - \frac{\partial}{\partial x} E_z &= -\mu \frac{\partial}{\partial t} H_y \end{aligned} \qquad \text{(Eq. 3.2.3.1.14)}$$

For equi-distant grids $\Delta x = \Delta y = \Delta$, Equation 3.2.3.1.12 can be simplified to

$$\Delta t \le \frac{n}{c} \cdot \frac{\Delta}{\sqrt{2}} \qquad \text{(Eq. 3.2.3.1.15)}$$

The simulations are performed using commercially-available software Lumerical FDTD solutions. The coupler is designed based on the specified parameters such as the grating period, wavelength, source profile, spacing between grids and time step. The coupling efficiency is measured by placing a power monitor at the waveguide segment which calculates power $E \times H$ as a function of time. The power of the other segments (such as BOX and reflections at the grating surface) can also be measured using a power monitor to see the power flow through different segments.

The FDTD method primarily limits its applications due to its computationally intensiveness. Although FDTD can handle almost any 2-D and 3-D structures, simulations of a 3-D structure require enormous memory and long computational times. However, this method readily can be used for 2-D structures. For our grating couplers analysis, we have used 2-D simulations of our 3-D structures based on the assumptions in Section 3.2.2. The accuracy of the results of the FDTD method relies mainly on the grid spacing that is exact in the limit that the spacing between grids goes to zero.

3.2.3.3 Validity check of FDTD for a grating coupler

In order to check the validity of the simulations using the Lumerical FDTD setup, we check against a published simulation results presented in [146]. The grating coupler designed in this paper is based on an engineered grating structure using a poly-silicon overlay. The non-uniform grating parameters are optimized using a genetic algorithm. Reproduction of the results of this design provides an opportunity to check the validity of the simulation setup used for numerical analysis of the designs in this thesis. The schematic of the reference grating coupler is depicted in Fig.3. 8.

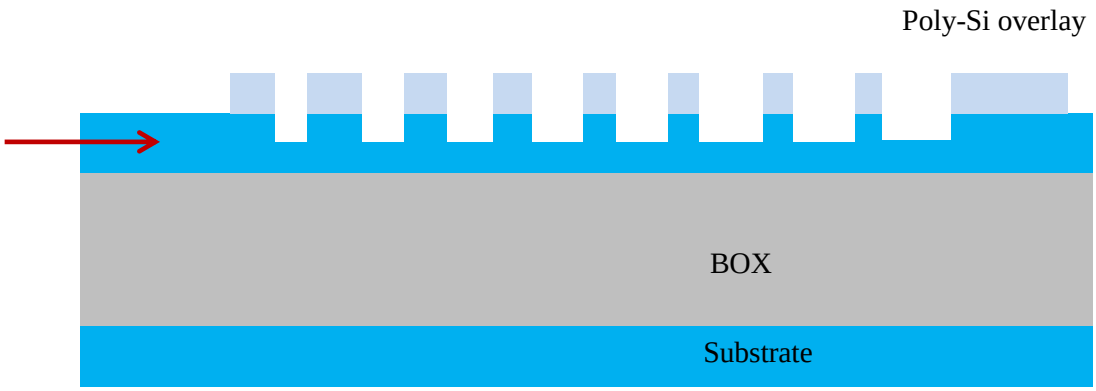

Fig.3. 8: Schematic of the reference grating coupler

The structure was then simulated using Lumerical FDTD solutions and the results are shown in Fig.3. 9. The coupling efficiency is calculated for the grating coupler with a poly-Si overlay as described in [146]. The simulated results are very similar with the published results as can be seen by comparing Fig.3. 9 (b) and (c). The coupling spectra show that the peaks of 78% and 78.6% respectively occur for published and simulated results.

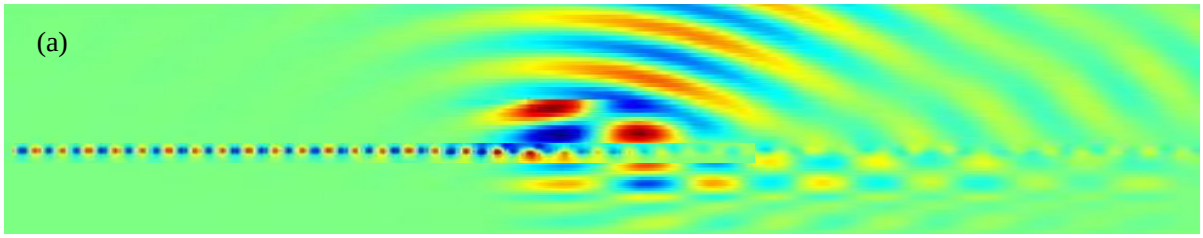

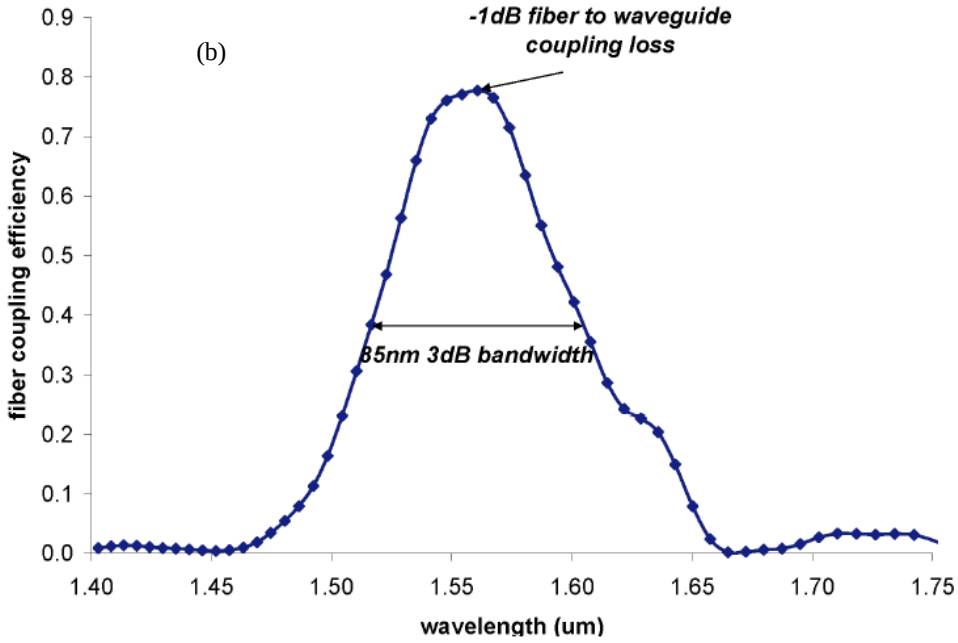

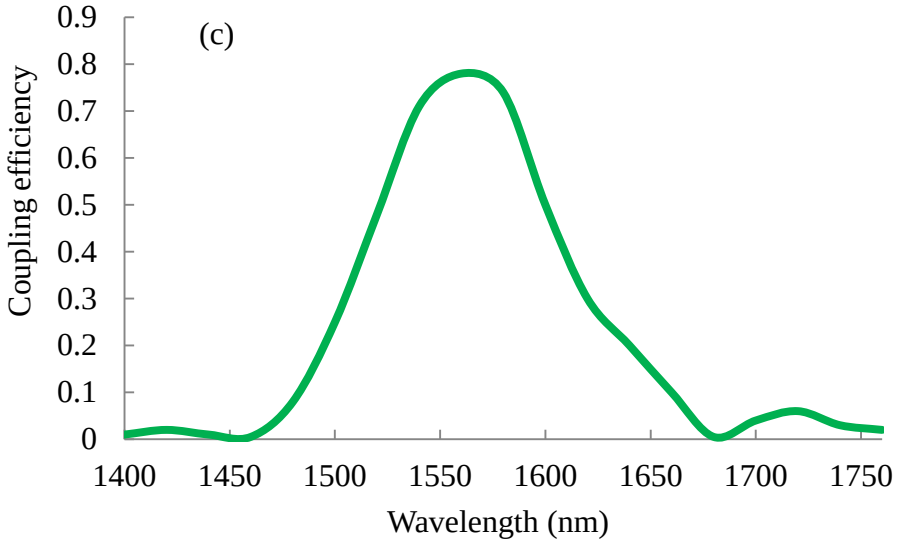

Fig.3. 9: (a) E-field distribution, coupling efficiency as function of wavelength: (b) published; (c) simulated.

3.2.4 Eigenmode Expansion (EME) Method

The Eigenmode Expansion method is a frequency domain method based on the rigorous solutions of the Maxwell's Equation which represents the electromagnetic fields everywhere in the form of a basic set of local modes. The guided and radiated modes together form a complete basis set. The solutions of the Maxwell's Equations can be expressed in terms of a superposition of forward and backward propagating modes as the following equations.

$$E(x,y,z)=\sum_{k=1}^{M}\left(a_k e^{i\beta_k z}+b_k e^{-i\beta_k z}\right)E_k(x,y) \qquad \text{(Eq. 3.2.4.1)}$$

$$H(x,y,z)=\sum_{k=1}^{M}\left(a_k e^{i\beta_k z}-b_k e^{-i\beta_k z}\right)H_k(x,y) \qquad \text{(Eq. 3.2.4.2)}$$

Equations 3.2.4.1 and 3.2.4.2 describe the electric field and magnetic field respectively. The exponential parts, $e^{i\beta_k z}$ and $e^{-i\beta_k z}$, in these equations represent the propagation constants whereas the constants, a_k and b_k, are the forward and backward amplitudes respectively. $E_k(x,y)$ and $H_k(x,y)$ represent mode profiles of electric and magnetic fields respectively.

Theoretically the exact solution of these equations can be obtained using an infinite number of modes toward expansion. However in practical terms, the number of modes is finite and thus introduces numerical errors like any numerical technique. By adding more modes the errors can be minimized. The EME method is fully vectorial and inherently bi-directional as Equations 3.2.4.1 and 3.2.4.2 imply. The algorithm utilizes the scattering matrix (S-matrix) technique to integrate different sections of the waveguide for modelling non-uniform structures. It takes all the reflections of the sections into account in the method. The propagation of the light can be simulated for any angle. A single simulation is needed for all input/output modes and polarizations. Computational cost scales well with propagation distance which makes EME ideal for analysis of light propagation in long devices, e.g. a taper.

The EME method in this study is implemented using Lumerical Mode Solutions. Basically the structure is divided into several cells. In each cell the modes are calculated

supported by the geometry. Once all the modes are calculated, the modes are then propagated so that the S-matrix can be calculated bi-directionally. The workflow of the EME method in Lumerical Mode Solutions is shown in Fig.3. 10.

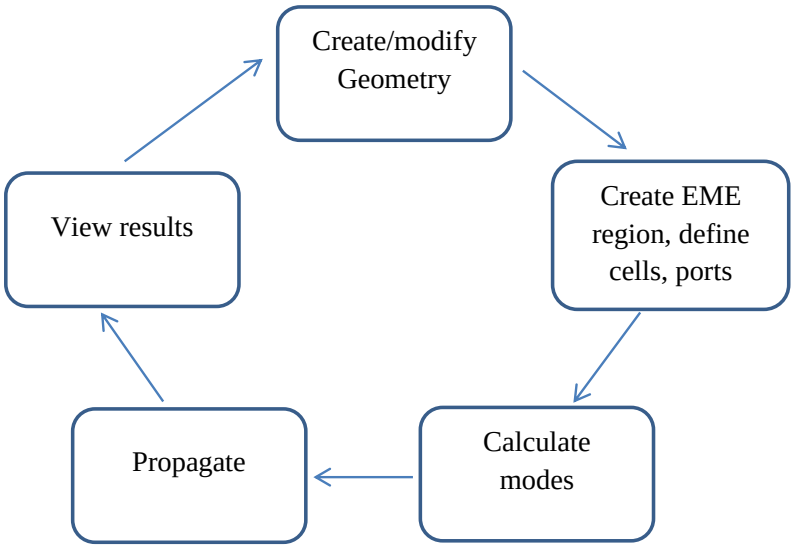

Fig.3. 10: Workflow diagram of EME method implementation in Lumerical Mode Solutions.

3.2.4.1 Validity check of EME for a grating coupler

We check the results presented in [203] using the Lumerical EME setup. The schematic of the reference grating coupler is shown in Fig.3. 11. The design

Fig.3. 11: Schematic of the reference grating coupler

presented in this reference is somewhat similar to the design described in Chapter 4 of this thesis and thus provides be a good opportunity to check the validity of the EME

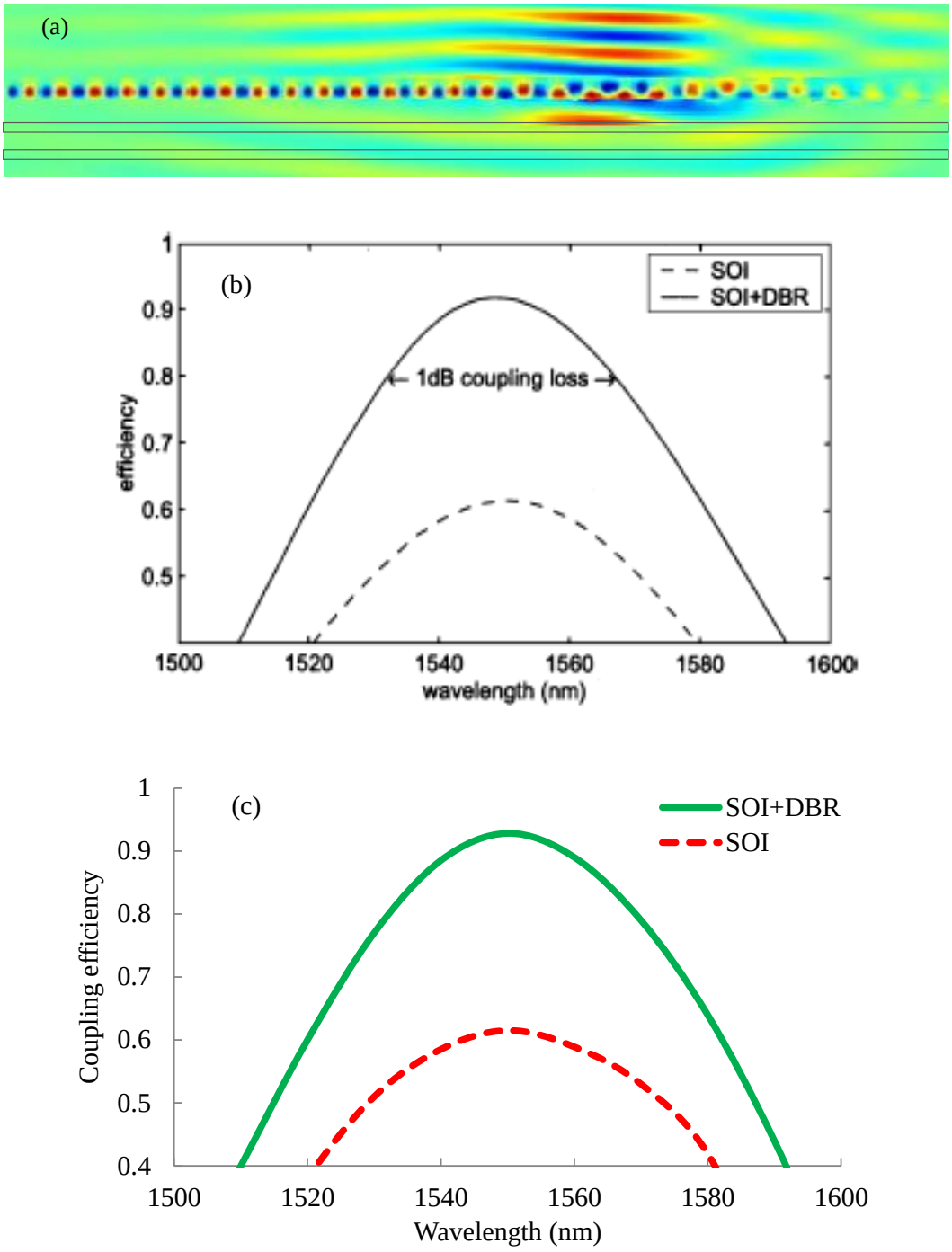

Fig.3. 12: (a) Simulated E-field distribution of the reference grating coupler, coupling efficiency vs. wavelength: (b) published; (c) simulated.

setup used in this thesis. The reference is simulated both with and without DBR and the results are shown in Fig.3. 12. The coupling spectra obtained using EME simulations are very similar to those of the results published in the paper. The peak coupling efficiency occurs at 1550 nm wavelength for cases with 92% and 92.8% published and

simulated respectively in designs with DBR. In cases without DBR, the coupling spectrum is slightly red shifted (~ 2 nm) in simulated results compared with published results.

3.2.5 Perfectly Matched Layer (PML)

One of the restrictions of the FDTD method is that the Maxwell's equations need to be solved with discretization and size, which have to be controlled. If the waves are reflected from the boundary, it will affect the simulation. The theoretically boundless problem can be solved by applying an extra layer that absorbs the waves at the boundary and thus avoids reflections.

In an electromagnetic simulation, such absorption is achieved using a perfectly matched layer (PML) developed by J. P. Berenger [204]. With this layer, the reflections due to any electromagnetic wave that is striking the interface of the medium-vacuum are theoretically null for any frequency and any angle of incident. So the computational domain surrounded by the PML absorbs all the waves at the boundary without any reflections.

Chapter 4

Silicon Reflector-Based Grating Couplers

4.1 Introduction

Over the last few years, intensive research has been carried out to improve the coupling efficiency and coupling bandwidth of the silicon-based grating coupler. Although Groups III-V materials such as InP and GaAs are good candidates for optical properties in grating couplers, their applications are mainly limited by their incompatibility with the CMOS process technology. Therefore, grating couplers based on only silicon and its oxide offer the best solution in terms of compatibility with CMOS: it allows integration of photonic functionality with electronic functionality on the same silicon substrate.

Silicon-on-insulator (SOI) technology that relies heavily on the contrasted indices of Si and SiO_2, enables the design and integration of these photonic devices on a submicronic scale, similar to the devices produced by a standard CMOS fabrication platform in the electronic industry [153] [205]. One of the key challenges with these submicronic waveguide devices is to enable efficient coupling with fiber. This challenge is caused mainly by the mode-field differences between fiber and the waveguide, and the related misalignments [62]. To overcome this, various techniques including prism, butt and grating couplings have been proposed. Among them, butt coupling is an elegant solution for low loss and wideband operation but it often requires post-processing for accurate polishing and dicing to taper the waveguide edges. Therefore, it is not suitable for wafer-scale testing [5] [66] [76] [206]. Grating couplers, which mostly perform out of the plane coupling between a fiber and a waveguide, are also an attractive solution as light can be coupled in and out anywhere on the chip, opening the way for wafer-scale testing [143] [207].

However, despite such advantages, grating couplers often exhibit low coupling efficiency (CE) due to downward radiation of light that propagates towards substrate through buried oxide (BOX) which comprises 35%-45% of total incident light [147]. To minimize this propagation, various attempts have been made to improve the directionality such as poly-silicon gate layer-based [208] and poly-silicon overlay-based [146] grating couplers with CE of 74% and 78% respectively, both of which require an additional layer of amorphous Si layer. A fully etched photonic crystal-based uniform gating coupler is demonstrated with CE of 42% [209]. CE of 65% is reported in [149] by optimizing the grating parameters. An apodized grating coupler with theoretical CE of 72% is reported in [210] by through-etched gratings. A subwavelength grating coupler by implementing waveguide dispersion engineered subwavelength structures is designed in [211] with CE of -2.72 dB. A comprehensive design method is presented in [212] for achieving high CE in a grating coupler where CE of -0.62 dB is reported with non-uniform grating and using a metal back mirror. An engineered RI of materials using fully etched photonic crystal holes in an apodized grating is presented in [213] with demonstrated CE of 67%. By suppressing the second order Brag reflection from the grating using asymmetric grating structure, a CE of 80% is reported in [159] with non-uniform grating for perfectly vertical coupling. A binary blazed grating coupler for perfectly vertical and near vertical coupling is proposed in [214] with CE of 75% and 84% respectively. All the above solutions have offered high directionality for improving CE but most designs are based on apodized and non-uniform gratings which often require complex steps in the CMOS process in comparison to uniform gratings.

Apart from optimization of grating structures and parameters, insertion of a mirror in the BOX is another solution to avoid the downward radiation in grating couplers. A grating coupler based on a gold bottom mirror is proposed in [215] with theoretical and demonstrated CE of 72% and 69% respectively. However, the addition of a gold mirror requires many extensive steps which are not compatible with CMOS. Another back-side metal (aluminum) based grating coupler is demonstrated in [216] to enhance directionality with CE of 69%. Although this design avoids the wafer-to-wafer bonding technique for adding an aluminum layer, it is beyond the Si photonics as materials being used are other than Si. Based on the Distributed Brag Reflector (DBR) a design is proposed in [56] with theoretical CE of 92% where the gratings are non-uniform. In

[217] the downward radiating light has been reflected toward the waveguide using a stack of amorphous-Si/ SiO_2 Bragg bottom reflectors with theoretical and demonstrated CE of 82% and 69.5% respectively where the dimensions of Si and SiO_2 layers need to be exactly one quarter of the wavelength.

We have designed a highly efficient, high bandwidth silicon coupler for interconnection between fiber and nano-scale waveguides by simultaneously applying techniques of light redirection, mirror-reflection and surface gratings. The grating approach in designing such couplers exploits its fabrication simplicity and allows wafer level testing for mass production. We took advantage of using a silicon mirror in the grating coupler that effectively overcame the efficiency-limiting factors associated with coupling through the BOX layer [50] and low bandwidth response of coupled light [209].

4.2 Proposed Wafer Structure with Multiple Pairs of Si-SiO_2 onto Si-substrate

As indicated earlier, coupling efficiency largely relies on how successfully that part of light passing through the BOX and the Si-substrate of a typical single layered structure can be reflected towards the waveguide. To enable that reflection, instead of a thicker SiO_2 BOX layer, a wafer structure with multiple thinner layers of Si-SiO_2 paired onto Si-substrate can be developed, a schematic diagram of which is shown in Fig.4. 1. Each Si-SiO_2 interface acts as a mirror to reflect a certain amount of light, and after several reflections, most of the light which has passed through the BOX and the Si-substrate combines with the light towards the waveguide. The insertion of Si and SiO_2 layers, however, is not straightforward, as the structure will complement coupling efficiency only if the reflected light waves from the Si-SiO_2 interfaces interfere constructively with the originally guided light wave towards the waveguide. Therefore, to enable constructive interference, the path lengths travelled by the reflected light and the angle of interference at Si-SiO_2 interfaces have to be chosen carefully.

In Fig.4. 1, let us assume that the reflected lights from the interfaces of Si and SiO_2 layers of a m-pair structure reach the top Si waveguide with angles $\theta_{r1}, \theta_{d11}, \theta_{d12}$,

θ_{d13} , θ_{d14} and θ_{d1n}. These angles mainly depend on the angle of incidence θ_{in} and the refractive indices (RIs) of Si and SiO_2, which, by using the basic laws of refraction, can be shown to be equal to each other and calculated as,

$$\theta_{d1} = \sin^{-1}\left[\left(\frac{n_{top}}{n_{si}}\right)\cdot \sin\theta_{in}\right] \qquad \text{(Eq. 4.2.1)}$$

where n_{top} and n_{si} are the RIs of top cladding (air) and Si waveguide respectively. θ_{in} is the angle of incidence measured clockwise from the normal to the gratings.

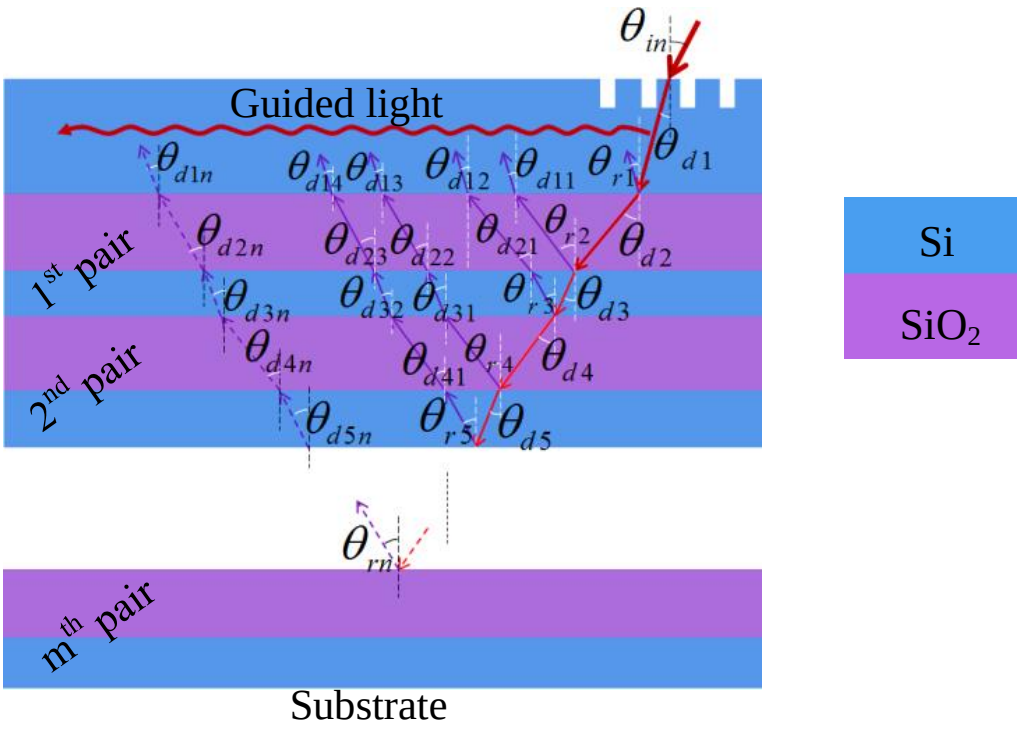

Fig.4. 1: Proposed structure with multiple layers of Si and SiO_2 (BOX) pair onto Si-substrate that reflects the light passing through the BOX and the Si-substrate of a typical single-layered BOX structure to interfere with the actual guided light wave at the waveguide. Only primary reflections towards the waveguide are shown.

The expected pattern of interference that is due to the superposition of the reflected light with the actual guided light can be determined by the difference in path lengths (PL) travelled by each wave of interest. Shown in Fig.4. 1 are two primary reflections per pair. Using Eq. 4.2.1 and geometry of the structure, the PL for each

reflected wave and the corresponding guided wave can be calculated by Eq. 4.2.2.

Path lengths travelled by the waves for the 1st pair of Si-SiO_2 can be calculated by

$$\left.\begin{aligned}
PL_{ref_{11}} &= 2\frac{t_{SiO_2}}{\cos\left[\sin^{-1}\left[\frac{n_{top}}{n_{SiO_2}}\cdot\sin\theta_{in}\right]\right]} \\
PL_{wave_{11}} &= 2\sqrt{\left[\frac{t_{SiO_2}}{\cos\left[\sin^{-1}\left[\frac{n_{top}}{n_{SiO_2}}\cdot\sin\theta_{in}\right]\right]}\right]^2 - t_{SiO_2}^2} \\
PL_{ref_{12}} &= 2\left[\frac{t_{si}}{\cos\left[\sin^{-1}\left[\frac{n_{top}}{n_{si}}\cdot\sin\theta_{in}\right]\right]} + \frac{t_{SiO_2}}{\cos\left[\sin^{-1}\left[\frac{n_{top}}{n_{SiO_2}}\cdot\sin\theta_{in}\right]\right]}\right] \\
PL_{wave_{12}} &= 2\left[\sqrt{\left[\frac{t_{si}}{\cos\left[\sin^{-1}\left[\frac{n_{top}}{n_{si}}\cdot\sin\theta_{in}\right]\right]}\right]^2 - t_{si}^2}\right] + \sqrt{\left[\frac{t_{SiO_2}}{\cos\left[\sin^{-1}\left[\frac{n_{top}}{n_{SiO_2}}\cdot\sin\theta_{in}\right]\right]}\right]^2 - t_{SiO_2}^2}
\end{aligned}\right\}$$

(Eq. 4.2.2)

where

$PL_{ref_{11}}$ and $PL_{ref_{12}}$: are the PLs for the reflected waves for SiO_2 and Si layers of 1^{st} pair respectively,

$PL_{wave_{11}}$ and $PL_{wave_{12}}$: are corresponding PLs for the guided waves,

t_{SiO_2} and t_{Si} : are the thicknesses of the SiO_2 layer and Si layer of the pair,

n_{top}, n_{SiO_2} and n_{Si} : respectively are the RIs for the top cladding, SiO_2 and Si layers, and

θ_{in} : is the angle of incidence of light at the surface of the waveguide.

To enable constructive interference between reflected and actual guided light, the difference of PLs needs to be an integer multiple of wavelength which can be calculated as in Eq.4.2.3.

$$\begin{aligned}
\Delta PL_{11} &= PL_{ref_{11}} - PL_{wave_{11}} = \left(k - \tfrac{1}{2}\right)\lambda \\
\Delta PL_{12} &= PL_{ref_{12}} - PL_{wave_{12}} = k\lambda
\end{aligned} \qquad \text{(Eq. 4.2.3)}$$

where

ΔPL : is the path length difference between reflected and actual guided light,

k : is an integer and

λ : is the wavelength of the light.

Using Eqs. 4.2.2 and 4.2.3, the value of k can be calculated for the thicknesses of SiO_2 and Si at which k is an integer as shown in Fig.4. 2 (a). Fig.4. 2 (b) shows the incident angles at which k is an integer.

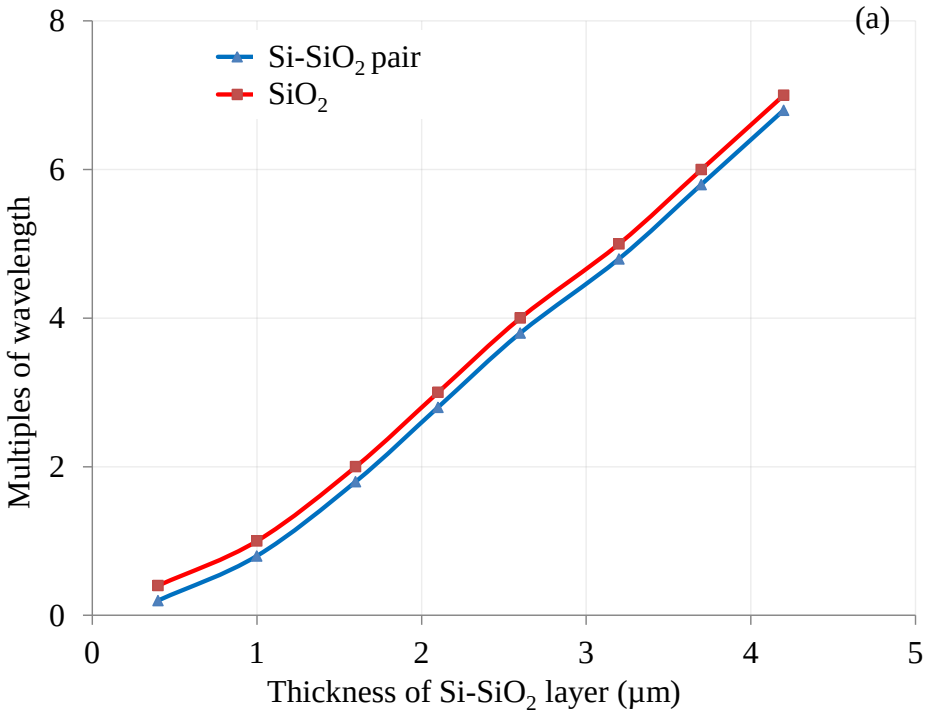

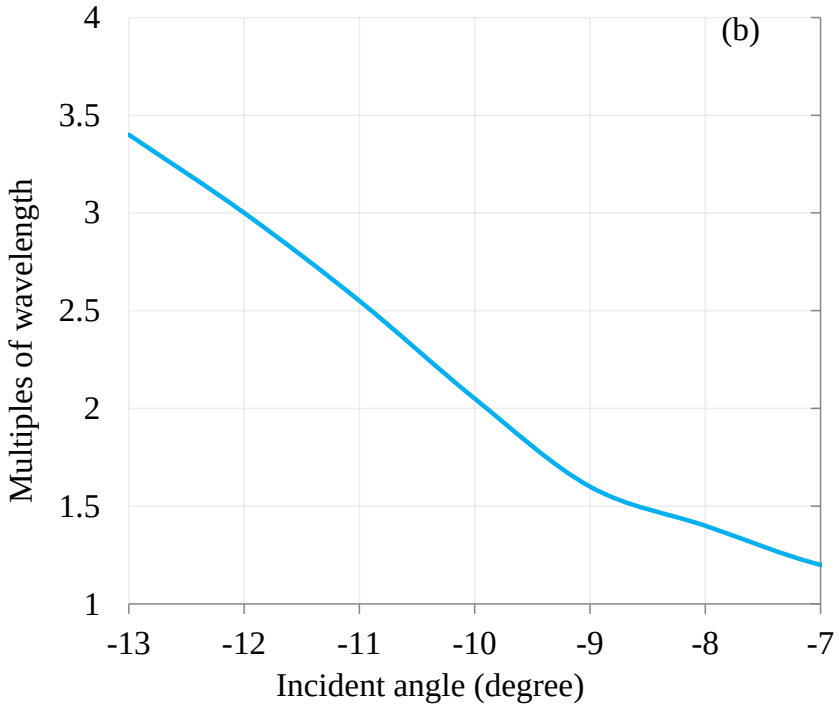

Fig.4. 2: Multiples of wavelengths for: (a) thicknesses of the SiO_2 and Si; (b) incident angle

Shown in Fig. 4.2.2, the integer values of k occur at the thicknesses of 1.000 µm ($k=1$), 1.600 µm ($k=2$), 2.100 µm ($k=3$), 2.600 µm ($k=4$), 3.200 µm ($k=5$), 3.700 µm ($k=6$), 4.200 µm ($k=7$) of SiO_2. Using Eq. 4.2.3, the thickness of SiO_2 (t_{SiO_2}), Si (t_{Si}) and thickness of Si-SiO_2 pair (t_{pair}) at which the constructive interferences occur are shown in Table 4.2.1.

TABLE 4.2.1: THICKNESSES OF THE 1ST PAIR FOR CONSTRUCTIVE INTERFERENCE BETWEEN REFLECTED AND GUIDED LIGHT

Value of k	1	2	3	4	5	6	7
t_{SiO_2} (µm)	0.500	1.100	1.600	2.100	2.600	3.200	3.700
t_{Si} (µm)	0.100	0.100	0.100	0.100	0.100	0.100	0.100
t_{pair} (µm)	0.600	1.200	1.700	2.200	2.700	3.300	3.800

The PLs for subsequent pairs can be expressed in terms of PLs of the 1st pair as

$$PL_{ref_{mn}} = \begin{cases} \frac{m+n}{2} PL_{ref_{11}} + \frac{m-n}{2} PL_{ref_{12}}, n=1 \\ \frac{m+1}{n} PL_{ref_{12}} + \frac{m}{n} PL_{ref_{11}}, n=2 \end{cases}$$

$$PL_{wave_{mn}} = \begin{cases} mPL_{wave_{11}} + (m-n) PL_{wave_{12}}, n=1 \\ m\left(PL_{wave_{11}} + PL_{wave_{12}}\right), n=2 \end{cases} \quad \text{(EQ. 4.2.4)}$$

where

m : is the number of pair and

n : is the layer of SiO_2 $(n=1)$ and Si $(n=2)$ of the m^{th} pair.

Using Eqs. 4.2.3 and 4.2.4, the optimum thickness of the 2nd pair can be calculated at which the value of k is an integer for constructive interference between reflected and guided light. Shown in Fig.4. 3, the integer values of k happen at the thicknesses of SiO_2 of 400 nm, 900 nm, 1400 nm and 1900 nm. Therefore the total thicknesses of the 2nd pair can be obtained by adding 100 nm of Si with the thicknesses of SiO_2.

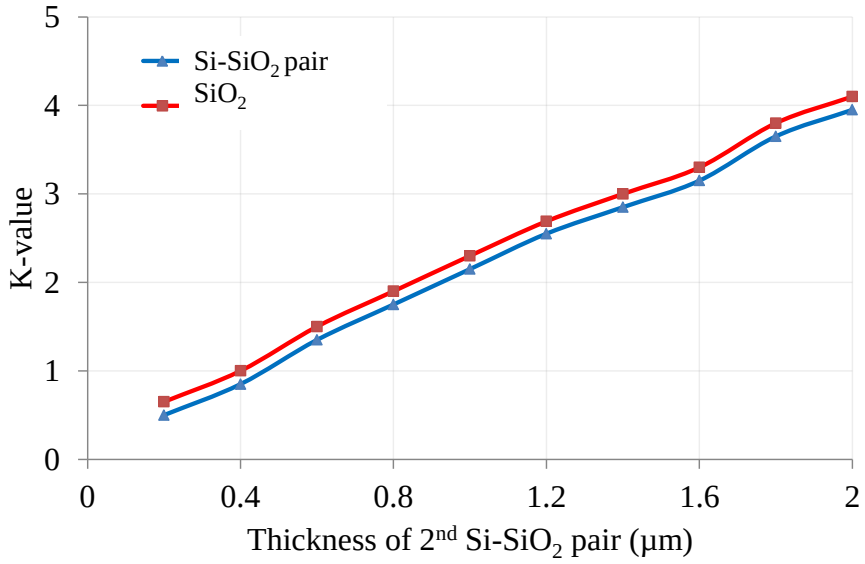

Fig.4. 3: Values of for the different thicknesses of 2nd pair of Si-SiO_2

4.3 Designed Grating Coupler based on the Proposed Multi-layer Structure

The schematic diagram and the specifications of the grating coupler designed based on the proposed multi-layer structure is shown in Fig.4. 4. It consists of a SOI wafer with top Si layer of 220 nm for single mode operation of the coupler. The BOX layer is incorporated with two pairs of Si-SiO_2, with a top pair of 500 nm SiO_2 and 100 nm Si layers and a bottom pair of 400 nm SiO_2 and 100 nm Si. The gratings are etched on the top Si layer. The grating period (Λ) is calculated using Equation 4.3.1:

$$\Lambda = \frac{\lambda}{n_{eff} - n_{top}\sin(\theta_{in})} \qquad \text{(Eq. 4.3.1)}$$

where

Λ : is the grating period

λ : is the wavelength of light incident on the surface of the grating structure, n_{eff} : the effective RI of the structure,

n_{top} is the RI of the top cladding, and

θ_{in} : the angle of incidence with normal to the surface of the structure.

By using fully vectorial mode solver of Lumerical Solutions™, n_{eff} is found to be 2.006, and by setting the target wavelength at $\lambda = 1550\,\text{nm}$, $n_{top} = 1$(air), and $\theta_{in} = -12^0$, the grating period is calculated to be 700 nm. The etch depth (*d*) and grating width (*w*) are also optimized for maximum efficiency and found to be 80 nm and 400 nm respectively, with a filling factor (w/Λ) of 0.571. Therefore, after etching the grating depth of 80 nm, a 140 nm silicon layer remains as a waveguide below the gratings.

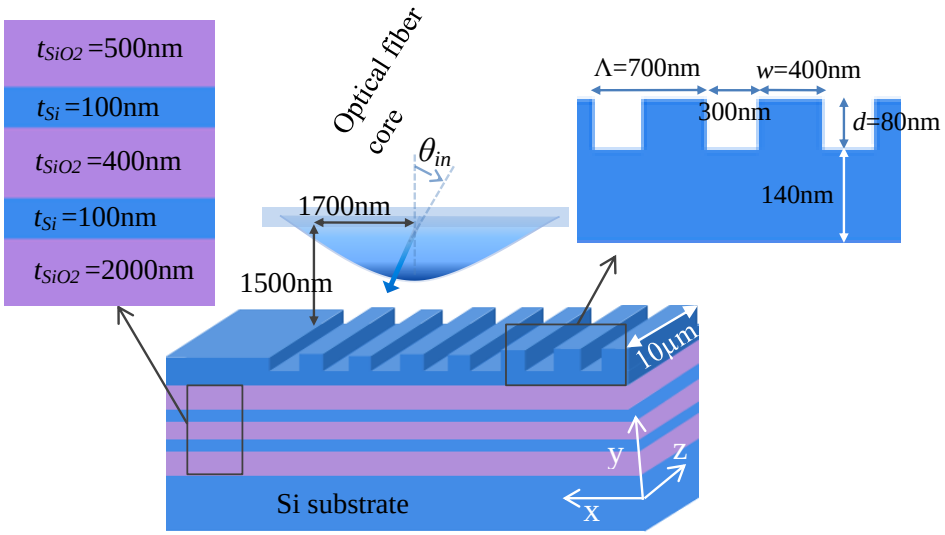

Fig.4. 4: Schematic diagram of the proposed multi-layer structure grating coupler with design parameters.

The fabrication of the proposed structure is fully compatible with standard CMOS process technology. To develop a photonic circuitry, a 2 μm SiO_2 layer for isolation can be deposited on a bare silicon wafer using plasma enhanced chemical vapor deposition (PECVD) process. To deposit the reflector layers on SiO_2, the surface of SiO_2 layer is needed to be polished by chemical mechanical polish (CMP). After deposition of reflector layers comprising of 100 nm Si → 400 nm SiO_2 → 100 nm Si → 500 nm SiO_2 by using PECVD, a 220 nm layer of poly-Si can also be deposited by using PECVD. Finally, the grating structure can be realized on top Si layer using 193 nm optical lithography and dry etching.

4.4 Performance Characterization and Discussion

The proposed grating coupler is simulated using 2-D FDTD of Lumerical Solutions^{TM}, a commercially available software package to design silicon photonics devices. A TE polarized Gaussian shaped light source is applied on the surface of the gratings with Mode-Field Diameter of 10 μm which is comparable to a standard single mode fiber (SMF). The position of the optical source is optimized as 1500 nm above the grating surface and 1700 nm away from the left end of grating as shown in Fig.4. 4. The TE mode field distribution in the BOX and the silicon waveguide region including

the impinging Gaussian beam region is shown in Fig.4. 5. Fig.4. 5 (a) shows the propagation of light when there was only a BOX layer (SiO_2) on the Si substrate and Fig.4. 5 (b) shows the propagation at the presence of multiple layers of Si-SiO_2 pairs onto Si-substrate. For a fair comparison, other parameters of the coupler were kept unchanged. Shown in Fig.4. 5 (b), light through the BOX layer has been reduced significantly in the presence of Si-SiO_2 layers. Fig.4. 5 (c)-(d) show the TE mode profiles of light from the point of incidence of the grating coupler along the Si waveguide. The incident light, that is scattered by the surface gratings, propagates in +x, –x, and –y directions. The lights along +x and -x directions diffract upwards and interfere with the incident light and form a standing wave with resonance around the point of incidence. As a result, maximum light occurs at the point of incidence (x = -5.5 µm) which is 1700 nm away from the lefternmost end of the grating, as shown in Fig.4. 5 (c)-(d). The addition of Si-SiO_2 layers onto Si-substrate increases the light up to 78%

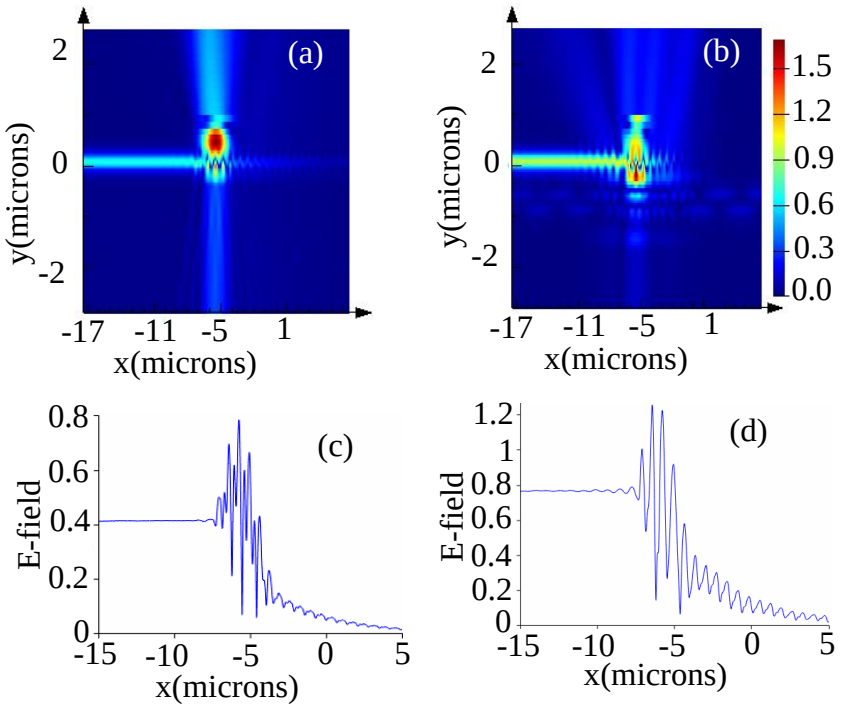

Fig.4. 5: TE mode distribution of light in the proposed grating coupler at the wavelength of 1550 nm for the structures (a): without any Si-SiO_2 pair inside the BOX, and (b): with Si-SiO_2 layers inside the BOX. (c) and (d) represent the respective profiles of the TE mode of light for the structures, again without and with Si-SiO_2 layers inside the BOX.

(Fig.4. 5 (d)) whereas light was about 40% without the Si-SiO_2 layers (Fig.4. 5 (c)). This is because light propagating through the BOX and Si-substrate was never collected back and was wasted completely. The Si-SiO_2 layers onto Si-substrate reflect the wasted light back to the waveguide and re-collected to increase the delivery of optical power.

To achieve high CE, the thickness of the SiO_2 at which constructive interference happens has been chosen based on Equations 4.2.2 and 4.2.3. Fig.4. 6 shows the CE over a range of telecommunications wavelengths where it can be seen that the maximum CE is achieved for the BOX thicknesses at which the value of k in Eq. 4.2.3 is an integer. Fig.4. 6 (a) shows CE for SiO_2 thicknesses of constructive interference whereas Fig.4. 6 (b) shows CE for some SiO_2 thicknesses of destructive interference where the value of k is other than an integer. Shown in Fig.4. 6 (a), the maximum CE happens at the thicknesses of 500 nm, 1100 nm, 1600 nm, 2100 nm as obtained in Table 1 using Eqs. 4.2.2 and 4.2.3. Although high CEs (81% and 80%) are achieved at the thickness of 1100 nm at 1557 nm wavelength and at the thickness of 1600 nm at 1554 nm wavelength respectively, the CEs are over a narrow wavelength range. For the thickness of 500 nm, the high CE (78%) is achieved over a wide range of wavelengths. When the thicknesses of SiO_2 are such that the value of k is apart from an integer, the CE decreases as shown in Fig.4. 6 (b). As the difference between thicknesses at which k is an integer and non-integer increases, the CE keep decreasing.

Similarly, the thickness of the 2^{nd} pair can be calculated using Eqs. 4.2.3 and 4.2.4 at which the value of k is an integer and hence the waves interfere constructively. Fig.4. 6 (c) and (d) show the CE over a range of wavelengths for the thicknesses of the 2^{nd} pair.

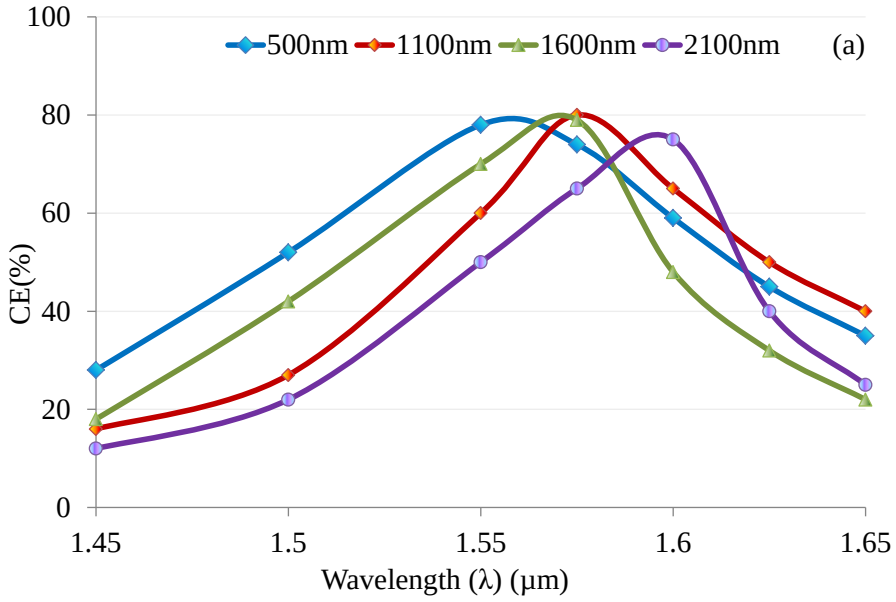
100
80
60
40
20
0
CE(%)
500nm
1100nm
1600nm
2100nm
(a)
1.45
1.5
1.55
1.6
1.65
Wavelength (λ) (μm)

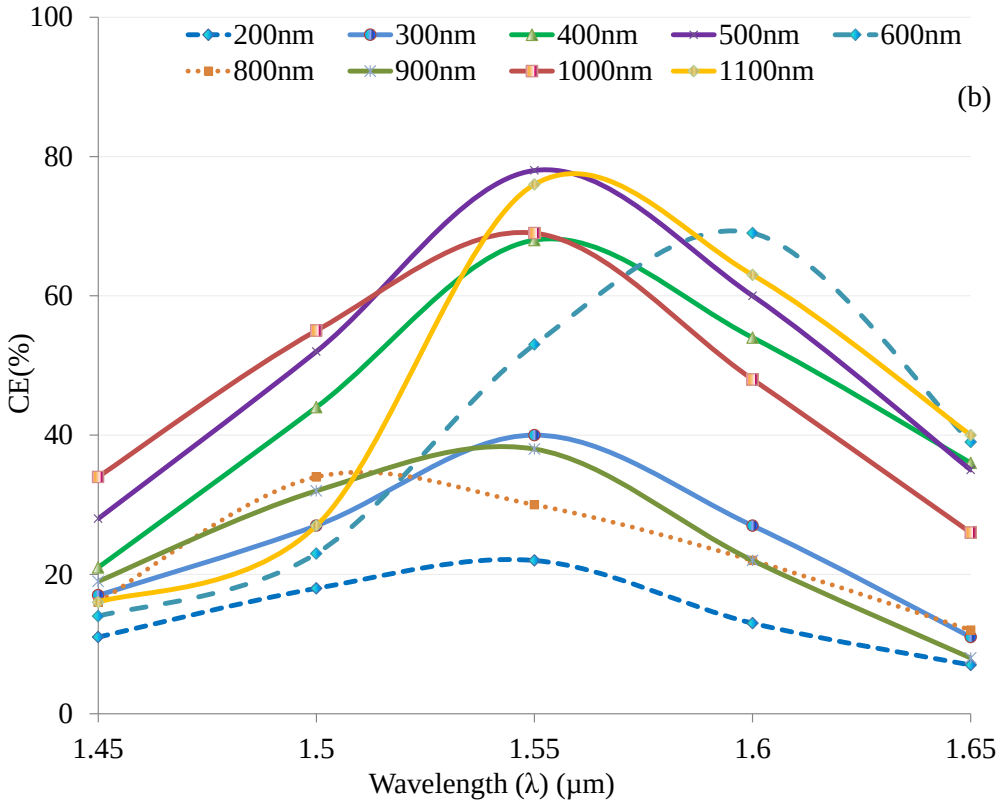
100
80
60
40
20
0
CE(%)
200nm
300nm
400nm
500nm
600nm
800nm
900nm
1000nm
1100nm
(b)
1.45
1.5
1.55
1.6
1.65
Wavelength (λ) (μm)

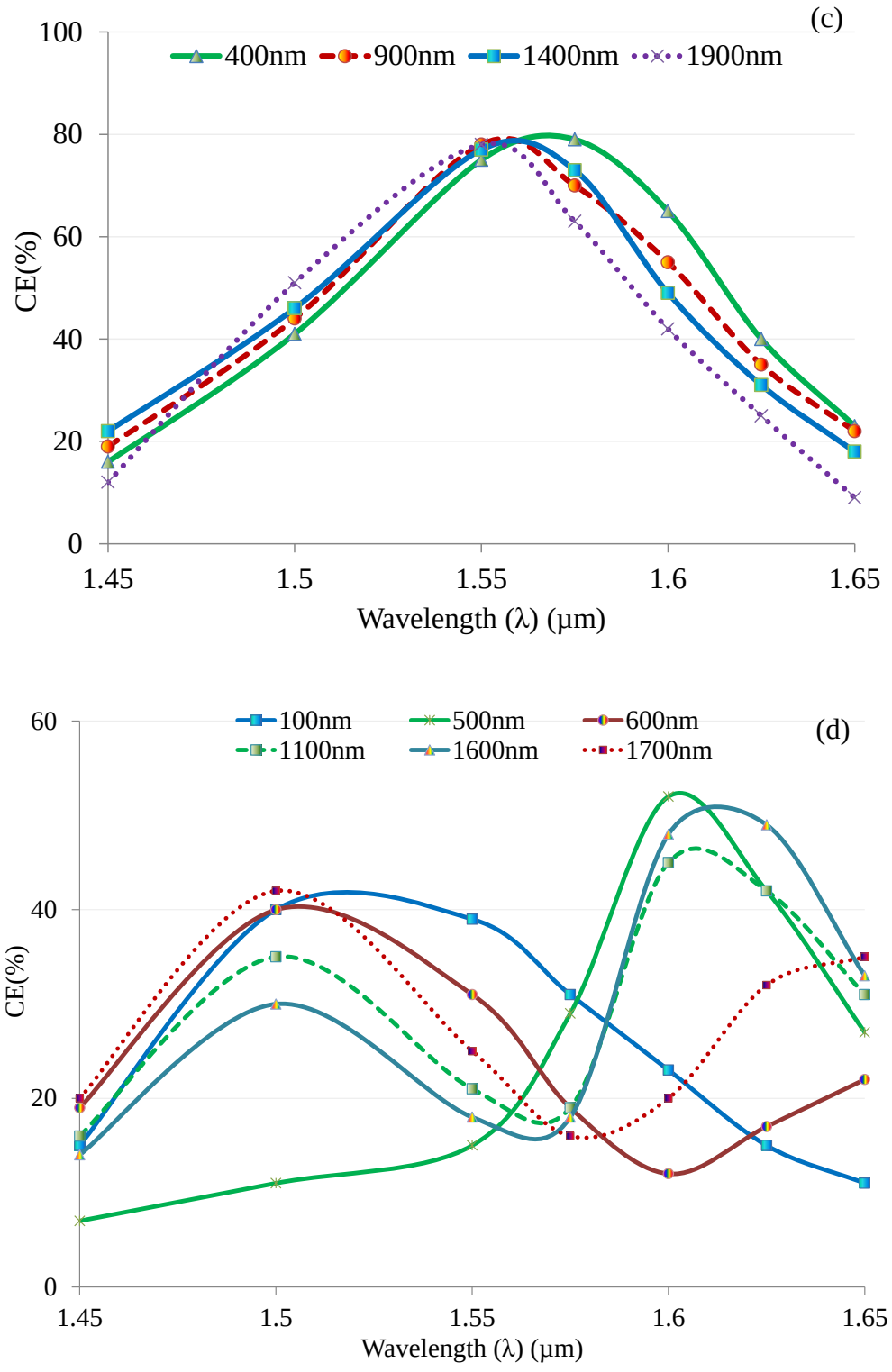

Fig.4. 6: Coupling efficiency vs. wavelengths: (a) thicknesses of SiO_2 for which is an integer and hence constructive interference occurs; (b) thicknesses of SiO_2 from 200 nm to 1100 nm. At 500 nm and 1100 nm thicknesses, constructive interferences occur and deviation from these

thicknesses results in destructive interference which causes lower CE: (c) for different thicknesses of the 2nd pair of Si-SiO_2 where constructive interferences occur, and (d) for different thicknesses of 2nd pair of Si-SiO_2 where destructive interferences occur.

For the thicknesses of 400 nm, 900 nm, 1400 nm and 1900 nm of SiO_2 of the 2nd pair, where the k value is an integer, the waves interfere constructively and the CE is enhanced to around 78% over a wide range of wavelengths are as shown in Fig.4. 6 (c). Whereas, for the thicknesses of SiO_2 at which the k value is other than an integer, the waves interfere destructively and the CE falls, as shown in Fig.4. 6 (d).

To quantify the optimum values of CE and CBW, the proposed coupler is characterized for various performance-influencing parameters including: (i) position of the fiber (optical source) on the grating surface; (ii) angle of incidence; (iii) grating filling factor; (iv) etch depth and waveguide thickness, and (v) number of Si-SiO_2 pairs onto Si-substrate. From this point on, all the characterizations of influencing parameters are performed by keeping the mirror thickness and position constant.

The relationships among various axial positions (both horizontal and vertical) of fiber on the grating surface, coupling efficiency and coupling bandwidth are shown in Fig.4. 7 (a). It shows that the horizontal positioning of fiber has a significant effect on both CE and CBW, whereas vertical positioning has very little to do in this regard. The maximum coupling efficiency (CE = 78%, -1.07 dB) and bandwidth ($CBW_{1\text{-}dB}$ = 77 nm) are achieved at 1500 nm above the grating surface and 1700 nm away from the lefternmost starting point of the grating structure. Fig.4. 7 (b) characterizes various CEs and CBWs with different angles of incidence of light. It shows that CE follows approximate periodic highs and lows with the changes in angles of incidence, while the picture is quite different for CBWs, which shows a gradual decrease from the highest value due to the changes in angles of incidence. Fig.4. 7 (b) also shows that the highest CE and CBW both happen at an incident angle of around -12^0.

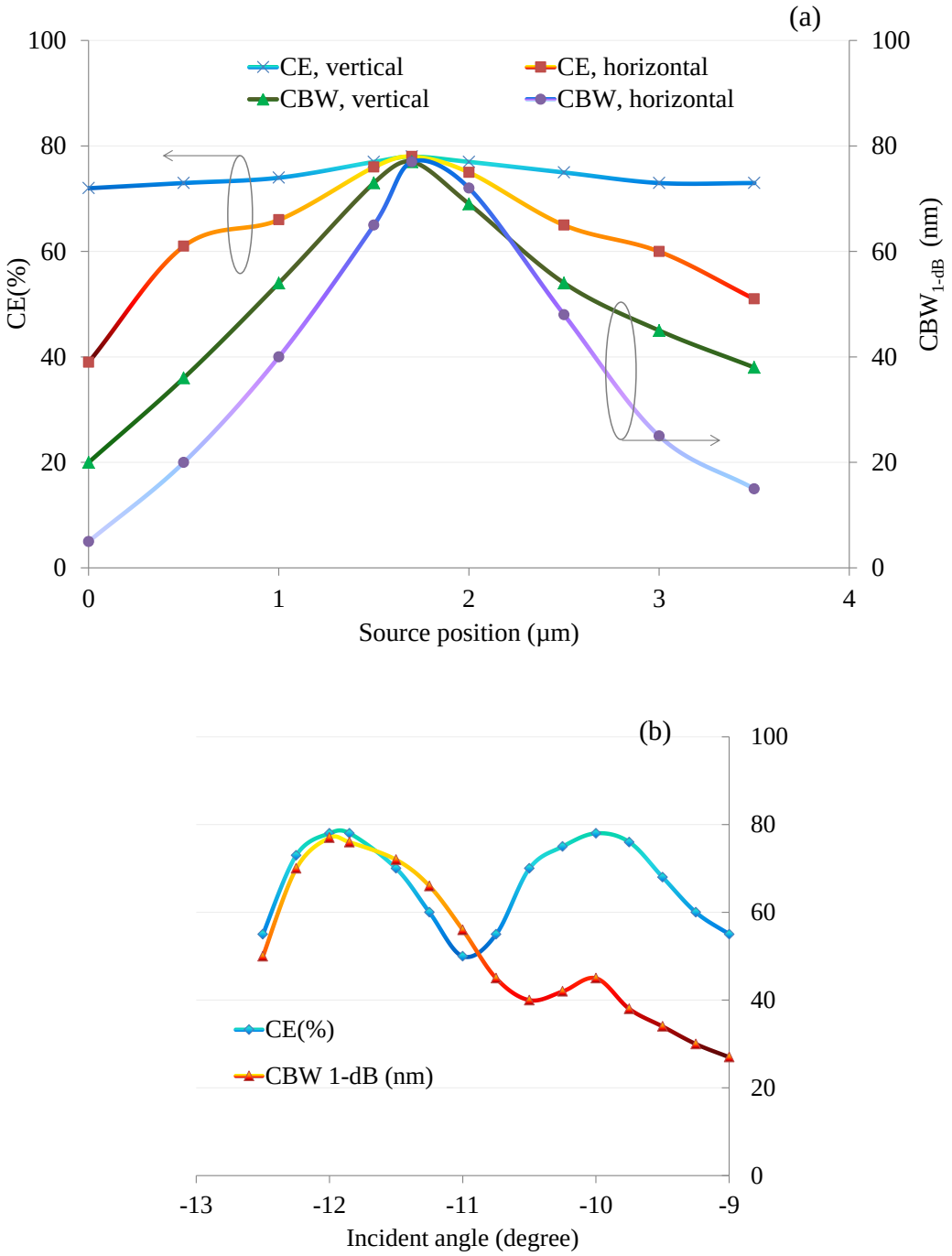

Fig.4. 7: (a): The relationships among various axial (both vertical and horizontal axis) positions of the fiber on the grating surface, coupling efficiency at wavelength of 1550 nm and coupling bandwidth. "0" in the horizontal scale refers to the lefternmost starting point of the grating structure. (b): The relationships among various incident angles, coupling efficiency at wavelength of 1550 nm and coupling bandwidth.

The coupling bandwidth of any grating coupler is highly reliant on the grating filling factor (ff), where a higher ff enables more light to couple to the waveguide of longer wavelengths, and lower ff enables coupling of more light of shorter wavelengths. The CEs in regard to wavelengths for 80% ff and 30% ff are shown in Fig.4. 8 (b). In order to achieve higher coupling bandwidths, the ff must be chosen in such a way that the coupling of light for both longer and shorter wavelengths is optimized simultaneously. In our design, the optimized filling factor ($ff = w/\Lambda$) is 57.1% at which the maximum bandwidth is achieved. The thickness of the Si waveguide is optimized as 220 nm and a grating is formed by etching this layer. The optimum etch depth is found to be 80 nm which is 40% of the waveguide thickness for maximum coupling efficiency and bandwidth as shown in Fig.4. 8 (a).

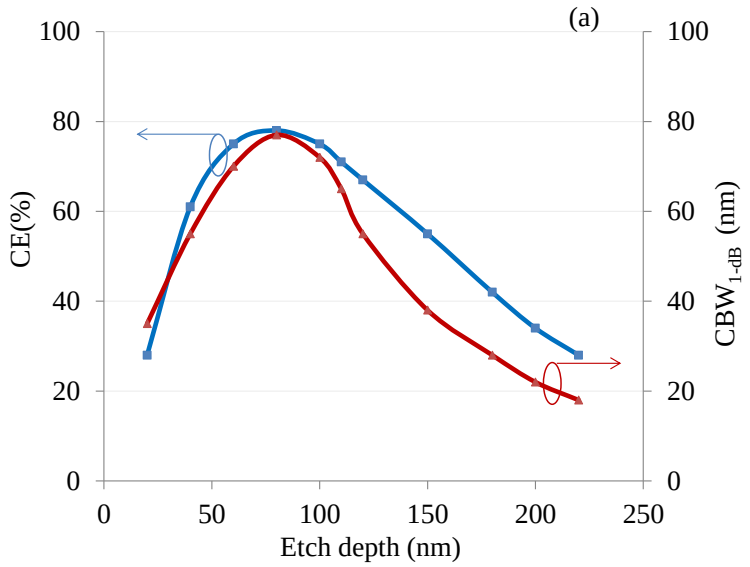

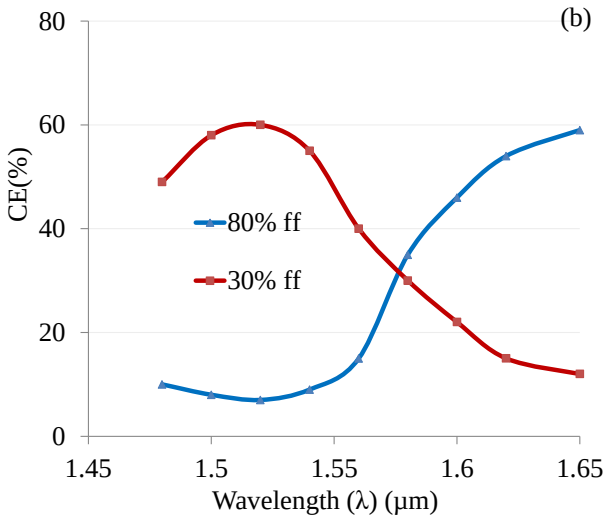

Fig.4. 8: Coupling efficiency at wavelength of 1550 nm and bandwidth with respect to the etch depth. "0" in the horizontal scale refers to non-etched and "220" to fully-etched for the waveguide thickness of 220 nm. (b): Coupling efficiency vs. wavelength for higher and lower grating filling factors.

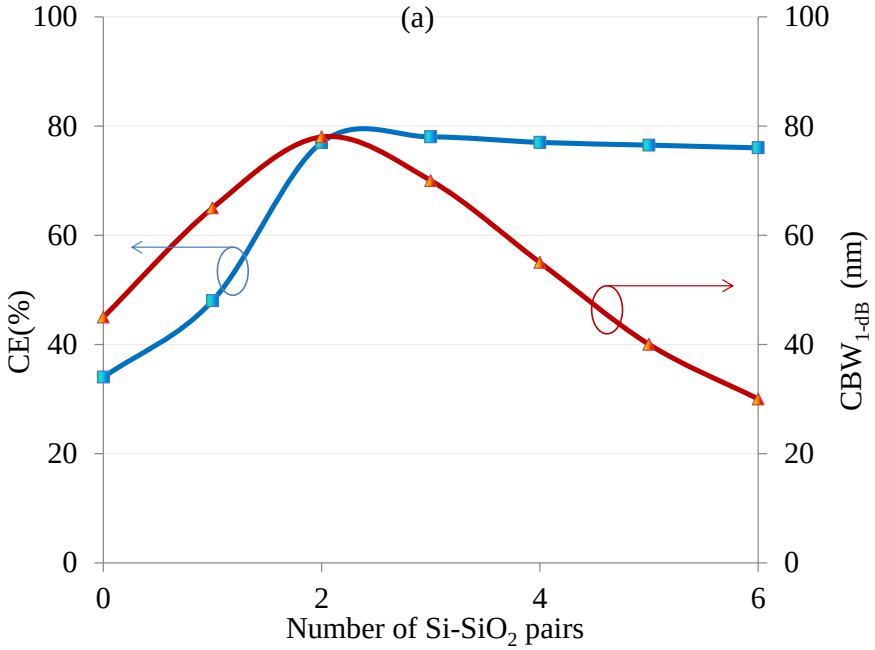

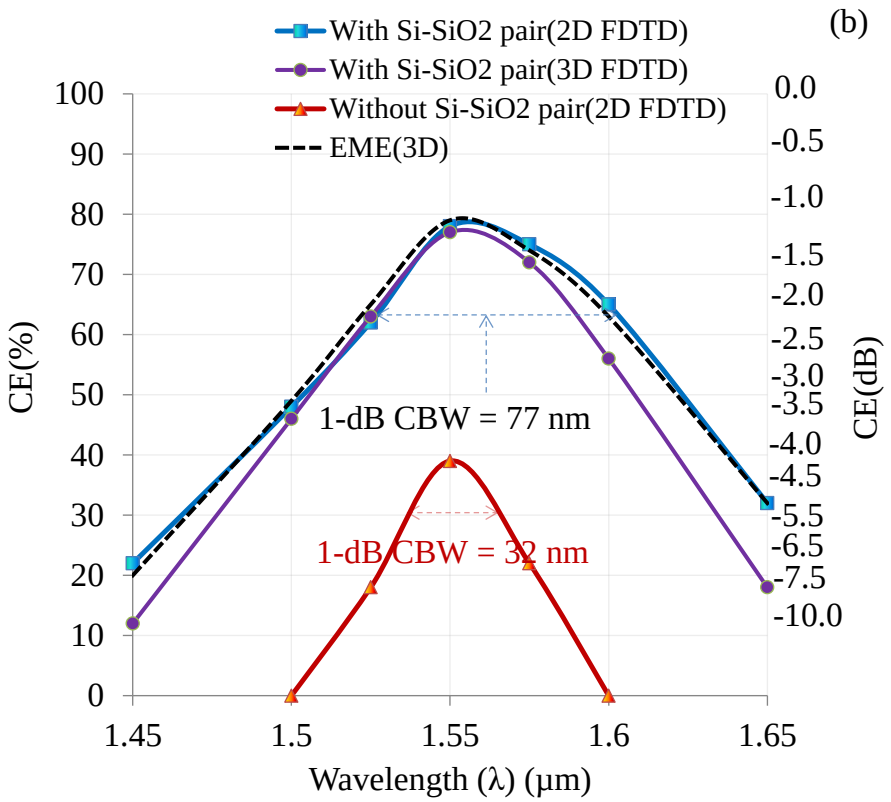

Fig.4. 9: (a): Coupling efficiency at a wavelength of 1550 nm and bandwidth for a number of Si-SiO_2 pairs inside the BOX. (b): Coupling bandwidth of the proposed grating coupler, with and without reflective pairs.

Fig.4. 9 (a) characterizes the coupling efficiency at a wavelength of 1550 nm and bandwidth for a number of Si-SiO_2 pairs in the BOX layer. It shows that coupling efficiency keeps increasing until it is virtually saturated after just two Si-SiO_2 pairs, whereas coupling bandwidth decreases with the number of additional Si-SiO_2 pairs after two, as shown in Fig.4. 9 (a).

With such optimized values of fiber positions (1500 nm above the grating surface and 1700 nm from the lefternmost end of the gratings), incident angle ($\theta_{in} = -12^0$), grating period ($\Lambda = 700\,nm$), filling factor ($ff = 57.1\%$), etch depth (80 nm), waveguide thickness (t_{wg} = *220 nm*) and two pairs of Si-SiO_2 on Si substrate, the 1-dB

coupling bandwidth of the proposed coupler is recalculated and found to be 77 nm, as shown in Fig.4. 9 (b).

The coupler with optimized design parameters obtained by 2D FDTD analysis is also simulated by 3D FDTD to see the actual performance of the coupler. To further validate the results, the coupler was analysed based on EME method using Lumerical Mode Solutions. In both cases the results are in excellent agreement with 2D FDTD results as shown in Fig.4. 9 (b). The peak coupling efficiency of 3D FDTD is 77.2% which is very close to the 78% obtained by 2D FDTD. However, the bandwidth of 72 nm is a little narrower in 3D FDTD when compared with 2D FDTD. The coupling spectrum obtained by the EME simulation is very similar to 2D FDTD.

4.5 Waveguide Dimensions and Coupler Performance

4.5.1 Single Mode Waveguide and Coupling Efficiency

The wave propagates along a silicon waveguide, which is the ultimate light wave detected at the end of the nano waveguide. The dimension of the waveguide has significant effects on the performance of the coupler. If the dimension is large, the waveguide allows multiple optical modes to reside within it. Therefore, the coupling efficiency will be calculated based on the multi-mode analysis. To preserve the single mode operation of the grating coupler, the waveguide thickness t_{wg} must be such that it supports only a single optical mode. For a silicon grating coupler, it is found that the cut-off thickness of the waveguide is $t_{wg} < 230\ nm$. For $t_{wg} > 230\ nm$: the waveguide supports multimode as shown in Fig.4. 10. At a thickness of 220 nm (Fig.4. 10 (c)), the waveguide supports just a single optical mode whereas thicknesses of 240 nm and 250 nm support multiple optical modes (Fig.4. 10 (a) and (b) respectively). In this design the waveguide thickness is optimized at 220 nm and grating is formed by etching this layer. The optimum etch depth is found to be 80 nm which is 40% of the waveguide thickness for maximum coupling efficiency and bandwidth as shown in Fig.4. 8 (a).

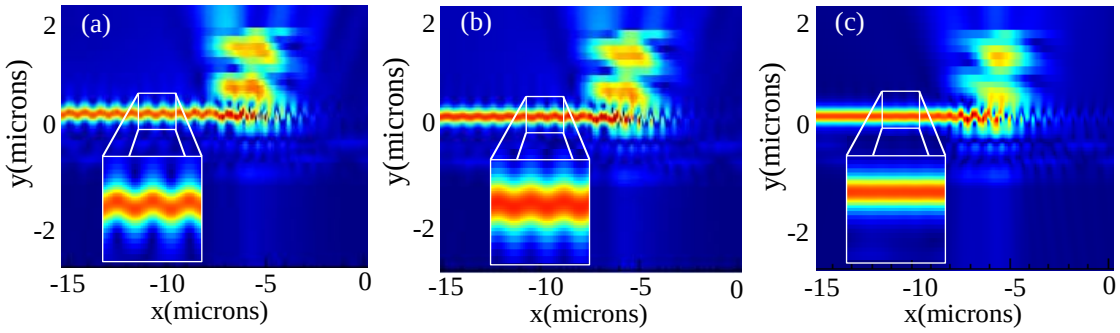

Fig.4. 10: Field distributions along Si waveguide for different thicknesses of the waveguide: (a) 250 nm; (b) 240 nm, and (c) 220 nm. Insets show the clear visualization of the field distributions in the Si waveguide.

4.5.2 Multimode Waveguide and Coupling Efficiency

The total optical power in a multimode waveguide is higher than that of a single mode waveguide. The field distribution in the former is shown in Fig.4. 11 at a wavelength of 1550 nm where: (a) shows TE field distributions, and (b) shows respective field profiles. From the results in Fig.4. 11, it can be observed that the BOX layer plays a significant role on the coupling efficiency and the quality of the wave in grating couplers. For a very thin layer of SiO_2, for example, BOX thicknesses of 100 nm and 200 nm in Fig.4. 11, the light in the waveguide layer and thin silicon layer below the BOX layer coupled and introduced more ripples. This results in noisy wave propagation. With increasing thicknesses of the BOX layer, the ripples reduce significantly and an almost ripple-free wave is achieved. A thickness of around 400 nm gives the highest coupling efficiency and high quality ripple-free wave propagation. However, if the thickness keeps increasing, the ripples return, as shown. This is because for greater thicknesses of the BOX layer, from around 500 nm in this structure, a complete mode of the wave starts and is completed at 2200 nm as can be seen in Fig.4. 11. At the starting point of a mode in the BOX layer, coupling efficiency decreases but after completion of that mode the efficiency again increases but causes a high ripple wave as shown in Fig.4. 11 for 500 nm to 2200 nm BOX layer thickness. From this, we can observe that for approximately every 300 nm thickness of the BOX

layer, a new mode begins. The formation of the confining mode in the BOX causes a periodic change in coupling efficiency which can be seen in Fig.4. 12.

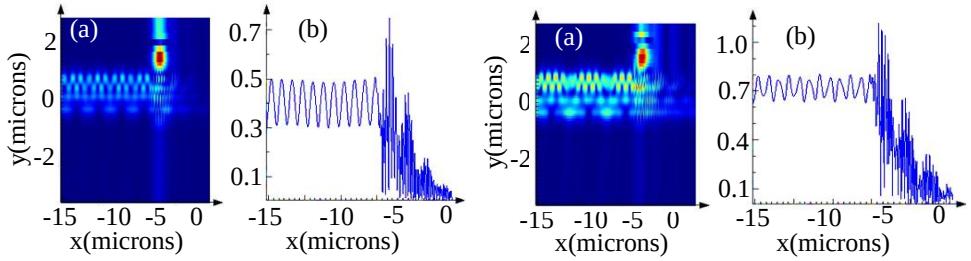

100 nm BOX 200 nm BOX

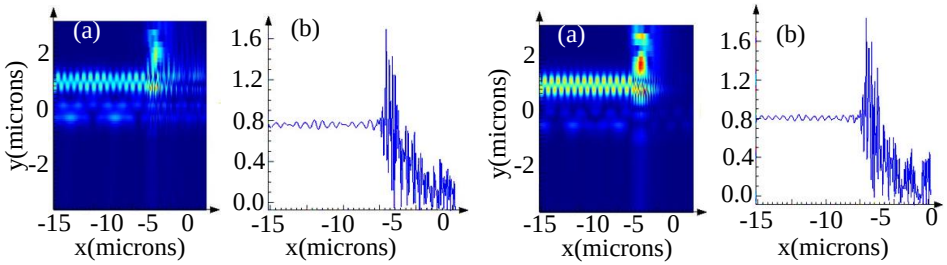

300 nm BOX 400 nm BOX

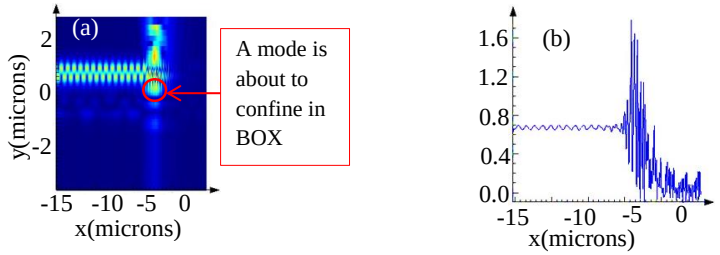

500 nm BOX

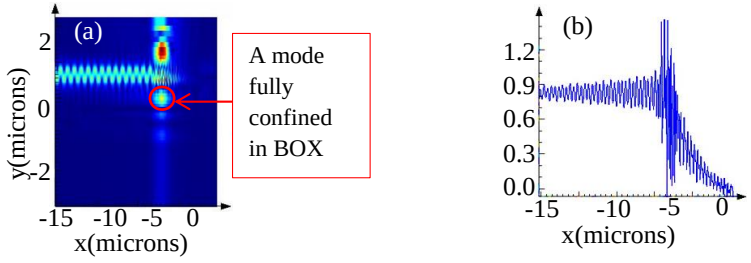

800 nm BOX

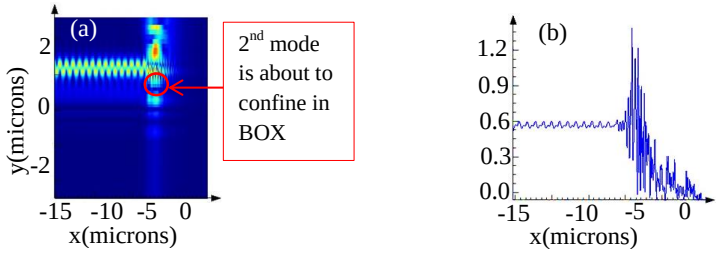

1000 nm BOX

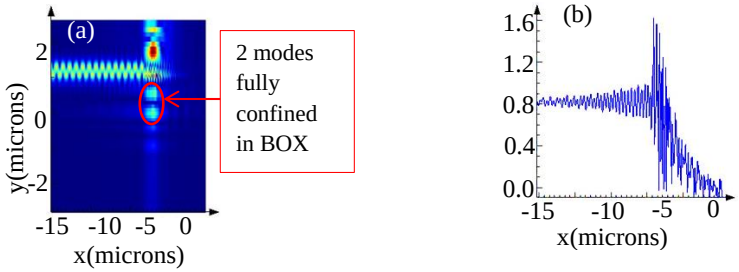

1300 nm BOX

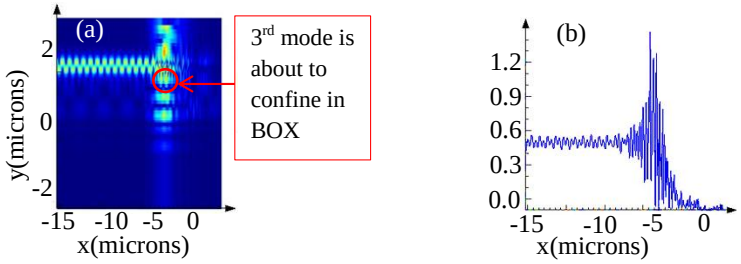

1600 nm BOX

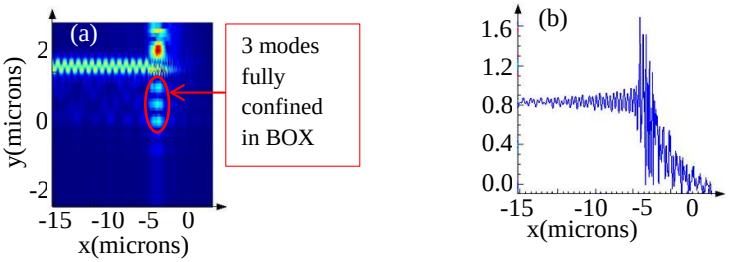

1900 nm BOX

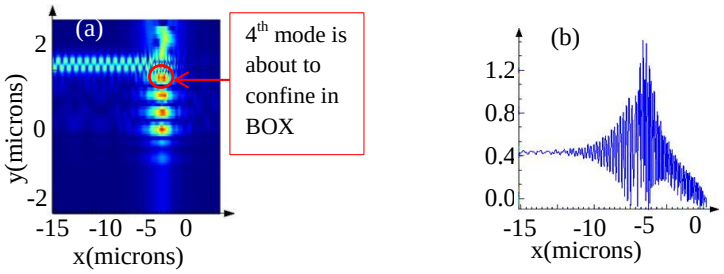

2200 nm BOX

Fig.4. 11: (a)s: TE Field distributions, and (b)s: intensity profiles for different thicknesses of a BOX layer

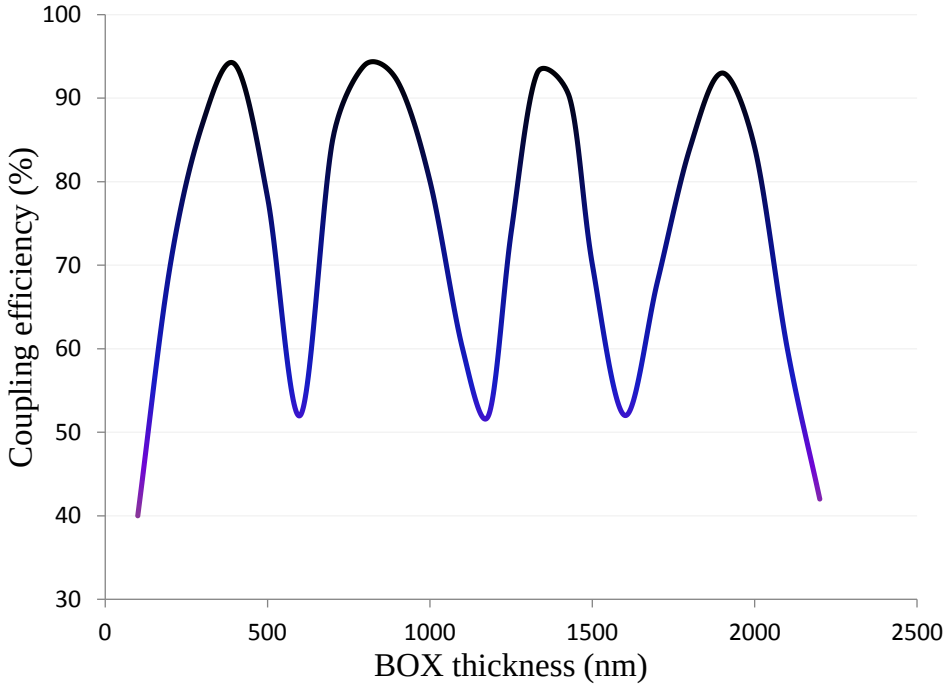

Fig.4. 12: Coupling efficiencies for different BOX thicknesses at 1550 nm wavelength. The bottom points of the intensity graph indicate the starting of the mode whereas the peaks indicate a complete confinement of the mode in the BOX.

4.6 Fabrication Tolerances and performance

The results discussed above are for the ideal structural parameters. In general, the exact shape of the structure deviates slightly from the ideal. This is due to the lack of fabrication fineness of the standard CMOS technology. The variations of the performances of the grating coupler for the structural parameters deviated from their ideal case have been investigated and are now discussed.

4.6.1 Effects of mirror thickness

During fabrication of this multi-layer device, it is very difficult to be exact in the thickness of the 100 nm mirrors. This is because deposition of the silicon dioxide layer on top of the silicon layer causes SiO_2 to bend due to greater thickness. To flatten that layer, a very high temperature (in the range of 1000^0C) is required and this causes some of the silicon to be oxidized. Therefore, if we use a 100 nm thick silicon mirror, it might be less than exactly 100 nm.

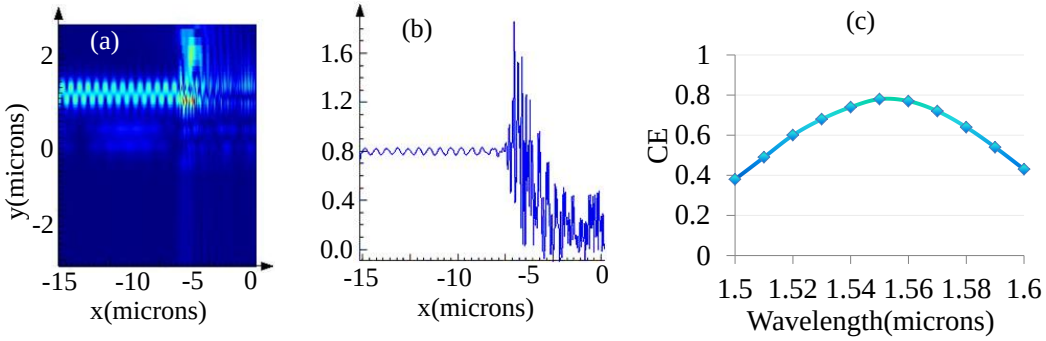

Fig.4. 13: For Si mirror thickness of 80 nm: (a) E-field distribution; (b) E-field profile at the wavelength of 1550 nm, and (c) coupling bandwidth.

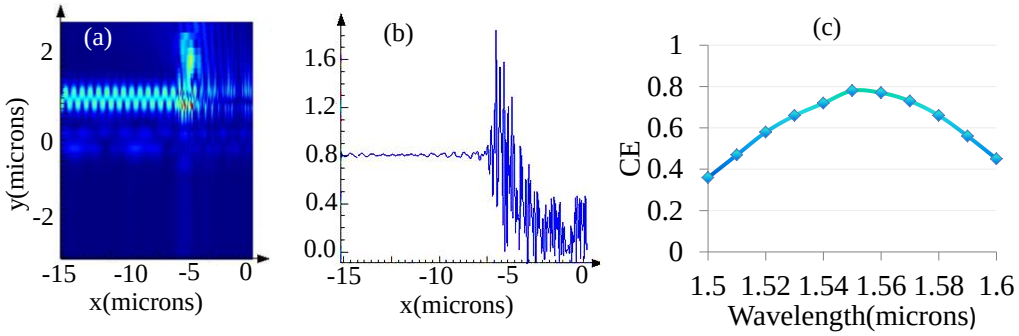

Fig.4. 14: For Si mirror thickness of 90 nm: (a) E-field distribution; (b) E-field profile at the wavelength of 1550 nm, and (c) coupling bandwidth.

Fig.4. 13 shows E-field distribution at 1550 nm wavelength with E-field profile and coupling bandwidth for the mirror thickness of 80 nm whereas Fig.4. 14 shows the same profile but for **a** mirror thickness of 90 nm. It can be seen that the effect of slight variation of mirror thickness is virtually insignificant for both coupling efficiency and bandwidth. So we can achieve high coupling efficiency and bandwidth even if the mirror thickness changes slightly, or in other words provides high fabrication flexibility.

4.6.2 Performance on different grating shape

Practically, the grating of perfect rectangular shape is almost impossible using standard CMOS technology. The grating's shape is mostly similar to sinusoidal form as shown in Fig.4. 15. The actual performance of the coupler will therefore slightly deviate from the performance of the ideal case.

Fig.4. 15: Grating shape: (a) ideal rectangular; (b) practical

For the ideal design, the width of the grating was 400 nm. We assume that during fabrication the width reduced to 300 nm, that is 50 nm from both sides of each grating.

Fig.4. 16 shows the angle difference between the ideal rectangular shapes grating and practically deviated grating shape. The deviation angle from its ideal rectangular form in our design has been calculated $\theta = \tan^{-1}\left(50/40\right) = 51.34^0$. The performance of this situation is depicted in Fig.4. 17.

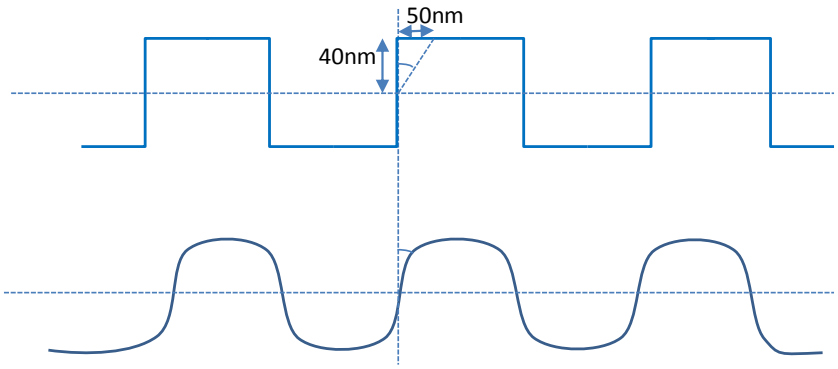

Fig.4. 16: Angle difference between ideal and practical grating shapes for our design

Similarly, we can assume for another case where the grating width reduced by 20 nm from both sides of each grating during fabrication, the grating width becomes 360nm. The deviation angle calculated in this case is $\theta = \tan^{-1}\left(20/40\right) = 26.56^0$. The performance of this situation has been shown in Fig.4. 18.

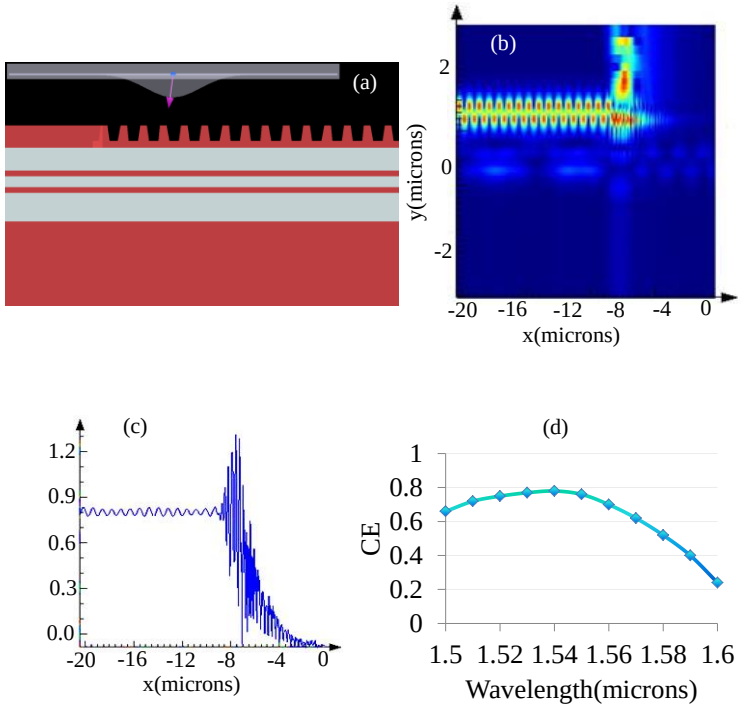

Fig.4. 17: (a) Cross section of the device with 200 nm grating width and 51.34^0 deviation angle: (b) E-field distribution: (c) E-field profile: (d) coupling efficiency vs wavelength

The effect of grating shapes is significant on the bandwidth of the coupler. The coupling efficiency does not alter much for changing the grating shape as can be seen by comparing the results of E-field profile in Fig.4. 17 (c) and Fig.4. 18 (c) for grating widths of 300 nm and 360 nm respectively. For a higher deviation angle, the coupling efficiency of the coupler is higher for shorter wavelengths and lower for longer wavelengths, as shown in Fig.4. 17 (d). On the other hand, when the grating shape is closer to the ideal form, the deviation angle is small and the coupling efficiency is higher around the wavelength of the telecommunications band of 1550 nm which is our interest of operation as shown in Fig.4. 18 (d) where the deviation angle is 26.56^0.

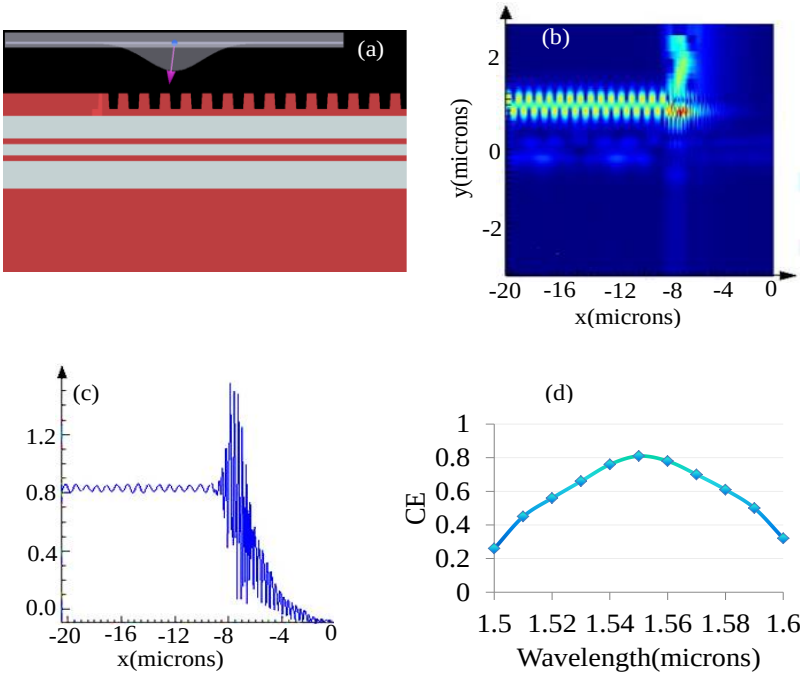

Fig.4. 18: (a) Cross-section of the device with 295 nm grating width and 26.56^0 deviation angle: (b) E-field distribution: (c) E-field profile: (d) coupling efficiency vs wavelength

4.6.3 Performance on different waveguide thickness

The etch depth of the grating also varies from its ideal case during the fabrication process using CMOS. The grating depth could be higher or lower and the height of the waveguide under the grating also varies accordingly. In our design, the waveguide height ideally was 140 nm for a grating depth of 80 nm. If we assume that during the fabrication the depth of the grating becomes 100 nm due to over-etching and consequently the waveguide height changes to 120 nm instead of 140 nm, the performance of this condition is shown in Fig.4. 19.

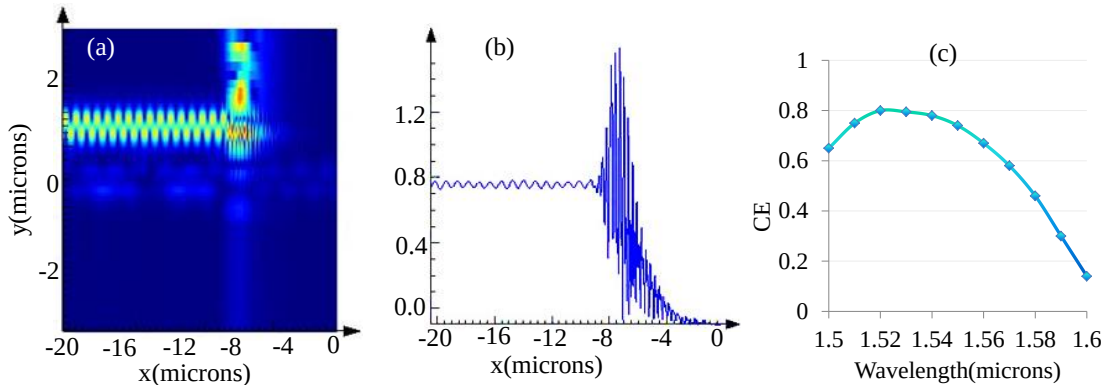

Fig.4. 19: 120 nm waveguide thickness with grating depth of 100 nm: (a) E-field distribution; (b) E-field profile; (c) coupling efficiency vs wavelength

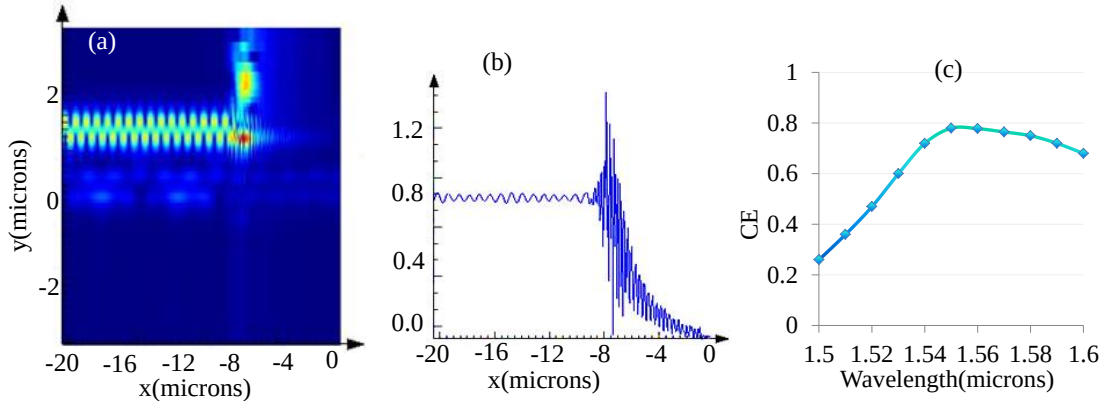

Fig.4. 20: 160 nm waveguide thickness with grating depth of 60 nm: (a) E-field distribution; (b) E-field profile; (c) coupling efficiency vs wavelength

Similarly, Fig.4. 20 shows the performance if the grating depth decreases to 60 nm due to under-etching where the waveguide height becomes 160 nm instead of 140 nm during fabrication. In both cases the coupling efficiency varies little while the bandwidth shifted between longer and shorter wavelengths of light. For a grating depth of 100 nm, the coupler couples light more efficiently with a shorter wavelength than with the longer wavelength. For a grating depth of 60 nm, coupler efficiency is greater

for light with a longer wavelength than with the shorter wavelength. However, for a wavelength of 1550 nm (which is the wavelength of interest) the coupling efficiency remains almost the same for both cases. This confirms the high fabrication flexibility of our design.

4.7 Summary

In this chapter, the downward radiation in a reflector-based grating coupler is numerically analyzed. Results show that the thicknesses of the BOX and reflector layers are the decisive factors for designing a highly efficient grating coupler. Mathematical formulas have been developed specifically for reflector-based grating couplers that can readily be used to calculate the optimum thicknesses of the layers for high coupling efficiency. Based on these findings, a highly efficient and wideband grating coupler with multiple Si-SiO_2 pairs in the BOX layer has been designed with a calculated coupling efficiency of 78% (-1.07 dB) at the wavelength of 1550 nm, and 1-dB bandwidth of 77 nm. To our knowledge, this designed coupling has the greatest efficiency and bandwidth reported for any diffraction-based grating coupler. The coupling efficiency can further be improved to over 90% by minimizing the back reflection and implementing the mode matching condition between optical fiber and waveguide modes: this can be achieved using an apodized grating.

Chapter 5

Perfectly vertical Grating Coupler based on Engineered Subwavelength Grating

5.1 Overview

As described earlier that diffraction gratings are arrangements of materials with periodic variations of the refractive index. Grating couplers are designed based on such diffraction principle of light. The light incident on grating surface diffracts in transmitted medium in some discrete number of orders direction of which is defined by the diffraction angle. Such discrete orders are known as the diffraction order. The total incident power is then distributed among those diffraction orders. The optical power that transmits in each individual order is called the diffraction efficiency. With some special arrangements of the gratings, it is possible to concentrate maximum power in a single diffraction order. If that diffraction order somehow can be coupled into guided mode then the coupling efficiency of the grating coupler can be improved without the need of bottom reflectors. In this chapter we will study the designing of subwavelength grating coupler for enhanced coupling efficiency.

5.2 Evolution of subwavelength structure

In subwavelength grating structure the period of the grating is such small that it can supress many of the diffraction orders. If the period is small enough then the all the diffraction orders will be suppressed and eventually the grating structure will be left with only the "zero" order diffraction. Such subwavelength grating structure is known from earlier days of electromagnetisms. One of the highly recognised experiments conducted by Hertz in late 19^{th} century where he used an array of wires to study the polarisation of wave [218]. In the experiment Hertz found that when the separation

between adjacent wires in the array is much smaller than the wavelength of the waves of interest, the waves are blocked for paralleled orientated array to the direction of the polarisation of the wave whereas for perpendicular orientation of the array has almost no effects. The subwavelength structures based on both metal and dielectric layers have been studied in [219] for propagation of electromagnetic waves. A theoretical study in 1950s shows that with tiny period the grating structure behaves like homogeneous medium [220]. Natural subwavlength structure in moth eyes was discovered in 1960s which reduces the reflections from eyes [221] and few years later based on the moth eyes structure, a subwavelength structure was developed with anti-reflective properties [222]. Over the years studies on subwavelength structure continues specially in free-space optics [223]-[229].

Rapid developments and applications in recent years are observed in the photonics integrated circuits with facilities of the fabrication of such nano scale grating structure based on high-resolution lithography. Various applications of subwavelength structures are found in the field of photonics such as fiber-chip grating couplers [230][242], vertical-cavity surface-emitting lasers (VCSELs) [243], wavelength multiplexers [1], low loss waveguide crossings [245], resonator with high Q-factor [246], multimode interference (MMI) couplers for broadband operation [247].

5.3 Theory of subwavelength grating coupler

We will start with the grating equation (3.1.5.6) derived in chapter 3. Here we will find out the how a particular diffraction mode is becomes cut-off. From equation (3.1.5.6) it can be seen that if the diffraction angle θ_m becomes imaginary then the diffracted mode of that particular order is evanescent and not diffracted.

Initially for the simplicity we consider the normal incident and the grating equation can be written as

$$n_t \sin\theta_m = -m\frac{\lambda}{\Lambda} \qquad \text{(Eq.5.3.1)}$$

The minimum diffraction orders that can exist due to reduction of the grating period are $m = \pm 1$. The cut-off condition for 1st order is given by

$$\sin\theta_{\pm 1} = \frac{\lambda}{\Lambda} \qquad \text{(Eq.5.3.2)}$$

So the condition for $\theta_{\pm 1}$ to be real is

$$\frac{\lambda}{\Lambda} < 1 \qquad \text{(Eq.5.3.3)}$$

Finally including the refractive index of the medium, equation (5.3.3) can be written as

$$\Lambda > \frac{\lambda}{n_t} \qquad \text{(Eq.5.3.4)}$$

Since we are working in a region with variable refractive index of different materials, it is more convenient to use n_{eff} instead of n_t . Therefore equation (5.3.4) can be rewritten as

$$\Lambda > \frac{\lambda}{n_{eff}} \qquad \text{(Eq.5.3.5)}$$

If the light incidents on the grating surface with an angle θ_i other than normal, then the cut-off condition for 1st diffraction order is modified as

$$\Lambda > \frac{\lambda}{n_i \sin\theta_i \pm n_{eff}} \qquad \text{(Eq.5.3.6)}$$

From equation (5.3.6) we can see that the grating period varies for the cut-off condition for positive 1st order and negative 1st order.

The conditions for existence of the diffractions orders are shown in table 5.3.1.

Table 5.3.1: Cut-off conditions for diffraction orders

Condition	Requirements
0-order mode	Always exists
No 1st - order modes	Grating period must be shorter than what causes $\theta_{\pm 1} = 90^0$
Exist 1st - order modes	Grating period must be larger than what causes $\theta_{\pm 1} = 90^0$
No 2nd - order modes	Grating period must be shorter than what causes $\theta_{\pm 2} = 90^0$
Exist 2nd - order modes	Grating period must be larger than what causes $\theta_{\pm 2} = 90^0$
No mth - order modes	Grating period must be shorter than what causes $\theta_{\pm m} = 90^0$
Exist mth - order modes	Grating period must be larger than what causes $\theta_{\pm m} = 90^0$

5.4 Parameter extraction for designing subwavelength grating coupler

Our design process was started by defining the parameters of the gratings written on a SOI wafer. The SOI wafer used for this purpose consists of 2 µm SiO_2 as buried oxide (BOX) layer and 220 nm Si as top layer that ensures single mode operation. The thickness of the BOX (t_{BOX}) is chosen to cause constructive interference between propagated and reflected waves, as described in. This is also the thickness used in commercially available SOI wafer. The geometry of the proposed structure is shown in Fig.5. 1.

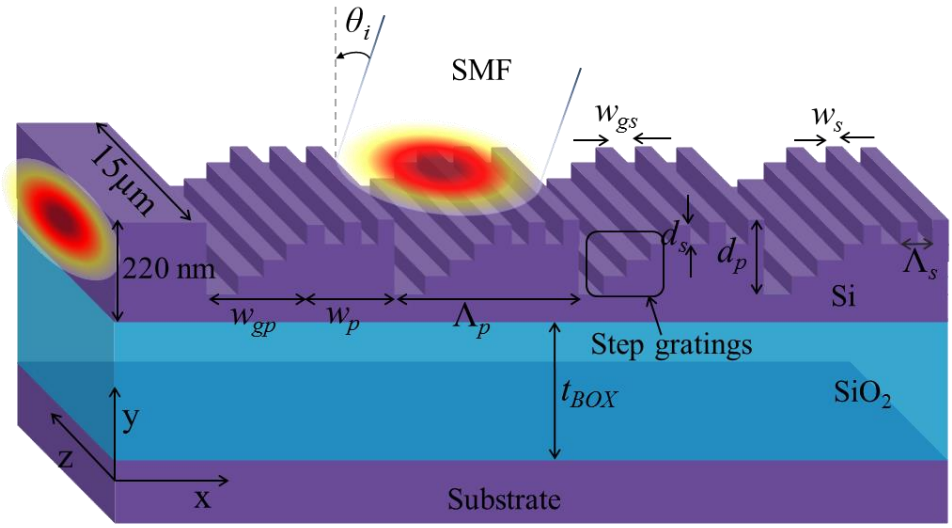

Fig.5. 1: Geometry of the engineered subwavelength grating coupler

The gratings written on the SOI waveguide can be divided into two groups: primary, denoted with *p*, and secondary, denoted with *s*. In order to obtain diffraction of light in gratings, we first require determining the period of primary grating (Λ_p) using following equation:

$$\Lambda_p = \frac{\lambda}{n_{eff} - n_i \sin\theta_i} \qquad \text{(Eq.5.4.1)}$$

where λ is the wavelength of the incident wave, n_{eff} is the effective refractive index of structure, n_i is the refractive index of the top cladding, and θ_i is the incident angle. A Gaussian shape transverse electric (TE) polarized optical source with mode field diameter (MFD) of 10 μm, similar to that of standard single mode fiber (SMF), is applied on the surface of the grating. The initial value of n_{eff} was calculated (without the secondary gratings) as 1.782 for fundamental mode by using fully vectorial mode solver. The period of the primary grating for vertically incident light was calculated as Λ_p = 870 nm for a targeted wavelength of 1550 nm. At the beginning of the design process, the duty cycle (DC_p) and etch depth (d_p) of the primary grating were set to 50% of total grating period and thickness of top Si layer respectively, which were subsequently found to be optimum at DC_p = 0.53 and d_p = 90 nm by using parameter sweep setup by employing Particle Swarm Optimization (PSO) [248] [249]. The structure was then updated with these optimum values to find grating width, w_p [w_p =

(Λ_p * DC_p)] as 461 nm, and groove width, w_{gp} [w_{gp} = (Λ_p – w_{gp})] as 409 nm. The number of order of diffraction that may exist for a grating period of 870 nm was calculated by using the equation as follows:

$$n_{eff} \sin\theta_m = n_i \sin\theta_i - m\frac{\lambda}{\Lambda_p} \qquad \text{(Eq.5.4.2)}$$

where m is the order of diffraction (m = ±1, ±2…….), and θ_m is the angle of diffraction of m^{th} order. Among various diffraction orders, it is found that only first order (m = -1) diffraction exists in designed GC that diffracts at an angle of $\theta_{-1} \sim 90^0$, confirming the propagation along the waveguide. However, there are 4 key processes involved in the wastage of diffracted light in a grating structure causing poor CE and CBW: (a): leakage of lights through the BOX, (b) reflection of light on the surface of the grating, (c): the back scattering of light towards opposite direction of propagation due to the symmetry of the structure, and (d): the specular (0^{th} order) diffraction that propagates almost vertically towards the substrate. Such directional attributions towards the poor performance of GC can be curtailed by implementing asymmetric grating trenches and appropriate adjustment of the grating structure which also potentially couple back the optical power with 0^{th} order into -1^{st} order diffraction to improve CE and CBW [250] [251] [252].

To achieve such redirection, the grating structure is remodelled with auxiliary engineered subwavelength grating, *s*, as indicated earlier and shown in Fig.5. 1. The design of secondary grating was started with the parameterization of the step gratings at one end of the groove of primary gratings, as shown in Fig.5. 2. Shown in Fig.5. 2, the diagonal of the vertices of the primary groove was used to determine the thickness (t_s) and width (w_{ss}) of the step gratings in such a way that for each step the angle between the diagonal of the primary groove and the vertices of the secondary steps are equal [$\varphi_p = \varphi_{s1} = \varphi_{s2} = \varphi_{s3} = \tan^{-1}(w_{gp} / d_p)$]. For the primary grating under discussion, it is found that the number of step gratings (N) required to fulfil this condition is 3 with keeping in mind the feature size limit of deep-ultraviolet optical lithography (feature size of ~100 nm), typically employed in an industrially driven fabrication processes. With such a value of N, the t_s and w_{ss} can be calculated as [$t_s = d_p / (N+1)$] 22.5 nm and [$w_{ss} = (w_{gp} / N)$] 136.33 nm respectively. Such selection of the step gratings makes the groove space

(G_s) equal to thickness w_{ss}, which is also the achievable maximum for any fixed thickness.

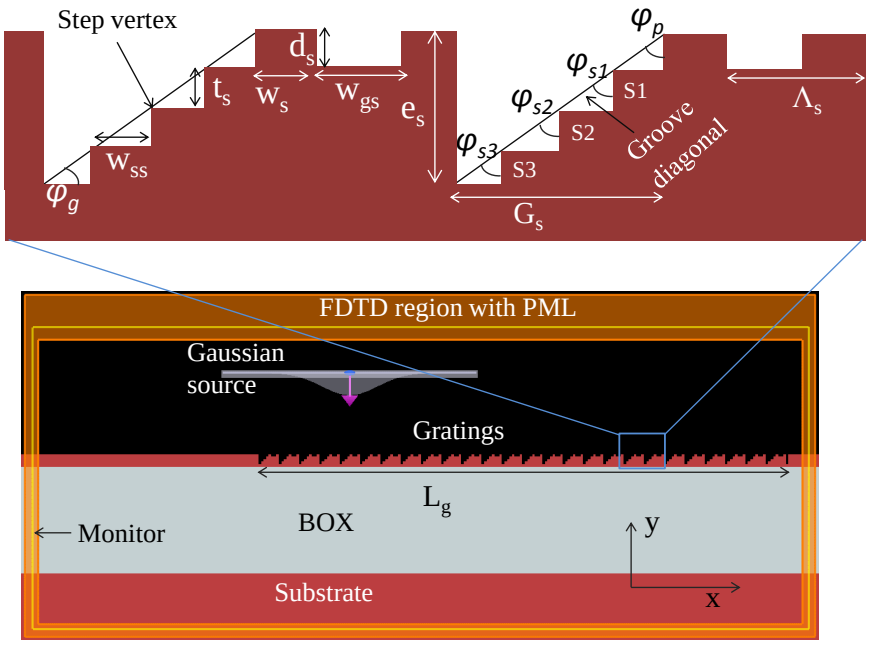

Fig.5. 2: 2D FDTD simulation environment setup. Inset: geometry of the secondary gratings (drawn not to scale).

The relationships among φ_p, G_s and w_{ss} can be expressed by a pair of equations as follows:

$$w_{ss} = \frac{\tan\left(\varphi_p\right)\cdot d_p}{N} \qquad \text{(Eq.5.4.3)}$$

$$G_s = w_{gp} - \left(w_{ss}\cdot N\right) \qquad \text{(Eq.5.4.4)}$$

Similarly, the relationships among primary groove angle at the bottom (φ_g), etch space (e_s), and t_s can also be expressed by another pair of equations as follows:

$$t_s = \frac{\tan\left(\varphi_g\right)\cdot w_{gp}}{N+1} \qquad \text{(Eq.5.4.5)}$$

$$e_s = d_p - \left[t_s\cdot\left(N+1\right)\right] \qquad \text{(Eq.5.4.6)}$$

The step grating width and the corresponding groove spacing calculated by using equations (5.4.3) & (5.4.4) for various primary top groove angles are shown in Fig.5. 3 (a).

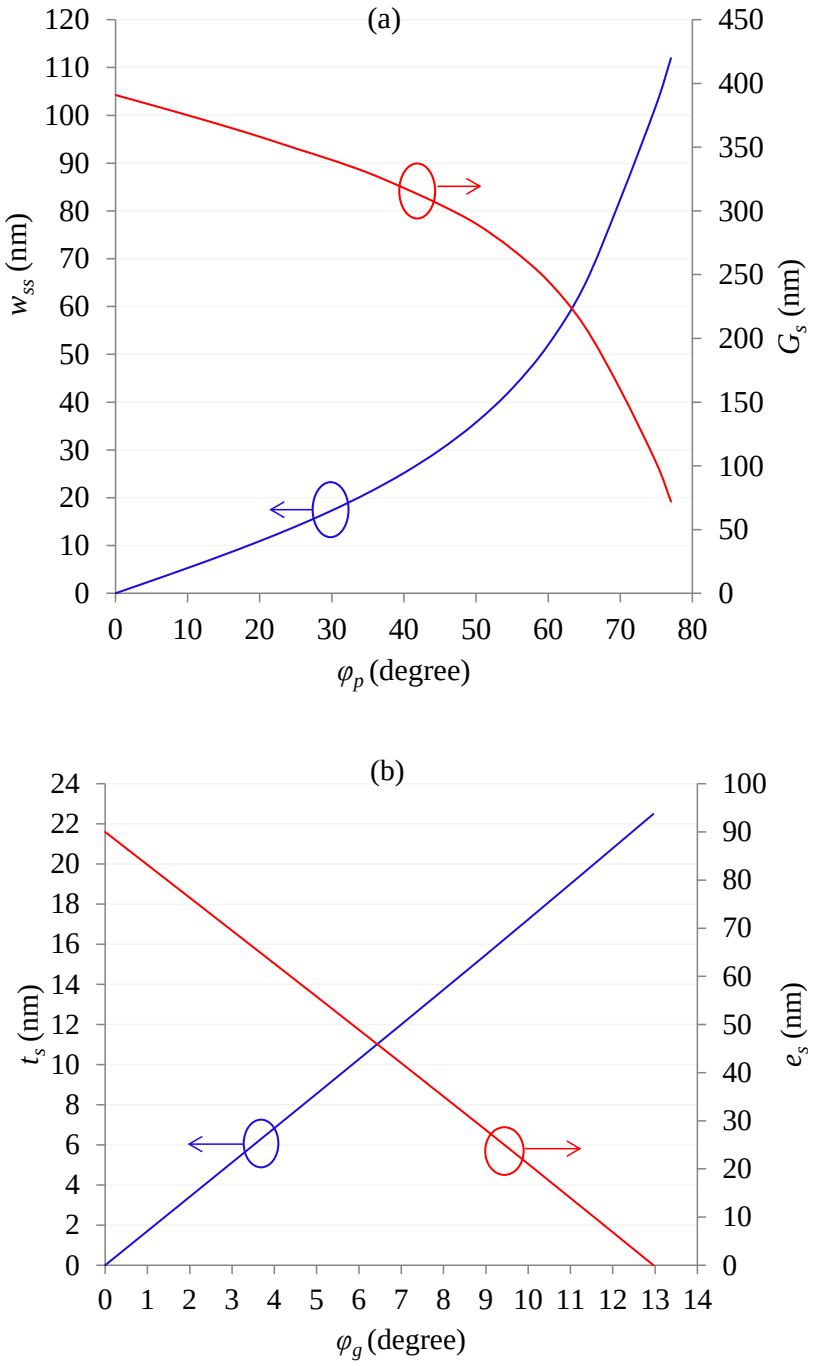

Fig.5. 3: (a) The relationships of φ_p, G_s and w_{ss} and (b) the relationships of φ_g, es and t_s.

Also the thickness of step gratings and the corresponding etch spacing calculated with equations (5.4.5) & (5.4.6) for various primary bottom groove angles are shown Fig.5. 3 (b). From these figures it is clear that when φ_p = 0, G_s = w_{gp} = 409 nm; and when φ_g = 0, e_s = d_p = 90 nm.

The design of top secondary gratings in the ridge of the primary grating was started with grating width (w_s) and etch depth (d_s) of 136.33 nm and 22.5 nm respectively, similar to that of the step gratings discussed earlier which gives a secondary groove width (w_{gs}) of 188.34 nm and a secondary grating period (Λ_s) of 324.67 nm with duty cycle DC_s [DC_s = (w_s / Λ_s)] as 0.42. In compare to the wavelength of interest, Λ_s is so small that secondary gratings act as a homogeneous medium to the incident light, therefore, rejecting the possibility of the presence of additional order of diffraction. The asymmetric trenches were developed by introducing the step gratings at one end of the primary groove while keeping the other end unaltered, as shown in Fig.5. 2. Implementation of such asymmetric groove tranches breaks the symmetry of propagation of light at the gratings, which can potentially cause higher propagation towards the desired direction, if modelled correctly. The influence of the structural parameters of the secondary grating, including groove spacing, on the CE and CBW is discussed in section 5.6.

5.5 Results and discussion

The structure was simulated based on two dimensional Finite Difference Time Domain (2D FDTD) method by using commercially available software package, Lumerical FDTD Solutions. Although GC is a 3D problem, the physical dimensions enabled the approximation of the 3D structure with 2D simulation with sufficient accuracy, as the width of the GC (= 15 µm) is much larger compare to the height (= 220 nm) and operating wavelength (1550 nm) of the waveguide. The grid spacing is set to as small as 10 nm for further higher accuracy. The perfectly matched layer (PML) incorporated within the FDTD simulator was used to prevent reflections from the boundary by implementing impedance matching between simulation region and its materials [204]. The schematic of such 2D FDTD simulation environment is shown in

Fig.5. 2. The structure was first simulated with primary gratings only from which E-field distribution along the grating structure and CE & CBW centered at 1550 nm were obtained and shown in Fig.5. 4 (a)-(c) respectively. Fig.5. 4 (a) shows the incident light that is diffracted in both desired forward and unwanted backward directions. It also shows the light reflected from the grating surface and leaked through the BOX, as indicated earlier. Clearly, the unwanted backward scattering is weaker than desired forward scattering due to the initial broken symmetry of the grating structure at the point of incidence, which was caused by intentionally placing the source toward the waveguide other than at the midpoint of the grating length (L_g), as shown in Fig.5. 2. However, there still remains substantial backward propagation, which along with reflected and leaked light, need to be better managed to attain higher CE and CBW. Fig.5. 4 (b) -(c) show that, as expected, the primary grating can attain only a 43% (-3.665 dB) CE with 1-dB CBW of 26 nm.

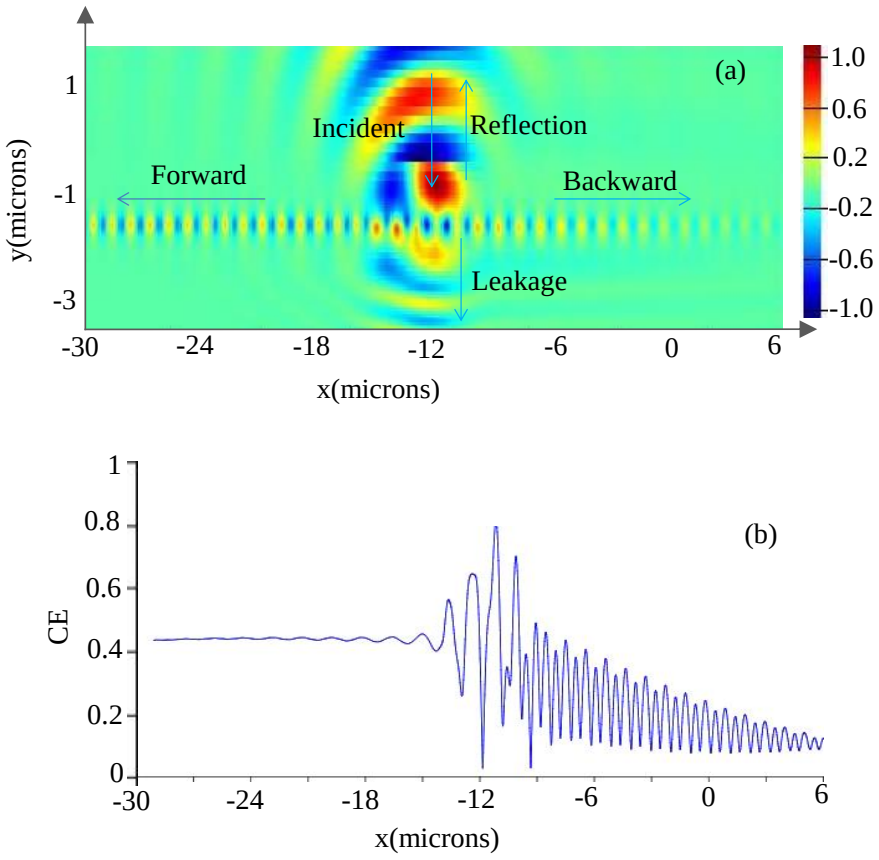

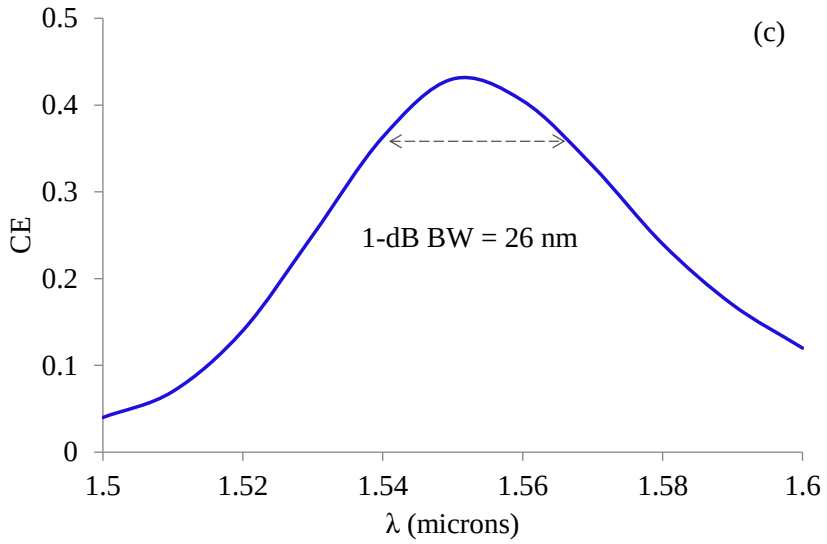

Fig.5. 4: (a) E-field distribution along grating structure (b) coupling efficiency at wavelength of 1550 nm and (c) coupling bandwidth.

The GC structure incorporating the secondary asymmetric step gratings was then simulated in the same simulation environment. Accordingly, the E-field distribution along the grating structure and CE & CBW centered at 1550 nm were obtained, as shown respectively in Fig.5. 5 (a) to (c). In comparison with the E-field depicted in Fig.5. 5 (a), transportation of light to the substrate through BOX and backward propagation are reduced significantly due to the incorporation of the secondary asymmetric step gratings, as can be seen clearly in Fig.5. 5 (a). The directionality of light in the GC towards the direction of propagation has been improved significantly, as can be seen from the values of CE in Fig.5. 5 (b)-(c). These figures show that, at the wavelength of 1550 nm, the calculated CE and CBW are 76% and 58 nm respectively.

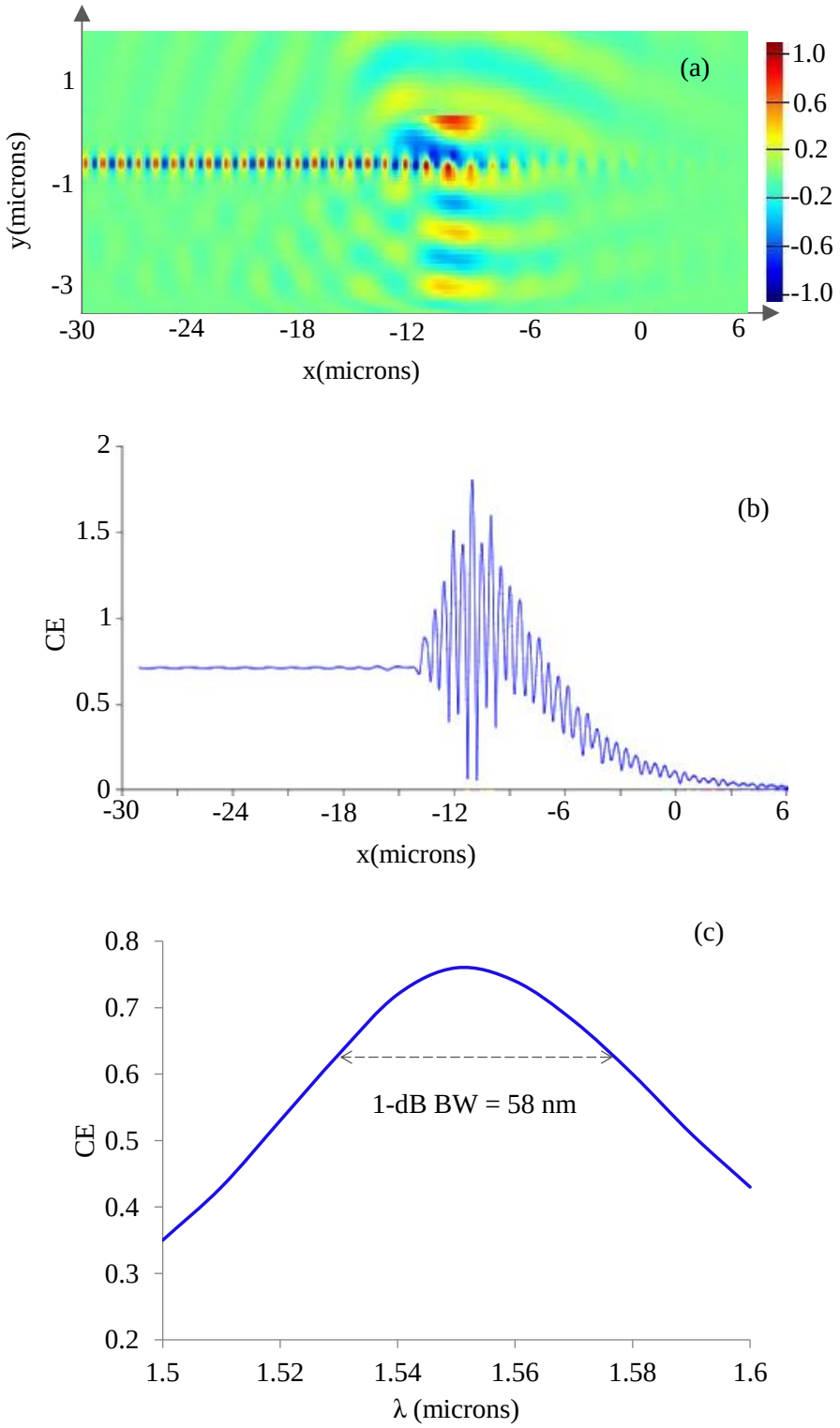

Fig.5. 5: (a) E-field distribution along grating structure (b) coupling efficiency at wavelength of 1550 nm and (c) coupling bandwidth for grating coupler with secondary ultra-subwavelength grating.

The reflection and transmission characteristics of the coupler are shown in Fig.5. 6 in terms of scattering parameters (S-parameters). The reflection at the incident is always lower than 5% for wavelengths of 1500–1600 nm in GC with our proposed engineered subwavelength grating as shown in Fig.5. 6 (b). It also can be noted that less than 2% reflection happens at 1550 nm wavelength for which the structure is designed. Whereas reflections vary between 15%-30% for the same wavelength range in GC with only primary grating with peak at around 1520 nm wavelength as shown in Fig.5. 6 (a). The back reflections are reduced significantly in GC comprising secondary gratings comparing with GC with only primary gratings.

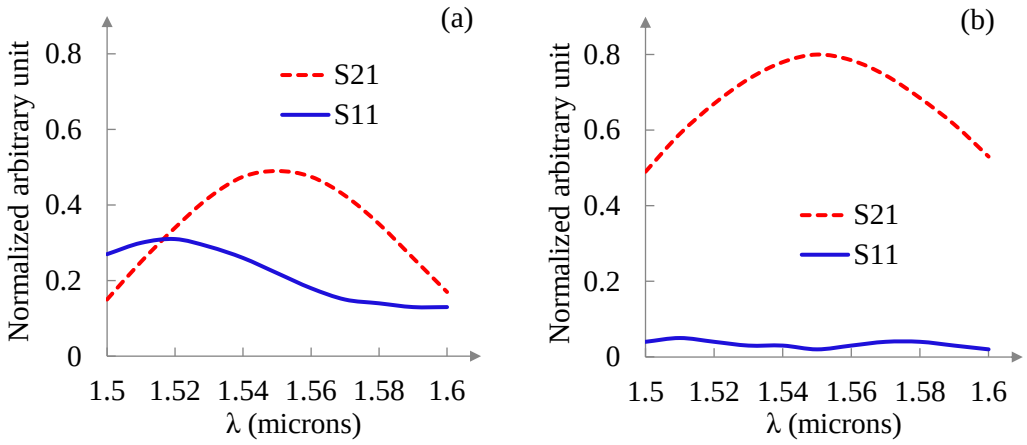

Fig.5. 6: Reflection (S11) and transmission (S21) with different wavelengths for vertical incident in (a) GC with only primary grating (b) GC with engineered subwavelength grating. Vertical axis is normalized to incident field intensity.

The influence of the BOX thickness on CE is also investigated and the results show that CE is virtually independent of the BOX thickness as shown Fig.5. 7. Although, it is well-known that coupling loss of the surface grating couplers strongly and periodically depends on the thickness of a BOX layer [253], such limitation is circumvented through higher directionality by implementing asymmetric grating trenches which inherently afford very high internal diffraction in proposed design.

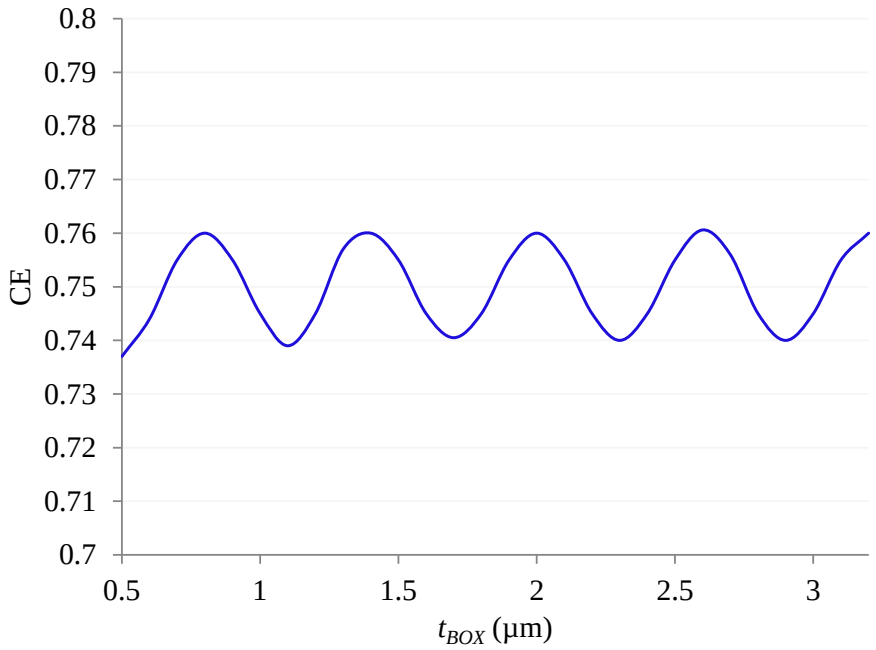

Fig.5. 7: Calculated CE for various thickness of BOX layer.

5.6 Performance characterization of the secondary gratings

In this section performance of the proposed GC was further investigated for various secondary grating parameters. First of all, the grating period (Λ_s) has been varied between 300 to 340 nm with a step of 10 nm over a range of wavelengths and the performance of the GC in terms of CE is shown in Fig.5. 8. It shows that the changes in CE with respect to wavelengths are quite similar for grating periods between 320 to 340 nm with a little exception that for longer grating periods the points of highest CE move slightly towards higher wavelengths. Also, shown in Fig.5. 8 the values of highest CE decrease gradually with the decrement of the grating period, which can be attributed to phase matching condition of grating diffraction [184]. Reducing Λ_s while keeping duty cycle fixed causes lower effective index which deteriorates phase matching between grating diffractions and consequently CE drops.

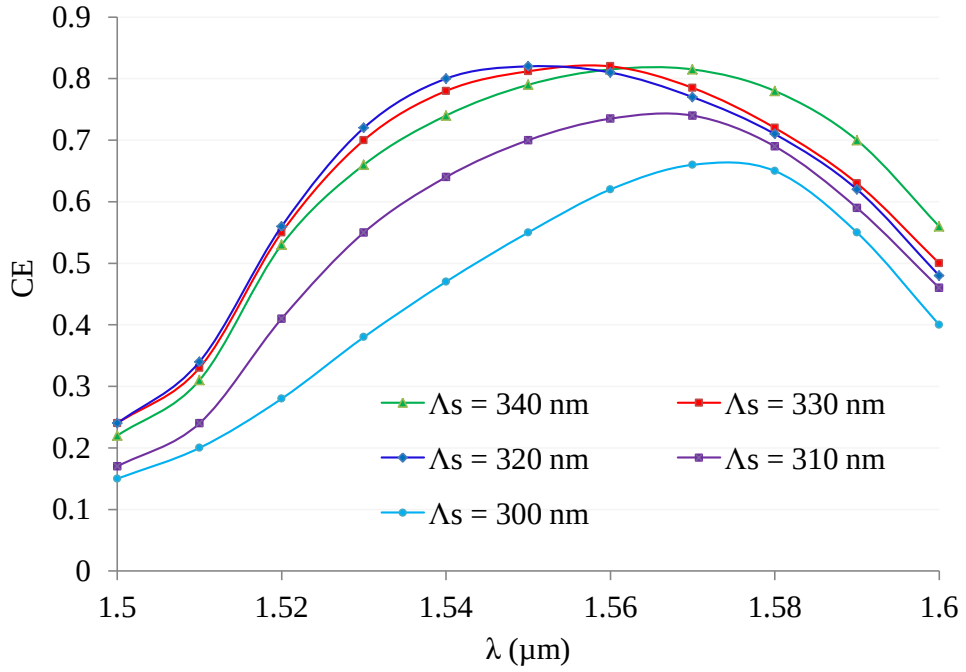

Fig.5. 8: Coupling efficiency vs wavelength for various secondary grating period.

The structure was also simulated for etch-depths of 10 to 30 nm with a step of 5 nm over a range of wavelengths and the performance of the GC is shown in Fig.5. 9 (a). It shows that thinner etch-depths exhibit better CE over shorter wavelengths, which is quite confronting for a thicker etch-depth. It also shows that, for etch depth of 15-25 nm, the peak CEs occur around the desired 1550 nm wavelength with more flatten spectral responses. The maximum CE of the structure found to be 82% which is caused for d_s of 20 nm. The characterization of the GC was further continued for different duty cycles of the secondary grating (DC_s), and the respective performance is captured in Fig.5. 9 (b). It shows that coupling spectra for DC_s from 40% to 50% are quite similar that causes the peak CE for DC_s around 40%. However for duty cycles below or above 40-50%, the spectra are quite deviated causing the peak CE shifted from 1550 nm, the wavelength of interest.

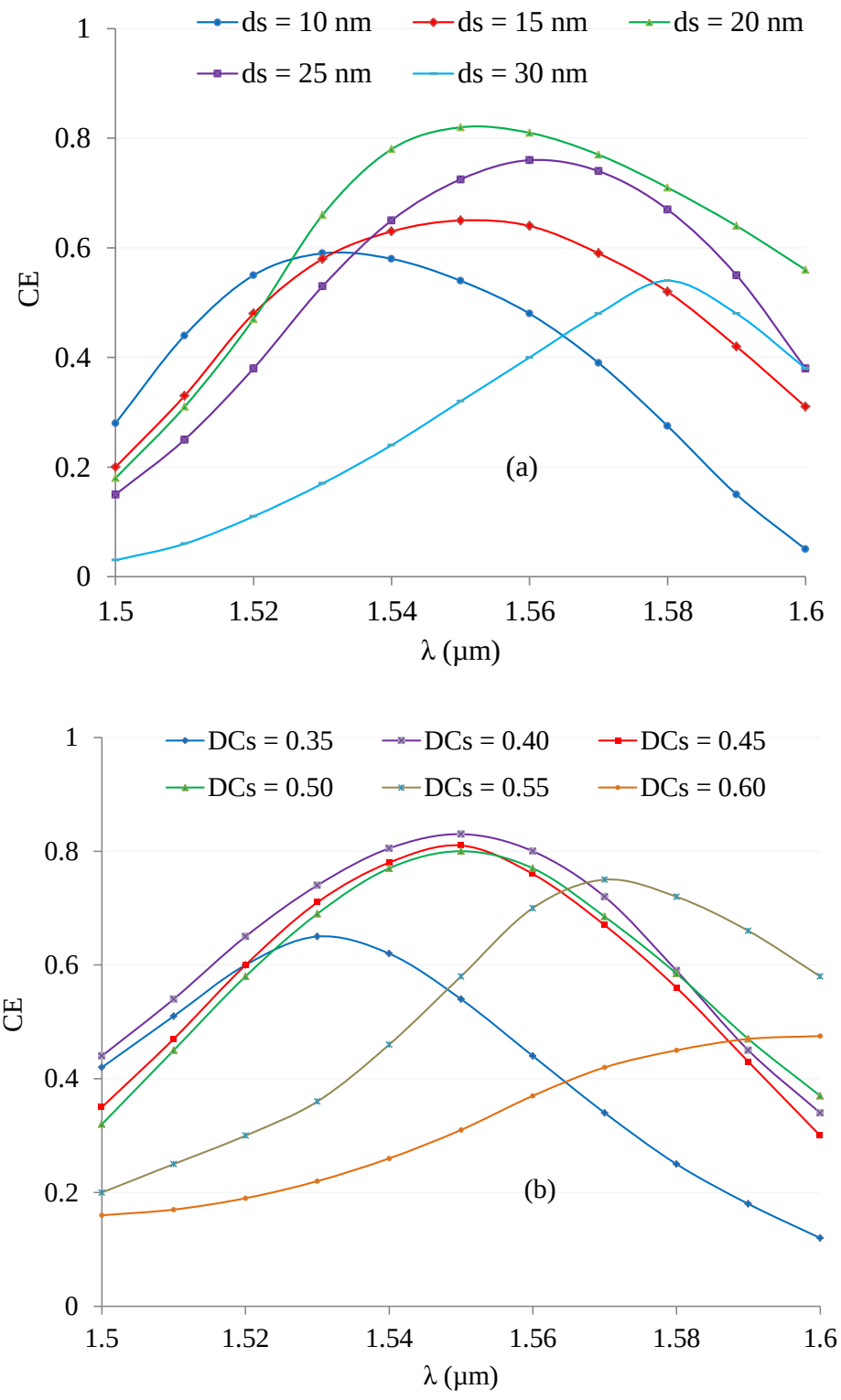

Fig.5. 9: Coupling efficiency vs wavelengths for various (a) secondary etch depth (d_s) and (b) secondary duty cycle (DC_s).

Characterization also considered equations (5.4.3) to (5.4.6) for further analysis. Fig.5. 10 (a)-(b) show the relationships between CE and the targeted characteristic

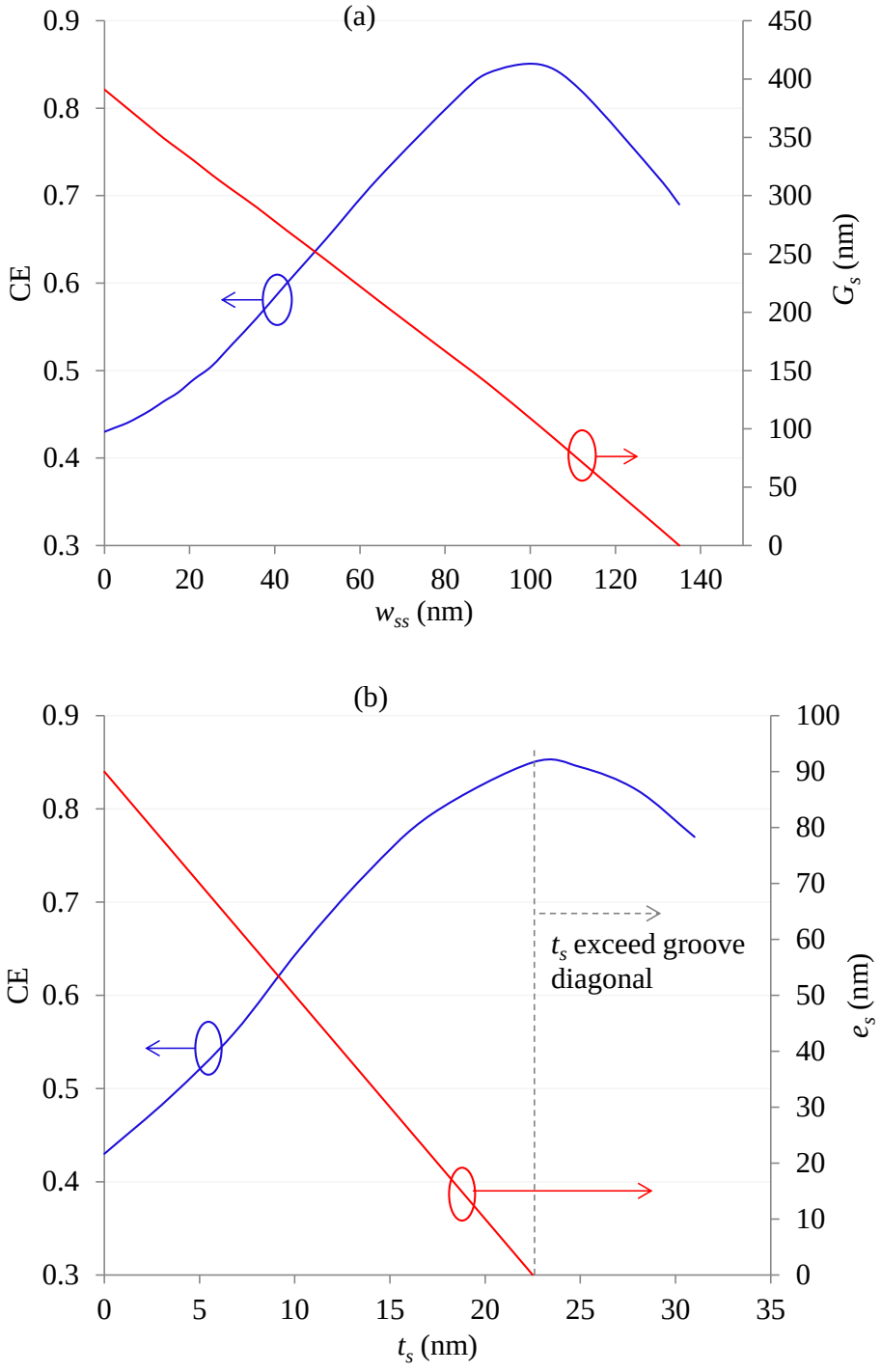

Fig.5. 10: Coupling efficiency for various (a) widths and corresponding groove spaces (b) thicknesses and corresponding etch spaces at 1550 nm wavelength.

parameters of step gratings including width and thickness of step grating, groove spacing and etch spacing. Shown in Fig.5. 10 (a), CE is predicted to be more than 80% for a width between 80-112 nm with a peak CE at 85% for the width of 102 nm and the corresponding groove space of 102 nm. Similarly, shown in Fig.5. 10 (b), CE increases almost linearly with thickness, but decreases with etch space. This suggests that there shouldn't be any gap on the wall of groove above the first step grating S1; please refer to Fig.5. 2 for further clarity. The results also show that if t_s exceed such that the vertices of step gratings go beyond groove diagonal, then CE drops further as can be seen in Fig.5. 10 (b).

Based on the characterizations presented above, the optimum values of the secondary grating parameters are tabulated in Table 5.6.1. These parameters were eventually used to estimate the attainable CE and CBW of the GC over the wavelength range of 1500-1600 nm, as shown in Fig.5. 11.

Table 5.6.1: Optimized secondary grating parameters

Λ_s (nm)	DC_s	w_s (nm)	w_{gs} (nm)	d_s (nm)	w_{ss} (nm)	t_s (nm)
320	0.4	128	192	20	102	22

Shown in Fig.5. 11, the attainable peak CE at 1550 nm is 85% (-0.7 dB) and 1-dB CBW is 53 nm centered at 1550 nm. This means that, although the CE improves with the optimized structure, the CBW, as expected, decreases little bit in compare to the attainment in Fig.5. 5 (c).

The structure is also simulated using 3D FDTD with optimized parameters obtained from 2D FDTD. The coupling spectra for both 2D and 3D FDTD simulations are in excellent agreement. Although similar peaks of the CE are attained (reduced by only around 1% in case of 3D FDTD), in both 2D and 3D FDTD methods, the bandwidth is reduced by 5 nm calculated using 3D FDTD compared with 2D FDTD as shown in Fig.5. 11 which is 1-dB CBW of 48 nm centered at 1550 nm. To check the further validity of the results attained by FDTD, the structure is simulated based on 3D EME method. The coupling spectrum obtained by 3D EME is very much similar to the spectrum calculated by 2D FDTD as shown in Fig.5. 11. The coupling peak is even higher by around 2% with slight wider 1-dB CBW of 54 nm compared with CE and CBW calculated by 2D FDTD.

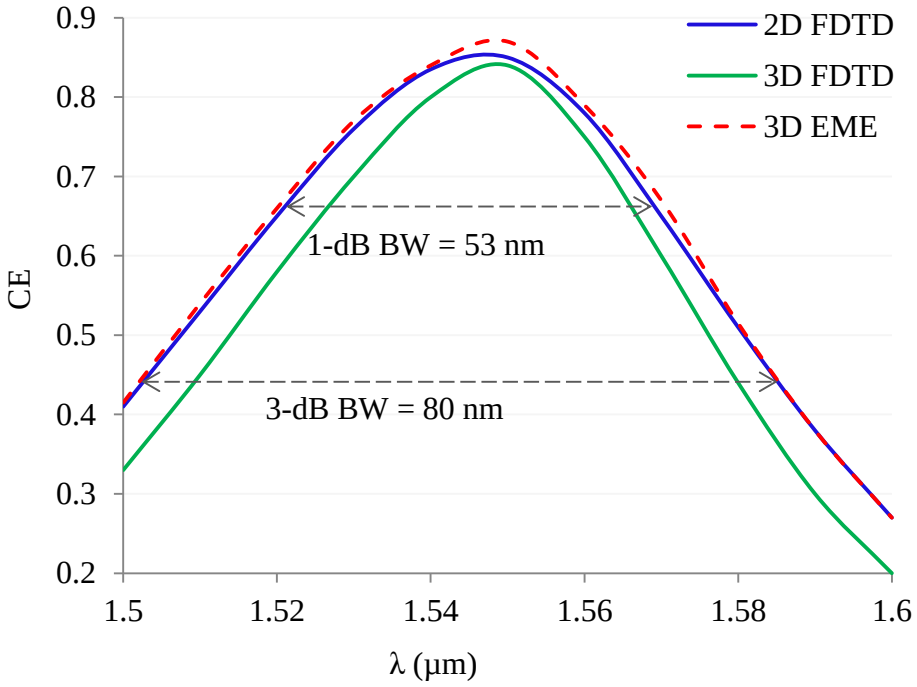

Fig.5. 11: Coupling efficiency vs. wavelength for optimized grating coupler.

In regard to the tolerances to fabrication errors, the structure exhibits sufficient robustness to the design tolerances more than 10 nm for most of the characteristic parameters of the secondary grating, as tabulated in Table 5.6.2, causing a performance degradation of CE and/or CBW by less than 5%.

Table 5.6.2: Variation of secondary grating parameters for 5% penalty of CE.

Λ_s (nm)	DC_s	w_s (nm)	w_{gs} (nm)	d_s (nm)	w_{ss} (nm)	t_s (nm)
320-340	0.4-0.5	125-145	180-200	15-25	80-112	17-27

The structure in Fig. 5.1 can be fabricated in two ways. One way is the etching the Si layer with 4 different etch depths which can be achieved by applying various etching rate for different stair grating as required using E-beam lithography. Alternatively the stair grating can be formed by depositing Si pillars inside primary groove with different widths and heights as required. Moreover, the structure more feasibly can be fabricated

using grayscale lithography which can produce 3-D structure in a photoresist layer, which can then transferred in Si by use of dry etching process.

5.7 Summary

In this chapter, a perfectly vertical grating coupler is proposed for light coupling between SOI waveguides and SMF. The symmetrical propagation nature of the diffracted waves from grating is broken by incorporating asymmetric grating trenches with step gratings. The directionality of the coupler is boosted by implementing effective index variation of the primary grating, which is achieved by combination of auxiliary subwavelength gratings in the ridge of primary gratings and step gratings. The calculated coupling efficiency is improved from 43%, estimated for GC without secondary gratings, to as high as 85% (-0.7 dB) for GC comprising our proposed engineered subwavelength secondary gratings. The proposed GC predicts coupling spectra as wide as 53 nm and 80 nm for 1-dB and 3-dB down level respectively. The structure possesses sufficient robustness to the possible errors that may arise during fabrication. The proposed coupler features less influence of the BOX thickness on the coupler performance which eases the choice for fabrication. Such efficient broadband perfectly vertical grating coupler is significantly advantageous in high dense photonic packaging.

Chapter 6

Compact Grating Coupler with Partially Overlay Tapered Waveguide

6.1 Introduction

Miniaturization of the integrated circuits (ICs) is a conventional trend in electronics industry. From the invention of first transistor to the modern day millions of transistors as well as multifunctional components are being integrated in a single chip, in other words, on a single substrate. Likewise, photonic integrated circuits (PICs) are not exception of that trend, even further miniaturizations are estimated in PICs [254].

As described earlier, grating coupler is one of the prime choices for coupling of light into/out between optical fiber and nano photonic waveguide. In order to couple light from grating structure into nano photonic waveguide both the vertical and lateral dimensions has to be matched with nano waveguide. However, the grating structure converts only the vertical dimensions into nano scale while the lateral dimension remains in micrometer scale. Therefore, for complete interface between grating structure and nano waveguide, the grating waveguide needs to be tapered down to nano scale.

A typical GC structure, along with its tapered spot size converter (SSC) is shown in Fig.6. 1. The width of the GC structure is tapered down adiabatically to a nano-scale dimension to enable effective coupling with Si waveguide devices. This tapered SSC, which often causes excessive attenuation of light at inadequate lengths, usually requires larger footprint in the photonic integrated circuit (PIC) for effective modal conversion. So the design of the compact grating coupler requires the waveguide to tapered down on shorter length while sustains the original coupling efficiency and coupling bandwidth of the grating coupler.

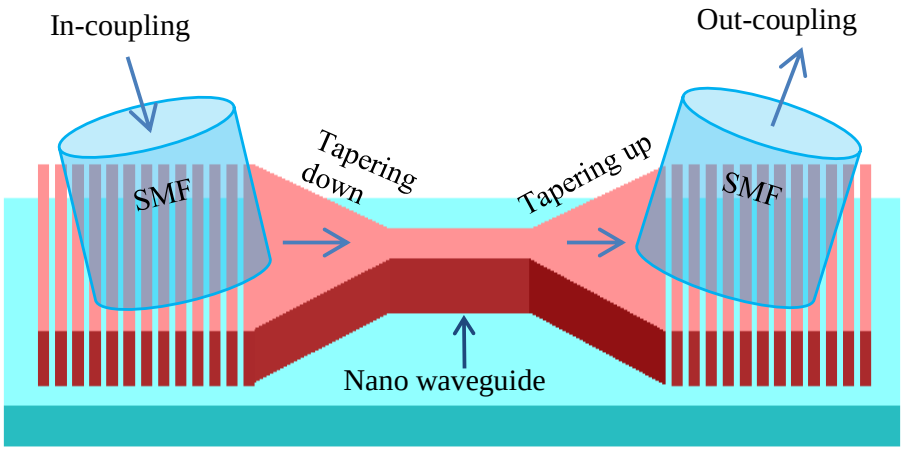

Fig.6. 1: Typical grating coupler with spot size converter

Various structures with compact sizes have been proposed to make small footprint of GCs in PICs. A GC in micrometric SOI rib waveguide is demonstrated in [142] with both conventional and inverse taper where the dimensions of 534.4 µm × 15 µm for conventional taper and 1534.4 × 15 µm for inverse taper with theoretical CE of -4.8 dB and -1.8 dB and experimental CE of -5.5 dB and -2.2 dB respectively. Although CE is improved in GC with inverse taper compare to conventional taper, the high dimension results in very large footprint in PICs.

In recent years, focusing grating couplers have attracted much attention for designing compact GC where the geometry of the gratings are cylindrical with a common focal point instead of straight line gratings. A broadband focusing grating coupler based on "fishbonelike" grating structures has been designed in [255] with dimension of 30 µm × 20 µm where theoretical and experimental CE achieved as -1.7 dB and -3.5 dB respectively at near-IR and at mid-IR the theoretical and experimental CE as -4.7 dB and -5.5 dB with 3-dB BW of 500 nm was predicted. An ultra-broadband focusing-curved GC based on subwavelength grating structure is presented in [211] with dimension of 40 µm × 20 µm and theoretical and experimental CE of -2.72 dB and -4.7 dB respectively at 1550 nm wavelength. An apodized focusing subwavelength GC for suspended membrane waveguides is designed in [154] with dimension of 40 µm × 20 µm with theoretical and experimental CE of -1.7 dB and -3.0 dB respectively. Focusing grating structures offer compact dimension of GCs, however the missing feature is the high CE and coupling bandwidth limiting their applications in

many optical interconnects such as wavelength-division-multiplexing (WDM) and frequency-comb generation where high CE and flat coupling spectrum are highly desired.

6.2 Extraction of Grating Parameters

In order to maintain the coupling efficiency and bandwidth of the grating coupler while designing compact structure, a partially overlay two tapered waveguides is designed for lateral matching with nano photonic waveguide. An aluminium (Al) mirror based shallow etched uniform grating coupler is also designed for vertical matching. In grating coupler downward radiation of light through BOX to substrate contributes mostly for low coupling efficiency [147]. One of the solutions to minimize such downward radiation is to use metal reflector in the BOX which redirect most radiated light towards waveguide. In most cases Al and gold are used as reflector materials. However Al is advantageous over gold due to its higher compatibility with CMOS process as unlike gold, Al does not need wafer-to-wafer bonding [212] [216].

The proposed structure is designed and simulated in 2-D Finite Difference Time Domain (FDTD) solver by using commercially available Lumerical™ FDTD Solutions.

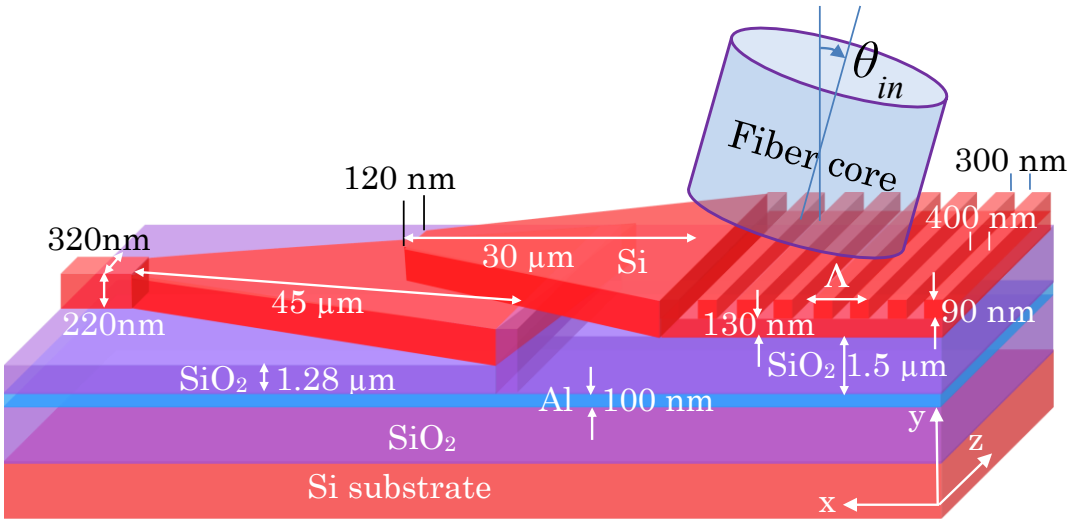

Fig.6. 2: Geometry of the grating coupler with partially overlay

The geometry of the proposed grating coupler is depicted in Fig.6. 2. It consists of a 2 µm buried SiO_2 layer (BOX) with 220 nm Si on top to construct the grating and the SSC under discussion. These thicknesses are chosen in such a way that the structure supports single mode propagation of light only.

The BOX is also incorporated with a 100 nm Aluminium (Al) reflector to recapture the light from the downward radiation. The placement of the Al layer is found to be optimum at 1.5 µm from the top Si to cause constructive interference between the guided and the reflected waves. The gratings are grooved on the top Si as shown in Fig.6. 2, the parameters of which are calculated from equation as follows:

$$\Lambda = \frac{\lambda}{n_{eff} - n_{top}.\sin\theta_{in}} \qquad \text{(Eq.6.2.1)}$$

where

Λ : is the grating period,

λ : is the wavelength of the incident light,

n_{eff} : is the effective refractive index of the optical mode on the gratings,

n_{top} : is the refractive index of the cladding on top of Si layer.

θ_{in} : is the incident angle with normal to the direction of incident. This slight tilted position of the optical fiber minimizes the second order reflection.

Wavelength of the design was set to 1550 nm to cover the high-speed single mode optical communication bands. The out of the plane positioning angle of the fiber was chosen to be -12^0 (= θ_{in}) to ensure minimized second order reflections. n_{eff} of the structure was calculated to be 2.31 by using fully vectorial mode solver, and n_{top} for air was considered as 1. All these specifications have resulted a grating period of Λ = 700 nm, as indicated in Fig.6. 2. Grating depth (d) and width (w) were also optimized for maximum efficiency and found to be 90 nm and 400 nm respectively, leaving a Si layer of 130 nm below the grooved gratings. The GC structure under consideration was composed of 21 gratings with a uniform period of 700 nm, making the total length (L_g)

of the gratings to be approx. 15 µm. A grating width (w_g) of 14 µm was also chosen to ensure sufficient surface area.

6.3 Results of Grating Coupler

A Gaussian shaped optical source is applied on the grating surface with MFD of 10 µm which is comparable with SSMF. The grating width (w_g) is optimized as 14 µm for maximum overlap. The position of the source is optimized at 1700 nm away from

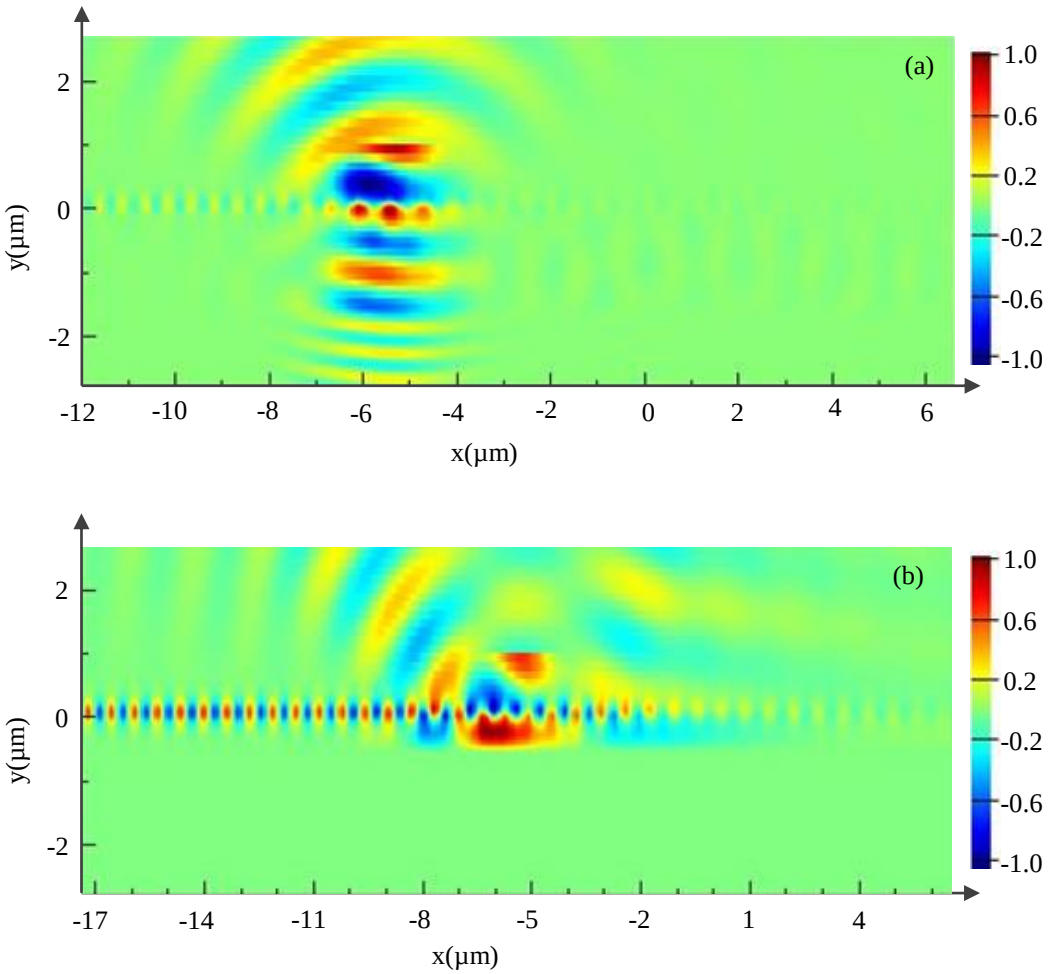

Fig.6. 3: E-field distributions at wavelength of 1550 nm (a) without mirror (b) with mirror in the BOX.

the left most of the grating and 1500 nm above the grating surface. The 2D-FDTD results of the E-field distribution are shown in Fig.6. 3. The propagation of light towards substrate is minimized in the presence of Al mirror and the light in the Si waveguide is increased significantly which also can be seen in Fig.6. 4 which depicts the light

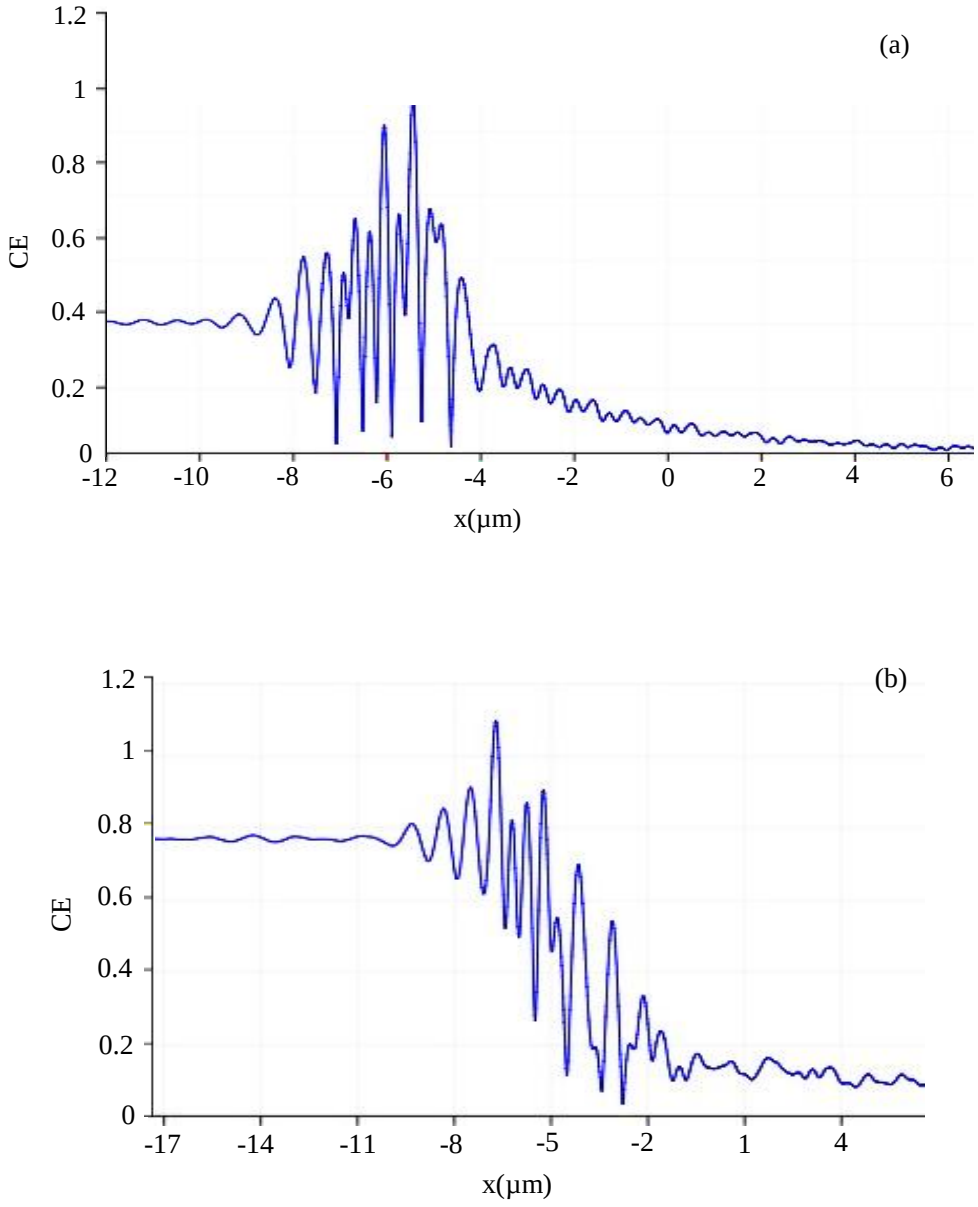

Fig.6. 4: Coupling efficiency at wavelength of 1550 nm (a) without mirror (b) with mirror in the BOX.

propagation profiles of the coupler. The propagating waves along +x/-x directions are in the wave-guided modes reflect back from the periodic grating trench edges, resulting an interference with the incident light. Consequently, a standing wave forms with resonance around the point of incidence localized in the grating region. The period of modulated interference patterns is determined by the grating patterns (depth, width, and shape). Hence the highest E-field level occurs at the point of incident. The wave stabilized as it propagates along the silicon waveguide which can be seen in Fig.6. 4.

Using the Al mirror based grating coupler, the vertical dimension of the waveguide is converted to 220 nm with 77% (shown in Fig.6. 4 (b)) of incident light at the grating waveguide. Coupling this light into nano photonic waveguide require further matching of the lateral dimension with nano waveguides as the lateral width of the grating waveguide (w_g) remains in the range of µm. Therefore direct connection of the grating coupler with nano photonic waveguides results in poor coupling efficiency due to unmatched lateral dimension of the waveguides. To overcome such limitations, the GC structure was then tapered down to 320 nm by designing a dual-taper partially overlay adiabatic SSC structure, as shown in Fig.6. 2.

6.4 Design of Partially Overlay Tapered Waveguides

The grating waveguide of the coupler is tapered down to 320 nm by designing a partially overlay 2-taper adiabatic SSC structure, as shown in Fig.6. 2. The top taper, which is connected directly to the grated waveguide, reduces the width of the GC structure to 120 nm at a taper length of 30 µm. The bottom taper, with an equal width of grated waveguide at the beginning, reduces the width of the taper to 320 nm at a taper length of 45 nm. The placement of the bottom taper below the top taper was found optimum from half of the length of the top taper, resulting in a total SSC length of 60 µm.

The transmission of light from the top to the bottom taper can be explained by the fact that the guided light in the top taper is intensified mid-axially along the length. This intensified light is highly delocalized and loosely confined at the taper tip, and enroutes

to the bottom taper due to the presence of high RI contrasts between top taper's loosely confined and bottom taper's highly confined modes. This difference in mode confining characteristics (modal mismatch) also causes an inter-dependent relationship between the tip-width of the top taper and the length of the bottom layer, as pointed out in Fig.6. 5. Fig.6. 5 quantifies the mismatches between the modes of the tapers with respect to various tip-widths of the top taper. The distributions of light within the modes are also shown in the Fig.6. 6 for tip-widths of 40, 120 and 180 nm. The lowest mismatch of 0.26 dB was seen to be caused at a tip-width of 120 nm. The relationships between the tip-widths of the top taper and the lengths of the bottom taper, along with their impact on the overall CE, are shown in Fig.6. 7. As expected, the highest CE (68%) and the shortest length of the bottom taper (30+15 µm) both happen at the top taper tip-width of 120 nm. The length of the top taper and the position of the bottom taper were also

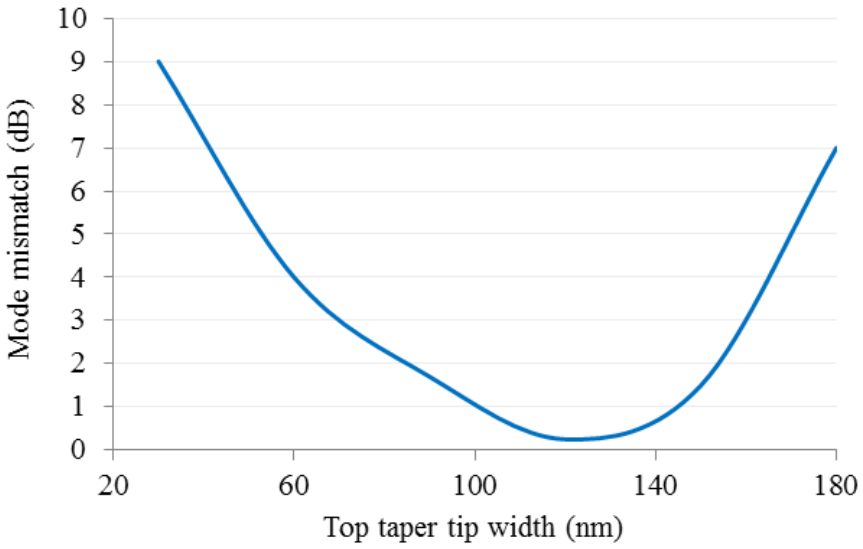

Fig.6. 5: Modal mismatch between the modes of the top and bottom tapers for various tip-widths of the top taper.

varied for optimum parameters by keeping the width of top taper-tip and the length of the bottom taper fixed at 120 nm and 45 µm respectively, the relationship of which with CE are shown in Fig.6. 8. It shows that the maximum CE occur at the top taper length of 30 µm with initial position of the bottom taper at the half-length of the top taper, as indicated in the inset of the Fig.6. 8. The E-field distribution and CE in the proposed GC at the wavelength of 1550 nm are also shown in Fig.6. 9 for a better clarity. The

proposed structure, therefore, down-sizes the width of the GC from 14 µm to 320 nm with an effective SSC length of 60 µm, causing a reduction of CE by 77%-68% = 9% only.

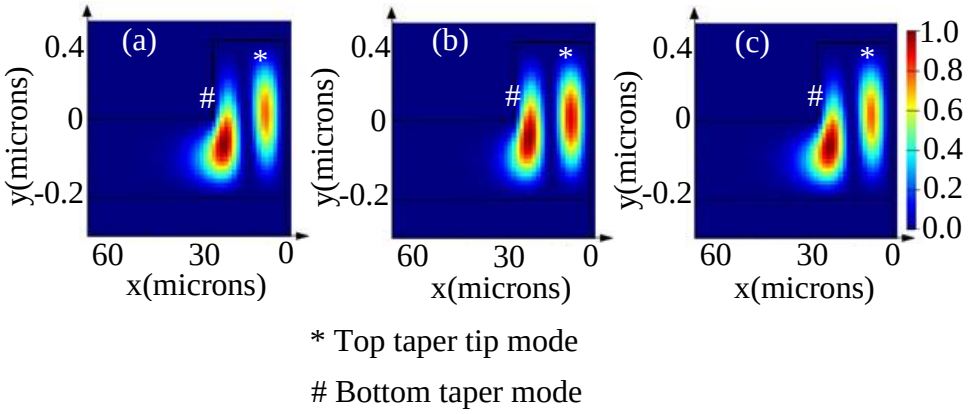

Fig.6. 6: Modal distribution of light within the modes of the top and bottom tapers for tip-widths of the top taper (a): tip-width = 40 nm, (b): tip-width =120 nm, and (c): tip-width =180 nm

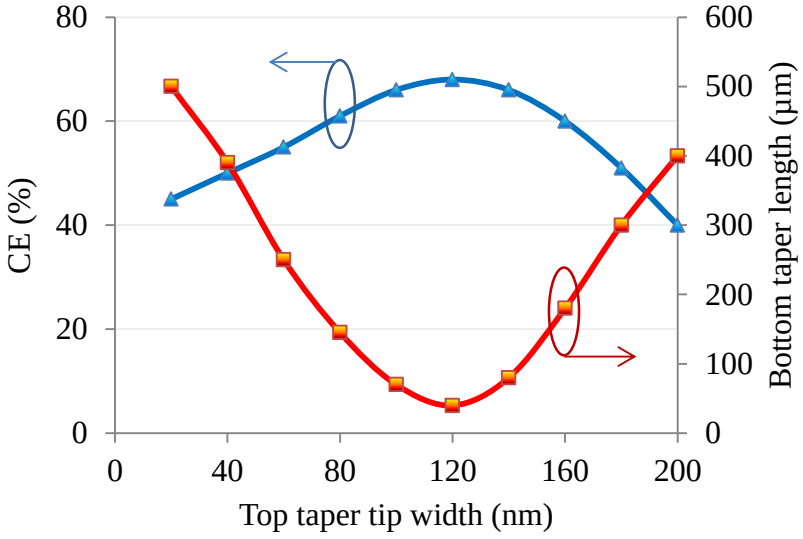

Fig.6. 7: Coupling efficiency for different top taper tip-widths and bottom taper lengths at the wavelength of 1550 nm.

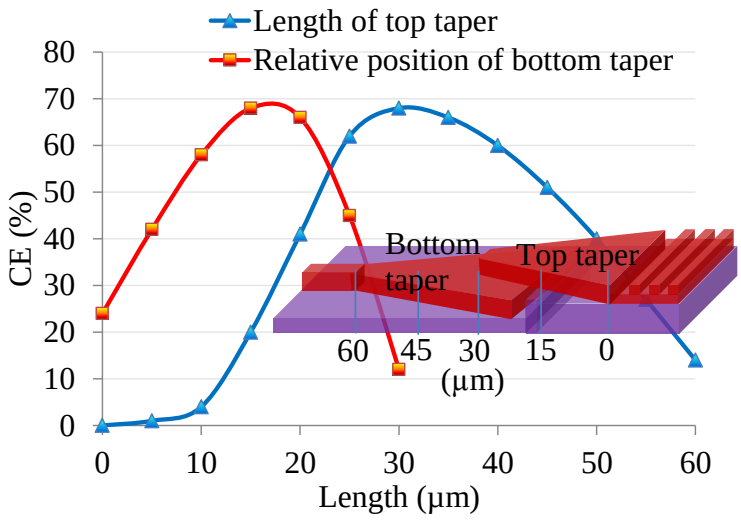

Fig.6. 8: CE for different lengths of the top taper and positions of the bottom taper with initial position of the bottom taper at the half-length of the top taper. Inset shows relative positions of the tapers with respect to each other.

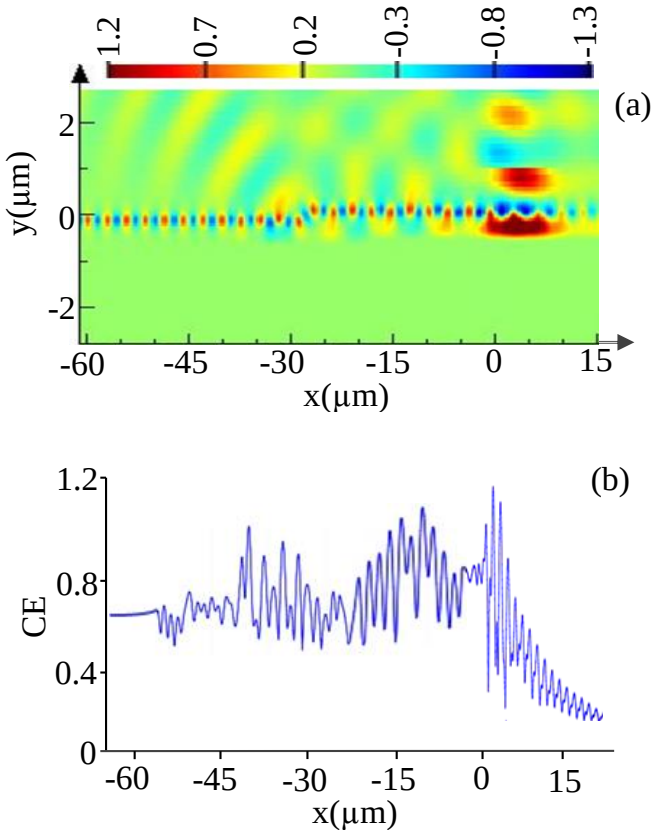

Fig.6. 9: (a): E-field distribution, and (b): CE in the proposed GC at wavelength of 1550 nm.

6.5 Comparisons with Conventional and Inverted Tapered Waveguides

Coupling of light from grating waveguide into nano photonic waveguide requires tapering down of the grating waveguides form μm scale to nm meter scale. The coupling efficiency between the waveguides highly relies on transitional slope of the tapered waveguide which determines the length of the taper. For very small slope angle (θ) results in longer taper which provides smooth modal transformation where modal loss is minimized. On the other hand, larger slope angle (θ') causes rapid modal transformation due to shorter taper length and increases the modal loss. A schematic of the long taper and short taper is shown in Fig.6. 10. In long tapered waveguides, the modal transformation is smother in comparing with shorter length which ultimately improve the modal loss in taper region.

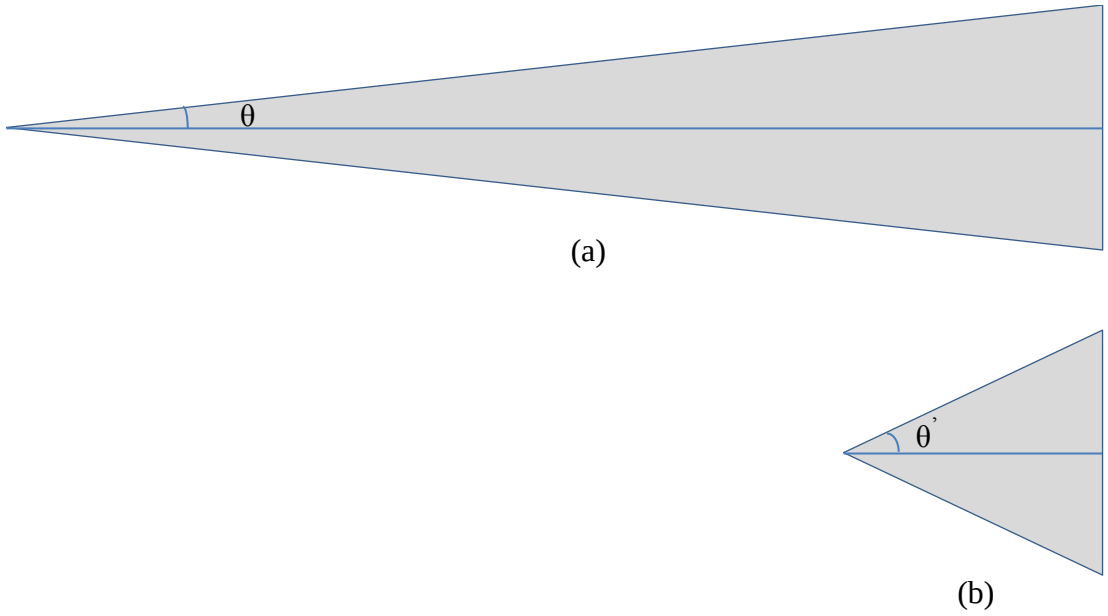

Fig.6. 10: Tapered waveguides (a): long taper and (b): short taper

The field distribution in the tapered waveguides mainly determined by two physical parameters,

i) The refractive index contrast between the taper medium and its surrounding medium and

ii) The width and the length of the tapered waveguide. The distribution of the E-field in the triangular taper can be expressed based on the following equation

$$E(z) = E_0 e^{(n_m - n_0)(x - |z_0 - z_l|)} \quad \text{(Eq.6.5.1)}$$

where $E(z)$ is the E-field distribution in the taper, E_0 is the light entering into the taper, n_m and n_0 are the RIs of the material of the taper and surrounding medium respectively, x is the length of the taper, z_0 is the mid-axis of the taper and z_l is the distance from z_0. The $|z_0 - z_l|$ also corresponds to the direction of x-axis, the maximum value of $|z_0 - z_l|$ is at the beginning of the taper and smaller when closer to the taper tip and at the tip end $z_0 = z_l$ where the maximum intensity occurs as shown in Fig.6. 11. In Eq. (6.5.1) the initial width of the taper is set to 10 µm and entering power level to 1. The n_m and n_0 are set to 3.5 and 1.0 respectively which are comparable with silicon and air. The numerical result

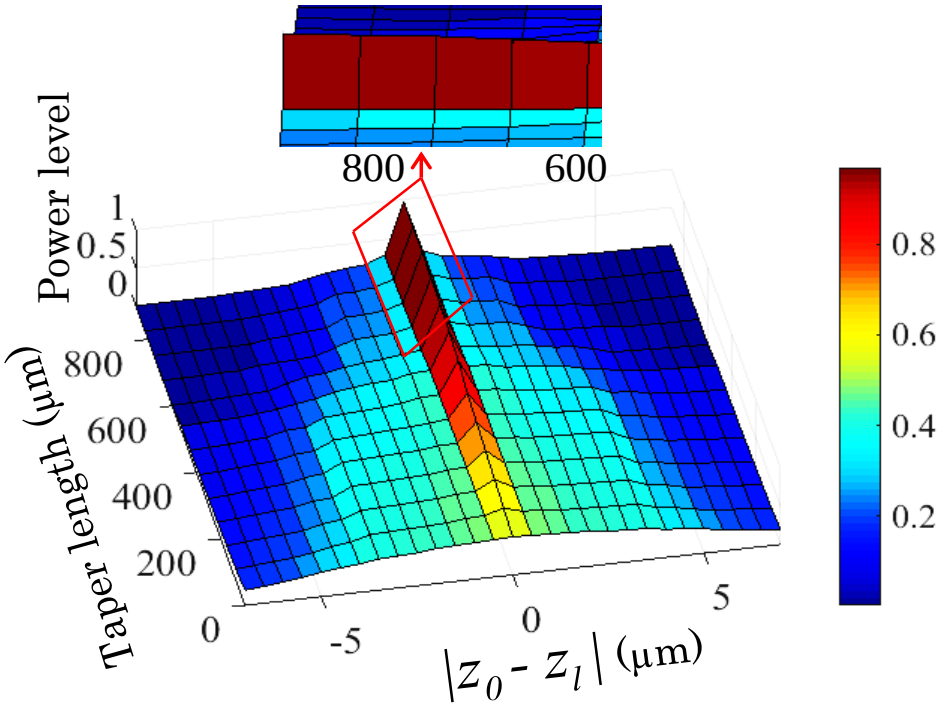

Fig.6. 11: E-field distribution in the conventional taper with initial width of 14 µm.

shows (Fig.6. 11) that the peak power level occurs at around 800 µm of taper length and virtually saturated with further additional length of the taper.

Based on the results, an 800 µm long conventional ($L_{conventional}$) taper is added with designed GC which comprises of 21 gratings with period of 700 nm that makes the grating length (L_g) of 15 µm as shown in Fig.6. 12 (a). The 2-D FDTD simulations results show that the optical power level at the taper tip is approx. 58% (shown in Fig.6. 12 (c)). Therefore the power penalty in conventional taper is (77% - 58%) about 19% in this design. For fair comparison we have also simulated the designed GC using inverse

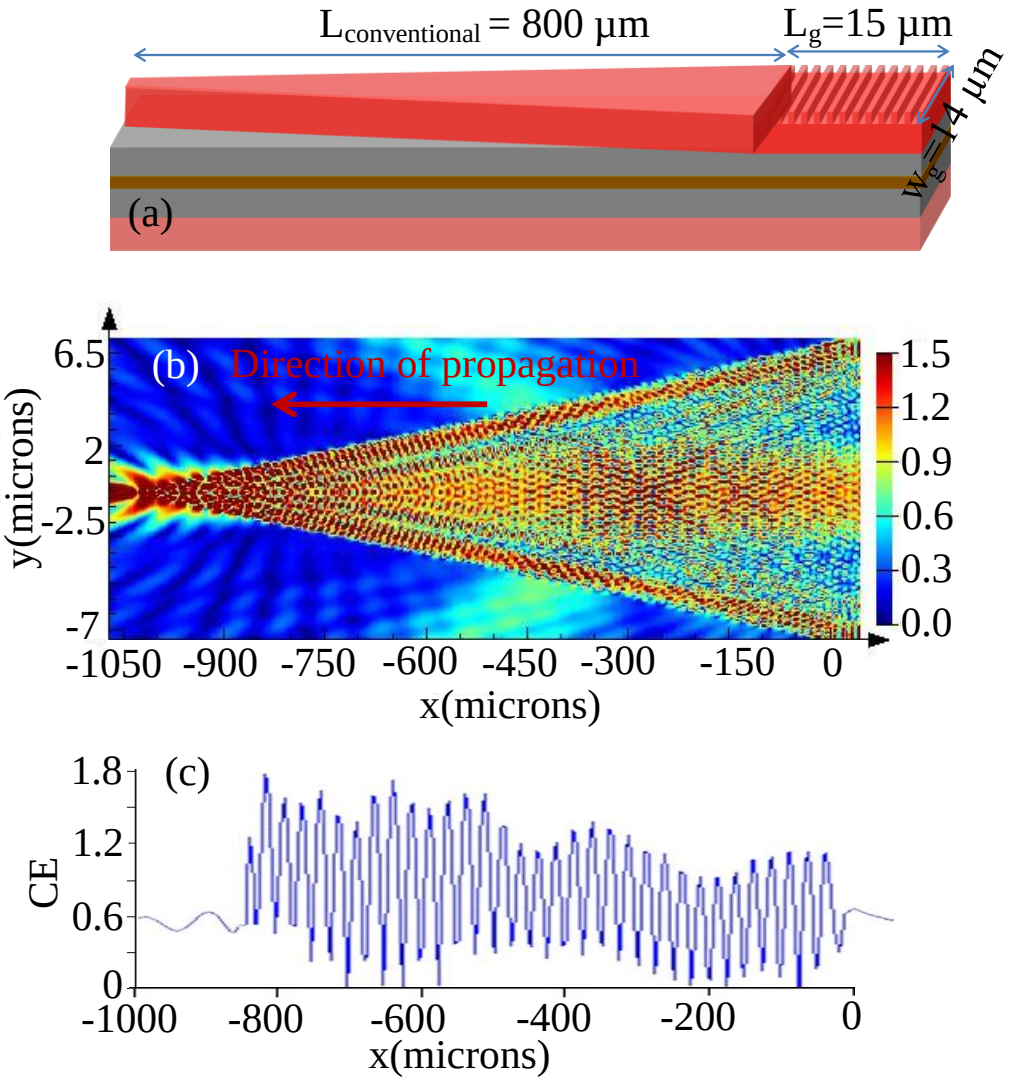

Fig.6. 12: (a): GC with single taper direct SSC, (b) and (c): E-field distribution and CE at the end of single taper direct SSC respectively at wavelength of 1550 nm.

taper to achieve similar power as conventional taper and the results (Fig.6. 13 (a-b)) show that the length of inverse taper is much higher than that of conventional taper. This is due to the fact that unlike conventional taper, where the expansion of the mode happens predominantly laterally rather vertically, in inverse taper the field expands both vertically and laterally. The results show that with inverse taper higher CE (CE = 80% shown in Fig.6. 13 (c)) can be achieved but in expense of larger footprint of the grating couplers.

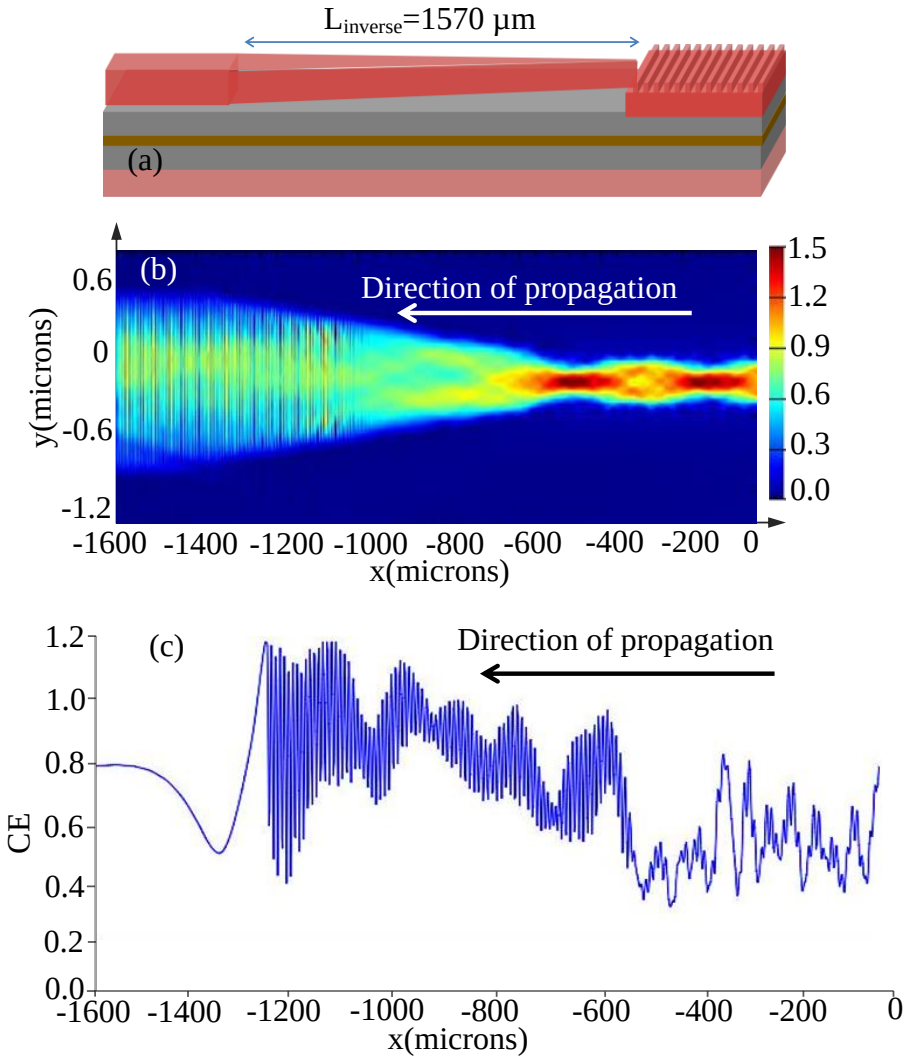

Fig.6. 13: (a) Inverse taper with GC (b) E-field distribution in the inverse taper and (c) CE at the end of inverse taper waveguide at wavelength of 1550 nm.

The comparison was further extended by replacing the 800 µm direct SSC with a 60 µm single taper SSC, equal to the size achieved by the proposed overlay structure, keeping other design parameters unchanged, as shown in Fig.6. 14. It shows that, with such a small SSC length, only 40% CE could be achieved.

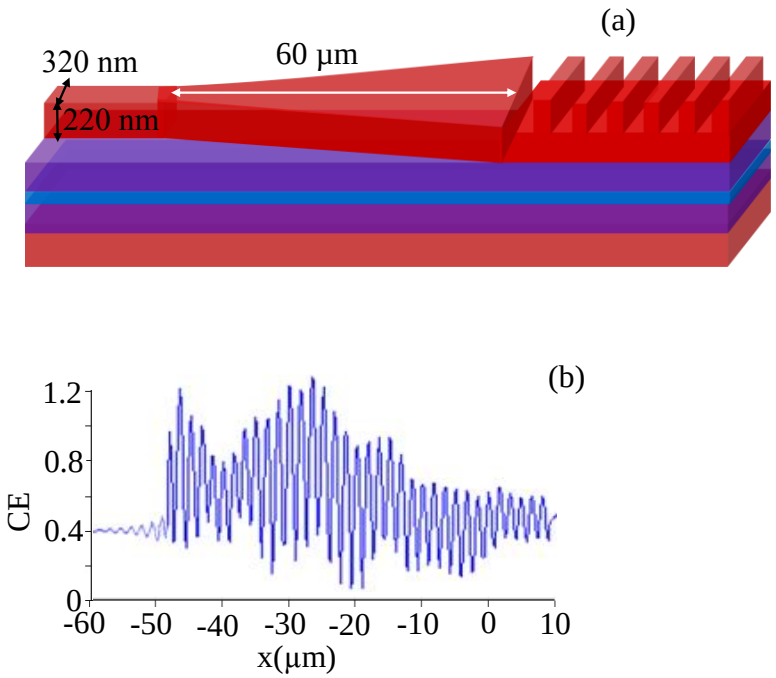

Fig.6. 14: (a): GC structure with a 60 µm single taper direct SSC and (b): the relevant CE at the nano waveguide at 1550 nm wavelength.

Fig.6. 15 shows the coupling efficiency for number of tapers with shorter lengths. The coupler best performs for 2-taper overlay structure. Increasing the number of tapers for shorter length drops the coupling efficiency significantly. This is due to fact that there exist modal conversion losses at every point of top taper tip mode and bottom taper mode. The CE for 4-taper structure is around 20% less than that of 2-taper structure at the wavelength of 1550 nm as shown in Fig.6. 15.

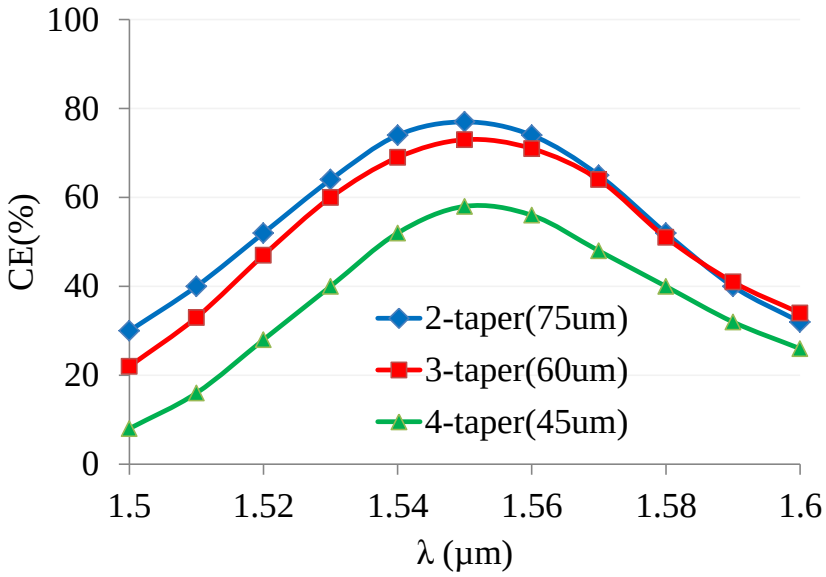

Fig.6. 15: CE of the GC structure with number of dual-taper partially overlay SSC for over a range of wavelength with centre at 1550 nm.

An estimation of CBW of the proposed GC structure with and without the partially overlay SSC under discussion is shown in Fig.6. 16. It shows that CBW does not change much with the inclusion of the proposed taper, although as expected, CE reduces by 9%, as indicated earlier. Using the optimized parameters obtained by 2D FDTD analysis, the structure is simulated based on 3D FDTD. The results are in excellent agreement for both 2D and 3D FDTD analysis as shown in Fig.6. 16. In both analyses similar coupling peaks occur at 1550 nm wavelength. However the coupling bandwidth calculated based on 3D FDTD is little lower than that of predicted using 2D FDTD. The validity check of the results is further extended with EME method. The coupling spectrum calculated based on EME very simular with 2D FDTD as shown in Fig.6. 16.

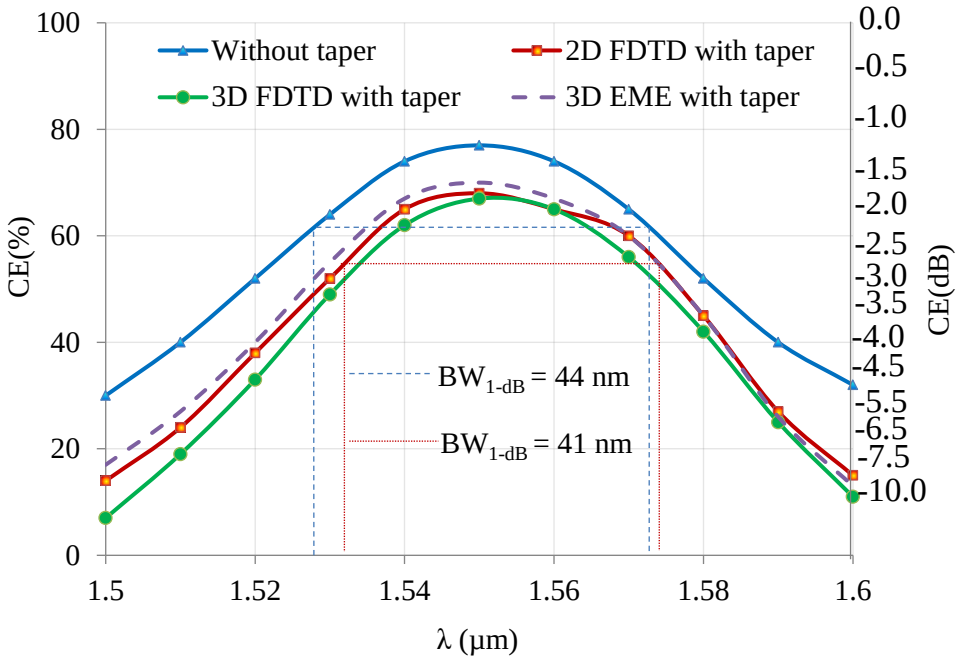

Fig.6. 16: CE and CBW of the GC structure with/ without the proposed 2 taper overlay SSC for over a range of wavelength with centered at 1550 nm

The comparison of the results of the proposed dual-taper design with recently reported compact grating coupler is depicted in Table 6.5.1. Although the focusing curved grating structures offers small footprint, their CEs are not much impressive. The proposed grating coupler with dual-taper partially overlay structure shows reasonably high CE with compact footprint in PICs.

Table 6.5.1: Theoretical results of recently reported compact grating couplers

Ref. No.	Grating types	Dimensions length ×width	CE (dB)	BW	
				1-dB	3-dB
[10]	Focusing and Uniform	Not reported	-2.7	42 nm	Not reported
[11]	Rib and Uniform	534.4 µm ×15 µm	-4.8	Not reported	Not reported
		1534.4 µm ×15 µm	-1.8	Not reported	40 nm
[14]	Focusing and Uniform	40 µm × 20 µm	-2.8	Not reported	50 nm
This work	Straight line and Uniform	75 µm ×14 µm	-1.67 (68%)	41 nm	67 nm

6.6 Summary

A compact grating coupler with two-taper partially overlay SSC waveguide is proposed, the overall dimension of which is reduced to 75 µm (length) × 14 µm (width) to achieve small footprint in PICs while ensures least conceivable coupling loss between optical fiber and nano waveguide. The proposed structure exhibits coupling efficiency of 68% (-1.67 dB) with 1-dB and 3-dB coupling bandwidth of 41 nm and 67 nm respectively. The results are comparable with most compact designs in literature taking the size, coupling efficiency and bandwidth into account. The coupling efficiency can further be improved by reducing back reflection and implementing apodized gratings to achieve higher mode matching between fiber mode and waveguide mode.

Chapter 7

Hollow Tapered Waveguide based Compact Grating Coupler

7.1 Introduction

As indicated earlier in chapter 6 that grating structure converts only the vertical dimension of the waveguide and keep lateral dimension unaltered. Therefore the issue remains to connect the grating coupler with nano photonic waveguide. This is because the typical cross sectional dimension of nano waveguide is in the range of ~ 200 nm (height) × 500 nm (width). Using grating coupler, the height of the waveguide can be converted into 220 nm as discussed in previous chapters. So in order to couple light with nano waveguide, the lateral dimension of the grating waveguide is needed to be tapered down at nano scale. In chapter 6, the grating structure is tapered down using partially overlay waveguides with coupling loss of ~ 9% between nano waveguide and grating waveguide. In this chapter, the design of hollow tapered waveguide (HTW) for coupling between grating waveguide and nano waveguide is studied. The results indicate that with the optimized design of HTW, higher coupling efficiency can be obtained.

7.2 Design Methodology and Background Parameter Extraction for the Proposed GC

The design exercise performed in this investigation rely on widely used Finite Difference Time Domain (FDTD) method, which is a numerical analysis technique used for modelling computational electromagnetics by solving Maxwell's equations.

Although, in real, GC is a computation-intensive 3D problem requiring huge computer memory for modelling, a 2D approximation of the structure can also mimic the same functionality with sufficient accuracy, as typical width of a GC (e.g. 15 µm) is much larger in compare to its height (e.g. 220 nm) and operating wavelength (e.g. 1550 nm). Theoretically, FDTD method performs its best for grid spacing (Δ_x, Δ_y, and Δ_z) approaching towards zeros. But, in practice, Δ is also perceived as a compromise between cost and complexity, and therefore, chosen to find the right balance among computational cost and accuracy. For the analysis under discussion, the modelling environment was created by using Lumerical's FDTD solution with grid spacing as small as $\Delta_x = \Delta_y = 10$ nm, which is sufficient to maintain higher accuracy. Reflections at the boundary of the structure was eliminated by using built-in perfectly matched layer (PML). The modelling also involved parameter sweeping module where parameters for best performance can be obtained and used to update other parameters by employing Particle Swarm Optimization (PSO) for optimum performance. The simulation environment created for the proposed GC is shown in Fig.7. 1.

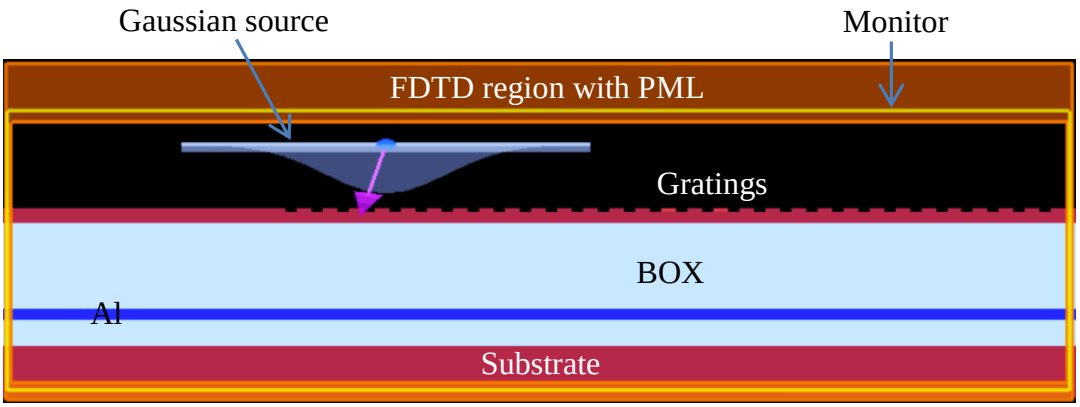

Fig.7. 1: Simulation environment setup using Lumerical FDTD Solutions.

To extract the background parameters for the proposed GC, a grating structure enabling typical vertical matching between SMF and nano-scale waveguide was designed, the schematic of which is shown in Fig.7. 2. It consists of 2 µm thick SiO_2 layer as BOX with 220 nm Si on top to ensure single mode operation. The BOX is incorporated with an Aluminum (Al) layer of thickness of 100 nm as reflector which

recaptures the light wasted through the BOX due to downward radiation. The thickness of the SiO_2 between top Si layer and Al layer is optimized as t_{BOX} = 1.6 µm that causes constructive interference among guided and reflected waves. The gratings are written on top Si layer for which design parameters were are calculated by using the following grating equation:

$$\Lambda = \frac{\lambda}{n_{eff} - n_{top}.\sin\theta_{in}} \qquad \text{(Eq.7.2.1)}$$

where Λ is the grating period, λ is the wavelength of incident light, n_{eff} is the effective refractive index (RI) experienced by the optical modes, n_{top} is the RI of the cladding on top of Si layer, and θ_{in} is the angle of incidence with normal to the direction of incidence causing a slightly tilted positioning of SMF to minimize second order reflections. For the fundamental mode, n_{eff} , which was calculated by using Full-Vectorial Mode Solver, was found to be 2.23. The targeted wavelength was set at λ = 1550 nm from which grating period was calculated as Λ = 636 nm for n_{top} = 1 (air) and θ_{in} = -12^0. Shown in Fig.7. 1, a TE polarized Gaussian type optical source with a mode-field diameter comparable to that of SMF (approx. 10 µm) is applied on the surface of the grating. The width of the grating waveguide is chosen to be 15 µm for sufficient overlapping. The position of the source is also optimized using parameter sweep setup which is 1700 nm

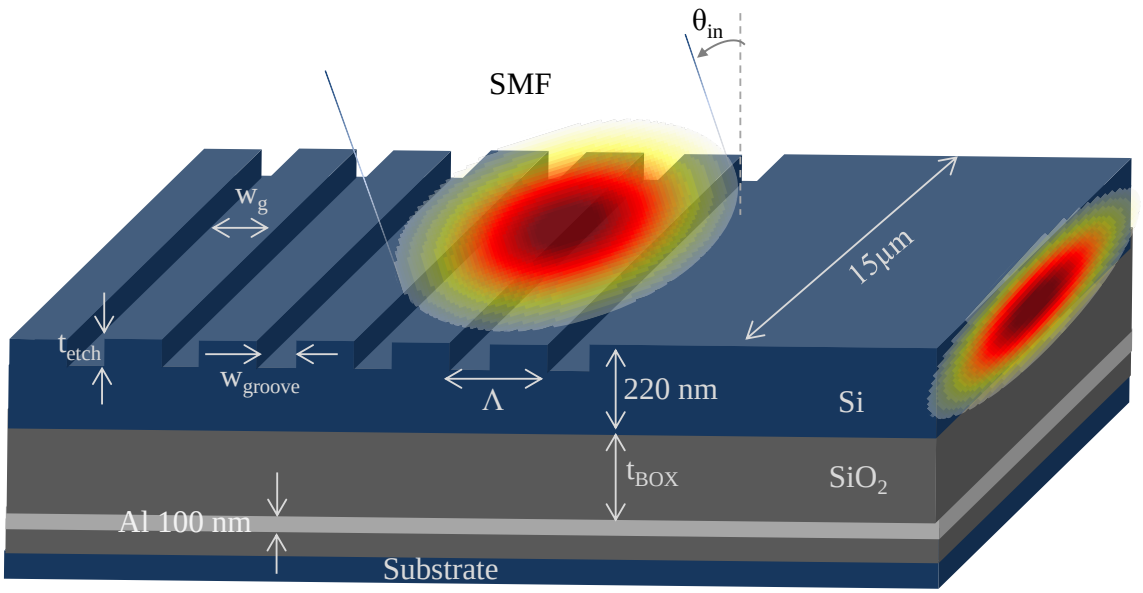

Fig.7. 2: Geometry of the grating coupler structure (drawn not in scale).

away from the leftmost end of the grating and 1500 nm above the grating surface. Initially grating depth (t_{etch}) and filling factor (ff) were set to 50% of the height of top Si waveguide and grating period respectively, which later was optimized as 95 nm and 350 nm respectively for maximum efficiency by using PSO. As $ff = (w_g/\Lambda) = 0.55$, groove width ($w_{groove}$) was left to be 286 nm. Also, as the total height of top Si layer is 220 nm, a 125 nm Si base remains as a waveguide after etching 95 nm-depth gratings.

With all these necessary parameters optimized, the E-field distribution and propagation of light along the structure are shown in Fig.7. 3 (a) – (b), which were obtained by placing a power monitor across the structure. Shown in Fig.7. 3 (b), light with a CE of 78% can be expected at the end of grating waveguide which then would be passed to the nano-scale waveguide device through the proposed HTW.

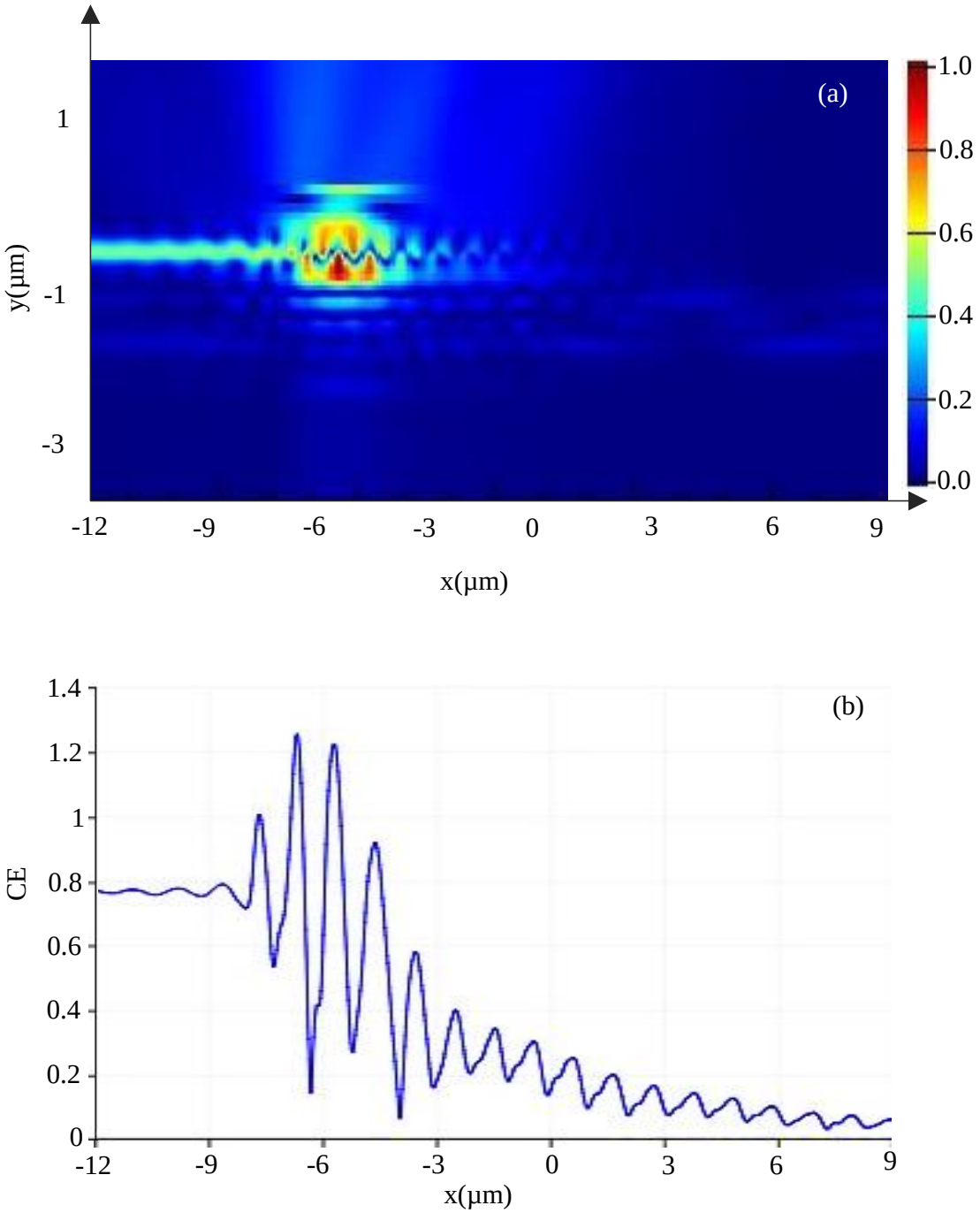

Fig.7. 3: (a) E-field distribution along the grating structure, and (b) propagation of light along the structure with predicated CE.

7.3 Proposed HTW for Compact GC

A HTW enabling lateral matching between grating waveguide and nano-scale waveguide devices with a smaller footprint is proposed and modelled by using Lumerical's 2D FDTD solution, the related simulation environment and background parameters of which were discussed in Section 7.2. In HTW, light is guided through a tapered hollow core where the optical modes are converted from loosely confined mode to highly confined mode. HTW is designed by inserting two Si strips one ends of which are connected with grating waveguide and other ends merge together to form a hollow core. For effective recapturing of the mode to couple to the nano-scale waveguide device, the widths of the Si strips are adiabatically increased until it supports a mode to confine within the merged Si strips. The schematic diagram of the compact GC incorporating the proposed HTW is shown in Fig.7. 4.

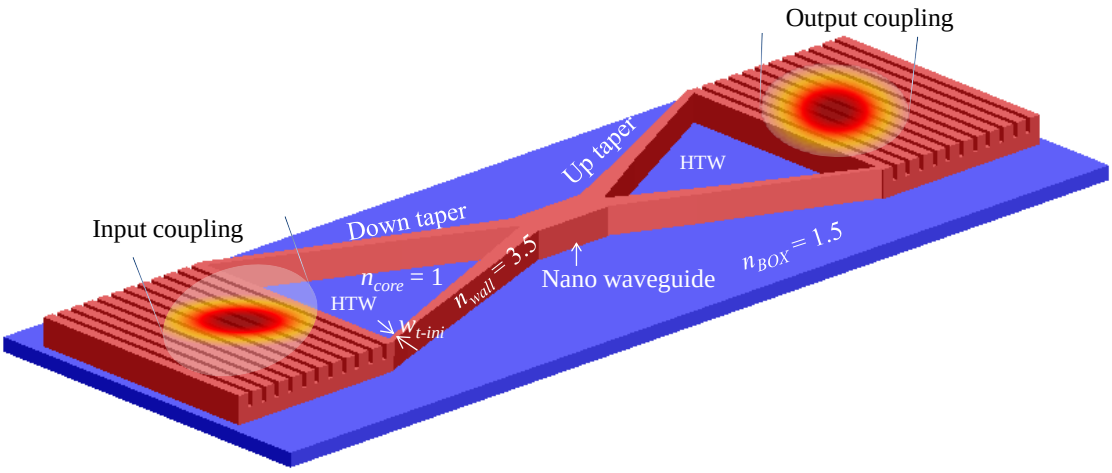

Fig.7. 4: Schematic diagram of a compact GC incorporating the proposed HTW spot-size converter (drawn not to scale).

Optical mode from the grating waveguide is confined within the hollow air core mainly due to two physical occurrences: (i) contrast of RI between Si wall (n_{wall} = 3.5) and air core (n_{core} = 1), and (ii) the narrow width of the Si strips ($w_{t\text{-}ini}$), which is thin enough to reject any mode inside the strip. Typical cross-section of a Si strip that fulfils the conditions for a single mode operation at 1300 to 1600 nm band is approximately

500 nm (width) × 200 nm (height) [256] [257]. The height of the strips is matched with grating waveguide to 220 nm, which also satisfies the conditions for single mode operation. To find the optimum width that rejects any part of the optical mode to reside within it, HTW structure is simulated by using Finite Difference Eigenmode (FDE) solver of the Lumerical's Mode Solutions with strip-width ($w_{t\text{-}ini}$) setting at 500 nm, 300 nm and 100 nm, the results of which are shown in Fig.7. 5 (a)-(c) respectively.

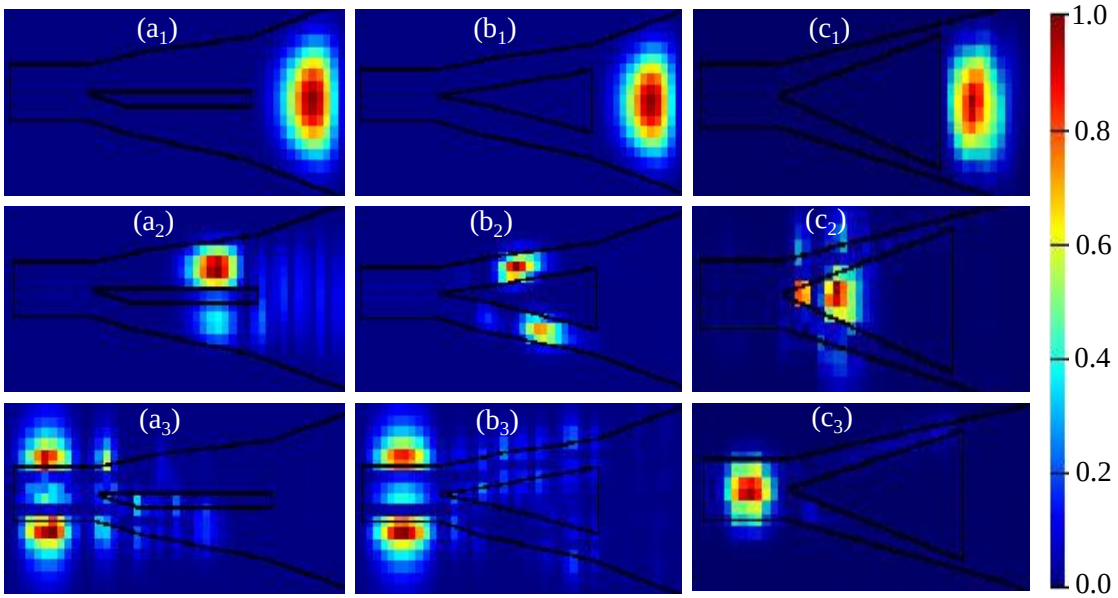

Fig.7. 5: Optical modes in different locations of the hollow structured waveguide for various widths of Si strip: (a_1)-(a_3) for a strip-width of 500 nm, (b_1)-(b_3) for a strip-width of 300 nm, and (c_1)-(c_3) for a strip-width of 100 nm.

Shown in Fig.7. 5 (a) for the strip-width of 500 nm, although the mode is fully confined within the waveguide at the beginning of HTW (Fig.7. 5 a_1), it appears to split and disperse gradually down the tapered waveguide (Fig.7. 5 a_2), and disperse completely at the narrow-end of HTW (Fig.7. 5 a_3), missing the coupling with the waveguide devices. Similar occurrences happen for the strip-width of 300 nm with a bit lower dispersion, as shown in Fig.7. 5 (b_1)-(b_3). The circumstances however improve significantly for strip-widths less than 200 nm. Shown in Fig.7. 5 (c_1)-(c_3) for the strip-width of 100 nm, mode is fully confined within the core of HTW both at the beginning and ending of the tapering, confirming the coupling with the nano-scale waveguide

devices. In all cases, the length of HTW was maintained 60 µm and an adiabatic control on Si strips was applied at the narrow-end so that a mode can be fully contained.

7.4 Performance Characterization of the Proposed HTW

From the findings of previous section, it is clear that the widths of Si strips at the grating end should be around 100 nm each that need to be increased gradually at the device end for effective coupling. The distribution of E-field along the HTW and the associated CE are shown in Fig.7. 6 (a)-(b). It shows that at a taper length of 60 µm, the CE estimated is only 47%. To check the influence of the taper length, the structure was further simulated with taper lengths of 10 to 140 µm and the respective estimations of CE are shown in Fig.7. 7. It confirms that CE with taper length of 60 µm is somewhat maximum and with taper lengths above 60 µm, it quickly saturates without any appreciable increment. By recalling the CE from the vertically matched grating waveguide, coupling loss in the HTW is approximately (78% - 47%) or 31%. This can be attributed to the modal loss at the waveguide device end where light is transported from loosely confined HTW to strongly confined nano-scale waveguide devices.

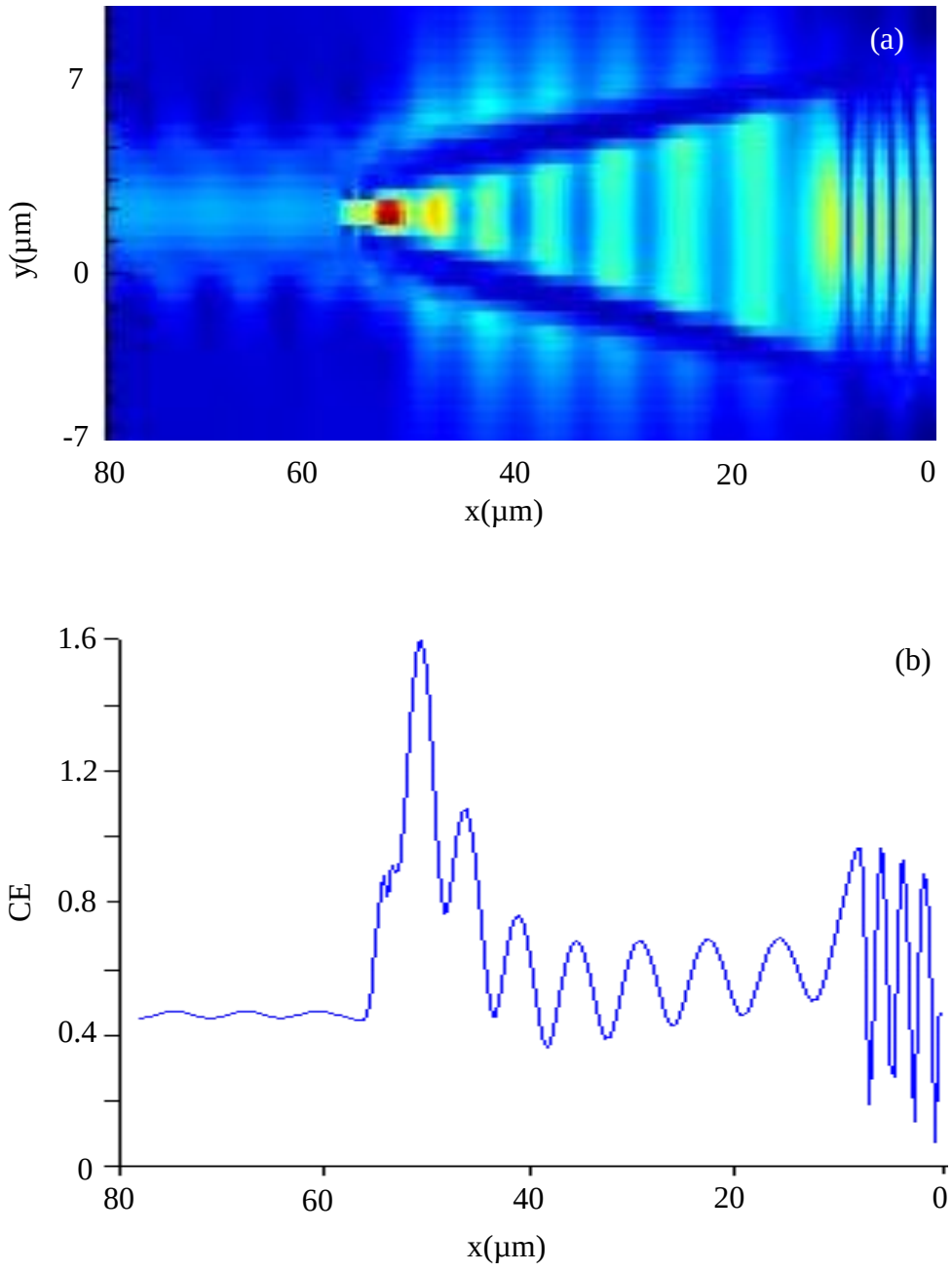

Fig.7. 6: Performance characterization of the proposed HTW: (a) E-field distribution along the HTW structure, (b) estimated CE with a fixed taper length of 60 µm.

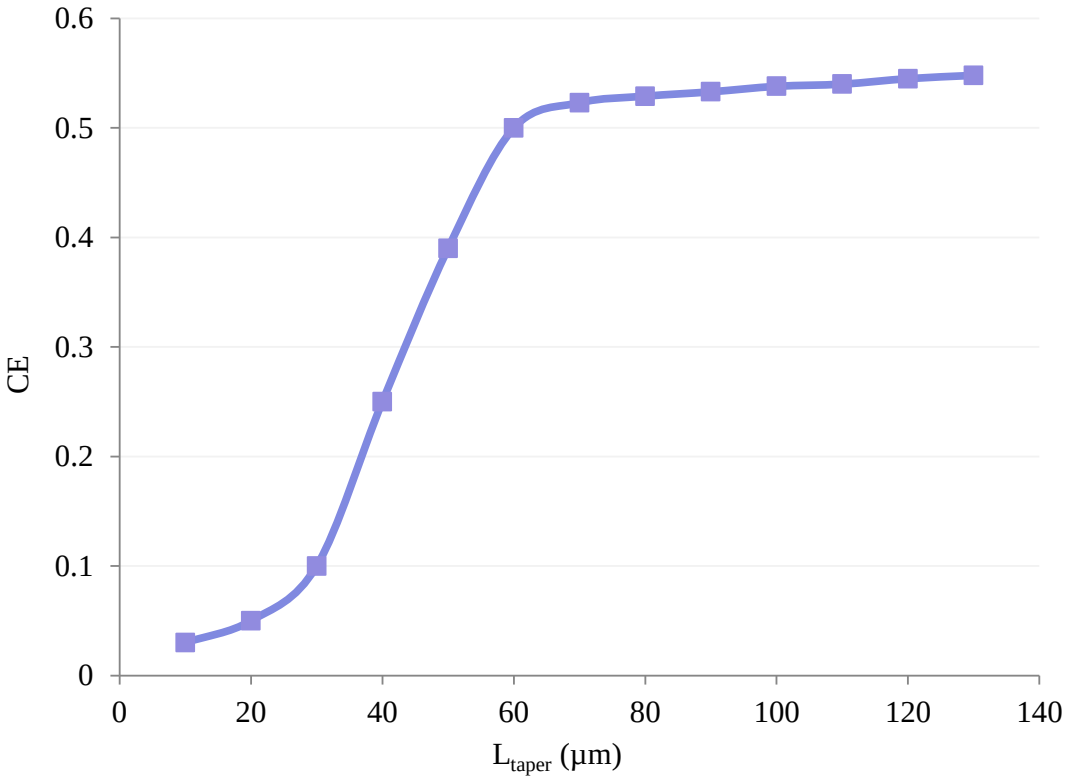

Fig.7. 7: Estimated CE with respect to various taper lengths.

To minimize the modal loss in the proposed HTW, additional Si strips can be inserted into hollow core. Such insertion essentially converts loosely confined modes of HTW to highly confined modes by reducing the effective width of the hollow core. The optimum number of Si strips can be calculated as follows:

$$n_{strip} = \frac{m - \left(\frac{m}{w_n}\right) w_s}{w_n} \qquad \text{(Eq.7.4.1)}$$

$$m = w_g - 2w_s \qquad \text{(Eq.7.4.2)}$$

where n_{strip} is the number of Si strips, w_g is width of grating, w_s is width of strip and w_n is width of nano-scale waveguide device.

The spacing between adjacent Si strips (w_H) in the HTW can be calculated as:

$$w_H = \frac{\left(\frac{m}{2} - \left(w_s \cdot \frac{n_{strip} - 1}{2}\right)\right)}{\left(\frac{n_{strip} - 1}{2}\right)} \qquad \text{(Eq.7.4.3)}$$

For the parameters of the GC/ HTW under consideration, optimum number of Si strips can be calculated as n_{strip} = 32.88 or 33 by using equation (7.4.1), and the width of the hollow space can be calculated as w_H = 362.5 nm by using equation (7.4.3). The complete structure of the GC comprising of the HTW is shown in Fig.7. 8.

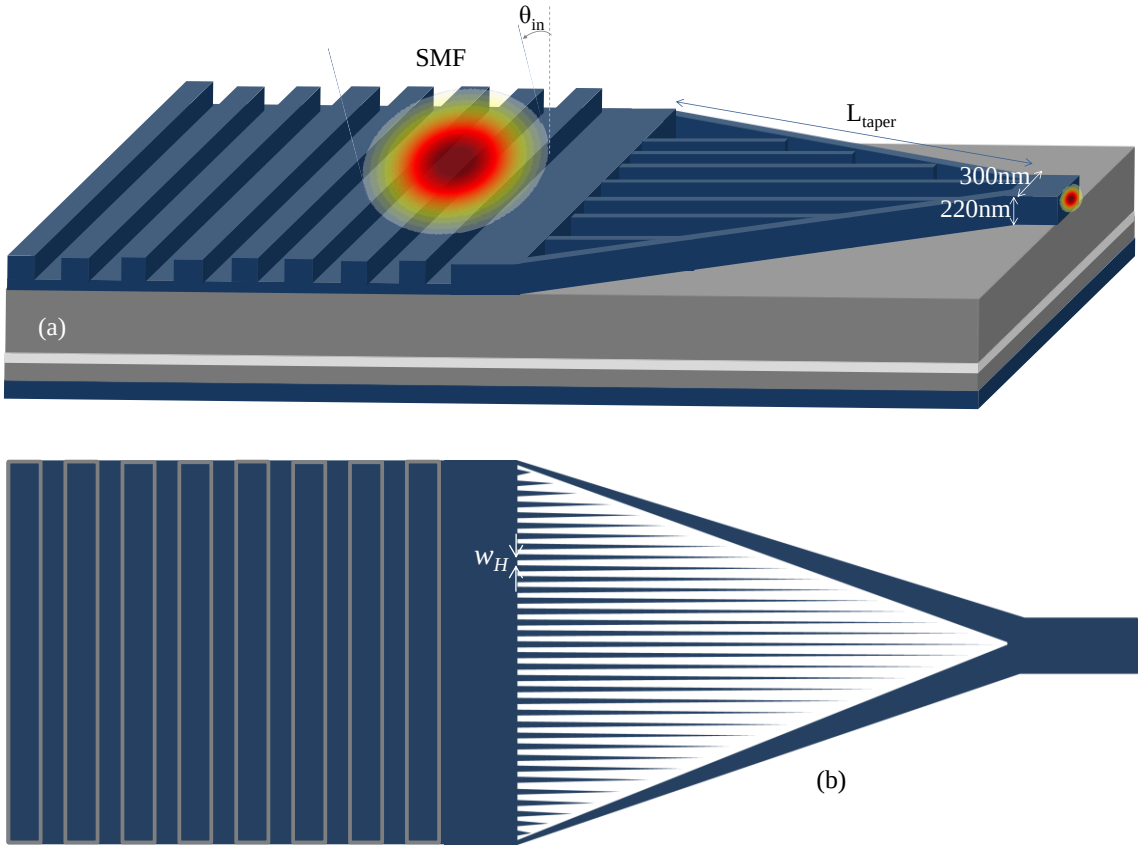

Fig.7. 8: (a) 3D view of the GC incorporating proposed HTW (for clear view only few Si strips are shown), (b) 2D top view of the full HTW core with 33 Si strips (drawn not to scale).

Fig.7. 9 (a) shows the changes in mode mismatch and CE with respect to the number of Si strips in the HTW, where mode mismatch is calculated based on intermodal overlap between HTW and nano-scale waveguide device modes using FDE solver of Lumerical's Mode solutions. Shown in Fig.7. 9 (a), maximum theoretical CE occurs for 33 Si strips in the HTW for which mode mismatch is minimum (0.23 dB). Further increase in Si strips causes degradation in CE. This is due to the fact that adding more Si strips in HTW causes narrower hollow core width which becomes inadequate to confine a mode within itself, and as a consequence, increases the mode mismatch between HTW mode and nano-scale waveguide mode rather than reducing it. The CE performance and E-field distribution along the HTW structure with 33 Si strips are shown in Fig.7. 9 (b)-(c), where it is evident that the insertion of additional strips has increased CE from 47% to 72% while kept other background parameters unchanged. Also, such insertion improved the mode confinement significantly, as can be seen from E-field distribution in Fig.7. 9 (c).

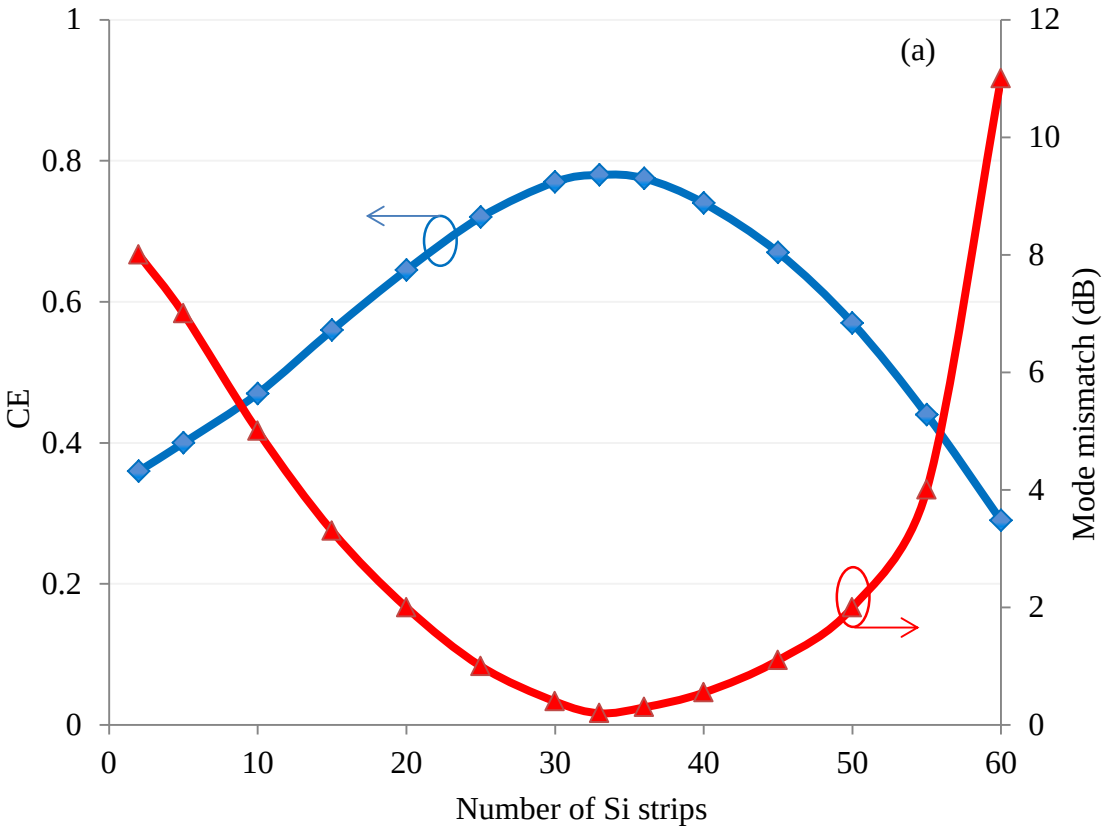

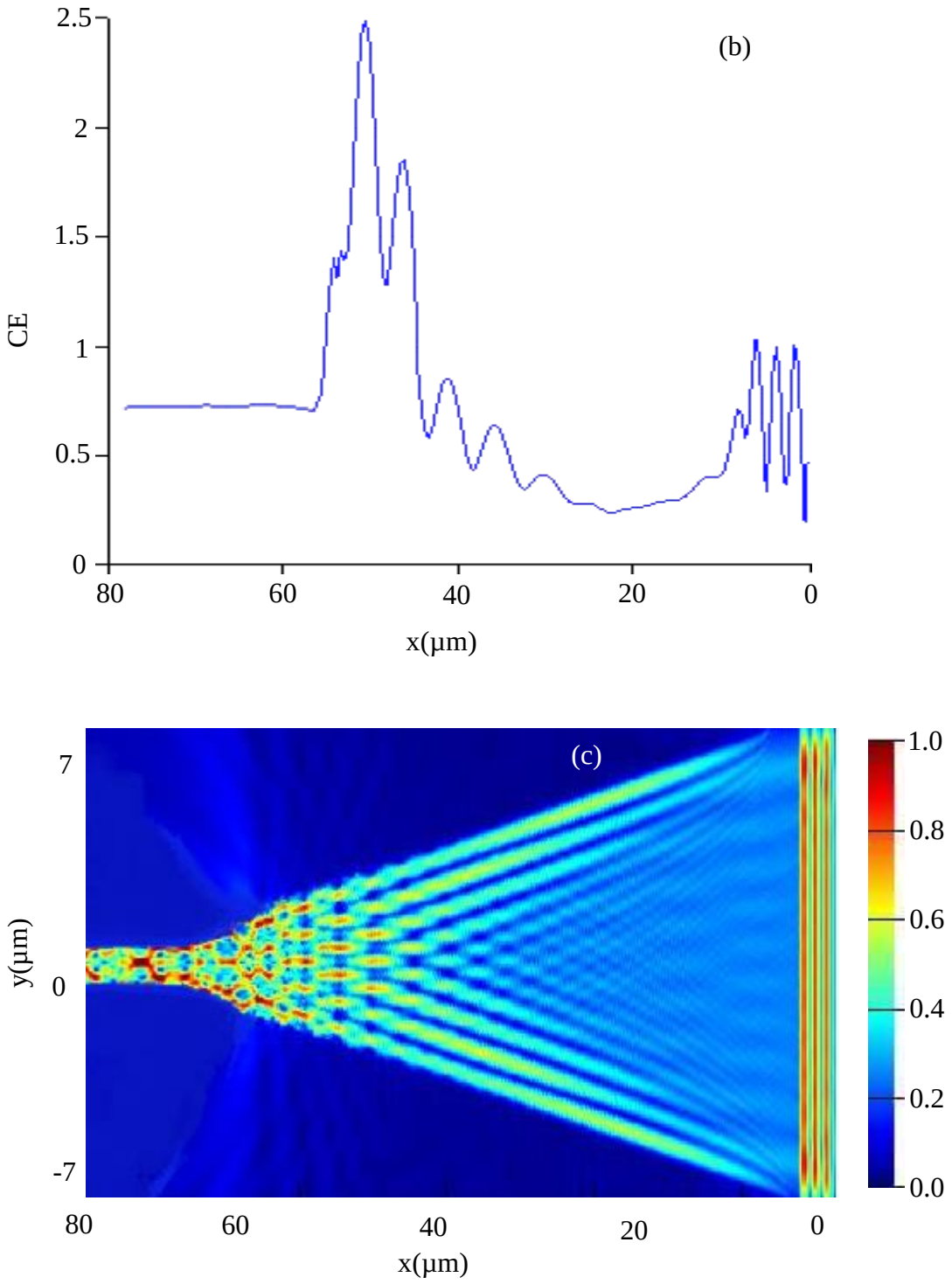

Fig.7. 9: Performance of the proposed HTW after insertion of additional strips while other background parameters kept unchanged. (a) Changes in mode mismatch and CE with respect to the number of Si strips, (b) CE performance along the HTW structure with optimum 33 Si strips

inserted, and (c) E-field distribution along the HTW structure with optimum 33 Si strips inserted

7.5 Performance Comparison

To quantify the improvements, proposed GC with HTW structure was compared with GCs having conventional taper (CT) and inverse taper (IT) with 60 µm taper lengths, equal to the optimum length of the proposed HTW structure. The tapers are used to couple light from 15 µm wide grating waveguide to 300 nm wide nano-scale waveguide. Height of the waveguide throughout the structure is kept 220 nm, which makes the cross-section of the nano-scale waveguide as 220 nm (height) × 300 nm (width). CE and CBW predicted for various taper structures are shown in Table 7.5.1. The results show that, for a taper length of 60 µm, conventional taper exhibits a CE of only 40% whereas the inverse taper exhibits even lower CE of 29%. Therefore, coupling loss between grating waveguide to nano-scale waveguide device is (78% - 40%) = 38% and (78% - 29%) = 49% for CT and IT respectively. In contrast, the proposed GC comprising of HTW with 33 Si strips exhibits CE up to 72% by reducing the tapering loss significantly.

Table 7.5.1: Performance comparison of the proposed GC with HTW under discussion with GCs incorporating CT and IT with taper length and nano-scale waveguide width of 60 µm and 300 nm respectively.

		GC+HTW		GC+CT	GC+IT
		Without strips	With strips		
CE	%	48	**72**	40	27
	dB	-3.18	**-1.42**	-3.97	-5.68
CBW(nm)	1-dB	39	**43**	34	22
	3-dB	62	**70**	51	43

Finally an estimation of CBWs of the designed GC without any taper and the proposed GC structure comprising of HTW with/without 33 Si strips are shown in

Fig.7. 10. It shows that CBW does not change much with the inclusion of the proposed taper, although as expected, CE reduces by 6% for HTW with 33 Si strips, as indicated earlier. The grating coupler with optimized HTW parameters obtained by 2D FDTD was then simulated based on 3D FDTD method. The calculated coupling spectra for both methods are nearly same except little lower coupling peak for 3D FDTD comparing with 2D FDTD as shown in Fig.7. 10. The structure also analysed using 3D EME method and the obtained results are in very good agreement with 2D FDTD method which further validate the results predicted with different methods.

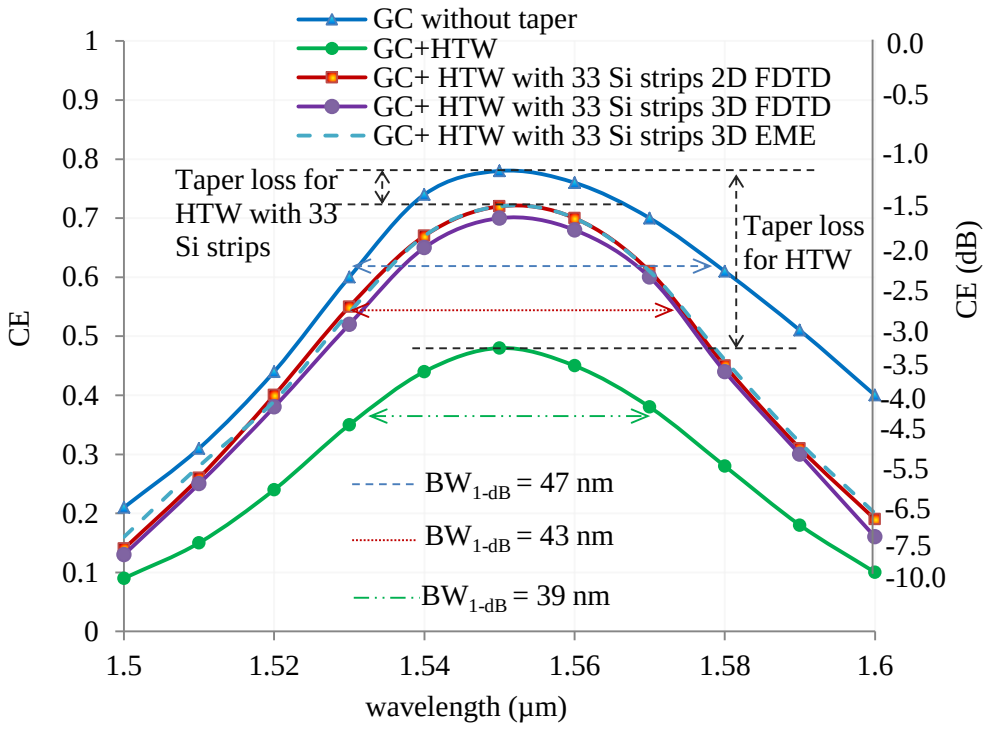

Fig.7. 10: Theoretically predicted CE of the proposed GC without any taper and with HTW, both including and excluding additional Si strips, over a range of wavelengths with centre at 1550 nm.

7.6 Fabrication Process and Tolerances

The fabrication of the structure can be started with a SOI wafer consisting 1.6 µm SiO_2 BOX and 220 nm top Si layer. There could be two-step lithography process necessary to realize two different etch depths for gratings and HTW. In first step the gratings can be defined using electron beam lithography (EBL) technique and the pattern transfers can be realized by means of dry etching until etch depth of 95 nm. In second lithography step, the HTW with 33 Si strips need to be defined which could be achieved by using hard mask, e.g. SiO_2 mask on top Si layer and then the top Si layer is etched until the BOX (etch depth of 220 nm) to form the proposed HTW.

Generally, slight variations of the designed parameters are expected in actually fabricated device. The effects of such variations on the performance of the coupler have been studied. The influence of the grating groove is shown in Fig.7. 11 (a)-(b) for fixed grating period. Shown in Fig.7. 11 (a), the coupling spectra for the groove width variation (Δw_{groove}) by +/- 10 nm from the designed width of 286 nm show that the peak of spectrum is shifted towards longer wavelength for smaller groove width while the change in opposite direction happens for larger groove width. Shown in Fig.7. 11 (b), CE as function of Δw_{groove} drops more for positive variation (larger grooves) than that of negative variation (smaller grooves). However, irrespective of larger or smaller groove, these variations are quite insignificant (less than 1%) for a groove width variation of +/- 10 nm. The effects of etch-depth variation is also studied and encapsulated in Fig.7. 11 (c). It shows that CE drops more for deeper etch-depth in compare to shallow etch-depth. A CE change of less than 1% ($\Delta CE < 1\%$) is predicted for etch-depth (t_{etch}) range of 90-100 nm. ΔCE will be around 4% only for the change of t_{etch} from 85 nm to 110 nm.

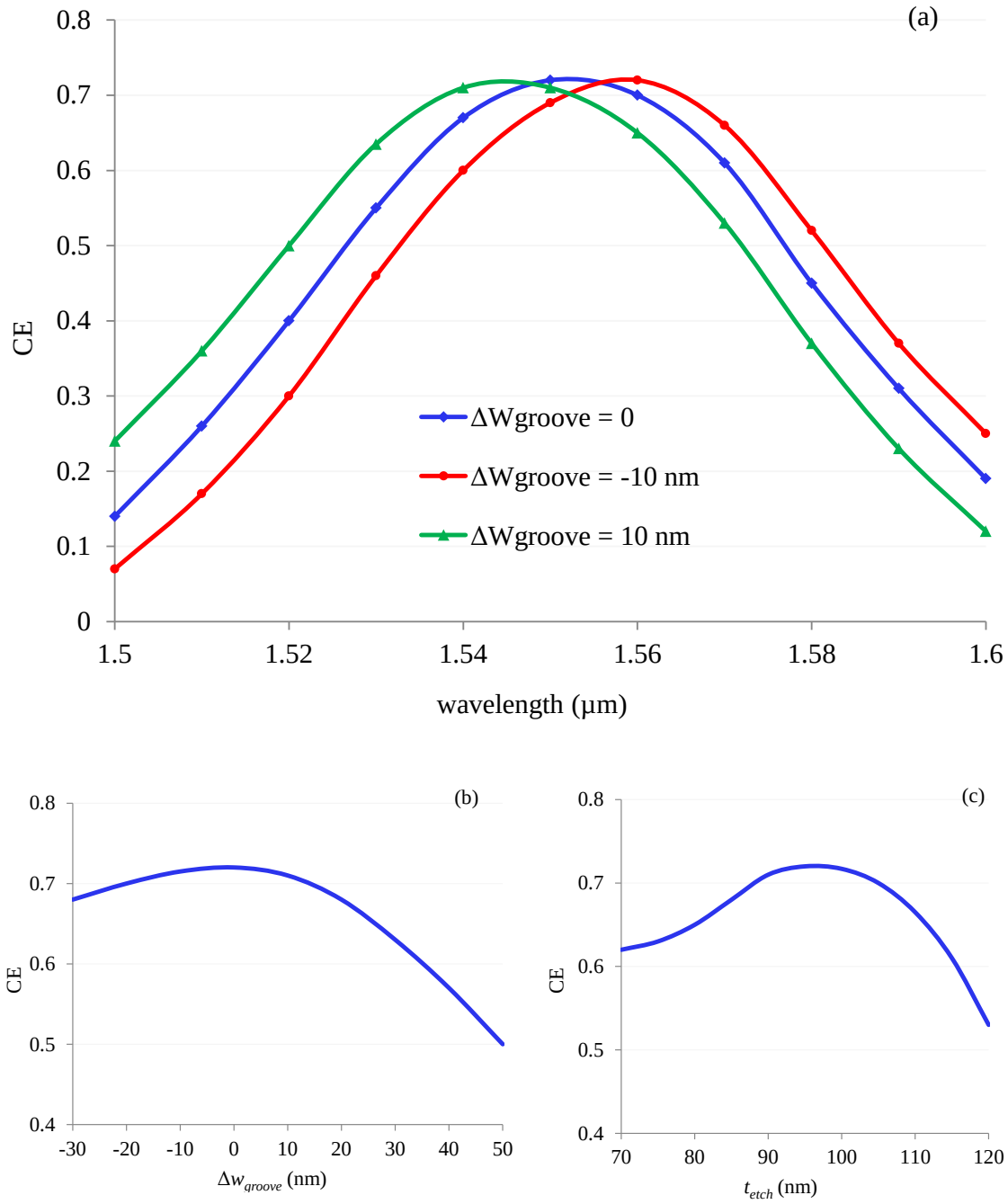

Fig.7. 11: (a) Coupling spectra for Δwgroove of +/- 10 nm, (b) predicted CE as function of Δwgroove, "0" in horizontal axis refers to no deviation of groove width which is 286 nm, (c) predicted CE as function of t_{etch} at the wavelength of 1550 nm.

The study of the fabrication tolerances was further extended to the HTW structure. First of all the influence of the initial width ($w_{t\text{-}ini}$) of the two outer Si trips is investigated. In section III we have found that $w_{t\text{-}ini}$ should be thinner than 200 nm to deny any mode to reside within it. So the HTW structure is simulated for $w_{t\text{-}ini}$ from 50 nm to 190 nm as shown in Fig.7. 12 (a). The results show that for $w_{t\text{-}ini}$ range of 80-120 nm, CE drops only 2%, which however changes sharply for $w_{t\text{-}ini}$ around 140 nm. This can be attributed to the fact that at such thickness mode starts escaping the hollow core and gradually penetrating into Si strips. The effects of hollow space (w_H) was also studied (shown in Fig.7. 12 (b)) and found that CE is more sensitive to w_H compare to other parameters. This is because w_H determines the mode mismatch between HTW and nano-scale waveguide modes. As w_H deviates from optimum value, mode mismatch increases and consequently drops CE. However fabrication tolerance is still well-within comfortable limit, as the change of w_H from 350 to 370 nm causes only 2% of ΔCE.

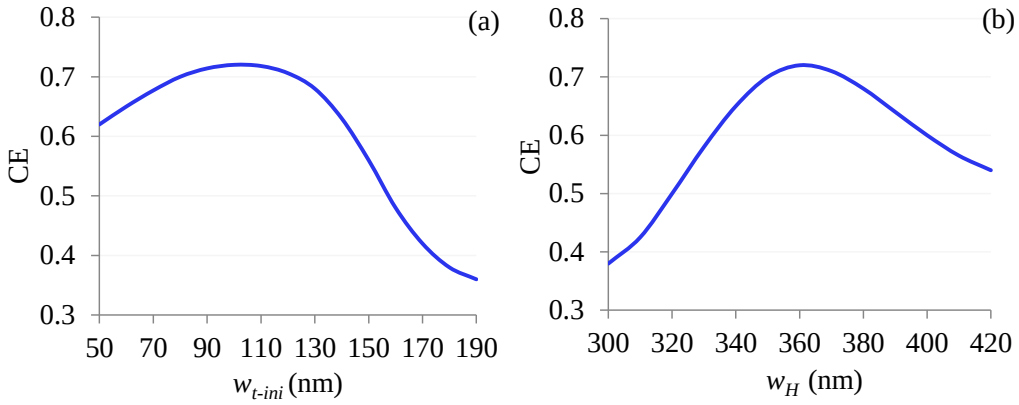

Fig.7. 12: Estimation of the fabrication tolerance of HTW with respect to (a) $w_{t\text{-}ini}$ and (b) w_H.

7.7 Summary

A compact GC with HTW spot-size converter is proposed. The overall dimension of the GC is reduced to 81 µm (length) × 15 µm (width) to enable smaller footprint in PICs, while ensuring least possible coupling loss between optical fibre and nano-scale waveguide devices. Light is transported from 15 µm wide grating waveguide to 300 nm

wide Si nano-scale waveguide with a proposed 60 μm long HTW. The 2D FDTD analysis shows that, with the basic HTW structure with 2 Si strips, only 47% of incident light could be coupled to the nano-scale waveguide. To increase CE, HTW structure was improved by implanting additional Si strips into the hollow core that minimize the mode mismatch between HTW and nano-scale waveguide modes. Such HTW structure with optimum number of Si strips exhibits CE of 72% (-1.42 dB) with 1-dB and 3-dB CBW of 43 nm and 69 nm respectively. Using the proposed HTW light can be coupled from grating waveguide to nano-scale waveguide with least possible taper loss, only 6% estimated in this case. The performance of the proposed HTW structure is compared with conventional and inverse tapers for similar taper lengths as of HTW and found that the proposed HTW structure shows superior performance over conventional and inverse tapers. The proposed structure is fully CMOS compatible and can be fabricated based on standard lithography and etching process. The fabrication tolerance also investigated and found that the device possess remarkable high tolerant to the fabrication errors. The results are comparable with most compact designs in literature taking the size, coupling efficiency and bandwidth into account. The coupling efficiency can further be improved by reducing back reflection and implementing apodized gratings to achieve higher mode matching between fibre and waveguide modes.

Chapter 8

Conclusions and Future Works

A summary of the works is presented in this chapter. We will also discuss the direction for future motivations based on the outcomes of the works.

8.1 Conclusion remarks of the works

The main aspect of this thesis is the coupling of light between optical fiber and nano photonic waveguide. An overview of the state-of-the-art in coupling mechanisms is presented in chapter 2. Among the various coupling techniques, the butt coupling and grating coupling are the most appeared in literature. Butt coupler is the technique well known for their ability to offer high coupling efficiency and bandwidth. Moreover, butt couplers are polarisation insensitive that means it can couples the light for both transverse electric (TE) and transverse magnetic (TM) polarisations simultaneously. However, they require to be tapered down from micro scale to nano scale and coupling efficiency highly relies on the length of the taper. To achieve high coupling efficiency the length of the taper should be long enough for smooth modal conversion. The typical length of the taper is in the range of hundreds of micrometers that results in large footprint of the photonic integrated circuits. The drawbacks of butt coupler further extended due to fabrication complexity. It often requires polishing and dicing the edges and facet of the taper which creates obstacle for wafer level testing.

Grating couplers, On the other hand, offers the flexibility to place them anywhere in the chip and do not require polishing and dicing, opening the way for wafer level testing. However, the choice of grating coupler as coupling method falls behind the choice of butt coupler due to low coupling efficiency and narrow coupling bandwidth. Grating couplers are also polarisation sensitive which limits their use in applications where both polarizations are required.

In chapters 4 and 5 we have designed grating couplers for better performance. The major contributing loss factor in grating coupler is the propagation of light through BOX layer. One of the ways to minimise such loss is to use reflector in the BOX layer. However placement of the reflector is very crucial as the reflector only complement coupling efficiency if the reflected waves constructively interfere with original guided wave. Otherwise destructive interfere occurs and degrades the performance of the coupler.

In chapter 4 we have developed mathematical formulas that can readily be used to calculate optimum thickness of the layers for ensuring the constructive interference and enhance the coupling efficiency. The results show that there could be different thicknesses of the layers at which constructive interference happens. Therefore, one can have choice of thicknesses suitable for specific design and more importantly for the fabrication feasibility. We also characterises the grating coupler for various performance influencing parameters such as etch depth, filling factor, position of the fiber etc. In this design 78% coupling efficiency is estimated with 1-dB coupling bandwidth of 77 nm.

In chapter 5 we have proposed and designed a perfectly vertical grating coupler for light coupling between SOI waveguides and SMF. The symmetrical propagation nature of the diffracted waves from grating is broken by incorporating asymmetric grating trenches with step gratings. The directionality of the coupler is boosted by implementing effective index variation of the primary grating, which is achieved by combination of auxiliary subwavelength gratings in the ridge of primary gratings and step gratings. The calculated coupling efficiency is improved from 43%, estimated for GC without secondary gratings, to as high as 85% (-0.7 dB) for GC comprising our proposed engineered subwavelength secondary gratings. The proposed GC predicts coupling spectra as wide as 53 nm and 80 nm for 1-dB and 3-dB down level respectively. The structure possesses sufficient robustness to the possible errors that may arise during fabrication. The proposed coupler features less influence of the BOX thickness on the coupler performance which eases the choice for fabrication. Such efficient broadband perfectly vertical grating coupler is significantly advantageous in high dense photonic packaging.

To interface the grating coupler with nano photonic waveguides, two types of spot-size converters are proposed and designed in chapter 6 and 7. Chapter 6 described the design of a partially overlay tapered waveguide structure. In this design the top tapered waveguide is directly connected with grating structure while the bottom tapered waveguide is connected with nano photonic waveguide and laid under the top waveguide. With such arrangement the grating coupler can be connected with photonic waveguide within very short length of ~ 60 µm. The overall dimension of such compact grating coupler with two-taper partially overlay SSC waveguide is reduced to 75 µm (length) × 14 µm (width) to achieve small footprint in PICs while ensures least conceivable coupling loss between optical fiber and nano waveguide. The proposed structure exhibits coupling efficiency of 68% (-1.67 dB) with 1-dB and 3-dB coupling bandwidth of 41 nm and 67 nm respectively. The results are comparable with most compact designs in literature taking the size, coupling efficiency and bandwidth into account. The coupling efficiency can further be improved by reducing back reflection and implementing apodized gratings to achieve higher mode matching between fiber mode and waveguide mode.

Another coupling mechanism between grating coupler and nanophotonic waveguides is described in chapter 7. In this design the connection is established based on hollow tapered waveguide (HTW). The hollow taper waveguide is formed by two ultra-thin silicon strips one ends of which are connected with grating structure while other ends are merged together and connected with nano waveguide. To minimise the modal loss between hollow mode and waveguide mode, the hollow waveguide is divided into sub-hollow waveguides. Such optimised design of hollow tapered waveguide offers the light to transfer from grating waveguide to nanophotonic waveguide with coupling loss of as low as only 7%. The overall dimension of the GC is reduced to 81 µm (length) × 15 µm (width) to enable smaller footprint in PICs, while ensuring least possible coupling loss between optical fibre and nano-scale waveguide devices. Light is transported from 15 µm wide grating waveguide to 300 nm wide Si nano-scale waveguide with a proposed 60 µm long HTW. The 2D FDTD analysis shows that, with the basic HTW structure with 2 Si strips, only 47% of incident light could be coupled to the nano-scale waveguide. To increase CE, HTW structure was improved by implanting additional Si strips into the hollow core that minimize the mode

mismatch between HTW and nano-scale waveguide modes. Such HTW structure with optimum number of Si strips exhibits CE of 72% (-1.42 dB) with 1-dB and 3-dB CBW of 43 nm and 69 nm respectively. Using the proposed HTW light can be coupled from grating waveguide to nano-scale waveguide with least possible taper loss, only 6% estimated in this case. The performance of the proposed HTW structure is compared with conventional and inverse tapers for similar taper lengths as of HTW and found that the proposed HTW structure shows superior performance over conventional and inverse tapers. The proposed structure is fully CMOS compatible and can be fabricated based on standard lithography and etching process. The fabrication tolerance also investigated and found that the device possess remarkable high tolerant to the fabrication errors.

8.2 Future perspectives

This thesis covers various topics on grating couplers that could be the subject for future continuation. The most apparent is the fabrications of any of the structures and demonstrate the results experimentally.

It is found in chapter 4 that coupling efficiency periodically depends on the BOX thickness due to constructive and destructive interference. Therefore, experiments of the couplers with 2 or 3 different BOX thickness would be interesting.

The further study on subwavelength structure could be the more interesting one. In this design we bound our analysis considering fabrication limitations of deep-ultraviolet optical lithography (feature size of ~100 nm), typically employed in an industrially driven fabrication processes. The analysis could further be extended considering narrower and higher number of step grating in primary groove. Although fabrication of such small step gratings is out of deep-ultraviolet optical lithography, electron beam lithography could be used. Another aspect towards fabrication that draws attention is if the gratings can be fabricated using single etching step with various etch rate simultaneously.

The fabrications of both partially overlay tapered waveguides and hollow tapered waveguides could be challenging as well. For the case of partially overlay tapered waveguides the tip of top taper is very sensitive. Slight variation of the tip width causes

significant impact on coupling efficiency. Also the edges of the both tapers should be very smooth to avoid scattering of the light. To achieve improved coupling efficiency in hollow tapered waveguide, the divisions of hollow core require 33 silicon strips with the width of 100 nm which further be shrinking-down along the length. Although such divisional hollow core can be made by etching the silicon waveguide, once again the feature should be small which raises the fabrication challenges.

References

[1] Kilby, J.S., "Invention of the integrated-circuit," *IEEE Trans. Electron Devices*, ED-23, 648–654, 1976.

[2] Soref, R.A., and Bennett, B.R., "Electrooptical effects in silicon," *IEEE J. Quant. Electron.*, QE-23, 123–129, 1987.

[3] Tang, C.K., Kewell, A.K., Reed, G.T., Rickman, A.G., and Namavar, F., "Development of a library of low-los silicon-on-insulatoroptoelectronic devices," *IEE Proc. Optoelectron.*, 143, 312–315, 1996.

[4] Liu, A., Jones, R., Liao, L., Samara-Rubio, D., Rubin, D., Cohen, O., Nicolaescu, R., and Paniccia, M., "A high-speed silicon optical modulator based on a metal-oxide-semiconductor capacitor," *Nature*, 427, 615–618, 2004.

[5] G. T. Reed and A. P. Knights, *Silicon Photonics: an introduction*, 1st ed., 2004.

[6] Pavesi, L., and Lockwood, D.J., *Silicon Photonics*, Springer-Verlag, Berlin, 2004.

[7] Analui, B., Guckenberger, D., Kucharski, D., and Narasimba, A., "A fully integrated 20Gb/s optoelectronic transceiver implemented in a standard 0.13 micron CMOS SOI technology," *IEEE J. Solid-State Circuits*, 41, 2945– 2955, 2006.

[8] Hui-Wen Chen, Jonathan D. Peters, and John E. Bowers, "Forty Gb/s hybrid silicon Mach-Zehnder modulator with low chirp", *Optics Express*, Vol. 19, No. 2, 1455, 17 January 2011.

[9] Fang, A.W., Park, H., Cohen, O., Jones, R., Paniccia, M.J., and Bowers, J.E., "Electrically pumped hybrid AlGaInAs-silicon evanescent laser," *Optics. Express*, vol. 14, 9203–9210, 2006.

[10] B. Jalali, S. Yegnanarayanan, T. Yoon, T. Yoshimoto, I. Rendina, and F. Coppinger, "Advances in silicon-on-insulator optoelectronics," *IEEE Journal of Selected Topics in Quantum Electronics*, vol. 4, pp. 938-947, 1998.

[11] L. Pavesi, "Will silicon be the photonic material of the third millenium?," *Journal of Physics: Condensed Matter*, vol. 15, p. R1169, 2003.

[12] Z. Fang and C. Z. Zhao, "Recent Progress in Silicon Photonics: A Review," *ISRN Optics*, vol. 2012, p. 27, 2012.

[13] Cocorullo, G., Della Corte, F.G., Iodice, M., Rendina, I., and Sarro, P.M., "Silicon-on-silicon rib waveguides with a high-confining ion-implanted lower cladding," *IEEE J. Sel. Top. Quantum Electron., 4*, 983–989, 1998.

[14] Janz, S., Baribeau, J.-M., Delage, A., Lafontaine, H., Mailhot, S., Williams, R.L., Xu, D.-X., Bruce, D.M., Jessop, P.E., and Robillard, M., “Optical properties of pseudomorphic Si1-xGex for Si-based waveguides at the λ = 1300nm and 1550 nm telecommunications wavelength bands,” *IEEE J. Sel. Top. Quantum Electron.*, 4, 990–996, 1998.

[15] J. Schmidtchen, A. Splett, B. Schuppert, K. Petermann, and G. Burbach, "Low loss singlemode optical waveguides with large cross-section in silicon-on-insulator," *Electronics Letters,* vol. 27, pp. 1486-1488, 1991.

[16] J. S. Foresi, M. R. Black, A. M. Agarwal, and L. C. Kimerling, "Losses in polycrystalline silicon waveguides," *Applied Physics Letters,* vol. 68, pp. 2052-2054, 1996.

[17] L. Vivien, S. Laval, B. Dumont, S. Lardenois, A. Koster, and E. Cassan, "Polarization-independent single-mode rib waveguides on silicon-on-insulator for telecommunication wavelengths," *Optics Communications,* vol. 210, pp. 43-49, 9/1/ 2002.

[18] D.-X. Xu, P. Cheben, D. Dalacu, A. Delâge, S. Janz, B. Lamontagne, *et al.*, "Eliminating the birefringence in silicon-on-insulator ridge waveguides by use of cladding stress," *Optics letters,* vol. 29, pp. 2384-2386, 2004.

[19] W. N. Ye, D. X. Xu, S. Janz, P. Cheben, M. J. Picard, B. Lamontagne, *et al.*, "Birefringence control using stress engineering in silicon-on-insulator (SOI) waveguides," *Journal of Lightwave Technology,* vol. 23, pp. 1308-1318, 2005.

[20] K. K. Lee, D. R. Lim, L. C. Kimerling, J. Shin, and F. Cerrina, "Fabrication of ultralow-loss Si/SiO2 waveguides by roughness reduction," *Optics Letters,* vol. 26, pp. 1888-1890, 2001/12/01 2001.

[21] K. K. Lee, D. R. Lim, H.-C. Luan, A. Agarwal, J. Foresi, and L. C. Kimerling, "Effect of size and roughness on light transmission in a Si/SiO2 waveguide: Experiments and model," *Applied Physics Letters,* vol. 77, pp. 1617-1619, 2000.

[22] G. T. Reed, G. Mashanovich, F. Y. Gardes, and D. J. Thomson, "Silicon optical modulators," *Nat Photon,* vol. 4, pp. 518-526, 08//print 2010.

[23] G. T. Reed, W. R. Headley, and C. E. J. Png, "Silicon photonics: the early years," 2005, pp. 1-18.

[24] M. Bruel, "Silicon on insulator material technology," *Electronics Letters,* vol. 31, pp. 1201-1202, 1995.

[25] E. Cortesi, F. Namavar, and R. A. Soref, "Novel silicon-on-insulator structures for silicon waveguides," in *SOS/SOI Technology Conference, 1989., 1989 IEEE*, 1989, p. 109.

[26] L. K. Rowe, M. Elsey, N. G. Tarr, A. P. Knights, and E. Post, "CMOS-compatible optical rib waveguides defined by local oxidation of silicon," *Electronics Letters*, vol. 43, pp. 392-393, 2007.

[27] F. Y. Gardes, G. T. Reed, A. P. Knights, G. Mashanovich, P. E. Jessop, L. Rowe, *et al.*, "Sub-micron optical waveguides for silicon photonics formed via the local oxidation of silicon (LOCOS)," 2008, pp. 68980R-68980R-4.

[28] R. Pafchek, R. Tummidi, J. Li, M. A. Webster, E. Chen, and T. L. Koch, "Low-loss silicon-on-insulator shallow-ridge TE and TM waveguides formed using thermal oxidation," *Applied Optics*, vol. 48, pp. 958-963, 2009/02/10 2009.

[29] J. Cardenas, C. B. Poitras, J. T. Robinson, K. Preston, L. Chen, and M. Lipson, "Low loss etchless silicon photonic waveguides," *Optics Express*, vol. 17, pp. 4752-4757, 2009/03/16 2009.

[30] KoosC, VorreauP, VallaitisT, DumonP, BogaertsW, BaetsR, *et al.*, "All-optical high-speed signal processing with silicon-organic hybrid slot waveguides," *Nat Photon*, vol. 3, pp. 216-219, 04//print 2009.

[31] A. Martínez, J. Blasco, P. Sanchis, J. V. Galán, J. García-Rupérez, E. Jordana, *et al.*, "Ultrafast All-Optical Switching in a Silicon-Nanocrystal-Based Silicon Slot Waveguide at Telecom Wavelengths," *Nano Letters*, vol. 10, pp. 1506-1511, 2010/04/14 2010.

[32] X. Li, X. Feng, X. Xiao, K. Cui, F. Liu, and Y. Huang, "Experimental demonstration of silicon slot waveguide with low transmission loss at 1064 nm," *Optics Communications*, vol. 329, pp. 168-172, 10/15/ 2014.

[33] X. Li, X. Feng, K. Cui, F. Liu, and Y. Huang, "Designing low transmission loss silicon slot waveguide at wavelength band of high material absorption," *Optics Communications*, vol. 306, pp. 131-134, 10/1/ 2013.

[34] S. J. McNab, N. Moll, and Y. A. Vlasov, "Ultra-low loss photonic integrated circuit with membrane-type photonic crystal waveguides," *Optics Express*, vol. 11, pp. 2927-2939, 2003/11/03 2003.

[35] M. Settle, M. Salib, A. Michaeli, and T. F. Krauss, "Low loss silicon on insulator photonic crystal waveguides made by 193nm optical lithography," *Optics Express*, vol. 14, pp. 2440-2445, 2006/03/20 2006.

[36] D. Gerace and L. C. Andreani, "Low-loss guided modes in photonic crystal waveguides," *Optics Express,* vol. 13, pp. 4939-4951, 2005.

[37] L. Jiang, H. Wu, W. Jia, and X. Li, "Optimization of low-loss and wide-band sharp photonic crystal waveguide bends using the genetic algorithm," *Optik - International Journal for Light and Electron Optics,* vol. 124, pp. 1721-1725, 7// 2013.

[38] A. Wadhwa and M. Kumar, "Simplified design of low-loss and flat dispersion photonic crystal waveguide on SOI," *Optik - International Journal for Light and Electron Optics,* vol. 125, pp. 2930-2933, 6// 2014.

[39] K. Tsuruda, M. Fujita, and T. Nagatsuma, "Extremely low-loss terahertz waveguide based on silicon photonic-crystal slab," *Optics Express,* vol. 23, pp. 31977-31990, 2015.

[40] W. N. Ye and Y. Xiong, "Review of silicon photonics: history and recent advances," *Journal of Modern Optics,* vol. 60, pp. 1299-1320, 2013.

[41] Y. Xiong and W. N. Ye, "Temperature-independent vertically coupled double-ring sensor," 2012, pp. 826603-826603-6.

[42] J. H. Schmid, M. Ibrahim, P. Cheben, J. Lapointe, S. Janz, P. J. Bock, *et al.*, "Temperature-independent silicon subwavelength grating waveguides," *Optics Letters,* vol. 36, pp. 2110-2112, 2011.

[43] M. Ibrahim, J. H. Schmid, A. Aleali, P. Cheben, J. Lapointe, S. Janz, *et al.*, "Athermal silicon waveguides with bridged subwavelength gratings for TE and TM polarizations," *Optics Express,* vol. 20, pp. 18356-18361, 2012.

[44] Pogossian, S.P., Vescan, L., and Vonsovici, A., "The single-mode condition for semiconductor rib waveguides with large cross-section," *J. Lightwave Technol.*, 16, 1851–1853, 1998.

[45] K. Pei Yap, A. Delge, J. Lapointe, B. Lamontagne, J. H. Schmid, P. Waldron, B. A. Syrett, and S. Janz, "Correlation of Scattering Loss, Sidewall Roughness and Waveguide Width in Silicon-on-Insulator (SOI) Ridge Waveguides," *IEEE J. Lightw. Technol.*, vol. 27, pp. 3999–4008, 2009.

[46] A. Samarelli, M. Gnan, R. M. De la Rue, and M. Sorel, "Low propagation loss photonic wire and ring resonator devices in silicon-on-insulator using hydrogen silsesquioxane electron-beam resist," *Proc. of 14th European Conference on Integrated Optics (ECIO),* vol. ThD1, pp. 309–312, 2008.

[47] J. Cardenas, C. B. Poitras, J. T. Robinson, K. Preston, L. Chen, and M. Lipson, "Low loss etchless silicon photonic waveguides," *Optics Express*, vol. 17, pp. 4752–4757, 2009.

[48] K. Okamoto, *Fundamentals of optical waveguides*. Academic Press, 2000.

[49] B. E. A. Saleh and M. C. Teich, *Fundamentals of Photonics*. John Wiley & Sons, 1991.

[50] D. Taillaert, W. Bogaerts, P. Bienstman, T. F. Krauss, P. Van Daele, I. Moerman, S. Verstuyft, K. De Mesel, and R. Baets, "An Out-of-Plane Grating Coupler for Efficient Butt-Coupling Between Compact Planar Waveguides and Single-Mode Fibers," *IEEE J. Quantum Electron.*, vol. 38, pp. 949–955, 2002.

[51] A. V. Krishnamoorthy, R.G. Rozer, J. E. Ford, and F. E. Kiamilev, "CMOS static RAM chip with high-speed optical read and write," IEEE Phot. Tech. Lett. Vol. 9, pp. 1517-1519, Nov 1997.

[52] Silicon photonics, Optical waveguides and silicon nanophotonics pave the way to energy-efficient supercomputers, IBM Research – Zurich, https://www.zurich.ibm.com/st/photonics/silicon.html

[53] Dr. Mario Paniccia, Victor Krutul, Sean Koehl, "Introducing Intel's Advances in Silicon Photonics", Intel Research, Feb 2004. http://www.intel.com.au/content/dam/www/public/us/en/documents/intel-research/Intel_Advances_Silicon_Photonics.pdf

[54] http://www.luxtera.com

[55] P. Yong-Le and R. K. Chang, "Highly efficient prism coupling to whispering gallery modes of a square & mu;-cavity," *Technical Digest. Summaries of Papers Presented at the quantum Electronics and Laser Science Conference, 2002, QELS'02,* pp. 27-28, 2002.

[56] D. Taillaert, P. Bienstman, R. Baets, "Compact efficient broadband grating coupler for silicon-on-insulator waveguide," *Opt. Lett.* 29, 2749-51 (2004).

[57] D. Taillaert, F. Van Laere, M. Ayre, W. Bogaerts, D. Van Thourhout, P. Bienstman, R. Baets, "Grating couplers for coupling between optical fibers and nanophotonic waveguides," *Jpn. J. Appl. Phys.*, Vol. 45, No. 8A, 6071-6077 (2006).

[58] F. Van Laere, T. Claes, J. Schrauwen, S. Scheerilinck, W. Bogaerts, D. Taillaert, "Compact focusing grating coupler for silicon-on-insulator integrated circuits," *IEEE Photonics Technology Letters,* Vol. 19, pp. 1919-1921, Nov-Dec 2007.

[59] F. Van Laere, G. Roelkens, M. Ayre, J. Schrauwen, D. Taillaert, D. Van Thourhout, "Compact and Highly Efficient Grating Coupler Between Optical Fiber and Nanophotonic Waveguides," *Journal of Lightwave Technology,* Vol. 25, pp. 151-156, 2007.

[60] S. K. Selvaraja, Diedrik Vermeulen, Marc Schaekers, Erik Sleeckx, Wim Bogaerts, Gunthe Roelkens, Pieter Dumon, Dries Van Thourhout, Roel Baets, Highly efficient grating coupler between optical fiber and silicon photonic circuit, in *Conference on Lasers and Electro-Optics, Technical Digest (CD) (Optical Society of America, 2009),* paper CTuC6.

[61] P. Cheven, S. Janz, D. X. Xu, B. Lamontagne, A. Delage, and S.Tanev, "A broad-band waveguide grating coupler with subwavelength grating mirror," ," *IEEE Photonics Technology Letters,* Vol. 18, pp. 13-15, 2006.

[62] G. Roelkens, D. Vermeulen, D. Van Thourhout, S. B. R. Baets, P. G. P. Lyan, and J.-M. Fédéli, "High efficiency diffractive grating couplers for interfacing a single mode optical fiber with a nanophotonic silicon-on-insulator waveguide circuit," *Appl. Phys. Lett.* 92, 1311101 (2008).

[63] A. Sure, T. Dillon, J. Murakowski, C. Lin, D. Pustai, and D. Prather, "Fabrication and characterization of three-dimensional silicon tapers," *Optics Express,* vol. 11, pp. 3555–3561, 2003.

[64] K. D. Mesel, "Spot-size converters for photonic integrated circuits". PhD thesis, Information Technology Group, Gent University, 2002.

[65] L. Vivien, S. Laval, E. Cassan, L. Roux, and D. Pascal, "2-D taper for low loss coupling between polarization-insensitive micro waveguides and single mode optical fibers," *IEEE J. Lightw. Technol.*, vol. 21, pp. 2429–2433, 2003.

[66] T. Shoji, T. Tsuchizawa, T. Wanatabe, K. Tamada, and H. Morita, "Low loss mode size converter from 0.3 μm square Si wire waveguides to single mode fibers," *Electron. Lett.*, vol. 38, pp. 1669–1670, 2002.

[67] R. K. Winn, and J. H. Harris, "Coupling form Multimode to Single-Mode Linear waveguides Using Horn-Shaped Structures," *IEEE transactions on Microwave Theory and Techniques,* Vol. Mt23, pp. 92-97, 1975.

[68] Y. S. Shani, C. H. Henry, R. C. Kistler, R. F. Kazarinov, and K. J. Orlowsky, "Integrated Optic Adiabatic Devices on Silicon," *IEEE Journal of Quantum Electronics,* Vol. 27, pp. 556-566, Mar 1991.

[69] Daoxin Dai, Sailing He, and Hon-Ki Tsang, Bilevel Mode Converter Between a Silicon Nanowire Waveguide and a Larger Waveguide, *Journal of Lightwave Technology*, Vol. 24, No. 6, 2428, June 2006.

[70] J. H. Schimd, B. Lamontagne, P. Cheven, A. Delage, S. Janz, A. Densmore, "Mode converters for coupling to high aspect ratio silicon-on-insulator channel waveguides," *IEEE Photonics Technology Letters*, Vol. 19, pp. 855-857, May-Jun 2007.

[71] T. Aalto, K. Solehmainen, M. Harjanne, M. Kapulainen and P. Haimala, "Low-loss converters between optical silicon waveguides of different sizes and types," *IEEE Photonics Technology Letters*, Vol. 18, pp. 709-711, 2006.

[72] A. N. M. M. Choudhury, T. R. Stanczyk, D. Richardson, A. Donval, R. Oron and M. Oron, "Method of improving light coupling efficiency between optical fibers and silicon waveguides," *IEEE Photonics Technology Letters*, Vol. 17, pp. 1881-1883, 2005.

[73] L. Zimmermann, T. Tekin, H. Schroeder, P. Dumon, and W. Bogaerts, "How to bring nanophotonics to application - silicon photonics packaging*," IEEE LEOS Newsletter December 2008*, pp. 4–14, 2008.

[74] J. K. Doylend and A. P. Knights, "Design and Simulation of an Integrated Fiber-to-Chip Coupler for Silicon-on-Insulator Waveguides," *IEEE J. Sel. Topics Quantum. Electron.*, vol. 12, pp. 1363–1370, 2006.

[75] A. Barkai, A. Liu, D. Kim, R. Cohen, N. Elek, H.-H. Chang, B. H. Malik, R. Gabay, R. Jones, M. Paniccia, and N. Izhaky, "Double-Stage Taper for Coupling Between SOI Waveguides and Single-Mode Fiber," *IEEE J. Lightw. Technol.*, vol. 26, pp. 3860–3865, 2008.

[76] V. R. Almeida, R. R. Panepucci, and M. Lipson, "Nanotaper for compact mode conversion," *Optics Letters*, vol. 28, pp. 1302–1304, 2003.

[77] G. Roelkens, P. Dumon, W. Bogaerts, D. Van Thourhout, and R. Baets, "Efficient Silicon-on-Insulator Fiber Coupler Fabricated Using 248-nm- Deep UV Lithography," *IEEE Photon. Technol. Lett.*, vol. 17, pp. 2613– 2615, 2005.

[78] S. J. McNab, N. Moll, and Y. A. Vlasov, "Ultra-low loss photonic integrated circuit with membrane-type photonic crystal waveguides," *Optics Express*, vol. 11, pp. 2927–2939, 2003.

[79] T. Tsuchizawa, K. Yamada, T. Watanabe, H. Fukuda, H. Nishi, H. Shinojima, and S. Itabashi, "Spot-Size Converters for Rib-Type Silicon Photonic Wire Waveguides," *Proc. of IEEE Group IV Photonics Conference*, p. 200, 2008.

[80] M. Pu, L. Liu, H. Ou, K. Yvind, and J. M. Hvam, "Ultra-low-loss inverted taper coupler for silicon-on-insulator ridge waveguide," *Optics Com.*, vol. 283, p. 36783682, 2010.

[81] Hongzhen Wei, Jinzhong Yu, and Xiaofeng Zhang, Compact 3-dB tapered multimode interference coupler in silicon-on-insulator, Optics Letters, Vol. 26, No. 12, 878-880, June 15, 2001.

[82] Marko Galarza, Kurt De Mesel, Roel Baets, Alfredo Martı´nez, Ca´ ndido Aramburu, and Manuel Lo´ pez-Amo, Compact spot-size converters with fiber-matched antiresonant reflecting optical waveguides, Applied Optics, Vol. 42, No. 24, 4842-4846, 20 August 2003.

[83] Daoxin Dai, Jian-Jun He, and Sailing He, Compact silicon-on insulator-based multimode interference coupler with bilevel taper structure, Applied Optics, Vol. 44, No. 24, 20 August 2005.

[84] A. Delâge, S. Janz, B. Lamontagne, A. Bogdanov, D. Dalacu, D.-X. Xu, K.P. Yap, Monolithically integrated asymmetric graded and step index couplers for microphotonic waveguides, Optics Express, Vol. 14, No. 1, 148, 9 January 2006.

[85] Shyqyri Haxha, Emmanuel O. Ladely, Majlinda Mjeku, Fathi AbdelMalek, and B. M. Azizur Rahman, Optimization of compact lateral, vertical, and combined tapered spot-size converters by use of the beam-propagation method, Applied Optics, Vol. 45, No. 2, 288-295, 10 January 2006.

[86] Q. Fang, J. F. Song, S. H. Tao, M. B. Yu, G. Q. Lo, and D. L. Kwong, Low Loss (~6.45dB/cm) Sub-Micron Polycrystalline Silicon Waveguide Integrated with Efficient SiON Waveguide Coupler, Optics Express, Vol. 16, No. 9, 6425, 28 April 2008.

[87] Fang-Zheng Lin, Yi-Jen Chiu, Shun-An Tsai, and Tsu-Hsiu Wu, Laterally tapered undercut active waveguide fabricated by simple wet etching method for vertical waveguide directional coupler, Optics Express, Vol. 16, No. 11, 7588, 26 May 2008.

[88] Marko Galarza, Dries Van Thourhout, Roel Baets, and Manuel Lopez-Amo, Compact and highly-efficient polarization independent vertical resonant couplers for active-passive monolithic integration, Optics Express, Vol. 16, No. 12, 8350, 9 June 2008.

[89] Rong Sun, Mark Beals, Andrew Pomerene, Jing Cheng, Ching-yin Hong, Lionel Kimerling, Jurgen Michel, Impedance matching vertical optical waveguide couplers for dense high index contrast circuits, Optics Express, Vol. 16, No. 16, 11682, 4 August 2008.

[90] Peng Sun and Ronald M. Reano, Cantilever couplers for intra-chip coupling to silicon photonic integrated circuits, Optics Express, Vol. 17, No. 6, 4565, 16 March 2009.

[91] Qing Fang, Tsung-Yang Liow, Jun Feng Song, Chee Wei Tan, Ming Bin Yu, Guo Qiang Lo and Dim-Lee Kwong, Suspended optical fiber-to-waveguide mode size converter for Silicon photonics, Optics Express, Vol. 18, No. 8, 7763, 12 April 2010.

[92] Anatol Khilo, Miloš A. Popović, Mohammad Araghchini, and Franz X. Kärtner, Efficient planar fiber-to-chip coupler based on two-stage adiabatic evolution, Optics Express, Vol. 18, No. 15, 15790, 19 July 2010.

[93] Ter-Hoe Loh, Qian Wang, Jie Zhu, Keh-Ting Ng, Yi-Cheng Lai, Yingyan Huang, and Seng-Tiong Ho, Ultra-compact multilayer Si/SiO2 GRIN lens mode-size converter for coupling single-mode fiber to Si-wire waveguide, Optics Express, Vol. 18, No. 21, 21519, 11 October 2010.

[94] H. Y. Xu, B. Zhang, G. Barbastathis, and H. D. Sun, Compact optical waveguide coupler using homogeneous uniaxial medium, J. Opt. Soc. Am. B, Vol. 28, No. 11, 2633, November 2011.

[95] Peng Sun and Ronald M. Reano, Vertical chip-to-chip coupling between silicon photonic integrated circuits using cantilever couplers, Optics Express, Vol. 19, No. 5, 4722, February 2011.

[96] Michael Wood, Peng Sun, and Ronald M. Reano, Compact cantilever couplers for low-loss fiber coupling to silicon photonic integrated circuits, Optics Express, Vol. 20, No. 1, 164, 2 January 2012.

[97] Petr Markov, Jason G. Valentine, and Sharon M. Weiss, Fiber-to-chip coupler designed using an optical transformation, Optics Express, Vol. 20, No. 13, 14705, 18 June 2012.

[98] Kazuo Shiraishi, Hidehiko Yoda, and Chen S. Tsai, A two-port polarization-insensitive coupler module between single-mode fiber and silicon-wire waveguide, Optics Express, Vol. 20, No. 22, 24370, 22 October 2012.

[99] Ibrahim Murat Soganci, Antonio La Porta and Bert Jan Offrein, Flip-chip optical couplers with scalable I/O count for silicon photonics, Optics Express, Vol. 21, No. 13, 16075, 1 July 2013.

[100] Hyundai Park, Sanggi Kim, Jaegyu Park, Jiho Joo, and Gyungock Kim, A fiber-to-chip coupler based on Si/SiON cascaded tapers for Si photonic chips, Optics Express, Vol. 21, No. 24, 29313, 2 December 2013.

[101] Doris Keh Ting Ng, Qian Wang, Jing Pu, Kim Peng Lim, Yongqiang Wei, Yadong Wang, Yicheng Lai, and Seng Tiong Ho, Demonstration of heterogeneous III–V/Si integration with a compact optical vertical interconnect access, Optics Letters, Vol. 38, No. 24, 5353, December 15, 2013.

[102] Kaisheng Chen, Zhuyang Huang, Gaoneng Dong, and Xinliang Zhang, Design of an ultra-short coupler in an asymmetric twin-waveguide structure using transformation optics, Applied Optics, Vol. 53, No. 33, 7831, 20 November 2014.

[103] Lianxi Jia1, Junfeng Song, Tsung-Yang Liow, Xianshu Luo, Xiaoguang Tu, Qing Fang, Sing-Chee Koh, Mingbin Yu, and Guoqiang Lo, Mode size converter between high- index-contrast waveguide and cleaved single mode fiber using SiON as intermediate material, Optics Express, Vol. 22, No. 19, 23652, 22 September 2014.

[104] Yunfei Fu, Tong Ye, Weijie Tang, and Tao Chu, Efficient adiabatic silicon-on-insulator waveguide taper, Photon. Res., Vol. 2, No. 3, A41, June 2014.

[105] Qiangsheng Huang, Jianxin Cheng, Liu Liu, Yongbo Tang, and Sailing He, Ultracompact tapered coupler for the Si/III–V heterogeneous integration, Applied Optics, Vol. 54, No. 14, 4327, May 10 2015.

[106] Yuriko Maegami, Ryohei Takei, Emiko Omoda, Takeru Amano, Makoto Okano, Masahiko Mori, Toshihiro Kamei, and Youichi Sakakibara, Spot-size converter with a SiO_2 spacer layer between tapered Si and SiON waveguides for fiber-to-chip coupling, Optics Express, Vol. 23, No. 16, 21287, 10 Aug 2015.

[107] Pavel Cheben, Jens H. Schmid, Shurui Wang, Dan-Xia Xu, Martin Vachon, Siegfried Janz, Jean Lapointe, Yves Painchaud, and Marie-Josée Picard, Broadband polarization independent nanophotonic coupler for silicon waveguides with ultra-high efficiency, Optics Express, Vol. 23, No. 17, 22553, 24 Aug 2015.

[108] Martin Papes, Pavel Cheben, Daniel Benedikovic, Jens H. Schmid, James Pond, Robert Halir, Alejandro Ortega-Moñux, Gonzalo Wangüemert-Pérez, Winnie N. Ye, Dan-Xia Xu, Siegfried Janz, Milan Dado, and Vladimír Vašinek, Fiber-chip edge

coupler with large mode size for silicon photonic wire waveguides, Optics Express, Vol. 24, No. 5, 5026, 7 Mar 2016.

[109] S¨oren Dhoore, Sarah Uvin, Dries Van Thourhout, Geert Morthier and Gunther Roelkens, Novel adiabatic tapered couplers for active III-V/SOI devices fabricated through transfer printing, Optics Express, Vol. 24, No. 12, 12976, 13 Jun 2016.

[110] Arnab Dewanjee, Jan Niklas Caspers, James Stewart Aitchison, and Mo. Mojahedi, Demonstration of a compact bilayer inverse taper coupler for Si-photonics with enhanced polarization insensitivity, Optics Express, Vol. 24, No. 25, 28194, 12 Dec 2016.

[111] Sujith Chandran, Meenatchi Sundaram, Sreevatsa Kurudi, and Bijoy Krishna Das, Design and fabrication of surface trimmed silicon-on-insulator waveguide with adiabatic spot-size converters, Applied Optics, Vol. 56, No. 6, 1708, February 20 2017.

[112] Hossein Eskandari, Mohammad Saeed Majedi, and Amir Reza Attari, Reflectionless compact nonmagnetic optical waveguide coupler design based on transformation optics, Applied Optics, Vol. 56, No. 20, 5599, July 10 2017.

[113] Purnima Sethi, Anubhab Haldar, and Shankar Kumar Selvaraja, Ultra-compact low-loss broadband waveguide taper in silicon-on-insulator, *Optics Express*, Vol. 25, No. 9, 10196, 1 May 2017.

[114] M. L. Dakss, L. Kuhn, P. F. Heidrich and B. A. Scott, "Grating Coupler for Efficient Excitation of Optical Guided Waves in Thin Films," *Applied Physics Letters,* Vol. 16, pp. 523-525, 1970.

[115] T. Tamir and H. L. Bertoni, "Lateral Displacement of Optical Beams at Multilayered and Periodic Structures," *Journal of Optical Society of America,* Vol. 61, pp. 1397-1413, 1971.

[116] R. Ulrich, "Efficiency of optical-grating couplers," *Journal of Optical Society of America,* Vol. 63, pp. 1419-1431, 1973.

[117] F. T. Stone and S. Austin, "Theoretical and Experimental-Study of Effect of Loss on Grating Couplers," *IEEE Journal of Quantum Electronics,* Vol. 12, pp. 727-732, 1976.

[118] H. W. Weber, R. Ulrich, E. A. Chandross and W. J. Tomlinson, "Light Guiding Structures of Photoresist Films," *Applied Physics Letters,* Vol. 20, pp. 143-145, 1972.

[119] T. Tamir and S. Peng, “Analysis and design of grating couplers,” *Applied Physics A: Materials Science & Processing,* Vol. 14, pp. 235-254, 1977.

[120] C. Ghizoni, C. Bor-Uei and T. Chung, “Theory and experiments on grating couplers for thin-films waveguides,” *IEEE Journal of Quantum Electronics,* Vol. 12, pp. 69-73, 1976.

[121] J. M. Hammer, R. A. Bartolini, A. Miller and C. C. Neil, “Optical grating coupling between low index fibers and high index films waveguides,” *Applied Physics Letters,* Vol. 28, pp. 192-194, 1976.

[122] C. Bulmer and M. Wilson, “Single mode grating coupling between thin-film and fiber optical waveguides,” *IEEE Journal of Quantum Electronics,* Vol. 14, pp. 741-749, 1978.

[123] H. Sun-Yan and L. Sing, “Blazed garting couplers on LiNbO3 optical channel waveguides and their applications to integrated optical circuits,” *Journal of Lightwave. Technology.*, vol. 4, pp. 1304–1310, 1986.

[124] R. C. Alferness, T. L. Koch, L. L. Buhl, F. Storz, F. Heisman and M. J. R. Martyak, “Grating assisted InGaAsP/InP vertical codirectional coupler filter,” *Applied Physics Letters,* Vol. 55, pp. 2011-2013, 1989.

[125] J. V. Galan, P. Sanchis, J. Blasco, J. Marti, “Study of High Efficiency Grating Couplers for Silicon-Based Horizontal Slot Waveguides,” *IEEE Photon. Technol. Lett.,* Vol.20, 985-987, 2008.

[126] R. M. Emmons, B. N. Kurdi, and D. G. Hall, “Buried-oxide silicon-on-insulator structures. I. Optical waveguide characteristics,” *IEEE Journal of Quantum Electronics,* Vol. 28, pp. 157-163, 1992.

[127] R. M. Emmons, and D. G. Hall, “Buried-oxide silicon-on-insulator structures. II. Waveguide grating couplers,” *IEEE Journal of Quantum Electronics,* Vol. 28, pp. 164-175, 1992.

[128] M. Hagberg, N. Eriksson, T. Kjellberg and A. Larsson, “Dependence of output coupling efficiency on detuning in surface grating output couplers,” *Optics Letters,* Vol. 20, pp. 180-182, 1995.

[129] A. Hardy, D. F. Welch and W. Streifer, “Analysis of second-order gratings,” *IEEE Journal of Quantum Electronics,* Vol. 25, pp. 2096-2105, 1989.

[130] W. Streifer, D. Scifres and R. Burnham, “Analysis of grating-coupled radiation in GaAs:GaAlAs lasers and waveguides,” *IEEE Journal of Quantum Electronics,* Vol. 12, pp. 422-428, 1976.

[131] M. Matsumoto, “Analysis of the blazing effect in second-order gratings,” *IEEE Journal of Quantum Electronics,* Vol. 28, pp. 2016-2023, 1992.

[132] D. Mehuys, A. Hardy, D. F. Welch, R. G. Waarts and R. Parke, “Analysis of detuned second-order grating output couplers with an integrated superlattice reflector,” *IEEE Photonics Technology Letters,* Vol. 3, pp. 342-344, 1991.

[133] K.C. Chang, V. Shah and T. Tamir, “Scattering and guiding of waves by dielectric grating with arbitrary profiles,” *Journal of Optical Society of America,* Vol. 70, pp. 804-813, 1980.

[134] T. W. Ang, G. T. Reed, A. Vonsovici, A. G. R. Evans, P. R. Routley and M. R. Josey, “Effects of grating heights on highly efficient unibond SOI waveguide garting couplers,” *IEEE Photonics Technology Letters,* Vol. 12, pp. 59-61, 2000.

[135] T. W. Ang, “Optical Grating Couplers in Silicon on Insulator,” PhD Thesis, School of Electronic, Information Technology and Mathematics, Surrey, Guildford, 1999.

[136] K.C. Chang and T. Tamir, “Simplified approach to surface-wave scattering by blazed dielectric gratings,” *Applied Optics,* Vol. 19, pp. 282-288, 1980.

[137] K.C. Chang and T. Tamir, “Bragg-reflection approach for blazed dielectric gratings,” *Optics Communications,* Vol. 26, pp. 327-330, 1978.

[138] L.Vivien, D. Pascal, S. Lardenois, D. Martis-Morini, E. Cassan, F. Grillot, et al., “Light injection in SOI microwaveguides using high-efficiency grating couplers,” *Journal of Lightwave. Technology.*, vol. 24, pp. 3810–3815, 2006.

[139] C. Kopp and A. Chelnokov, “Fiber grating couplers for silicon nanophotonic circuits: Design modelling methodology and fabrication tolerances,” *Optics Communications,* Vol. 282, pp. 4242-4248, 2009.

[140] R. Parke, R. Waarts, D. F. Welch, A. Hardy, and W. Streifer, “High efficiency, high uniformity, grating coupled surface emitting lasers,” Electronics Letters, Vol. 26, pp. 125-127, 1990.

[141] N. Eriksson, M. Hagberg, and A. Larsson, “Highly efficient grating-coupled surface-emitters with single outcoupling elements,” *IEEE Photonics Technology Letters,* Vol. 7, pp. 1394-1396, 1995.

[142] C. Alonso-Ramos, A. Ortega-Moñux, L. Zavargo-Peche, R. Halir, J. de Oliva-Rubio, I. Molina-Fernández, P. Cheben, D.-X. Xu, S. Janz, N. Kim, B. Lamontagne, “Single-etch grating coupler for micrometric silicon rib waveguides”, *Optics Letters,* Vol. 36, No. 14, 2647-2649, 2011.

[143] Neil Na, Harel Frish, I-Wei Hsieh, Oshrit Harel, Roshan George, Assia Barkai, Haisheng Rong, "Efficient broadband silicon-on-insulator grating coupler with low backreflection", *Optics Letters*, Vol. 36, No. 11, 2101-2103, 2011.

[144] B. B. Bakir, A. Vazquez de Gyves, R. Orobtchouk, P. Lyan, C. Porzier, A. Roman, and J.-M. Fedeli, "Low-Loss (<1dB) and Polarization- Insensitive Edge Fiber Couplers Fabricated on 200-mm Silicon-on-Insulator Wafers," *IEEE Photon. Technol. Lett.*, vol. 22, pp. 739–741, 2010.

[145] F. Van Laere, G. Roelkens, J. Schrauwen, D. Taillaert, P. Dumon, W. Bogaerts, D. Van Thourhout, and R. Baets, "Compact Grating Couplers Between Optical Fibers and Silicon-on-Insulator Photonic Wire Waveguides with 69 Coupling Efficiency," *Proc. of Optical Fiber Communication Conference and Exposition and The National Fiber Optic Engineers Conference*, Technical Digest, p. PDP15, 2006.

[146] G. Roelkens, D. Van Thourhout, and R. Baets, " High efficiency Silicon-on-Insulator grating coupler based on a poly-Silicon overlay," *Optics Express*, vol. 14, pp. 11622–11630, 2006.

[147] D. Vermeulen, S. Selvaraja, P. Verheyen, G. Lepage, W. Bogaerts, P. Absil, D. Van Thourhout, and G. Roelkens, "High-efficiency fiber-to-chip grating couplers realized using an advanced CMOS-compatible Silicon-On-Insulator platform," *Optics Express*, vol. 18, pp. 18278–18283, 2010.

[148] Xia Chen, Chao Li, Christy K. Y. Fung, Stanley M. G. Lo, and Hon K. Tsang, Apodized Waveguide Grating Couplers for Efficient Coupling to Optical Fibers, *IEEE Photonics Technology Letters*, Vol. 22, No. 15, 1156, August 1, 2010.

[149] Zhe Xiao,Feng Luan,Tsung-Yang Liow, Jing Zhang, Ping Shum, "Design for broadband high-efficiency grating couplers", *Optics Letters*, Vol. 37, No. 4, 2012.

[150] Christopher R. Doerr, Long Chen, Young-Kai Chen, and Larry L. Buhl, "Wide Bandwidth Silicon Nitride Grating Coupler", *IEEE Photon. Technol. Lett.*, vol. 22, no. 19, 2010.

[151] X. Chen, C. Fung, Y. M. Chen, and H. K. Tsang, "Subwavelength Waveguide Grating Coupler for Fiber-to-Chip Coupling on SOI with 80nm 1dB-Bandwidth" in *Proceedings of IEEE Conference on Lasers and Electro-Optics*, 2011.

[152] P. Cheben, D.-X. Xu, S. Janz, and A. Densmore, "Subwavelength waveguide grating for mode conversion and light coupling in integrated optics," *Optics Express*, vol. 14, pp. 4695–4702, 2006.

[153] Xiaochuan Xu, Harish Subbaraman, John Covey, David Kwong, Amir Hosseini, "Complementary metal–oxide–semiconductor compatible high efficiency subwavelength grating couplers for silicon integrated photonics", *Appl. Phys. Lett.* 101, 031109, 2012.

[154] Zhenzhou Cheng, Xia Chen, Chi Yan Wong, Ke Xu, Hon Ki Tsang, "Apodized focusing subwavelength grating couplers for suspended membrane waveguides", *Appl. Phys. Lett.* 101, 101104, 2012.

[155] P. Dumon, W. Bogaerts, D. Van Thourhout, D. Taillaert, R. Baets, J. Wouters, S. Beckx, and P. Jaenen, "Compact wavelength router based on a Silicon-on-insulator arrayed waveguide grating pigtailed to a fiber array," *Optics Express*, vol. 14, pp. 664–669, 2006.

[156] B. Wang, J. Jiang, and G. P. Nordin, "Compact slanted grating couplers," *Optics Express*, vol. 12, pp. 3313–3326, 2004.

[157] B. Wang, J. Jiang, D. M. Chambers, J. Cai, and G. P. Nordin, "Stratified waveguide grating coupler for normal fiber incidence," *Optics Letters*, vol. 30, pp. 845–847, 2005.

[158] G. Roelkens, D. V. Thourhout, and R. Baets, "High efficiency grating coupler between silicon-on-insulator waveguides and perfectly vertical optical fibers," *Optics Letters*, vol. 32, pp. 1495–1497, 2007.

[159] C. Gunn, "Fully Integrated VLSI CMOS and Photonics," *IEEE Symposium on VLSI Technology*, pp. 6–9, 2007.

[160] J. V. Galan, P. Sanchis, G. Sanchez, and J. Marti, "Polarization insensitive low-loss coupling technique between SOI waveguides and high mode field diameter single-mode fibers," *Optics Express*, vol. 15, pp. 7058–7065, 2007.

[161] C. Peng and W. A. Challener, "Input-grating couplers for narrow Gaussian beam: influence of groove depth," *Optics Express*, vol. 12, pp. 6481–6490, 2004.

[162] D. Van Thourhout, G. Roelkens, R. Baets, W. Bogaerts, J. Brouckaert, P. DEbackere, P. Dumon, S. Scheerlinck, J. Schrauwen, D. Taillaert, F. Van Laere, and J. Van Campenhout, "Coupling mechanisms for a heterogeneus silicon nanowire platform," *Semicond. Sci. Technol.*, vol. 23, p. 064004, 2008.

[163] Frederik Van Laere, Günther Roelkens, Melanie Ayre, Jonathan Schrauwen, Dirk Taillaert, Dries Van Thourhout, Thomas F. Krauss, and Roel Baets, Compact and Highly Efficient Grating Couplers Between Optical Fiber and Nanophotonic Waveguides, *Journal of Lightwave Technology*, Vol. 25, No. 1, 151, January 2007.

[164] Robert Halir, Pavel Cheben, Siegfried Janz, Dan-Xia Xu, Íñigo Molina-Fernández, and Juan G. Wangüemert-Pérez, Waveguide grating coupler with subwavelength microstructures, *Optics Letters*, Vol. 34, No. 9, 1408, May 1, 2009.

[165] D. Vermeulen, Y. De Koninck, Y. Li, E. Lambert, W. Bogaerts, R. Baets, and G. Roelkens, Reflectionless grating couplers for Silicon-on-Insulator photonic integrated circuits, *Optics Express*, Vol. 20, No. 20, 22278, 24 September 2012.

[166] Shiqian Shao and Yi Wang, Highly compact polarization-independent grating coupler, *Optics Letters*, Vol. 35, No. 11, 1834, June 1, 2010.

[167] C. Alonso-Ramos, L. Zavargo-Peche, A. Ortega-Moñux, R. Halir, I. Molina-Fernández, and P. Cheben, Polarization-independent grating coupler for micrometric silicon rib waveguides, *Optics Letters*, Vol. 37, No. 17, 3663, September 1, 2012.

[168] Chao Li, Huijuan Zhang, Mingbin Yu, and G. Q. Lo, CMOS-compatible high efficiency double-etched apodized waveguide grating coupler, *Optics Express*, Vol. 21, No. 7, 7868, 8 April 2013.

[169] Yunhong Ding, Haiyan Ou, and Christophe Peucheret, Ultrahigh-efficiency apodized grating coupler using fully etched photonic crystals, *Optics Letters*, Vol. 38, No. 15, 2732, August 1, 2013.

[170] Wesley D. Sacher, Ying Huang, Liang Ding, Benjamin J. F. Taylor, Hasitha Jayatilleka, Guo-Qiang Lo, and Joyce K. S. Poon, Wide bandwidth and high coupling efficiency Si_3N_4-on-SOI dual-level grating coupler, *Optics Express*, Vol. 22, No. 9, 10938, 5 May 2014.

[171] Yun Wang, Xu Wang, Jonas Flueckiger, Han Yun, Wei Shi, Richard Bojko, Nicolas A. F. Jaeger, and Lukas Chrostowski, Focusing sub-wavelength grating couplers with low back reflections for rapid prototyping of silicon photonic circuits, *Optics Express*, Vol. 22, No. 17, 20652, 25 August 2014.

[172] Zhenzhou Cheng and Hon Ki Tsang, Experimental demonstration of polarization-insensitive air-cladding grating couplers for silicon-on-insulator waveguides, *Optics Letters*, Vol. 39, No. 7, 2206, April 1, 2014.

[173] Yunhong Ding, Christophe Peucheret, Haiyan Ou, and Kresten Yvind, Fully etched apodized grating coupler on the SOI platform with −0.58 dB coupling efficiency, *Optics Letters*, Vol. 39, No. 18, 5348, September 15, 2014.

[174] C. Alonso-Ramos, P. Cheben, A. Ortega-Moñux, J. H. Schmid,2 D.-X. Xu, and I. Molina-Fernández, Fiber-chip grating coupler based on interleaved trenches with

directionality exceeding 95%, *Optics Letters*, Vol. 39, No. 18, 5351, September 15, 2014.

[175] Pavel Cheben, Jens H. Schmid, Shurui Wang, Dan-Xia Xu, Martin Vachon, Siegfried Janz, Jean Lapointe, Yves Painchaud, and Marie-Josée Picard, Broadband polarization independent nanophotonic coupler for silicon waveguides with ultra-high efficiency, *Optics Express*, Vol. 23, No. 17, 22553, 24 Aug 2015.

[176] Daniel Benedikovic, Pavel Cheben, Jens H. Schmid, Dan-Xia Xu, Boris Lamontagne, Shurui Wang, Jean Lapointe, Robert Halir, Alejandro Ortega-Mo˜nux, Siegfried Janz, and Milan Dado, Subwavelength index engineered surface grating coupler with sub-decibel efficiency for 220-nm silicon-on-insulator waveguides, *Optics Express*, Vol. 23, No. 17, 22628, 24 Aug 2015.

[177] Jinghui Zou, Yu Yu, Mengyuan Ye, Lei Liu, Shupeng Deng, and Xinliang Zhang, Ultra efficient silicon nitride grating coupler with bottom grating reflector, *Optics Express*, Vol. 23, No. 20, 26305, 5 Oct 2015.

[178] Daniel Benedikovic, Carlos Alonso-ramos, Pavel Cheben, Jens H. Schmid, Shurui Wang, Dan-xia Xu, Jean Lapointe, Siegfried Janz, Robert Halir, Alejandro Ortega-moñux, J. Gonzalo Wangüemert-pérez, Iñigo Molina-fernández, Jean-marc Fédéli, Laurent Vivien, and Milan Dado, High-directionality fiber-chip grating coupler with interleaved trenches and subwavelength index-matching structure, *Optics Letters*, Vol. 40, No. 18, 4190, September 15 2015.

[179] Xiangjie Zhao, Danping Li, Cheng Zeng, Ge Gao, Zengzhi Huang, Qinzhong Huang, Yi Wang, and Jinsong Xia, Compact Grating Coupler for 700-nm Silicon Nitride Strip Waveguides, *Journal of Lightwave Technology*, Vol. 34, No. 4, 1322, February 15, 2016.

[180] Fan Qi, Qingyan Ma, Yufei Wang, and Wanhua Zheng, Large-aperture subwavelength grating couplers, *Applied Optics*, Vol. 55, No. 11, 2960, April 10 2016.

[181] Masatoshi Tokushima and Jun Ushida, Anti-phase reflection coating maximizing the directionality of grating couplers, *Optics Express*, Vol. 24, No. 10, 11075, 2016.

[182] Daniel Benedikovic, Carlos Alonso-Ramos, Pavel Cheben, Jens H. Schmid, Shurui Wang, Robert Halir, Alejandro Ortega-Moñux, Dan-Xia Xu, Laurent Vivien, Jean Lapointe, Siegfried Janz, and Milan Dado, Single-etch subwavelength engineered fiber-chip grating couplers for 1.3 μm datacom wavelength band, *Optics Express*, Vol. 24, No. 12, 12893, 13 Jun 2016.

[183] Liu Liu, Jianhao Zhang, Chenzhao Zhang, Siya Wang, Chichao Jin, Yujie Chen, Kaixuan Chen, Tuowen Xiang, and Yaocheng Shi, Silicon waveguide grating coupler for perfectly vertical fiber based on a tilted membrane structure, *Optics Letters*, Vol. 41, No. 4, 820, February 15 2016.

[184] Xia Chen, David J. Thomson, Lee Crudginton, Ali Z. Khokhar, and Graham T. Reed, Dual-etch apodised grating couplers for efficient fibre-chip coupling near 1310 nm wavelength, *Optics Express*, Vol. 25, No. 15, 17864, 24 Jul 2017.

[185] Yun Wang, Luhua Xu, Amar Kumar, Yannick D'mello, David Patel, Zhenping Xing, Rui Li, Md Ghulam Saber, Eslam El-Fiky, and David V. Plant, Compact single-etched sub-wavelength grating couplers for O-band application, *Optics Express*, Vol. 25, No. 24, 30582, 27 Nov 2017.

[186] Daniel Benedikovic, Carlos Alonso-Ramos, Diego Pérez-Galacho, Sylvain Guerber, Vladyslav Vakarin, Guillaume Marcaud, Xavier Le Roux, Eric Cassan, Delphinemarris-Morini, Pavel Cheben, Frédéric Boeuf, Charles Baudot, and Laurent Vivien, L-shaped fiber-chip grating couplers with high directionality and low reflectivity fabricated with deep-UV lithography, *Optics Letters*, Vol. 42, No. 17, 3439, September 1 2017.

[187] G. Roelkens, D. Vermeulen, F. Van Laere, S. Selvaraja, S. Scheerlinck, D. Taillaert, W. Bogaerts, P. Dumon, D. Van Thourhout, and R. Baets, "Bridging the Gap Between Nanophotonic Waveguide Circuits and Single Mode Optical Fibers Using Diffractive Grating Structures," *J. Nanosci. Nanotechnol.*, vol. 10, p. 15511562, 2010.

[188] Jinghui Zou, Yu Yu, and Xinliang Zhang, Two-dimensional grating coupler with a low polarization dependent loss of 0.25 dB covering the C-band, *Optics Letters*, Vol. 41, No. 18, 4206, September 15 2016.

[189] Xia Chen and Hon K. Tsang, Polarization-independent grating couplers for silicon-on-insulator nanophotonic waveguides, *Optics Letters*, Vol. 36, No. 6, March 15, 2011.

[190] B. S. Eastwood "Francesco Maria Grimaldi," *Dictionary of Scientific Biography*, Gillispie, Charles. C. ed., 16 vols., vol 5. pp. 543-544, New York: Charles Scribner and Sons, 1972.

[191] E. Hecht and A. Zajac, *Optics,* Addison Wesley, Reading, MA, 1975, pp. 329-393.

[192] R. Waldhausl et al., "Efficient coupling into polymer waveguides by gratings," *Applied Optics*, vol. 36, no. 36, pp. 9383-9390, Dec 1997.

[193] J. H. Harris et al., "Theory and Design of Periodic Couplers," *Applied Optics*, vol. 11, no. 10, pp. 2234-2241, Oct 1972.

[194] D. F. G. Gallagher and T. P. Felici, "Eigenmode expansion methods for simulation of optical propagation in photonics - Pros and cons," in *Conference on Integrated Optics - Device, Materials and Technologies VII*, San Jose, CA, 2003, pp. 69-82.

[195] Dirk Taillaert, "Grating couplers as Interface between Optical Fibers and Nanophotonic Waveguides," Ph.D. dissertation, INTEC, Ghent Univ., Ghent, Netherlands, 2004.

[196] V. A. Sychugov et al., "Optimization and control of grating coupling to or from a silicon-based optical waveguide," *Optical Engineering*, vol. 35, no. 11, pp. 3092-3100, Nov 1996.

[197] T.Tsuchizawa, K.Yamada, H.Fukuda, T.Watanabe, J.Takahashi, M.Takahashi,T.Shoji, E.Tamechika, S.Itabashi and H.Morita, "Microphotonics Devices Based on Silicon Microfabrication Technology", *IEEE Journal Of Selected Topics In Quantum Electronics*, Vol. 11, no. 1, pp. 232-240, 2005.

[198] Laurent Vivien, Daniel Pascal, Sebastien Lardenois, Delphine Marris-Morini, Eric Cassan, Frédéric Grillot, Suzanne Laval, Jean-Marc Fédéli, and Loubna El Melhaoui, "Light Injection in SOI Microwaveguides Using High-Efficiency Grating Couplers", *Journal Of Lightwave Technology*, Vol. 24, no. 10, pp.3810-3815, October 2006.

[199] D. Lee, *Electromagnetic principles of integrated optics*. John Wiley & Sons, New York, 1986. ISBN 0-471-87978-9.

[200] J. A. Kong, Electromagnetic Wave Theory, EMW Publishing, Cambridge, MA, 2000.

[201] K.Kawano and T. Kitoh, "Introduction to Optical Waveguide Analysis: Solving Maxwell's Equations and the Schrödinger Equation", John Wiley & Sons, 2001.

[202] K. S. Yee, Numerical solution of initial boundary value problems involving Maxwell's equations in isotropic media, *IEEE Transactions on Antenna and Propagation*, Ap-14(3): 302, 1966.

[203] Dirk Taillaert, Peter Bienstman, and Roel Baets, Compact efficient broadband grating coupler for silicon-on-insulator waveguides, *Optics Letters*, Vol. 29, No. 23, 2749, December 1, 2004.

[204] J.P. Berenger, "A Perfectly Matched Layer for the Absorption of Electromagnetic Waves", *Journal of Computational Physics*, Vol. 114, pp. 185-200, 1994.

[205] Haishan Sun, Antao Chen, Attila Szep, and Larry R. Dalton, “Efficient fiber coupler for vertical silicon slot waveguides,” *Opt. Express*, 17(25), 22571-22577, 2009.

[206] S. McNab, N. Moll, and Y. Vlasov, “Ultra-low loss photonic integrated circuit with membrane-type photonic crystal waveguides,” *Opt. Express*, 11, 2927-2939, 2003.

[207] Tapas Kumar Saha and Weidong Zhou, “High efficiency diffractive grating coupler based on transferred silicon nanomembrane overlay on photonicwaveguide, ” *J. Phys. D: Appl. Phys.* 42, 085115, 1-9, 2009.

[208] Chao Qiu, Zhen Sheng, Le Li, Albert Pang, Zhiqi Wang, Aimin Wu, Xi Wang, Shichang Zou, and Fuwan Gan, “Poly-Silicon Grating Couplers for Efficient Coupling With Optical Fibers,” *IEEE Photon. Technol. Lett.* 24, 1614-1617, 2012.

[209] Liu Liu, Minhao Pu, Kresten Yvind, and Jørn M. Hvam, "High-efficiency, large bandwidth silicon-on-insulator grating coupler based on a fully-etched photonic crystal structure," *Appl. Phys. Lett.*, vol. 96, pp. 0511261-3, 2010.

[210] Mikael Antelius, Kristinn B. Gylfason, Hans Sohlstrom, “An apodized SOI waveguide-to-fiber surface grating coupler for single lithography silicon photonics,” *Opt. Express* 19, 3592-3598, 2011.

[211] Qiuhang Zhong, Venkat Veerasubramanian, Yun Wang, Wei Shi, David Patel, Samir Ghosh, Alireza Samani, Lukas Chrostowski, Richard Bojko, David V. Plant, “Focusing-curved subwavelength grating couplers for ultra-broadband silicon photonics optical interfaces,” *Opt. Express* 22, 18224-18231, 2014.

[212] Wissem Sfar Zaoui, Andreas Kunze, Wolfgang Vogel, Manfred Berroth, Jörg Butschke, Florian Letzkus, Joachim Burghartz, “Bridging the gap between optical fibers and silicon photonic integrated circuits,” *Opt. Express* 22, 1277-1286, 2014.

[213] Yunhong Ding, Haiyan Ou, Christophe Peucheret, “Ultrahigh-efficiency apodized grating coupler using fully etched photonic crystals,” *Opt. Lett.* 38, 2732-2734, 2013.

[214] Li Yu,LuLiu,ZhipingZhou, XingjunWang, “High efficiency binary blazed grating coupler for perfectly-vertical and near-vertical coupling in chip level optical interconnections,” *Optics Communications* 355, 161-166, 2015.

[215] F. Van Laere et al., "Compact Focusing Grating Couplers Between Optical Fibers and Silicon-On-Insulator Photonic Wire Waveguides," in *Optical Fiber Communication and the National Fiber Optic Engineers Conference*, Anaheim, CA, 2007, pp. 1-3.

[216] Wissem Sfar Zaoui, María Félix Rosa, Wolfgang Vogel, Manfred Berroth, Jörg Butschke, Florian Letzkus, "Cost-effective CMOS-compatible grating couplers with backside metal mirror and 69% coupling efficiency," *Opt. Express* 20, 238-243, 2012.

[217] Shankar Kumar Selvaraja, Diedrik Vermeulen, Marc Schaekers, Erik Sleeckx, Wim Bogaerts, Gunther Roelkens, Pieter Dumon, Dries Van Thourhout, Roel Baets, "Highly efficient grating coupler between optical fiber and silicon photonic circuit," in *Conference on Lasers and Electro-Optics, Technical Digest (CD) (Optical Society of America, 2009),* paper CTuC6.

[218] H. Hertz, "The forces of electric oscillations, treated according to Maxwell's theory," Wiedemanns Ann. 36, 1 (1889), translated and reprinted in Electric Waves (Dover, New York, 1962), pp. 137-159.

[219] I. E. Tamm and V. L. Ginzburg, "Theory of electromagnetic processes in a layered core," *Izv. Akad. Nauk SSSR* 7, pp.30–51, 1943.

[220] S. M. Rytov, "Electromagnetic Properties of a Finely Stratified Medium," *Sov. Phys.* JETP **2**, 466 475, 1956.

[221] C. Bernhard and W. H. Miller, "A corneal nipple pattern in insect compound eyes" *Acta Physiol. Scand.* 56, pp. 385–386, 1962.

[222] P. Clapham and M. Hutley, "Reduction of lens reflection by the "moth eye" principle," *Nature* 244, pp. 281–282, 1973.

[223] J. N.Mait and D.W. Prather, "New Principle for Optical Filters," *Selected Papers on Subwavelength Diffractive Optics* (SPIE Optical Engineering Press, Bellingham, WA, 2001).

[224] P. Yeh, "A new optical model for wire grid polarizers," *Opt. Commun.* 26, pp. 289–292, 1978.

[225] E. B. Grann, M. G. Moharam, and D. A. Pommet, "Artificial uniaxial and biaxial dielectrics with use of two-dimensional subwavelength binary gratings," *J. Opt. Soc. Am. A* 11, 2695–2703 (1994).

[226] R. C. Enger and S. K. Case, "Optical elements with ultrahigh spatial-frequency surface corrugations," *Appl. Opt.* 22, 3220–3228, 1983.

[227] M. E. Motamedi, W. H. Southwell, and W. J. Gunning, "Antireflection surfaces in silicon using binary optics technology," *Appl. Opt.* 31, 4371–4376, 1992.

[228] J. Van der Ziel, "Phase−matched harmonic generation in a laminar structure with wave propagation in the plane of the layers," *Appl. Phys. Lett.* 26, 60–62, 1975.

[229] A. Fiore, V. Berger, E. Rosencher, P. Bravetti, and J. Nagle, "Phase matching using an isotropic nonlinear optical material," *Nature* 391, 463–466, 1998.

[230] R. Halir, A. Maese-Novo, A. Ortega-Moñux, I. Molina-Fernández, J.G.Wangüemert-Pérez, P. Cheben, D.-X. Xu, J. H. Schmid, and S. Janz, "Colorless directional coupler with dispersion engineered sub-wavelength structure," *Optics Express*, Vol. 20, pp. 13470-13477, 2012.

[231] C. Alonso-Ramos, P. Cheben, A. Ortega-Moñux, J. H. Schmid, D.-X. Xu, and I. Molina-Fernández, "Fiber-chip grating coupler based on interleaved trenches with directionality exceeding 95%," *Optics Letters*, Vol. 39, Issue 18, pp. 5351-5354, 2014.

[232] Alejandro Ortega-Moñux, Carlos Alonso-Ramos, Alejandro Maese-Novo, Robert Halir, Luis Zavargo-Peche, Diego Pérez-Galacho, Iñigo Molina-Fernández, J. Gonzalo Wangüemert-Pérez, Pavel Cheben, Jens H. Schmid, Jean Lapointe, Danxia Xu, and Siegfried Janz, "An ultra-compact multimode interference coupler with a subwavelength grating slot,", *Laser and Photonics Review*, Vol. 7, pp. L12-L15, 2013.

[233] R. Halir, A. Maese-Novo, A. Ortega-Moñux, I. Molina-Fernández, J.G.Wangüemert-Pérez, P. Cheben, D.-X. Xu, J. H. Schmid, and S. Janz, "Colorless directional coupler with dispersion engineered sub-wavelength structure," *Optics Express*, Vol. 20, pp. 13470-13477, 2012.

[234] R. Halir, L. Zavargo-Peche, D.-X. Xu, P. Cheben, R. Ma, J. H. Schmid, S.Janz A. Densmore, A. Ortega-Moñux, Í. Molina-Fernández, M. Fournier and J.-M. Fédeli, "Single etch grating couplers for mass fabrication with DUV lithography", *Optical and Quantum Electronics*, Volume 44, Issue 12, pp. 521-526, (2012) DOI 10.1007/s11082-012-9563-2 (invited).

[235] J.H. Schmid, P. Cheben, P. J. Bock, R. Halir, J. Lapointe, S. Janz, A. Delâge, A. Densmore, T. J. Hall, B. Lamontagne, R. Ma, I. Molina-Fernández and D.-X. Xu, "Refractive Index Engineering with Subwavelength Gratings in Silicon Microphotonic Waveguides," *IEEE Photon. J.*, 597-607, 2011, doi:10.1109/jphot.2011.2139198.

[236] Przemek J. Bock, Pavel Cheben, Jens H. Schmid, Jean Lapointe, André Delâge, Siegfried Janz, Geof C. Aers, Dan-Xia Xu, Adam Densmore, and Trevor J. Hall, "Subwavelength grating periodic structures in silicon-on-insulator: a new type of

microphotonic waveguide," *Optics Express*, Vol. 18, Issue 19, pp. 20251-20262, 2010.

[237] Przemek J. Bock, Pavel Cheben, Jens H. Schmid, Jean Lapointe, André Delâge, Dan-Xia Xu, Siegfried Janz, Adam Densmore, and Trevor J. Hall, "Subwavelength grating crossings for silicon wire waveguides," *Optics Express*, Vol. 18, Issue 15, pp. 16146-16155, 2010.

[238] Robert Halir, A. Ortega-Moñux, Í. Molina-Fernández, J. G. Wangüemert-Pérez, Pavel Cheben, Dan-Xia Xu, Boris Lamontagne, and Siegfried Janz, "Compact High Performance Multi-Mode Interference Couplers in Silicon-Insulator," *IEEE Photonics Technology Letters*, Volume 21, pp. 1600-1602, 2009.

[239] P. J. Bock, P. Cheben, J. H. Schmid, A. Delâge, D.-X. Xu, S. Janz, and T. J. Hall, "Sub-wavelength grating mode transformers in silicon slab waveguides," *Opt. Express* 17, 19120-19133, 2009.

[240] J.H. Schmid, P. Cheben, J. Lapointe, S. Janz, A. Delâge, A. Densmore, D.–X. Xu, "High reflectivity gratings on silicon-on-insulator waveguide facets," *Optics Express*, Vol. 16, Issue 21, pp. 16481-16488, 2008.

[241] R. Halir, I. M. Fernandez, A.Ortega-Monux, J.G. Wanguemert-Perez, D.-X. Xu, P. Cheben, and S. Janz, "A design procedure for high performance rib waveguide multimode interference couplers in silicon-on-insulator," *Journal of Lightwave Technology*, Vol. 26, No. 16, pp. 2928-2936, 2008.

[242] Cheben, P., Janz, S., Xu, D.-X., Lamontagne, B., Delâge, A., and Tanev, S. "A broad-band waveguide grating coupler with a sub-wavelength grating mirror," *IEEE Photonics Technol. Letters* 18, 13-15, 2006.

[243] M. C. Huang, Y. Zhou, and C. J. Chang-Hasnain, "A nanoelectromechanical tunable laser," *Nature Photonics* 1, 119–122, 2007.

[244] Pavel Cheben, Przemek J. Bock, Jens H. Schmid, Jean Lapointe, Siegfried Janz, Dan-Xia Xu, Adam Densmore, André Delâge, Boris Lamontagne, and Trevor J. Hall, "Refractive index engineering with subwavelength gratings for efficient microphotonic couplers and planar waveguide multiplexers," *Opt. Lett.* 35, 2526–2528, 2010.

[245] Przemek J. Bock, Pavel Cheben, Jens H. Schmid, Jean Lapointe, André Delâge, Dan-Xia Xu, Siegfried Janz, Adam Densmore, and Trevor J. Hall, "Subwavelength grating crossings for silicon wire waveguides," *Opt. Express* 18, 16146–16155, 2010.

[246] J.Wang, I. Glesk, and L. R. Chen, “Subwavelength grating filtering devices,” *Opt. Express* 22, 15335–15345, 2014.

[247] A. Maese-Novo, R. Halir, S. Romero-Garc´ıa, D. P´erez- Galacho, L. Zavargo-Peche, A. Ortega-Mo˜nux, I. Molina Fern´andez, J. Wang¨uemert-P´erez, and P. Cheben, “Wavelength independent multimode interference coupler,” *Opt. Express* 21, 7033–7040, 2013.

[248] J. Robinson and Y. Rahmat-Samii, Particle swarm optimization in Electromagnetics, *IEEE Trans. Antennas and Propagat.* 52, pp.397 – 407, (2004).

[249] R. Magnusson, M. Shokooh-Saremi, and E. G. Johnson, Guided-mode resonant wave plates, *Optics Letters* 35, 2472, (2010).

[250] Chubing Peng and William A Challener, “Input-grating couplers for narrow Gaussian beam: influence of groove depth”, *Opt. Express* 12, No. 26, 6481, (2004).

[251] T. Clausnitzer, T. Kämpfe, E.-B. Kley and A. Tünnermann, “An intelligible explanation of highly-efficient diffraction in deep dielectric rectangular transmission gratings”, *Opt. Express* 13, No. 26, 10448, (2005).

[252] Martin Rumpel, Michael Moeller, Christian Moormann, Thomas Graf, and Marwan Abdou Ahmed, “Broadband pulse compression gratings with measured 99.7% diffraction efficiency”, *Opt. Express* 39, No. 2, 323, (2014).

[253] Huijuan Zhang, Chao Li, Xiaoguang Tu, Junfeng Song, Haifeng Zhou, Xianshu Luo, Ying Huang, Mingbin Yu, and G. Q. Lo, “Efficient silicon nitride grating coupler with distributed Bragg reflectors”, *Opt. Express*, Vol. 22, No. 18, 21800, (2014).

[254] W. N. Ye and Y. Xiong, “Review of silicon photonics: history and recent advances,” *Journal of Modern Optics*, vol. 60, pp. 1299-1320, 2013.

[255] Zhenzhou Cheng, Xia Chen, Chi Yan Wong, Ke Xu, and Hon Ki Tsang, “Broadband focusing grating couplers for suspended-membrane waveguides,” *Opt. Lett.* 37, p. 5181, 2012.

[256] K. Yamada, Chapter 1, Silicon Photonic Wire, Waveguides: Fundamentals and Applications. In Topics in Applied Physic, D.J. Lockwood, L. Pavesi (Eds.): Silicon Photonics II., Springer-Verlag Berlin Heidelberg 2011, Vol. 119, pp. 1-29.

[257] Frédéric Grillot, Laurent Vivien, Suzanne Laval and Eric Cassan, Propagation Loss in Single-Mode Ultra small Square Silicon-on-Insulator Optical Waveguides, *Journal of Lightwave Technology*, Vol. 24, 891, (2006).

University Library

A gateway to Melbourne's research publications

Minerva Access is the Institutional Repository of The University of Melbourne

Author/s:
Asaduzzaman, Md

Title:
Light coupling in dimension mismatch waveguides for silicon photonic integrated circuits

Date:
2018

Persistent Link:
http://hdl.handle.net/11343/213424

File Description:
Light Coupling in Dimension Mismatch Waveguides for Silicon Photonic Integrated Circuits

Terms and Conditions:
Terms and Conditions: Copyright in works deposited in Minerva Access is retained by the copyright owner. The work may not be altered without permission from the copyright owner. Readers may only download, print and save electronic copies of whole works for their own personal non-commercial use. Any use that exceeds these limits requires permission from the copyright owner. Attribution is essential when quoting or paraphrasing from these works.